Institute of Low Temperature and Structure Research

Polish Academy of Sciences

DOCTORAL DISSERTATION

in the form of a thematically consistent series of articles published in scientific journals

High-sensitive luminescent thermometers based on formate hybrid perovskites containing Cr^{3+} ions

mgr inż. Adam Kabański

Supervisor: dr hab. Dagmara Stefańska, prof. INTiBS PAN

Wrocław, 2026

To my Dad

Acknowledgements

At this point, I would like to sincerely thank:

my supervisor, ***dr hab. Dagmara Stefańska, prof. INTiBS PAN****,*
for giving me the opportunity to perform this work, for scientific mentoring,
and for creating an environment in which I was able to develop on so many levels.
I also thank you for the support and inspiration that allowed me
to reach the point where I am today. I am deeply grateful.

dr hab. Maciej Ptak, prof. INTiBS PAN *— for invaluable support,*
insightful perspectives on important matters, and kindness,

my colleagues *from the Optical Spectroscopy Division*
and the Structural Research Division for the wonderful atmosphere
of support and warmth. Thanks to you, I have gained
more than just scientific development — I have gained friends,

my mother and sister*, for unconditional love*
and support during difficult moments,
and for sharing joy in times of success.
You are my inspiration and my refuge,

my beloved Agnieszka *— for relief,*

all my friends *from such distant worlds — including Szymony,*
Grunwald, Koneserzy, and many, many others — for lifting me up.

Although I cannot here thank everyone who deserves it, ***I would like to express***
my sincere gratitude *to all those who, even unknowingly, contributed to the creation*
of this work. Thank you for your support, kindness, and for giving me a sense of purpose.

This research was supported by the National Science Center
(Narodowe Centrum Nauki) in Poland under the project SONATA 16
no. 2020/39/D/ST5/01289

NATIONAL SCIENCE CENTRE
POLAND

Table of contents

1. Abstract 1
2. Streszczenie 3
3. Dissertation objectives 5
4. The list of abbreviations 7
5. Introduction 8
    5.1. Hybrid materials 8
        5.1.1. Hybrid organic-inorganic perovskites 9
    5.2. Fundamentals of luminescence 13
    5.3. Spectroscopic properties of Cr^{3+} ions 14
        5.3.1. Temperature-dependent luminescence of Cr^{3+} ions 19
    5.4. Luminescence thermometry 23
        5.4.1. Conventional thermometric methods 23
        5.4.2. Luminescence-based sensors 24
            5.4.2.1. Ratiometric-approach 25
            5.4.2.2. Lifetime-based approach 26
        5.4.3. Luminescent thermometers containing Cr^{3+} ions 27
6. Experimental section 30
    6.1. Synthesis 31
    6.2. Characterization methods 33
        6.2.1. Powder and Single-crystal X-Ray Diffraction 33
        6.2.2. Raman and IR spectroscopy 33
        6.2.3 Differential scanning calorimetry 33
        6.2.4. Diffuse-reflectance spectroscopy 34
        6.2.5. Temperature-dependent luminescence studies 34

7. Results published in the series of publications P1-P5 36
7.1. Publication P1 36
7.2. Publication P2 40
7.3. Publication P3 43
7.4. Publication P4 49
7.5. Publication P5 52
8. Summary 57
9. References 64
10. Copies of publication P1-P5 77
10.1. Publication P1 77
10.2. Publication P2 95
10.3. Publication P3 123
10.4. Publication P4 152
10.5. Publication P5 167
11. Copies of co-authors' statements 184
12. *Curriculum vitae* and scientific achievement 197

1. Abstract

The dynamic development of areas such as science, industry, and medicine requires the implementation of highly accurate methods of monitoring the temperature. This parameter is directly related to a wide range of physical and chemical properties as well as strongly affects the dynamics of many phenomena. Even though conventional temperature sensors provide sufficient characteristics for the majority of the undemanding applications, the specific scientific, industrial, and biomedical sectors require the use of highly sensitive non-contact and remote sensing systems.

Conventional contact thermometers are based on the temperature-induced change of the physical parameters, e.g., thermal expansion in common liquid-based thermometers or electric resistance in thermistors. Currently, the most commercially available non-contact sensing approach is thermal imaging. This method is based on the analysis of infrared radiation intensity emitted and reflected by the measured object. Luminescent thermometers, in turn, use temperature-dependent spectroscopic properties. There are three standard approaches to a luminescence-based temperature detection: analysis of a change in luminescence decay kinetics; monitoring the spectral shift of an emission band; and the comparison of the emission intensity of two spectrum ranges characterized by different temperature dependencies. The last one is known as a ratiometric approach and has become the most commonly reported method.

Although there are a number of thermometric compounds, the vast majority of materials are based on inorganic compounds, usually doped with lanthanides.[1] However, the group of metal-organic frameworks (MOFs) are promising material for luminescent thermometry.[2,3] MOFs may exhibit several interesting properties simultaneously, and their characteristics can often be tuned by the substitution of the building blocks. Among various MOFs, the group of materials with perovskite stoichiometry containing formate ($HCOO^-$) linkers, doped with chromium(III) ions (Cr^{3+}), is particularly noteworthy. Their high stability as well as reliability and accessibility of preparation, overcoming most of the halide-based compounds, make these materials a valuable choice for studies concerning the influence of chemical composition on spectroscopic and, subsequently, thermometric properties. Depending on the chemical composition of the analyzed materials, including the type of amine, the type of metal, and the concentration of chromium(III) ions, it is possible to obtain different spectroscopic properties related to the Cr^{3+} luminescence. The local environment of the chromium ions can be described by the crystal field strength, which induces the dominant emission type of the Cr^{3+} ions: narrow spin-forbidden $^2E_g \rightarrow {}^4A_{2g}$ or broad spin-allowed $^4T_{2g} \rightarrow {}^4A_{2g}$ transitions. Hybrid compounds based on Cr^{3+} ions exhibit a significant temperature dependence of their luminescent properties, which has become a starting point for their application in the field of luminescent thermometry. The observed influence of chemical composition on luminescent properties also affects their thermometric characteristics.

The primary objective of this work is to describe the relationship between the chemical composition of hybrid formate materials doped with Cr^{3+} ions, described by single- and double-perovskite stoichiometry, and their spectroscopic properties as well as, consequently, their thermometric performance. In this dissertation, 5 series of compounds differing in chemical

compositions were synthesized, analysed, and further described in a series of five thematically coherent publications **P1-P5**. Among the investigated series, two of them focus on materials with double-perovskite stoichiometry (**P1-P2**), while others are devoted to single-perovskite-like materials (**P3-P5**). Taking included works into account, the analysis of the 38 individual samples has been performed.

The study provides a detailed description of their structural, phonon, and spectroscopic properties as well as their relation to chemical composition, which was tuned by modifying the fundamental building blocks of the hybrid frameworks. Based on the collected data, the general relations between crystal-field strength, the type of metal ions and organic cations, dopant concentration, and resulting luminescent and thermometric behaviour were established. Thermometric analyses demonstrated the possibility of achieving high relative sensitivities, reaching up to 3.91%·K^{-1} at 140 K (ratiometric method) and 5.14%·K^{-1} at 143 K (lifetime-based method). Through multiparametric thermometric analysis, various sensing strategies were systematically compared, enabling further optimization of thermometric model development. The proposed prototype thermometric setups, operating under steady-state conditions and in the time domain, illustrate the potential of the investigated materials as cryogenic temperature sensors.

2. Streszczenie

Dynamiczny rozwój takich obszarów jak nauka, przemysł i medycyna wymaga wdrażania wysoce precyzyjnych metod monitorowania temperatury. Parametr ten jest bezpośrednio związany z szerokim zakresem właściwości fizycznych i chemicznych oraz ma istotny wpływ na dynamikę wielu zjawisk. Mimo że konwencjonalne czujniki temperatury zapewniają wystarczające parametry dla większości niewymagających zastosowań, specyficzne sektory naukowe, przemysłowe i biomedyczne wymagają stosowania wysoce czułych, bezkontaktowych oraz zdalnych systemów pomiarowych.

Konwencjonalne termometry kontaktowe opierają się na zmianach właściwości fizycznych indukowanych przez zmianę temperatury, np. rozszerzalności cieplnej w popularnych termometrach cieczowych lub zmianie oporu elektrycznego w termistorach. Obecnie najczęściej stosowanym komercyjnie rozwiązaniem bezkontaktowym jest obrazowanie termiczne. Metoda ta polega na analizie intensywności promieniowania podczerwonego emitowanego oraz odbijanego przez mierzony obiekt. Termometry luminescencyjne z kolei wykorzystują zależne od temperatury właściwości spektroskopowe. Istnieją trzy standardowe podejścia do detekcji temperatury opartej na luminescencji: analiza zmian czasu życia emisji; monitorowanie przesunięcia określonego pasma; oraz porównanie intensywności emisji w dwóch zakresach widma charakteryzujących się różną zależnością intensywności w funkcji temperaturowy. Ostatnie z tych podejść, znane jako metoda oparta na stosunki intensywności pasm (ang. *ratiometric, ratio* – stosunek, proporcja), jest obecnie najczęściej opisywanym w literaturze podejściem.

Chociaż opisano wiele związków termometrycznych, to zdecydowana większość materiałów oparta jest na związkach nieorganicznych, zazwyczaj domieszkowanych jonami lantanowców. Jednak grupa związków metalo-organicznych (ang. *Metal-Organic Frameworks, MOF*) stanowi obiecującą klasę materiałów do zastosowań w termometrii luminescencyjnej. Związki te wykazują równocześnie szereg interesujących właściwości, a ich charakterystyki można często modyfikować poprzez zmianę składu chemicznego. Wśród różnych MOF-ów, związki o stechiometrii perowskitu zawierające łączniki mrówczanowe ($HCOO^-$), domieszkowane jonami chromu(III) (Cr^{3+}), zasługują na szczególną uwagę. Dzięki ich stabilności oraz przystępności i powtarzalności syntezy, większej niż w przypadku niektórych związków halogenkowych, związki te stanowią dobry wybór w kontekście prowadzenia badań nad wpływem zmiany ich składu chemicznego na właściwości spektroskopowe oraz, w rezultacie, termometryczne. W zależności od składu chemicznego analizowanych materiałów - w tym rodzaju aminy, typu metalu oraz stężenia jonów chromu(III) - możliwe jest uzyskanie odmiennych właściwości spektroskopowych związanych z luminescencją Cr^{3+}. Lokalne otoczenie jonów chromu można opisać poprzez siłę pola krystalicznego, która determinuje dominujący typ emisji jonów Cr^{3+}: wąskopasmową emisję spinowo zabronioną $^2E_g \rightarrow {}^4A_{2g}$ lub szerokopasmową emisję spinowo dozwoloną $^4T_{2g} \rightarrow {}^4A_{2g}$. Związki hybrydowe oparte na jonach Cr^{3+} wykazują znaczącą zależność właściwości luminescencyjnych od temperatury, co stało się punktem wyjścia do zastosowania ichw obszarze termometrii luminescencyjnej. Obserwowany wpływ składu chemicznego na właściwości luminescencyjne przekłada się również na zmienną charakterystykę termometryczną tych materiałów.

Głównym celem niniejszej pracy było opisanie wpływu składu chemicznego serii materiałów hybrydowych o strukturze pojedynczego oraz podwójnego perowskitu domieszkowanych jonami Cr^{3+} na ich właściwości spektroskopowe, a w konsekwencji również na ich charakterystykę termometryczną. W toku prac dokonano syntezy oraz analizy 5 grup związków różniących się składem chemicznym, przedstawionych w cyklu pięciu tematycznie spójnych publikacji **P1-P5**. Spośród badanych serii dwie koncentrują się na materiałach o stechiometrii podwójnego perowskitu (**P1-P2**), natomiast pozostałe trzy dotyczą materiałów o stechiometrii pojedynczego perowskitu (**P3–P5**). Sumarycznie przeprowadzono analizę 38 próbek. W niniejszej rozprawie opisano właściwości strukturalne, fononowe i spektroskopowe oraz ich zależność od składu chemicznego, dostosowywanego poprzez zmianę podstawowych bloków budulcowych związków hybrydowych. Na podstawie wyników określono szereg zależności między siłą pola krystalicznego, rodzajem jonów metali i kationów organicznych, oraz stężenia jonów domieszki na właściwości luminescencyjne i termometryczne. Przeprowadzone analizy termometryczne wykazały możliwość uzyskania wysokiej czułości względnej – do $3.91\%\cdot K^{-1}$ w 140 K (metoda oparta na stosunku intensywności pasm emisyjnych) oraz $5.14\%\cdot K^{-1}$ w 143 K (metoda oparta na kinetyce zaniku luminescencji). Poprzez wieloparametryczną analizę uzyskano porównanie możliwych strategii termometrycznych, co umożliwia dalszą optymalizację procesu wyznaczania modelu termometrycznego. Zaproponowane prototypowe układy termometryczne pracujące w warunkach statycznych oraz przy zmiennej temperaturze obrazują wysoki potencjał badanych materiałów jako czujników temperatury w zakresie kriogenicznym.

3. Dissertation objectives

The main objective of this PhD dissertation is to systematically investigate the potential of hybrid compounds with single- and double-perovskite stoichiometry as highly sensitive luminescent thermometers, with particular emphasis on elucidating the role of chemical composition and Cr^{3+} ion concentration in determining their structural, spectroscopic, and thermometric properties. An additional aim is to verify the commonly accepted models underlying Cr^{3+}-based luminescent thermometry and to assess the practical applicability of the investigated materials for temperature sensing in the cryogenic range.

The realization of the main objective was pursued through the following specific objectives:

1. Development of a synthesis method for hybrid compounds, differing in the type of amines used, metal cations, and the concentration of Cr^{3+} ions. Among the studied materials, two main groups can be distinguished:

- **materials with a single perovskite stoichiometry**: $[A]M^{II}(HCOO)_3$: xCr^{3+}, where A represents a protonated amine (EA^+, DMA^+), M^{II} is a divalent metal cation (Zn^{2+}, Mg^{2+}, Mn^{2+}, Co^{2+}, Ni^{2+}), and x is a chromium(III) content (up to 5 mol.%),
- **materials with a double perovskite stoichiometry**: $[A]_2M^IM^{III}(HCOO)_6$: xCr^{3+}, where A is a protonated amine (EA^+), M^I and M^{III} stand for mono- (Na^+) and trivalent (Al^{3+}, Ga^{3+}) metal cations, respectively, and x is a chromium(III) content (up to 100 mol.%).

The obtained materials were examined in terms of their structural and phonon characteristics with pXRD, scXRD, and DSC techniques, as well as with Raman and IR analysis.

2. Spectroscopic analysis of the obtained compounds, with particular emphasis on their photoluminescent characteristics under varying temperature conditions. This area can be further divided into the following aspects:

- optical studies (excitation, emission, and luminescence decay kinetics),
- analysis of the relationship between the chemical composition, the corresponding crystal field strength, and the resulting emission assigned to $^2E_g \rightarrow {}^4A_{2g}$ and $^4T_{2g} \rightarrow {}^4A_{2g}$ transitions,
- development of a thermometric model and further determination of key parameters describing thermometric performance, most notably the relative sensitivity,
- meta-analytical approach to assessing the influence of chemical composition on thermometric properties.

3. Verification of commonly applied paradigms underlying the determination of thermometric models and **assessment of the practical applicability** of the investigated compounds for temperature monitoring in the cryogenic range. An additional aim of this dissertation was to provide a broader perspective on the development and optimization of thermometric models based on the luminescence of Cr^{3+} ions. For this purpose, the following aspects were considered:

- comparative analysis of thermometric performance of studied compounds,
- investigation of the usefulness of both ratiometric and lifetime-based thermometric approaches,
- investigation of the multimodal ratiometric approach.

Moreover, as part of the study, prototype thermometric systems were proposed for time-resolved temperature monitoring and temperature distribution imaging in real systems.

By achieving the above objectives, this dissertation aims to broaden the current understanding of how chemical composition (type of protonated amine and metal ion, and Cr^{3+} concentration) influences spectroscopic properties and, consequently, thermometric performance. This knowledge will enable more conscious design of other materials with desirable structural properties and useful thermometric characteristics.

4. The list of abbreviations

ATR	Attenuated Total Reflectance
CCDC	Cambridge Crystallographic Data Centre
CF	Crystal Field
CFT	Crystal Field Theory
DMA	Dimethylamine
DRS	Diffuse-Reflectance Spectroscopy
DSC	Differential Scanning Calorimetry
EA	Ethylamine
EDS	Energy-Dispersive X-ray Spectroscopy
EPR	Electronic Paramagnetic Resonance
FWHM	Full With at Half Maximum
GA	Guanidinium
HTP	High-Temperature Phase
IR	Infrared
LHP	Low-Temperature Phase
LIR	Luminescence Intensity Ratio
LT	Lifetime
MOFs	Metal-Organic Frameworks
MRP	Multiphonon Relaxation
PT	Phase Transition
PL	Photoluminescence
pXRD	Powder X-Ray Diffraction
RM	Ratiometric Method
RT	Room Temperature
scXRD	Single-Crystal X-Ray Diffraction
SHG	Second-Harmonic Generation
TEA	Triethylamine
TM	Transition Metal
XRD	X-ray Diffraction
τ_{avg}	Average Luminescence Lifetime
τ_{fit}	Fitted Average Luminescence Lifetime

5. Introduction

5.1 Hybrid materials

Materials that combine organic and inorganic components, known as hybrid materials, represent a significant aspect of the development of functional materials. Due to the presence of both organic and inorganic building blocks, it is possible to obtain unique properties that arise directly from the specific components used. This combination often results in materials with unique physical and chemical properties that are not achievable with purely organic or inorganic compounds. By uniting the complementary attributes of disparate materials, hybrids enable performance characteristics that surpass those of their individual components.[4–6]

The field of hybrid materials is, in principle, very wide and contains various approaches and perspectives on the topic of properties merging. Among the many hybrid materials that have been intensively studied in recent years, the group of materials forming metal-organic frameworks (MOFs) is particularly noteworthy. MOF-type compounds form an extended three-dimensional framework in which metal ions (or clusters) are connected by linkers, most often organic ones.[7,8] These frameworks form highly porous structures with exceptionally high surface areas and tunable pore sizes. MOFs have found applications in gas storage, catalysis, drug delivery, and sensing, owing to their structural versatility and chemical functionality.[8–11] Nonetheless, MOFs have been implemented as a part of other hybrid solutions, such as with a combination of covalent organic frameworks (COFs), characterized by a fully organic nature. It enables precise control over pore structure and π-conjugation, making them promising for energy storage, photocatalysis, and optoelectronics.[12–15] The potential of hybrids is also demonstrated by other groups of organic-inorganic solutions. Exemplary, polymeric nanocomposites incorporating nanoparticles, nanoclasters, or quantum dots into polymer matrices have been developed for lightweight structural components and flexible electronic devices.[16,17] Another valuable group of hybrid materials is bio-inspired hybrids, mimicking specific biological tissues or bones, which illustrate the potential of hybrid design principles for achieving exceptional mechanical, physical, and chemical properties.[18–20]

Although there are significant amounts of prominent hybrid materials, the group of metal-organic materials exhibiting perovskite-like architecture has gained increasing attention due to their unique structural characteristics as well as chemical and physical properties.[21–23] This class of MOFs does not exhibit a developed porosity, such as is crucial for many MOF-based systems, designed for sorption or catalytic requirements. In this case, the molecular cavities of the metal-organic framework are filled during the synthesis, resulting in a system containing a rigid *metal-linker framework* and organic *infill*.[24–27] Due to their compositional modularity, well-defined architecture, and possibility of various metal ion incorporation, the group of hybrid perovskite-like materials shows a significant potential from the point of view of materials science.[23,28–30]

5.1.1 Hybrid organic-inorganic perovskites

One of the important subgroups of hybrid materials is the field of organic-inorganic compounds with a perovskite architecture. Originally, the term *perovskite* refers to the common name of a mineral — calcium titanate, $CaTiO_3$. However, today this term is widely used to name compounds that exhibit an analogous stoichiometry and geometrical characteristics, also described by the general formula AMX_3, in which A is a cation (e.g., Cs^+, Ca^{2+}) occupying a cuboctahedral cavity formed by the MX_6 octahedra, where M is metal ion (e.g. Pb^{2+}, Ti^{4+}) and X is an ionic linker (e.g. O^{2-}, Cl^-). Although the *proper* perovskite - $CaTiO_3$, at room temperature (RT) adopts $Pm\bar{3}m$ space group (cubic O_h symmetry), the compositional diversity leads to the variety of actual structural characteristics of compounds meeting the perovskite stoichiometry.[31–33] Exemplary, the strontium titanate, $SrTiO_3$, adopts the tetragonal *I4/mcm* space group (RT), while rhombohedrally distorted $LaAlO_3$ at RT shows $R\bar{3}c$ space group.[34]

Hybrid compounds with a perovskite stoichiometry can also be described by a general formula $[A]M^{val}X_{val+1}$, where A represents an organic cation (e.g., protonated amine), M is a metal cation, X stands for the linking anion, and *val* describes the valence of the metal ion. Among hybrid *perovskites*, the group of single perovskite-like compounds with divalent metal ions, described as $[A]M^{II}X_3$, has gained particular attention. Exemplary, $[MA]PbI_3$ and $[FA]SnI_3$ have been proposed as effective materials for photovoltaics.[35,36] However, this group of materials may also exhibit interesting magnetic and electronic characteristics.[37,38] Hybrid perovskites can also form compounds with a more developed double architecture, with a general formula $[A]_2M^IM^{III}X_6$, where M^I and M^{III} stand for mono- (e.g. Na^+, K^+) and trivalent metal ions (e.g. Fe^{3+}, Cr^{3+}), respectively (**Figure 1**). Such compounds represent valuable materials in which the use of trivalent metal ions leads to new, unique properties, e.g., luminescence, ferroelasticity or semiconductivity.[39–41]

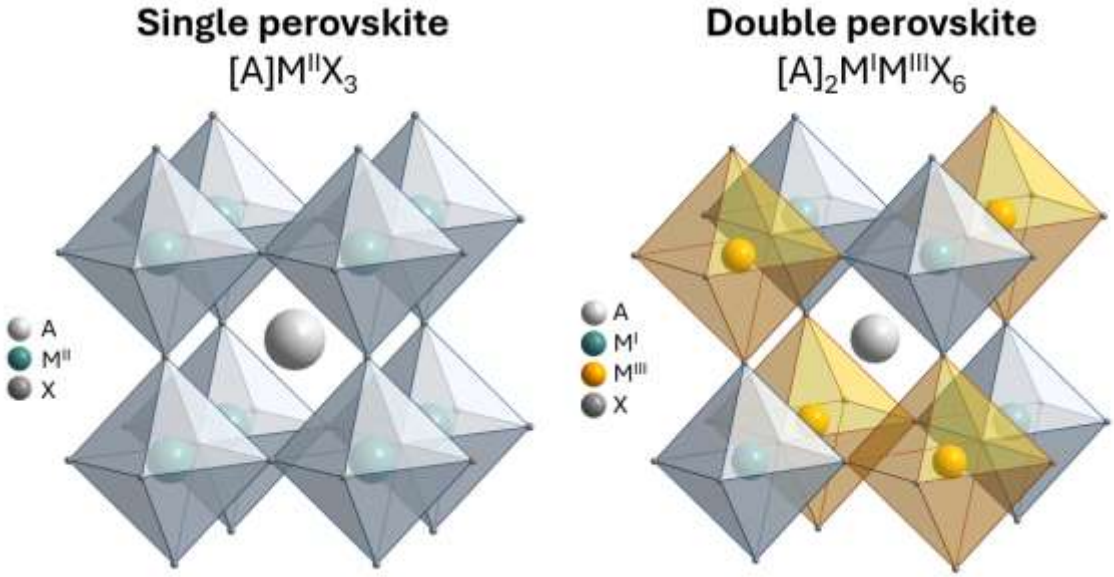

Figure 1. The visualization of the single- and double perovskite architecture

Although hybrid perovskite-like compounds offer substantial flexibility in terms of their possible building blocks (A-, M-, and X-site constituents), their stability is strongly related to

their geometric characteristics, which can be described by the so-called *Goldschmidt tolerance factor*.[42,43] For the inorganic compounds following AMX_3 stoichiometry, it can be calculated according to:

$$TF = \frac{r_A + r_X}{\sqrt{2}(r_M + r_X)}, \quad (1)$$

where *r* is a ionic radius of particular A-, B-, and X-ions. Values of TF close to 1 typically indicate that the material shows perovskite-like structure, whereas significant deviations predict octahedral tilting, symmetry lowering, or complete destabilization of the structure. Usually, the range of TF from 0.8 to 1.0 is presented as the most stable.[42] In organic-inorganic perovskite-like materials, with general formula $[A]M^{II}X_3$ (single perovskite stoichiometry), application of the presented tolerance factor should include additional elements, mainly the non-spherical, flexible geometry of molecular A-site cations and their possible hydrogen-bonding and orientational dynamics. To accommodate these effects, the development of the formula (1) is applied:

$$TF = \frac{r_{A,eff} + r_X}{\sqrt{2}(r_{M^{II}} + r_X)}, \quad (2)$$

where $r_{A,eff}$ is the effective radius of a A-site organic cation, calculated according to van der Waals dimensions or from analyses of crystallographic data. There is a notable amount of hybrid perovskite-like materials going beyond the 0.8-1.0 range of TF values, which indicates the more complex interatomic relation compared to inorganic structures.[42,44]

Although the following approach is suitable for hybrid materials with single perovskite stoichiometry, the group of double perovskite-like compounds, with a general formula $[A]_2M^IM^{III}X_6$, should be described by a more developed tolerance factor. The presence of two types of metal ions makes it necessary to distinguish an additional parameter – an average M-site ionic radius $r_{m,avg}$. Then, the TF formula is:

$$TF = \frac{r_{A,eff} + r_X}{\sqrt{2}\left(\frac{r_{M^I} + r_{M^{III}}}{2} + r_X\right)}, \quad (3)$$

where ionic radii of M^I and M^{III} cations are taken into consideration.[45]

The perovskite-like hybrid compounds may create the developed three-dimensional framework, built with the metal cations creating MX_6 octahedra. Organic cation, in turn, is localized inside the framework's voids. Described compounds can also adopt two-, one, and zero-dimensional structures, significantly affecting their characteristics.[46–49] However, three-dimensional hybrids are the most common, thus particular attention will be devoted to this group of materials. They are characterized by the possibility of modifying their basic building blocks, which results in a variety of structural, magnetic, dielectric, optical, and other properties. The diversity in the possible chemical composition is based on their inherent modularity, which is the ability to obtain materials that differ only by one of their structural components.[50,51]

Within the group of materials with perovskite stoichiometry, compounds containing protonated amines are commonly described. For example, materials containing methylammonium [MA^+], ethylammonium [EA^+], formamidinium [FA^+], or hydrazinium [Hy^+] cations are extensively investigated for their structural, magnetic, and electronic properties.[52–58] The choice of a specific organic cation is limited by the size of the structural cavity and the stability of the framework itself. The most commonly used metals are Pb^{2+}, Sn^{2+}, and Cd^{2+}. However, compounds based on metals such as Mn^{2+}, Ni^{2+}, Co^{2+}, or Fe^{2+} are gaining increasing attention.[59,60] Modulation of properties can also be achieved by changing the type of ionic linker, enabling the obtaining of compounds in which the distances between the MX_6 octahedra are modified, and as a result, larger organic cations can be fitted inside the framework's voids (**Figure 2**).[61] Among the most frequently implemented anions are halides (Cl^-, Br^-, I^-), as well as cyanides (CN^-), thiocyanates (SCO^-), and azides (N_3^-). However, special attention should also be given to formate ($HCOO^-$), hypophosphite ($H_2PO_2^-$), and dicyanamide anions ($N(CN)_2^-$), forming frameworks with larger cavities, in which larger organic cations with more degree of freedom can be allocated.[62,63]

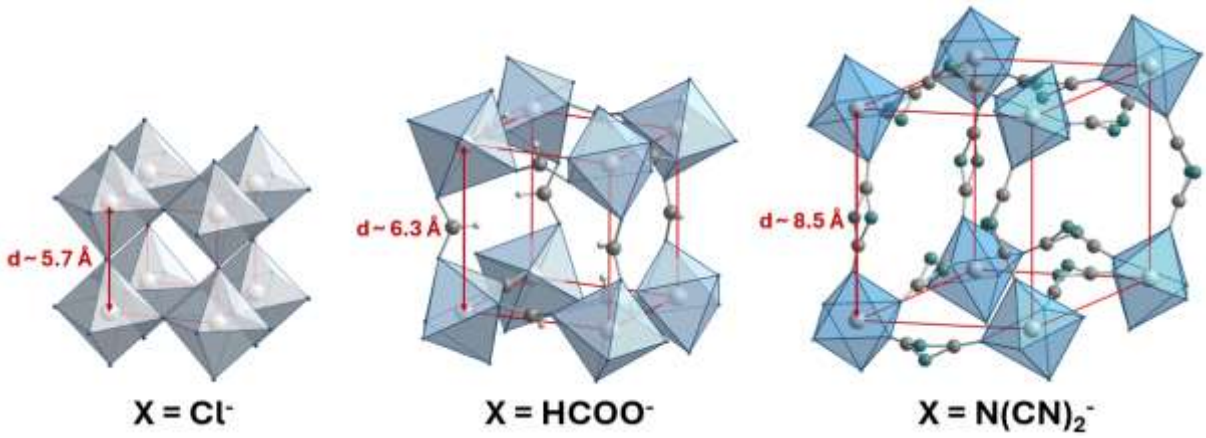

Figure 2. Diversity of the hybrid perovskites depending on the type of implemented X-site anion with metal-metal distance markers (*d*)

Moreover, the presence of highly electronegative atoms within these anions (oxygen or nitrogen) enables the formation of additional hydrogen bonds, which can influence both the material's stability and the dynamics of the organic cation.[63–65] As a result, these linkers represent valuable structural building blocks for materials intended for systematic studies on how factors such as the type of amine or metal ion affect their structural, phononic, and spectroscopic properties. An additional factor contributing to the exceptionally wide range of possible chemical compositions is the possibility of using mixed compositions (e.g., simultaneous implementation of two X-site linkers), which allows for obtaining new, desirable properties.[36,66,67]

Within the field of compounds with hybrid perovskite-like composition, particular attention should be given to the group of compounds containing formate anions ($HCOO^-$). Although these compounds have not yet been extensively described in the literature, they exhibit interesting structural, magnetic, and optical properties — both linear and nonlinear.[68–71]

Due to the use of the more complex formate anion instead of halide ions, it is possible to obtain a structure stable enough to allow the incorporation of larger, more complex organic cations.[72,73] Hybrid formates have been identified as possible materials for spintronics as well as advanced electronic and magnetic technologies due to their unique multiferroic and magnetic properties. Exemplary, in the work of Scatena *et al*.,[74] the investigation of $[DMA]Cu(HCOO)_3$ suggests that formate ligands mediate the magnetic exchange, which, due to its directional nature, is essential for designing spintronic materials. The multiferroic characteristics of formate-based hybrid are, in turn, presented within the series of $[GA]Mn_{1-x}Fe_{2x/3}(HCOO)_3$, where $0 \leq x \leq 0.88$, reported by Bulled *et al*.[75] It shows that ion substitution and resulting vacancies ordering can induce percolative ferrimagnetic phases, which indicates a route to design magnetic properties of hybrid materials. However, individual studies have also pointed out their high potential as luminescent materials operating under low-temperature conditions. The pioneering results, presented by Ptak *et al*.,[76] describe a series of $[MA]M_{0.5}Cr_xAl_{0.5-x}(HCOO)_3$, where M = Na, K; x = 0, 0.025, 0.5. Due to the presence of the Cr^{3+} ion, which exhibits significant temperature-dependent luminescence, it can be further used to determine the thermometric model. This work also indicates the potential of formate-based materials with double-perovskite stoichiometry as host matrices for ions exhibiting specific properties, such as magnetic characteristics of Fe^{3+} ions.[77,78] The possibility of incorporating trivalent ions, including the Cr^{3+} ion, which is of particular interest in this work, allows for the design of luminescent materials whose spectroscopic characteristics depend not only on the surrounding environment but also on the composition of the hybrid host material.[76]

5.2 Fundamentals of luminescence

The dynamic technological development of recent decades has created the need to design technological solutions that enable the monitoring of particular physical parameters, such as temperature. Nowadays, there are many different types of sensors — operating under various environmental conditions, differing in design, and based on diverse methodological principles.[79,80] In the context of this dissertation, particular attention should be given to luminescent sensors, in which the determination of specific physical quantities, with a special focus on temperature, is carried out through the analysis of luminescent properties.[81,82]

Luminescence is the phenomenon of electromagnetic radiation emission by a substance that has previously absorbed energy in another form. Depending on the origin of electron excitation, luminescence can be divided into several categories, such as chemiluminescence (resulting from a chemical reaction), electroluminescence (induced by an electric field), mechanoluminescence (resulting from mechanical interaction — scratching, friction), or, particularly important for this dissertation, photoluminescence.[83] The phenomenon of photoluminescence occurs when a material absorbs incident radiation and subsequently emits phonons. This type of luminescence has been widely implemented in the study of solid materials due to the simplicity of the measurement process, combined with broad possibilities for its modification, and the ability of this method to provide valuable analytical information.[83,84]

The phenomenon of photoluminescence involves two fundamental processes: absorption and emission of radiation. During absorption, a photon of sufficient energy promotes an electron to a higher, more energetic electronic state. After excitation, the system relaxes through a series of intermediate processes, resulting in photon emission as the electron returns to the ground state. The emitted radiation typically has lower energy (longer wavelength) than the absorbed phonons, due to the presence of non-radiative relaxation pathways. The schematic representation of the mentioned processes is presented in **Figure 3**.

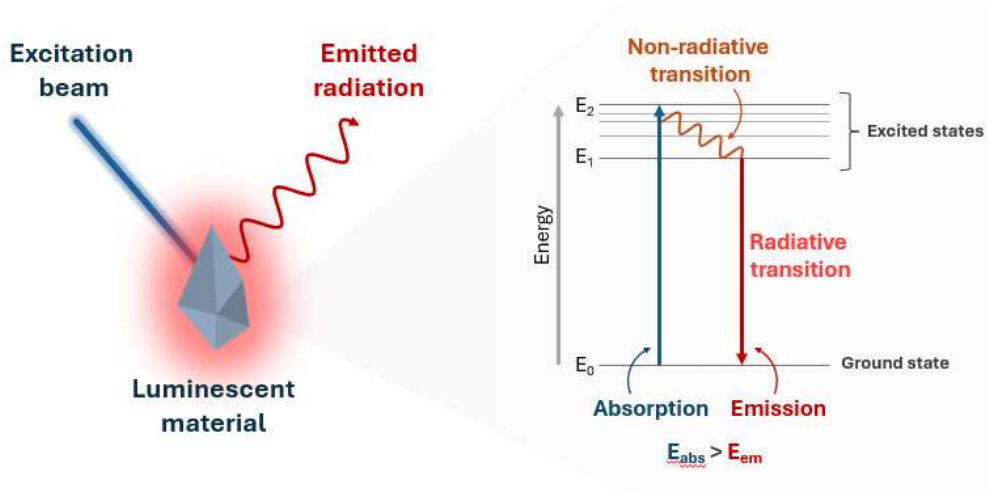

Figure 3. The schematic representation of the photoluminescence phenomena

Excited states can be depopulated via two types of mechanisms: radiative and non-radiative processes. Radiative processes involve photon emission — the essence of luminescence - while

non-radiative processes lead to energy dissipation through heat, lattice vibrations (phonons), and by energy transfer via neighbouring ions to a nonradiative recombination centre. This can be observed, among other effects, as a reduction in luminescence efficiency when the concentration of the luminescent centres exceeds an optimal threshold, which is known as concentration quenching.[83] The efficiency of non-radiative relaxation increases with temperature, resulting in thermal quenching of luminescence, which is described in detail in a further part of this work (see **Chapter 5.3.1**).

Photoluminescence is a valuable tool in the development of various types of sensors due to the remarkable influence of the environmental conditions (e.g., temperature, pressure, presence of particular molecules and ions) on its characteristics.[84–86] The growing field of luminescent thermometers, which is also the focus of this dissertation, clearly illustrates the potential of sensors based on the analysis of temperature-dependent spectroscopic properties. The sensing model may be constructed on the change in the shape and intensity of the luminescence spectrum or in the kinetics of the emission decay (see **Chapter 5.4**). Nevertheless, photoluminescence is also successfully applied in other areas, such as pressure sensors.[87–89] One of the most notable examples is the use of synthetic ruby (Al_2O_3: Cr^{3+}) in high-pressure studies within diamond anvil cells.[88,90] Photoluminescence-based sensors also show great potential in analytical chemistry, where methods relying on this phenomenon can be used to detect contamination by specific ions,[91,92] the presence of certain chemical molecules in the food industry,[93] or to analyze a wide range of environmental parameters, such as humidity[94–96] or pH.[97,98] The remarkable versatility of photoluminescence as a sensing mechanism, coupled with the wide multiplicity of reported and precisely characterized luminescent materials, positions the field of luminescent sensors as exceptionally promising for a broad range of analytical and technological applications. This combination enables the design of highly sensitive and selective sensors capable of detecting diverse physical and chemical parameters under varied environmental conditions.

5.3 Spectroscopic properties of Cr^{3+} ions

Chromium(III) ions, classified as transition metal (TM) ions, exhibit a number of properties that make them particularly interesting from the perspective of luminescent sensors. One of the crucial characteristics of Cr^{3+} ions is their sensitivity to the local crystal environment. Chromium(III) ions possess a $3d^3$ electronic configuration, meaning that their *3d* electrons are not shielded, as is the case for *4f* electrons in lanthanide ions.[83] Changes in the local environment of Cr^{3+} ions, caused by ion-ligand interactions, crystallographic characteristics, as well as macroscopic properties such as specimen morphology, can lead to variations in the observed spectroscopic properties.[83,99,100] It includes not only the change in some qualities of an emission spectrum, but also in luminescence decay kinetics. As a result, compounds containing Cr^{3+} ions may exhibit distinct luminescent properties depending on the implemented host matrix. In some host materials, even slight changes in their chemical composition have a measurable impact on the luminescent characteristics.

The influence of the local crystal environment on spectroscopic characteristics of Cr^{3+} ions may be described with crystal field theory (CFT). It describes how the degenerate energy levels of transition-metal *d*-orbitals split when a metal ion is surrounded by ligands that create an electrostatic field. The theory assumes that ligands act as point charges or dipoles, and their negative electric fields interact with the positively charged metal cation. This interaction affects the degeneracy of the d-orbitals, creating distinct energy levels whose separation depends on the geometry and strength of the ligand field.[83,101] The schematic representation of this process, for the particularly representative O_h symmetry, is presented in **Figure 4**.

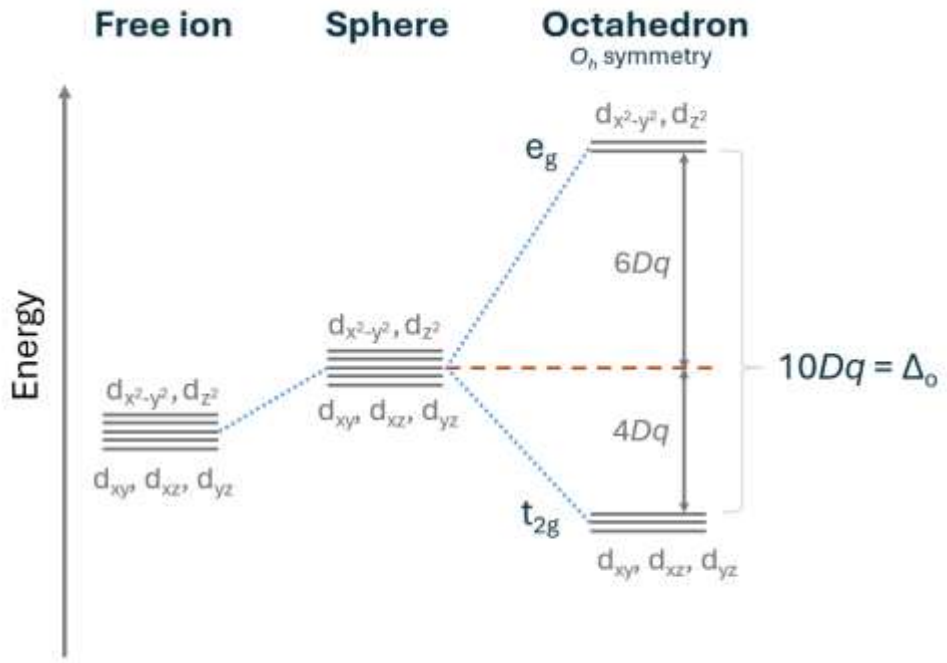

Figure 4. The simplified diagram showing a d-orbital splitting in transition metal ions in the O_h symmetry (octahedral coordination)

In the form of the free ion Cr^{3+}, all five d-orbitals (d_{xy}, d_{xz}, d_{yz}, d_{z^2}, $d_{x^2-y^2}$) have the same energy. In this state, the ion is unaffected by any external electric field, so no preferential energy separation exists among the orbitals. When the ion is placed in a spherically symmetric field, the overall energy of the d-electrons increases due to electrostatic repulsion with surrounding charges, but the degeneracy of the orbitals is still maintained, so all five orbitals remain energetically equivalent. When the Cr^{3+} ion is coordinated by six ligands in an octahedral geometry (O_h symmetry), the degeneracy is not maintained due to the directional nature of the ligand field. The five d-orbitals split into two energy levels:

- t_{2g} (d_{xy}, d_{xz}, d_{yz}) – lower energy
- e_g ($d_{x^2-y^2}$, d_{z^2}) – higher energy

The energy separation between t_{2g} and e_g is known as the crystal field splitting parameter, marked as Δ or $10Dq$. This parameter is related to electrostatic interactions between the d-electrons and the surrounding ligands, which is the origin of the surrounding-related dependence of energetic characteristics of Cr^{3+}-based materials.[83,101]

The luminescent properties of chromium(III) ions arise from its electronic configuration - Cr^{3+}: [Ar]$3d^3$. In a free-ion state, several energy states can be distinguished, depending on the electron distribution and responding quantum numbers (and resulting L and S, described below).[83,101] Exemplary, the following states can be described:

- low-energy distribution (3 unpaired electrons): L = 3, and S = $\frac{3}{2}$,
- high-energy distribution (e.g. 2 paired and 1 unpaired electrons): L = 4, and S = $\frac{1}{2}$,

where L is the total orbital angular momentum, and S is the total spin angular momentum. To determine the following terms, the given formula may be used:

$$^{2S+1}L, \tag{4}$$

where L is typically marked with letter symbol {S, P, D, F, G, …} for L = {0, 1, 2, 3, 4, …}, respectively.[102,103] Thus, the low-energy term of Cr^{3+} is ^4F (ground state), while one of the excited states, described above, is ^2G. Within the context of Cr^{3+} ions, containing 3 electrons on the d-subshell (10 possible electrons), 120 individual microstates can be distinguished. Furthermore, 8 terms, according to the Russell–Saunders model, can be determined – ^4F, ^4P, ^2P, $^1D_{(1)}$, $^2D_{(2)}$, ^2F, ^2G, and ^2H.[101] Among the mentioned terms, two of them — ^4F (lowest-energy) and ^2G (higher-energy), directly translate into the observed luminescent characteristics, thus further considerations are mainly devoted to these particular terms.

Under the octahedral symmetry, the ^4F term splits into three states:

- $\mathbf{^4A_{2g}}$ – the ground state,
- $\mathbf{^4T_{1g}}$ – higher energy excited level,
- $\mathbf{^4T_{2g}}$ – lower energy excited level.

While the higher energy ^2G term splits into the $\mathbf{^2E_g}$ excited state. Under the excitation wavelength, the electron may be excited from the $^4A_{2g}$ ground state to higher-energy levels. Due to the efficient non-radiative transition from the $^4T_{1g}$ level to a nearby $^4T_{2g}$, the photon emission from higher-energetic $^4T_{1g}$ is not observed. Thus, the radiative relaxation may occur from the $^4T_{2g}$ and ^2E_g levels. The radiative processes: spin-forbidden $^2E_g \rightarrow {}^4A_{2g}$ and spin-allowed $^4T_{2g} \rightarrow {}^4A_{2g}$, exhibit different luminescent characteristics. The transition from the ^2E_g excited level, showing spin-forbidden nature (change from doublet to quarter state), is observed in the form of a narrow emission lines, with the most intensive line – called the R_1 line – is localized around 680-720 nm. Additionally, several additional lines can be observed, such as the R_2 line (higher-energy, weaker companion line[104]) and N-lines (lower-energy, from exchange-coupled Cr^{3+}-Cr^{3+} pairs[105]). The spin-allowed $^4T_{2g} \rightarrow {}^4A_{2g}$ radiative relaxation, occurring without a change of the spin state, forms, in turn, broadband emission within the 750-1000 nm. These two characteristic types of luminescence also differ in their emission decay times. For the $^2E_g \rightarrow {}^4A_{2g}$ transitions, decay times are typically on the order of hundreds of microseconds to several milliseconds, whereas for the $^4T_{2g} \rightarrow {}^4A_{2g}$ transitions, they are approximately an order of magnitude shorter.[106,107]

The occurrence and intensity of a specific type of emission are related to the energies of particular electronic levels, which in turn depend on the local environment of the Cr^{3+} ions. A particularly important parameter in this context is the so-called *crystal field strength* (CF strength, *Dq/B*), expressed as the formula:

$$CF\ strength \equiv \frac{Dq}{B}, \tag{5}$$

where *Dq* describes the splitting between the e_g and t_{2g} orbitals, and *B* is a Racah parameter representing an approximation of the bond strength between the ligand and the metal, based on electron-electron repulsion.

Optical measurements (mainly absorption, excitation, and photoluminescence) can provide information about the energies of individual transitions from the excited $^4T_{2g}$ and ^2E_g levels to the ground $^4A_{2g}$ level. Based on experimental data, it is then possible to determine the *Dq/B* parameter using the following equations:

$$Dq = \frac{E\ ^4A_{2g} \rightarrow\ ^4T_{2g}}{10}, \tag{6}$$

$$x = \frac{E\ ^4A_{2g} \rightarrow\ ^4T_{1g} - E\ ^4A_{2g} \rightarrow\ ^4T_{2g}}{Dq}, \tag{7}$$

$$\frac{Dq}{B} = \frac{15(x-8)}{(x^2-10x)}, \tag{8}$$

where *E* is an energy of the given transition.[108,109] If it is not possible to determine the energies of transitions with sufficient accuracy, the *Dq* parameter can be estimated based on the metal–ligand distance; taking into account the octahedral geometry, according to the following expression:[110,111]

$$Dq \sim \frac{1}{R^5}, \tag{9}$$

where R is a metal-ligand distance. Such an approach may be a useful tool for materials, in which the absorption bands of Cr^{3+} ions overlap with those of other elements present in the studied compound (e.g., the pair of Cr^{3+} and Mn^{2+}).[106,111]

The value of the crystal field strength (*Dq/B*) directly affects the observed luminescent characteristics of materials containing Cr^{3+} ions. The relationship between the relative energies of individual electronic levels and the crystal field strength is illustrated by the Tanabe-Sugano diagram (**Figure 5**). The particular emphasis should be paid to the dependence of the ^2E_g and $^4T_{2g}$ levels energies on the *Dq/B* parameter. These levels exhibit different sensitivities to changes in the crystal field strength: the ^2E_g level remains nearly constant over a wide range of crystal field strengths, while the energy of the $^4T_{2g}$ level increases significantly with an increasing *Dq/B* ratio. However, to provide a more comprehensive analysis, the additional Racah parameter *C* should be distinguished. It can be calculated according to the experimental results with the formula:

$$C = 0.328E_{\,^4A_{2g}\rightarrow\,^2E_g} - 2.59B + 0.58\frac{B^2}{Dq}. \quad (10)$$

Both parameters *B* and *C* describe electron-electron repulsion; however, *C* is used to describe a separation between states of different spin multiplicities, while B is related to states with the crystal-field splitting strength (*Dq*). Usually, the *C/B* ratio is implemented.[112,113] The change in *C/B* ratio significantly changes the scheme of energy levels (**Figure 5).** In Tanabe–Sugano diagrams, the positions of multiplet energy levels depend on the balance between crystal-field splitting and electron—electron repulsion, which can be described by *Dq/B* and *C/B* relations. As a result, increasing *C/B* causes the doublet levels (e.g., ^2E_g, $^2T_{1g}$, $^2A_{2g}$) to shift upward, while the quartet levels (e.g., $^4T_{2g}$, $^4T_{1g}$) remain almost unchanged. It originates from the nature of these two groups of levels; doublets are defined by electron-electron interactions and therefore sensitive to changes in the Racah parameters, whereas quartet levels are related to the crystal-field splitting, thus their sensitivity to changes in *B* and *C* values is minimized.[83,112]

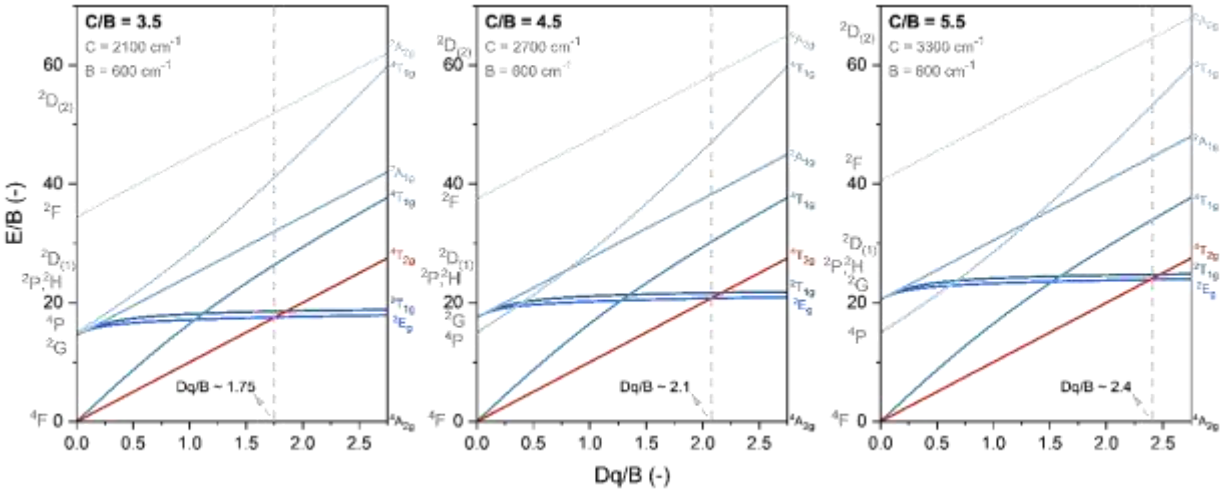

Figure 5. The Tunabe-Sugano diagrams for d^3 electron configuration (O_h symmetry) for various *C/B* values, simulated with *TanabeSugano: Python-based Eigensolver for Tanabe-Sugano Diagrams*, by Anselm Hahn, 2024, DOI: 10.5281/zenodo.206847682, URL: https://github.com/Anselmoo/TanabeSugano

Within the context of Cr^{3+}-doped phosphors, particular attention should be paid to the relation between crystal field parameters, visualized by the Tanabe-Sugano diagram, and consequent luminescent characteristics. The intersection point of the curves assigned to ^2E_g and $^4T_{2g}$ levels determines the lowest excited energy level, which in turn defines the dominant type of Cr^{3+} ion emission. Depending on the *C/B* ratio, this intersection may assume various values, as presented in **Figure 5**. Exemplary, for the value of the *C/B* ratio equal to 4.5, the intersection is around *Dq/B* = 2.1. This marks the boundary between weak (*Dq/B* < 2.1) and strong (*Dq/B* > 2.1) crystal fields. In a weak crystal field, the lowest excited level is the $^4T_{2g}$ level, resulting in the dominance of the $^4T_{2g}\rightarrow{}^4A_{2g}$ emission. Increase in *Dq/B* over threshold value changes the lowest excited level for ^2E_g, leading to an enhancement of the $^2E_g\rightarrow{}^4A_{2g}$ transition. Materials with *Dq/B* close to the threshold value can be classified as having an intermediate crystal field,

where emissions from both $^4T_{2g}$ and ^2E_g levels are observed.[83,114] The influence of crystal field strength on the radiative relaxation processes in compounds containing Cr^{3+} ions is illustrated in **Figure 6**.

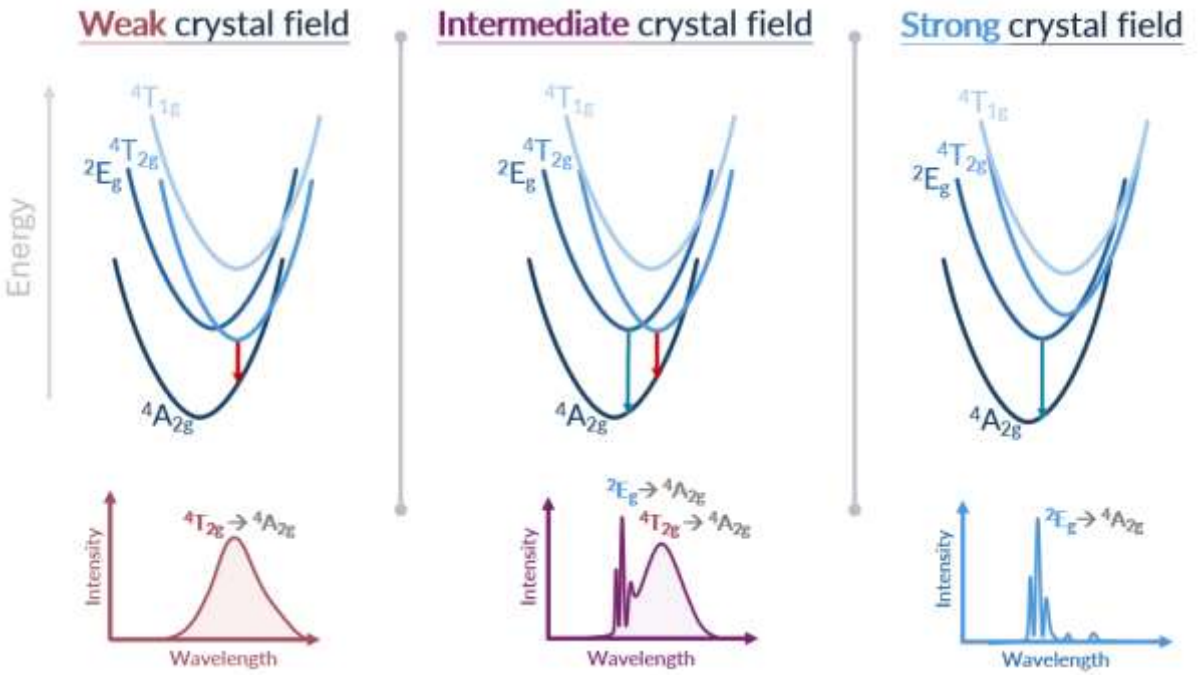

Figure 6. The schematic configurational coordinate diagrams for Cr^{3+} ions (octahedral coordination) affected by various crystal fields, with the following luminescence spectra (simplified)

The concentration of Cr^{3+} may be an important factor not only due to the concentration quenching phenomenon. When chromium(III) ions occupy neighbouring sites, they can interact through exchange coupling or electron–phonon mediated energy transfer. Such coupled ions are referred to as Cr^{3+}-Cr^{3+} pairs. The presence of chromium(III) pairs may be observed in the form of broad, red-shifted bands, less energetic than the emission band assigned to the transition from the $^4T_{2g}$ excited level. Due to the significant similarity of the emission from $^4T_{2g}$ state and the Cr^{3+}-Cr^{3+} pair, their determination according to emission spectrum may be significantly hindered. Thus, the decay kinetics should be considered – chromium(III) pairs luminescence shows longer decay time, compared to the $^4T_{2g} \rightarrow {}^4A_{2g}$ transition in the isolated Cr^{3+} ion.[115–117] Moreover, an increase in the concentration of Cr^{3+} ions may lead to a weakening of the crystal field strength and, consequently, an increased contribution of emission from the $^4T_{2g}$ level.[3,118]

5.3.1 Temperature-dependent luminescence of Cr^{3+} ions

The spectroscopic properties of Cr^{3+} ions are highly sensitive to changes in temperature. With increasing temperature, the intensity and lifetime of luminescence generally decrease. This phenomenon is known as *thermal quenching*. The increase in temperature intensifies a non-radiative relaxation from the emitting state — ^2E_g or $^4T_{2g}$, depending on the crystal field

strength — to the $^4A_{2g}$ ground state. The thermal quenching of luminescence is mainly related to two mechanisms: thermal crossover of excited states and multiphonon relaxation (**Figure 7**).[83,114]

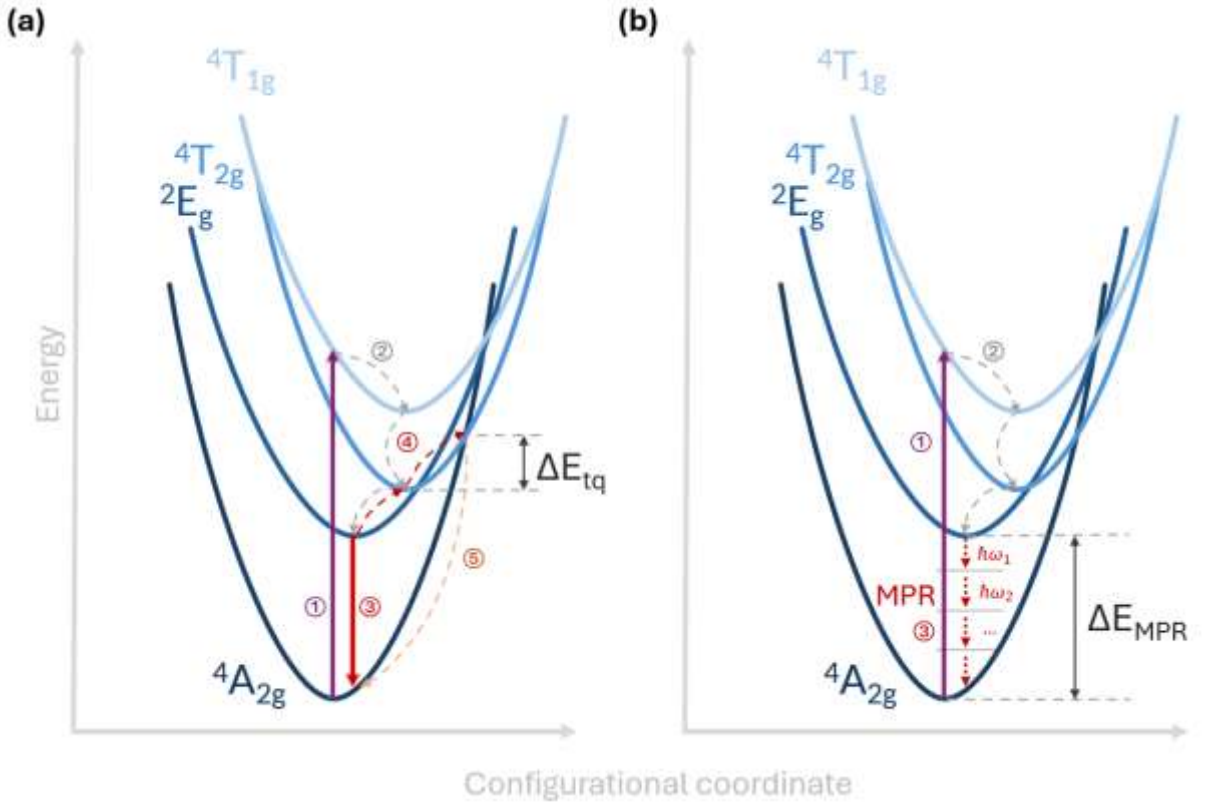

Figure 7. Schematic illustration of the thermal quenching mechanisms: **(a)** thermal crossover, where ① is an excitation from the $^4A_{2g}$ ground state do $^4T_{1g}$ level, ② is a series of non-radiative relaxation to the lowest excited level – such as ^2E_g level under strong CF, ③ stands for radiative relaxation (emission), ④ is a thermally-induced electron-phonon coupling leading to the excitation of the electron to the intersection of $^4T_{2g}$ and $^4A_{2g}$ levels, ⑤ is a non-radiative relaxation to the ground state, and ΔE_{tq} is a thermal quenching activation energy; as well as **(b)** multiphonon relaxation, where ① and ② stand for excitation and series of non-radiative relaxation, respectively, ③ is a multiphonon relaxation process, and ΔE_{MPR} is a difference is energies between depopulating level and lower state

The excited levels in Cr^{3+} ions, located in the near-intermediate crystal field, are thermally coupled due to the *thermal crossover* between closely spaced energy levels. Exemplary, in an intermediate-to-strong crystal field, an electron from the metastable ^2E_g level to the vibronically coupled $^4T_{2g}$ state, from which non-radiative relaxation to the $^4A_{2g}$ ground quenches the luminescence (**Figure 7a**). The process of thermal quenching shows an Arrhenius-type behavior with an activation energy ΔE_{tq}, defined as the energy difference between the equilibrium position of the excited state and the parabola's intersection point (ΔE_{tq} in **Figure 7a**).[114,119,120]

The energy activation of thermal quenching can be estimated with the following formula:

$$I(T) = \frac{I_0}{1 + Aexp\left(\frac{-\Delta E_{tq}}{kT}\right)}, \quad (11)$$

where I(T) is an intensity of the emission at temperature T, I_0 is an initial temperature of the quenching process, A stands for preexponential coefficient, ΔE_{tq} is energy activation of thermal quenching, and k is Boltzmann constant. The determination of the ΔE_{tq} parameter is performed with the analysis of the slope of the linear regression of the $\ln[I_0/I(T)-1)]$ as a function of 1/kT.[121,122]

The second mechanism is *multiphonon relaxation* (MPR), in which the excitation energy is dissipated through the emission of multiple lattice vibrations (phonons) (**Figure 7b**). Due to the significant differences between the energy band gap of the excited and ground state (thousands of cm^{-1}) and the energy of a single phonon (hundreds of cm^{-1}), this process involves the simultaneous emission of multiple phonons. The rate of the multiphonon relaxation may be described with the formula:

$$W_{MPR} = W_0 \exp\left[-\alpha\left(\frac{\Delta E_{MPR}}{\hbar\omega}\right)\right], \quad (12)$$

where W_0 is the pre-exponential factor related to the electron-phonon coupling strength, α is a parameter assigned to the particular host lattice, ΔE_{MPR} is an energy gap between the emitting level and the lower state in the process of MPR, and $\hbar\omega$ is an average phonon energy. This relation implies that nonradiative relaxation related to a multiphonon process becomes negligible when ΔE is much larger than a few times the phonon energy, but becomes dominant when ΔE is small (e.g., < 5 times of $\hbar\omega$).[83,123,124] The $^4T_{2g}$ level is strongly vibronically coupled, making it particularly sensitive to MPR. In contrast, the ^2E_g level, being localized and weakly coupled to phonons, exhibits higher stability. Thus, low-phonon host materials showing a strong crystal field may provide sufficient conditions for temperature-stable phosphors. On the other hand, weak CF strength combined with high-phonon hosts may show a rapid quenching of the broadband $^4T_{2g}$ luminescence.

Both of the mentioned processes lead to a reduction of luminescence intensity and a shortening of the decay time as temperature rises. Because radiative and nonradiative processes compete, the total decay rate (1/τ) can be described with the formula:

$$\frac{1}{\tau(T)} = W_r + W_{nr}(T), \quad (13)$$

where W_r is a radiative relaxation rate (independent of weakly related to temperature) and $W_{nr}(T)$ stands for a nonradiative relaxation rate, strongly dependent on temperature. An increase in temperature significantly intensifies the nonradiative relaxation rate (W_{nr}), thus luminescence lifetime (τ) decreases.

The extent of thermal quenching is highly dependent on the properties of the host material. Hosts, in which luminescent ions are in strong crystal fields (large *Dq/B* values),

exhibit larger energies of thermal quenching (ΔE_{tq}), leading to the suppression of thermally-driven crossover.[125,126] Similarly, materials with low phonon energies, such as fluorides ($\hbar\omega \approx 400$ cm^{-1}), reduce the probability of multiphonon relaxation. On the other hand, materials showing higher phonon energies, like some oxides ($\hbar\omega \approx 800$ cm^{-1}) or boranes ($\hbar\omega \approx 1400$ cm^{-1}), exhibit more effective nonradiative processes.[127,128] Other important factors include site symmetry, lattice rigidity, and covalency of the metal-ligand bonds — all of these qualities influence vibronic coupling and the probability of nonradiative transitions. The description of the hybrid structures, such as materials with perovskite-like stoichiometry, containing organic cations, is more advanced. The vibrational characteristics of these compounds may be assigned to their two components: framework and organic cations. The vibrational modes related to the framework, such as octahedral librations and metal-ligand stretching, are usually observed to ~200 cm^{-1}.[129,129–133] However, the presence of organic cation leads to the presence of the multiple vibrational modes related to, e.g., bending, rocking, and twisting of some parts of the molecules, such as stretching vibrations of NH_3^+ (~3100 cm^{-1}) or in-plane bending vibration of CH bonds (~1340-1380 cm^{-1}). These modes are usually visible up to ~3500 cm^{-1}.[132,134] The implementation of more complex linkers (e.g., $HCOO^-$, $H_2PO_2^-$) induces the additional possibility of internal transitions. Exemplary, for formates ($HCOO^-$), the vibrations assigned to the OCO part of the linker, e.g., bending (~800 cm^{-1}) or stretching (up to ~1600 cm^{-1}) may be observed.[130,131] The stretching of the C-H bond in formate ion can be observed up to 2870 cm^{-1}.[134,135] Thus, the maximal phonon energy of the framework is strongly dependent on the type of linker and organic cation, which may significantly affect the probability of multiphonon phenomena.[136,137]

The sensitivity of Cr^{3+} luminescence to thermal quenching is the essence of its potential as a luminescent thermometer. Temperature-enhanced nonradiative processes affect both emission intensities and luminescence decay time, providing measurable optical signals that correlate precisely with temperature. By tuning the host lattice (e.g., adjusting phonon energy or crystal field strength), Cr^{3+}-based materials may exhibit high sensitivities and be optimized for specific temperature sensing ranges. Thus, understanding the mechanisms of temperature-dependent luminescence and thermal quenching in Cr^{3+} systems is not only essential for interpreting their spectroscopical characteristics but also advances the development of high-performance optical temperature sensors.

5.4 Temperature sensing

5.4.1 Conventional thermometric methods

Temperature constitutes one of the most essential parameters influencing almost every aspect of the surrounding world. The progress of the past three centuries in science and technology has induced the development of a wide range of thermometric methods - technological solutions designed for temperature measurement. However, the history of thermometry, i.e., the scientific discipline concerned with both theoretical and practical aspects of temperature measurement, extends back more than two millennia.

One of the precursors of modern thermometers was the *thermoscope*, constructed around 210 BCE by the Greek writer and engineer Philo of Byzantium.[138] This device, later improved by Hero of Alexandria, enabled the observation of temperature differences through the indirect detection of volume changes in a gas enclosed within a glass tube, partially filled with a liquid – wine or vinegar.[138] This concept was further developed in the early modern period by Galileo Galilei (around 1600), whose work inspired the creation of the first liquid-based thermometer equipped with a scale - an invention attributed to Ferdinand II de' Medici, Grand Duke of Tuscany, around 1644. The 17th century can thus be distinguished as a turning point in the history of thermometry.[138–140]

In the second half of the 17th century, the English physicist Robert Boyle proposed the freezing point of water as a fundamental reference on the temperature scale, while the Dutch physicist Christiaan Huygens described the invariance of the boiling point of water under isobaric conditions.[138,141] The advancement of thermometric methods, both in theoretical, phenomenological, and technical terms, proceeded in parallel with the scientific progress of the 18th and 19th centuries. A milestone in temperature measurement was the development of the first precise and practical temperature scale by Gabriel Daniel Fahrenheit in 1724. Subsequently, in 1742, Anders Celsius introduced an alternative scale that remains in widespread use today.[138,142] Despite the passage of nearly three centuries, both scales continue to serve as standard tools for practical applications. Additionally, the Kelvin scale, proposed in 1848 by the British physicist William Thomson, 1st Baron Kelvin, is extensively employed in science and engineering. The fundamental advantage of this scale lies in its absolute nature, where 0 K corresponds to the lowest theoretically possible temperature of a physical system.[79,141]

The simultaneous development of technological solutions (such as the liquid-based thermometer and its subsequent refinements), the methodological foundations of measurement itself, and the establishment of metrological theory and standardized temperature scales contributed to defining the central role of thermometry in science, technology, and consequently, everyday life. The technological revolution of the 20th century brought significant advancements in temperature measurement techniques. New types of measuring instruments were not based solely on the thermal expansion of gases or liquids, but also exploited phenomena such as the variation of electrical resistance (e.g., *thermistors*), the potential difference at the junction of two materials (the *Seebeck effect*, employed in *thermocouples*), or the magnetic properties of specific substances.[79,141] A major milestone in the evolution of

thermometry was the development of methods utilizing the analysis of electromagnetic radiation emitted and/or reflected by a given object. Thermographic cameras and pyrometers have since become fundamental tools for remote and non-contact temperature measurements.[79]

Regardless of the method enabling continuous and reversible temperature analysis, all thermometric technologies consist of two fundamental components:

- **sensing medium**, which responds in a well-defined manner to temperature changes,
- **thermometric model**, providing an interpretation of variations in the medium's properties in order to determine temperature according to a specific scale.

Only the combination of these two elements enables the formation of a system that can be defined as a *thermometer*.

5.4.2 Luminescence-based temperature sensors

Electromagnetic radiation emitted by some materials can be use, under appropriate conditions, as a starting point for the development of a luminescent thermometer. In such a system, the studied materials serve as the thermometric medium, and specific changes in their spectroscopic characteristics can be described as a function of temperature, distinguishing the thermometric model. Luminescent materials may exhibit a significant temperature dependence of their spectroscopic properties,[82,143,144] which can manifest as:

- **changes in emission intensity** - both in spectral regions and the overall spectrum,
- alterations in **luminescence decay kinetics**,
- **spectral shifts** of emission bands,
- variations in the **full width at half maximum** (FWHM) of emission bands.

The graphical representation of the spectroscopic utilities implemented within the context of the luminescence thermometry is presented in **Figure 8.**

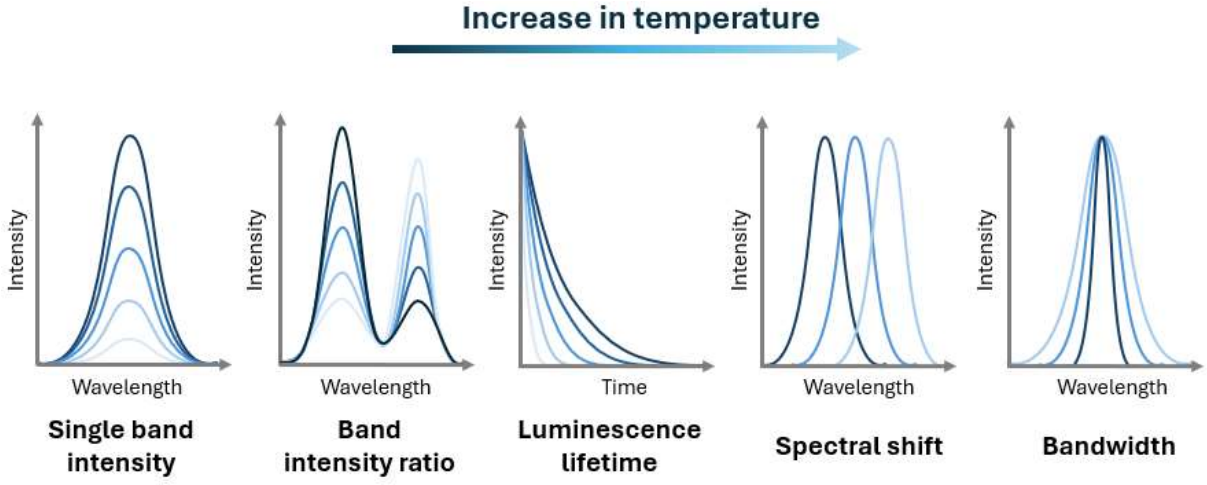

Figure 8. The schematic representation of the methods of luminescence thermometry

The choice of a thermometric model should be based on the characteristics of the given material and the specific technical assumptions. Similar to other types of thermometers, the luminescent method relies on fitting the obtained spectroscopic measurement results to a calibration pattern, here the model was established according to the temperature-dependent laboratory measurements. Among the mentioned approaches, the methods based on the analysis of the intensity ratio of two emission bands (so-called *ratiometric method*) and those based on the analysis of luminescence decay kinetics have found particular application in the materials discussed in this dissertation. Nevertheless, other approaches are also commonly reported for different types of materials.[82,145,145]

5.4.2.1 Ratiometric approach

The ratiometric method is one of the leading approaches in the field of luminescent thermometry. It is based on exploiting the differing temperature dependencies of two distinct regions within the emission spectrum. These applied bands may be assigned to the luminescence originating from the single type of ions, as in the case of Cr^{3+}-doped compounds[146] (transitions from thermally coupled ^2E_g and $^4T_{2g}$ levels), as well as originating from two luminescent centres, such as in the case of the combination of Cr^{3+} and Yb^{3+} ions[147]. Nevertheless, it is also possible to utilize spectral components originating from the same transition, e.g., the R_1 and N lines, which arise from the $^2E_g \rightarrow {}^4A_{2g}$ transition in Cr^{3+} ions.[106,111,148] This method has gained popularity due to a number of useful features that contribute to its convenience of implementation and high sensitivity. The main advantage of this particular method is its self-referencing nature. The value of the thermometric parameter depends on an intensity ratio rather than absolute intensity. It translates to higher independence of excitation power, detector sensitivity, or sample geometry. The method also provides high thermometric sensitivity, which, combined with a basic experimental setup and fast response, makes it suitable for real-time temperature monitoring. However, the ratiometric technique also has certain limitations. Accurate measurements require well-separated emission bands to avoid spectral overlap. Also, the effect of the background luminescence and cross-sensitivity should be considered as a limiting factor.[82,145,149,150]

The ratiometric method is based on analyzing the ratio of two emission bands that differ in their temperature dependence. In such a case, under isothermal conditions, two spectral regions (for example, A and B) are identified within the emission spectrum. These regions are further described as thermometric ranges. The defined regions are then used to determine the integral intensities I_A and I_B. Next, the obtained values are compared with one another to determine their ratio, called the luminescence intensity ratio (LIR), sometimes also named *fluorescence intensity ratio* (FIR). This operation combines two temperature-dependent parts of the emission spectrum into one thermometric parameter. This relationship is described by Equation (14):

$$LIR = \frac{I_A}{I_B}, \tag{14}$$

where I_A and I_B stand for integral intensities of A and B thermometric ranges, respectively.

By performing a series of measurements under controlled temperature conditions, a dataset of {LIR_{T1}, LIR_{T2}, …, LIR_{Tn}} is obtained as a function of temperature from T_1 to T_n, which can be further expressed as a function LIR(T). Temperature determination is performed using this function, transformed into the form T(LIR). To describe the usefulness of the LIR(T) thermometric model, its sensitivities - *absolute* and *relative* - are determined. The absolute sensitivity (S_a, K^{-1}), defined as the change in the thermometric parameter (LIR) per unit change in temperature, is expressed by the formula:

$$S_a = \frac{\Delta LIR}{\Delta T}, \tag{15}$$

where ΔLIR is a change in luminescence intensity ratio and ΔT stands for the change in temperature. Relative sensitivity (S_r, $\%\cdot K^{-1}$), on the other hand, is a measure of how much the value of the thermometric parameter changes relative to its current value for a unit change in temperature. This parameter is described by the equation:

$$S_r = \frac{1}{LIR} \cdot \frac{\Delta LIR}{\Delta T} \cdot 100\%. \tag{16}$$

The uncertainty in determining the LIR parameter is an important factor characterizing the studied thermometric model. This parameter describes how much the measured result may deviate from the actual temperature. It is described by the equation:

$$dT = \frac{1}{S_r} \cdot \frac{\Delta LIR}{LIR}. \tag{17}$$

Another important factor describing the usefulness of a given thermometer is its sensing range. This term refers to a temperature interval within which the temperature readout can be determined with sufficiently high confidence. This is influenced by two particular factors: a certain threshold for the relative sensitivity (S_{th}, set arbitrarily) and the uncertainty in determining the LIR parameter, which must be smaller than the analyzed temperature change. This relationship is described by the following equation[150]:

$$(S_r \geq S_{th}) \wedge (\Delta LIR \geq \delta LIR), \tag{18}$$

where S_{th} is the sensitivity threshold, ΔLIR is an increment in LIR value, and δLIR is an error in the determination of LIR. All the variables are determined at a given temperature. The S_{th} value depends on the specific application requirements. Determining the sensing range focuses on establishing the interval within which both of these conditions are met. This range can be extended by lowering the threshold value of the relative sensitivity and by increasing the accuracy of the LIR parameter determination.[82,145,149,150]

5.4.2.2 Lifetime-based approach

Luminescence thermometry based on emission lifetime is another valuable approach. Although this approach is not as commonly reported as a ratiometric method, it has some

noteworthy properties, making it valuable.[151,152] Due to the immunity of the luminescence decay to excitation intensity variations and phosphor concentration, the analyzed thermometric parameter shows higher stability, which increases the sensing ability. The lifetime-based (LT-based) method also exhibits significantly lower sensitivity to photon-environment interactions compared to the ratiometric method. This advantage minimizes the possible influence of the surrounding medium on the observed emission spectrum of the luminescent probe. What is more, the possibility of its implementation for phosphors exhibiting a single emission band significantly extends the possible range of implemented materials. Nonetheless, due to the more complex nature of the measurement itself, it is necessary to implement more complicated equipment than in the ratiometric method, which cannot be overlooked when comparing these two methods.[146,151,153]

In this particular method, the thermometric parameter is the luminescence lifetime. In the context of this dissertation, particular attention should be given to the approach based on determining the average luminescence lifetime (τ_{avg}) using the equation:

$$\tau_{avg} = \frac{\int I(t)tdt}{\int I(t)dt}, \tag{19}$$

where I(t) is the signal intensity at a given time t. This approach is especially effective for quasi-automated analysis of measurement data, as it eliminates the need to fit an approximating function to the decay curve. The resulting set of elements $\{\tau_{avg,\,T1}, \tau_{avg,\,T2}, \ldots, \tau_{avg,\,Tn}\}$ for temperatures from T_1 to T_n, obtained during temperature-dependent measurements, serves as an analog of the LIR parameter used in the ratiometric method. To describe the thermometric properties of the system, an analogous approach based on absolute and relative sensitivities is applied. In this case, the expression describing the absolute sensitivity takes the form:

$$S_a = \frac{\Delta\tau_{avg}}{\Delta T}, \tag{20}$$

where $\Delta\tau_{avg}$ is a change in luminescence intensity ratio and ΔT stands for the change in temperature. The relative sensitivity, in turn, is described by the equation:

$$S_r = \frac{1}{\tau_{avg}} \cdot \frac{\Delta\tau_{avg}}{\Delta T} \cdot 100\%, \tag{21}$$

where τ_{avg} is the current average luminescence lifetime, $\Delta\tau_{avg}$ stands for a change in luminescence intensity ratio, and ΔT is the temperature change.

5.4.3 Luminescent thermometers containing Cr^{3+} ions

Chromium(III) ions exhibit a set of spectroscopic features that make them highly attractive for luminescence thermometry. One of the most valuable aspects of materials containing Cr^{3+} ions is their broad and intense absorption band, typically around 400-450 nm associated with a $^4A_{2g} \rightarrow {}^4T_{1g}$ transition, which enables efficient excitation using widely available light sources, such as laser diodes to LEDs.[154–156] Upon excitation, Cr^{3+} ions can

exhibit intense luminescence in the red region of the visible spectrum. As it was shown in **Chapters 5.3** and **5.3.1**, the characteristic of luminescence is strongly dependent on crystal field strength and temperature. The diversity in possible host materials makes Cr^{3+}-based compounds a significantly broad field, offering various spectroscopic qualities meeting thermometric requirements. Another important characteristic of Cr^{3+} luminescence is its relatively long lifetime, typically ranging from hundreds of μs to a few ms, depending on the host matrix. This allows the use of lifetime-based thermometric methods.[146,157]

The potential of Cr^{3+}-based luminescent thermometers has been demonstrated with various host lattices, offering different spectroscopic properties. Although there are a significant number of noteworthy compounds, to visualize the variety of possible thermometric characteristics, to following exemplary inorganic materials can be mentioned: $MgAl_2O_4$: Cr^{3+}, operating within the physiological temperature range with high relative sensitivity (up to 3.5%·K^{-1} at 300 K)[158]; $Ba_{1.3}Ga_{12}O_{19.3}$: Cr^{3+} for a wide operating range 173-573 K (S_r over 1%·K^{-1})[159]; and α/β-Ga_2O_3: Cr^{3+}, showing significant influence of the structure characteristics on observed sensitivity[160]. The potential of Cr^{3+}-doped compound for ultra-sensitive ratiometric thermometry has been presented with the $Li_{1.97}Zn_{1.03}Ge_3O_8$: 0.08% Cr^{3+} — up to. 13.09%·K^{-1} (50 K) with 50-300 K sensing range.[161]

Furthermore, Cr^{3+} can efficiently interact with other luminescent centres through energy transfer mechanisms, expanding its functionality in multimodal thermometers. Chromium(III)-based materials co-doped with rare-earth or transition metal ions have been proposed as sensing systems, in which the energy transfer between Cr^{3+} and the co-dopant ion enables, e.g., dual emission suitable for self-referenced thermometry, combined optical heating and sensing, or more efficient excitation of the particular luminescent centre via *antenna effect*.[162–165] Among many reported Cr^{3+}-co-doped materials exhibiting valuable thermometric characteristics, to show a diversity of possible thermometric characteristics, the given compounds can be marked: $LaGaO_3$: Cr^{3+}, Nd^{3+}, in which the Cr^{3+}→Nd^{3+} is well observed and dual-mode sensing may be achieved (S_r up to 1.9%·K^{-1} at 300 K with 300-625 K range)[166]; $ZnAl_2O_4$: Cr^{3+}, Mn^{2+}, showing the efficient Mn^{2+}→Cr^{3+} energy transfer, enhancing Cr^{3+} luminescence and improving sensing capabilities (up to 3.7%·K^{-1} at 80 K)[167]; Ga_2O_3: Cr^{3+}, Ni^{2+}, exhibiting an increase in the luminescence intensity by 2.4 times compared to the material doped solely with Ni^{2+} ions[168].

The use of Cr^{3+} ions in metal–organic frameworks (MOFs) for luminescent thermometry is essentially an unexplored area. Despite the growing scientific interest in hybrid compounds, including MOFs, a significant research gap can be observed in the application of hybrid compounds based on chromium(III) ions in the role of luminescent temperature sensors. Nevertheless, the potential of hybrid formate perovskites has been reported in works describing the structural and spectroscopic properties of a series of $[CH_3NH_3]M_{0.5}Cr_xAl_{0.5x}(HCOO)_3$, M = Na, K, and x = 0,0.025, 0.5, as well as a comparison of $[C_3N_2H_5]Na_{0.5}Cr_{0.5}(HCOO)_3$ and $[C_3N_2H_5]Na_{0.5}Al_{0.475}Cr_{0.025}(HCOO)_3$ perovskites.[169,170] Although the mentioned works do not provide a detailed thermometric analysis of the investigated compounds, their temperature-dependent spectroscopic properties, such as rapid thermal quenching, clearly demonstrate the considerable potential of chromium(III)-containing materials for highly sensitive luminescent

thermometry in the cryogenic range. These findings have, in a sense, served as a foundation for the further research presented in this dissertation.

The field of luminescent thermometers containing Cr^{3+} ions is characterized by significant potential, both in terms of materials containing only chromium(III) ions and co-doped materials. By varying the host matrix, the concentration of chromium(III), as well as the type and amount of co-dopants, it is possible to obtain materials with diverse spectroscopic properties. Different temperature dependencies of luminescence make these materials suitable for use in both high-sensitivity thermometry, particularly in the cryogenic range, and wide-range sensors. A summary of representative thermometric materials containing Cr^{3+} ions, containing solely Cr^{3+} ions, and in combination with co-dopants, is presented in **Table 1**.

Table 1. The collation of exemplary luminescent thermometers containing Cr^{3+} ions with their highest relative sensitivity ($S_{r,\,max}$) at working temperature ($T_{Sr,\,max}$), with sensing range (if provided). By default, the presented results are determined with the ratiometric method (LIR), unless stated otherwise.

Compound	$S_{r,\,max}$ (%·K^{-1})	$T_{Sr,\,max}$ (K)	Sensing range (K)	Reference
$MgAl_2O_4$: Cr^{3+}	3.5	300	300-540	[158]
$Ba_{1.3}Ga_{12}O_{19.3}$: Cr^{3+}	6.78	113	173–573	[159]
α-Ga_2O_3: Cr^{3+}	1.05	300	200-450	[160]
β-Ga_2O_3: Cr^{3+}	0.64	300		
$Li_{1.97}Zn_{1.03}Ge_3O_8$: Cr^{3+}	13.09	50	50-300	[161]
$LaGaO_3$: Cr^{3+}, Nd^{3+}	1.9	300	300-625	[166]
$ZnAl_2O_4$: Cr^{3+}, Mn^{2+}	3.7	80	80-310	[167]
Ga_2O_3: Cr^{3+}, Ni^{2+}	5.26	293	-	[168]
$CaHfO_3$: Cr^{3+}	2	40	40-150	[171]
$LaSr_2Ga_{11}O_{20}$: Cr^{3+}	2.6	190	190-460	[172]
$InTaO_4$: Cr^{3+}	2.50 (LIR)	347	240-420	[173]
	2.27 (LT)	347		
La_2MgTiO_6:V^{4+},Cr^{3+}	1.96	165	80-250	[174]
$MgTiO_3$: Cr^{3+}, Nd^{3+}@SiO_2	1.18	343	303–343	[175]
$Mg_2Al_4Si_5O_{18}$: Ce^{3+}, Cr^{3+}	0.51	525	-	[155]
$Sr_2MgAl_{22}O_{36}$: Cr^{3+}	1.7	310	-	[176]

6. Experimental section

This section focuses on the preparation methods and subsequent characterization of the investigated hybrid materials. Five scientific publications (**P1–P5**) have been included as part of this dissertation:

- **P1**: **Kabański A***, Ptak M., and Stefańska D.* (**2023**). *Metal–Organic Framework Optical Thermometer Based on Cr^{3+} Ion Luminescence*, ACS Applied Materials & Interfaces 15(5), 7074-7082 DOI: 10.1021/acsami.2c19957 https://pubs.acs.org/doi/full/10.1021/acsami.2c19957

- **P2**: Ptak M.*, **Kabański A**., Dziuk B., Balciunas S., Usevicius G., Zeręba J., Banys J., Simenas M.*, Sieradzki A., Stefańska D. (**2024**) *Mechanism of isosymmetric polar order–disorder phase transition in pyroelectric $[CH_3CH_2NH_3]_2NaGa(HCOO)_6$ double perovskite*, Journal of Materials Chemistry C 12(13), 4663-4675 DOI: 10.1039/D3TC04529C https://pubs.rsc.org/en/content/articlelanding/2024/tc/d3tc04529c

- **P3**: **Kabański A**.*, Ptak M, Carlos L.D., Stefańska D.* (**2025**). *Real-Time Temperature Monitoring with Cr^{3+}-Based Hybrid Formate Perovskites: Insights into the Relation Between Chemical Composition and Thermometric Performance*, Advanced Optical Materials 13, e01057 DOI:10.1002/adom.202501057 https://advanced.onlinelibrary.wiley.com/doi/10.1002/adom.202501057

- **P4**: **Kabański A.***, Caputa K., Stefańska D.* (**2025**) *High-sensitivity optical thermometry with Cr^{3+}-doped hybrid formate perovskites: comparative analysis of ratiometric and lifetime-based approaches*, Dalton Transactions 54, 15899–15908 DOI: 10.1039/D5DT01748C https://pubs.rsc.org/en/content/articlelanding/2025/dt/d5dt01748c

- **P5**: **Kabański A.***, Caputa K., Stefańska D.* (**2025**) *Multimodal temperature sensing in hybrid perovskites doped with Cr^{3+}: strategy for optimizing luminescence thermometers*, Journal of Materials Chemistry C 2025, 13, 23935-23944 DOI: 10.1039/D5TC02943K https://pubs.rsc.org/en/content/articlelanding/2025/tc/d5tc02943k

In the following sections of this work, methods associated with specific publications are denoted by corresponding symbols – from **P1** to **P5**.

6.1 Synthesis

Within the dissertation, two synthesis methods were employed to obtain hybrid materials containing various concentrations of Cr^{3+} ions: the microwave-assisted hydrothermal method (**P1, P2**) and the slow-diffusion method (**P3**, **P4**, **P5**). The hydrothermal approach was used to synthesize materials with a double perovskite architecture, whereas the slow diffusion method was applied to obtain single perovskite-type materials. The selection of each synthesis method for a given group of compounds was based on insights from previous research on hybrid materials, which indicated preferred synthetic routes for particular material architectures. A summary of the investigated materials, categorized by synthesis method and corresponding publication, is presented in **Figure 9**.

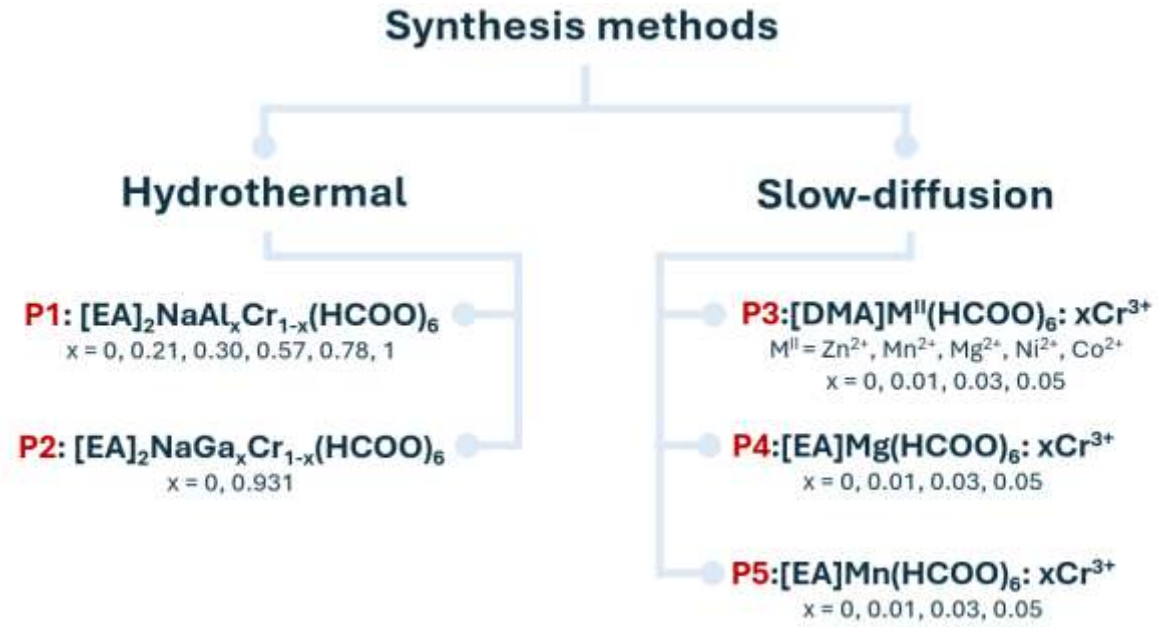

Figure 9. The categorized presentation of the investigated series of materials obtained with hydrothermal and slow-diffusion methods

The microwave-assisted hydrothermal method was successfully employed for the synthesis of double perovskite-like materials. It was used to prepare two series of compounds described in publications **P1** and **P2**. The process involves preparing an aqueous solution containing the precursors:

- 4 mmol of trivalent metal precursor (e.g. $Ga(NO_3)_3{\cdot}nH_2O$) or the mixture of a M^{III} compound and $CrCl_3{\cdot}6H_2O$ (for doped samples)
- 4 mmol (0.3262 g) of ethylamine hydrochloride (EA·HCl),
- 8 mmol (0.5441 g) of sodium formate (HCOONa),
- 25 mL of *N*-ethylformamide ($HCONHC_2H_5$),
- 5 mL of 98% formic acid (HCOOH),
- 10 mL of water.

The mixture was placed in a Teflon-lined vessel and heated (140°C) in a microwave-assisted mineralizer (Ertec Magnum II) for 24 hours. After the process, the solution was transferred to

a container and then left to slowly evaporate at room temperature (several days). The obtained crystals were then separated, washed with anhydrous ethanol, and dried in air. The schematic representation of the applied hydrothermal synthesis procedure is shown in **Figure 10**.

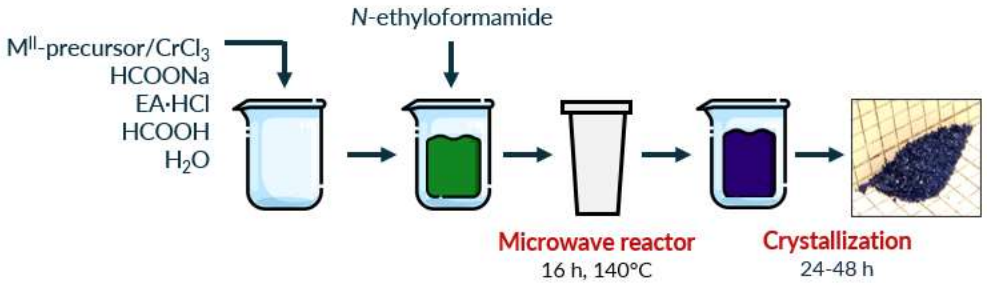

Figure 10. The simplified scheme of the hydrothermal synthesis procedure

The slow-diffusion method was utilized for the synthesis of the series of hybrid materials described in **P3**–**P5**. This technique relies on the gradual crystallization of the desired compounds at the interface between two solutions (A – heavy phase, and B – light phase) differing in density. In the first step, solution A is prepared by dissolving 8 mmol of an amine precursor (such as EA·HCl) in 7.5 mL of methanol (MeOH), followed by the addition of 1.5 mL of 98% formic acid (HCOOH) and 0.7 mL of triethylamine (TEA). The composition of solution B depends on the targeted chromium concentration. For undoped samples, solution B is prepared by dissolving 2 mmol of a divalent metal precursor (e.g., $MnCl_2$) in 5 mL of MeOH. For Cr^{3+}-doped compounds, a stoichiometric amount of $CrCl_3$ to maintain the total concentration of metal ions equals 2 mmol. After both solutions are prepared, they are transferred into a glass tube (1 cm in diameter, 18 cm in length): solution A is added first (forming the heavier phase), followed by careful injection of solution B (the lighter phase) using a syringe to form an unmixed interface. The tube is then sealed and left undisturbed to allow crystal growth (several days). The resulting crystals are separated from the liquid, washed with anhydrous methanol (or ethanol), and air-dried. The schematic representation of the performed slow-diffusion method is presented in **Figure 11**.

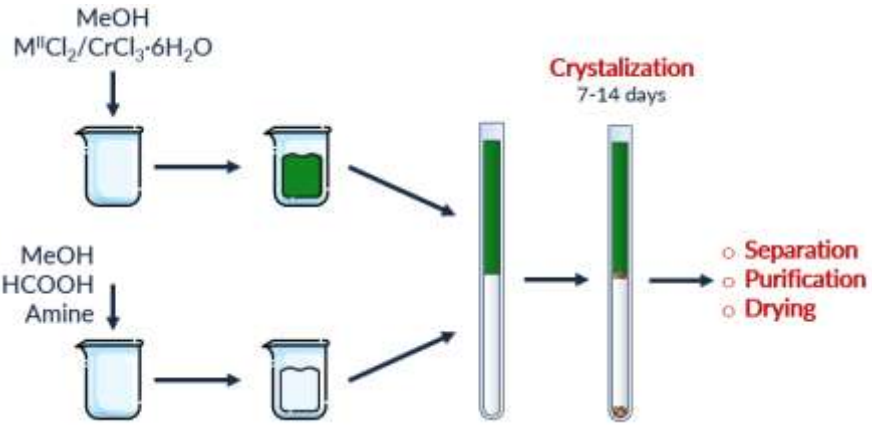

Figure 11. The simplified scheme of the slow-diffusion method

Details regarding the suppliers of chemical reagents are provided in the synthesis descriptions included in publications **P1**–**P5**, attached to this dissertation (**Chapter 11**).

6.2 Characterization methods

6.2.1 Powder and Single-crystal X-Ray Diffraction

The purity of the samples presented in publications **P1** and **P3-P5** was examined by powder X-ray diffraction (pXRD) technique in the range 2θ = 10-80°, depending on the particular series (see details in **Chapter 11**). The implemented system was based on X'PertPro device, equipped with PIXcel detector and Ni-filtered CuKα radiation (λ = 1.54056 Å).

Within the publication **P2**, the single-crystal X-ray diffraction (scXRD) technique was applied. The used device was a CCD Xcalibur diffractometer with graphite-monochromatic MoKα radiation (λ = 0.71073 Å). The scXRD measurements were conducted at 293 K and 391 K. The corrections of the reflection intensities were applied in the form of Lorentz and polarization factors. The SHELX software was used to directly solve the obtained structures. The positions of the hydrogen atoms were established based on geometric considerations and refined using a riding model, with isotropic displacement parameters set to 1.2 times the U_{eq} value of the corresponding parent atom. Other atoms were identified from difference Fourier maps and refined by the full-matrix least-squares method employing an anisotropic approximation. Publication **P2** includes two deposits in the *Cambridge Crystallographic Data Centre*: 2254366 (293 K) and 2254367 (391 K), containing supplementary crystallographic data. The deposits are available at https://www.ccdc.cam.ac.uk/structures. The structure drawings were prepared using Diamond 3 software (**P1-P5**).

6.2.2 Raman and IR spectroscopy

The RT Raman studies were performed for the materials described in publications **P1-P3**. The Raman spectra presented in **P1** and **P3** were measured using a Bruker MultiRAM spectrometer (2 cm^{-1} resolution, range 3600–21 cm^{-1}). As an excitation source, the 1064 nm YAG: Nd^{3+} laser was used. Alternatively, for the work **P2**, the Bruker FT-Raman RFS 100/S spectrometer (range: 3600-80 cm^{-1}) with a 1064 nm excitation line (YAG: Nd^{3+}) was used. The temperature-dependent IR spectra were presented in the publication **P2**. The measurements of the investigated materials diluted in KBr pellets were conducted with a Nicolet iN10 FTIR microscope and a Linkam THMS600 stage equipped with ZnSe windows. The measurement range was 3250-675 cm^{-1}, while temperature varied from 80 K to 410 K (40 K-step). Additionally, within the results presented in work **P3**, mid-IR ATR (attenuated total reflection) spectra were collected using a Nicolet iS50 infrared spectrometer equipped with the ATR module and diamond crystal.

6.2.3 Differential Scanning Calorimetry

The differential scanning calorimetry (DSC) was performed in the **P1** publication. The heat capacity was measured from RT to 400 K using a Mettler Toledo DSC-1 calorimeter (0.4 μW resolution) with a nitrogen flow as a purging medium. The rates of heating and cooling

were 5 $K \cdot min^{-1}$. The excess heat capacity assigned to the phase transition (PT) was determined by subtracting a baseline (representing the system variation without PT) from the obtained data.

6.2.4 Diffuse-reflectance spectroscopy

The RT diffuse reflection spectra were obtained for the materials in all of the publications **P1-P5**. For this method, the Varian Cary 5E UV/VIS-NIR spectrophotometer with a 0.5 nm step was implemented. The measurements were performed within a 200-2500 nm range with an Al_2O_3 reference.

6.2.5 Temperature-dependent luminescence studies

Temperature-dependent spectroscopic measurements are a key element of this dissertation and were therefore performed for all materials described in publications **P1-P5**. For this purpose, three measurement setups were employed.

The first system was based on a temperature-controlled Linkam THMS600 heating/freezing stage (range from 80 K up to 400 K). The Hamamatsu PMA-12 photonic multichannel analyser paired with a BT-CCD sensor was employed to obtain emission spectra. To reduce the emission intensity-to-noise ratio, each emission spectrum at a given temperature was obtained with multiple signal averaging. The number of averages was adjusted according to the experiment and the signal quality. As an excitation source, a 405 nm diode (PSU-III-LED, 100 mW) was applied. The particular setup was used to characterize materials in publications **P1-P5**.
A schematic diagram of the measurement setup is presented in **Figure 12**.

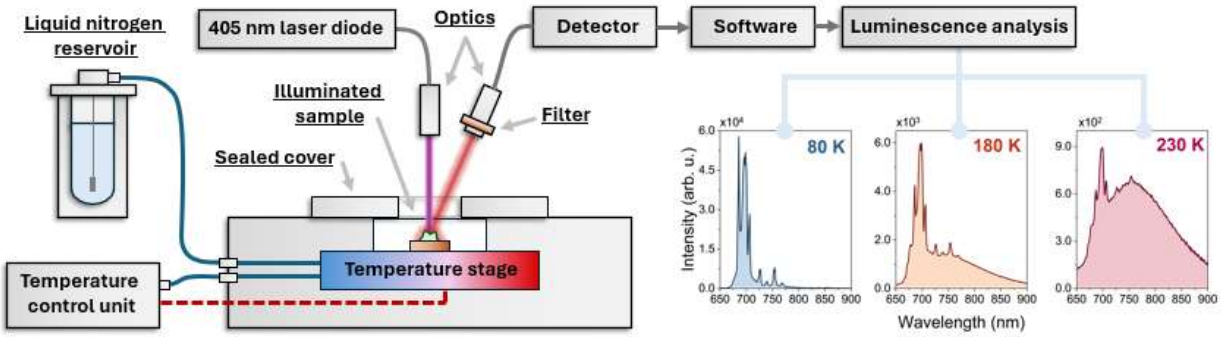

Figure 12. The schematic representation of the setup used for temperature-dependent luminescence measurements

The second applied measurement system was based on the Linkam THMS600 heating/freezing stage (range from 80 K up to 400 K) conjugated with the FLS1000 Fluorescence Spectrometer by Edinburgh Instruments (**Figure 13**). The PMT-980 detector was used for emission and excitation measurements, as well as for decay kinetics analysis. As an excitation source, the 450 W Xe2 xenon lamp (emission, excitation) and 100 W microsecond pulse lamp (model μF2) were applied. As an excitation wavelength, the 405 nm beam was

chosen to maintain the complementary excitation conditions to the first applied method. The setup was used for the characteristics of the materials presented in publications **P3**-**P5**.

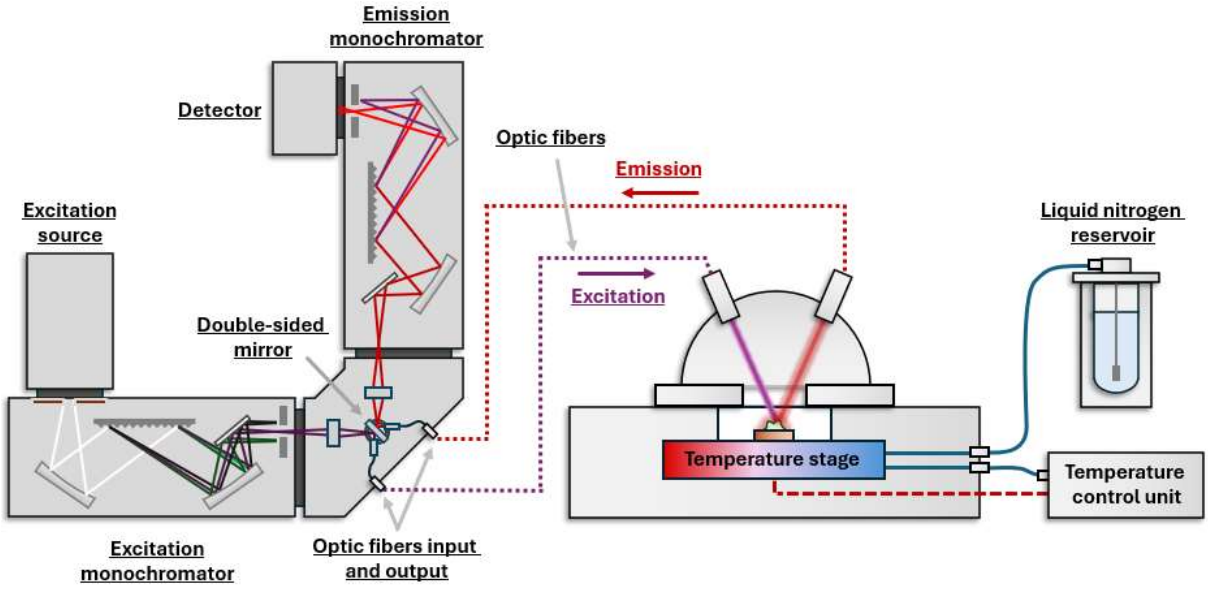

Figure 13. The simplified representation of the FLS1000/Linkam setup used for temperature-dependent luminescence measurements

Alternatively, for the measurements of luminescence decay kinetics presented in publication **P1**, the setup was based on a Ti-sapphire laser pumped with YAG: Nd^{3+} as the excitation source, combined with a McPherson optical system equipped with a Hamamatsu R7154P photomultiplier tube as a detector and a digital oscilloscope Tektronix MDO3052. Details regarding the setup configurations are provided in the method descriptions included in publications **P1**–**P5**, attached to this dissertation (see **Chapter 11**).

7. Results published in the series of publications P1-P5

7.1 Publication P1

ACS Applied Materials & Interfaces (2023), 15, 7074-7082

Metal-Organic Framework Optical Thermometer Based on Cr^{3+} Ion Luminescence

Adam Kabański[a],* Maciej Ptak[a], Dagmara Stefańska[a]*

[a]*Institute of Low Temperature and Structure Research, Polish Academy of Sciences, 50-422 Wrocław, Poland*

The publication **P1** is the first work in a series of scientific reports concerning the potential of hybrid organic-inorganic materials doped with Cr^{3+} ions as highly sensitive luminescent thermometers. This publication describes an analysis of the $[EA]_2NaAl_{1-x}Cr_x(HCOO)_6$ series, where x = 0, 0.21, 0.30, 0.57, 0.78, and 1. The materials were synthesized using the hydrothermal method. The purity was confirmed by pXRD analysis, as well as Raman and (IR) spectroscopy. The compounds crystallize in the *Pn* space group; however, at approximately 373 K, they undergo a phase transition to the $P2_1/n$ group, which is accompanied by an order-disorder transition. The investigated materials show a significant compositional diversity. Thus, preparation of the full concentration range of Cr^{3+} ions (0-100 mol.%) extends the current understanding of structural transitions and order-disorder phenomena in hybrid materials, as well as provides an excellent scope on the influence of Cr^{3+} concentration on spectroscopic characteristics and further thermometric potential.

By preparing a series of compounds in which the concentration of chromium(III) varies across the entire compositional range, it was possible to perform a comprehensive analysis of the effect of Cr^{3+} ion concentration on the spectroscopic characteristics. Raman measurements revealed that increasing the Cr^{3+} content leads to a decrease in the intensity of bands at 227, 290, 308, 630, 936, 1352, and 1682 cm^{-1}, while new bands appear at 245, 1340, 1383, and 1672 cm^{-1}. Some of these bands exhibit significant changes in their relative intensity. These variations are associated with differences in the phonon properties of Cr^{3+}/Al^{3+}-O bonds and with local structural distortions arising from mixed CrO_6/AlO_6 octahedra. In particular, a pronounced spectral change was observed around 1352 cm^{-1} (**Figure 14a**). The variation in the relative intensity of selected Raman peaks can be used to estimate the Cr^{3+} ion concentration in the samples (**Figure 14b**). Due to the wide availability of Raman spectroscopy, the determination of metal ion concentration from Raman spectra can serve as a useful analytical tool in materials science. Consequently, this approach represents an interesting direction for future research.

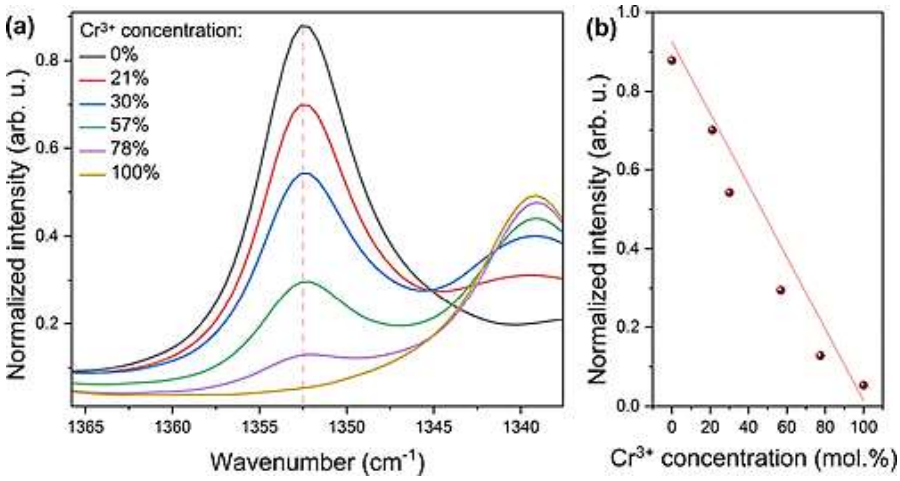

Figure 14. (a) Comparison of the normalized Raman spectra for the band at 1352 cm^{-1}, and (b) dependence of the band intensity at 1352 cm^{-1} on the Cr^{3+} ion concentration, including the corresponding linear fit.

The DRS measurements showed that the studied material series exhibits characteristic absorption bands associated with Cr^{3+} ions (**Figure 15a**). The calculated *Dq/B* parameters indicate a non-linear variation in the crystal field strength as a function of Cr^{3+} ion concentration (**Figure 15b**). According to these calculations, the compounds demonstrate a gradual change in crystal field strength from strong-field to medium-field with increasing Cr^{3+} content. These results are consistent with the observed luminescence characteristics of the materials.

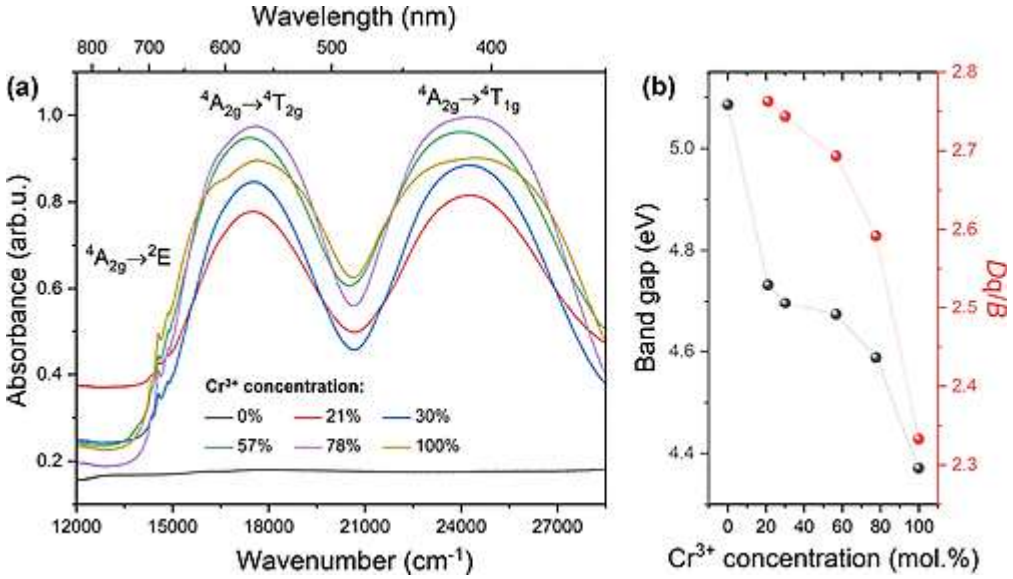

Figure 15. (a) Diffuse reflectance spectra of the investigated series of materials; (b) variation of the optical band gap and crystal field strength

Due to the medium-to-strong crystal field, a high emission intensity from the $^2E_g\rightarrow{}^4A_{2g}$ transition was observed (**Figure 16a**). Investigated materials show a significant thermal quenching of the narrow spin-forbidden emission. Simultaneously, the broadband emission assigned to the $^4T_{2g}\rightarrow{}^4A_{2g}$ transition intensifies (**Figure 16b**), reaching its maximum around 220 K. This behaviour is attributed to a thermally induced energy transfer from the lower ^2E_g

state to the higher $^4T_{2g}$ state. Increasing the Cr^{3+} concentration enhances the relative contribution of the broadband emission compared to the narrow, spin-forbidden $^2E_g \rightarrow {}^4A_{2g}$ transition. This effect originates from the weakening of the crystal field and corresponding changes in the energy levels.

The observed temperature dependence of luminescence was the basis for developing a thermometric model based on the intensity ratio of emission bands (ratiometric approach). As the thermometric band, the parts of the emission spectra assigned to $^2E_g \rightarrow {}^4A_{2g}$ and $^4T_{2g} \rightarrow {}^4A_{2g}$ were established. The obtained luminescence intensity ratio (LIR) values are shown in **Figure 16c**. To provide a more detailed description of the thermometric performance, both absolute sensitivity (S_a) and relative sensitivity S_r were determined (**Figures 16d-e**). The maximum S_r value of $2.84\%\cdot K^{-1}$ was achieved for the sample containing 21 mol.% of Cr^{3+} ions at 160 K. With increasing Cr^{3+} concentration, the temperature corresponding to the maximum relative sensitivity shifts toward higher values (**Figure 16f**). The ability to tune the optimal detection temperature range through adjustment of the Cr^{3+} concentration significantly extends the potential of the thermometric system.

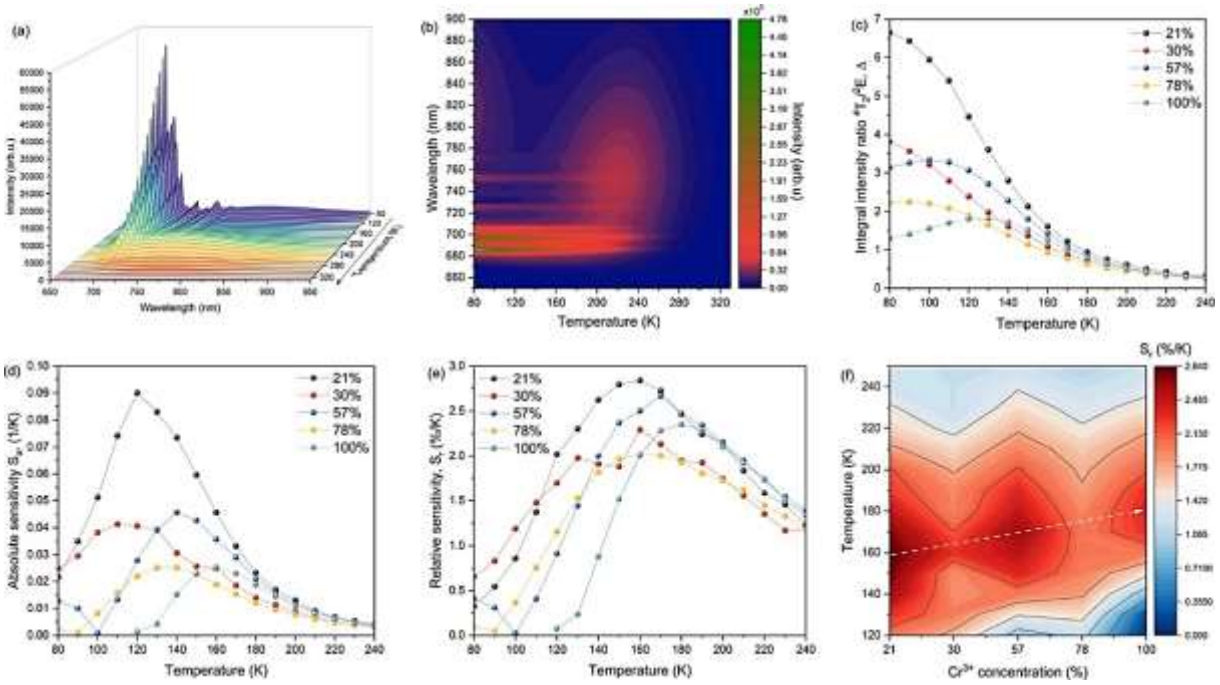

Figure 16. (a) Temperature-dependent emission spectra and (b) emission intensity map recorded for $[EA]_2NaAl_{1-x}Cr_x(HCOO)_6$; (c) thermometric parameter (FIR); (d) absolute sensitivity (S_a); (e) relative sensitivity (S_r); and (f) combined influence of Cr^{3+} concentration and temperature on S_r

To demonstrate the practical applicability of luminescent thermometry based on the investigated compounds, a prototype measurement setup was designed using one of the studied compounds. Initial tests were performed using a copper tube, where one end was placed in a container filled with liquid nitrogen (**Figure 17a-b**). The $[EA]_2NaAl_{1-x}Cr_x(HCOO)_6$ crystals were attached to the tube surface with thermally conductive silver paste at three points, as shown in **Figure 17b**. The determination of temperature was performed according to the

model based on preliminary measurements under laboratory conditions (**Figure 17c**). The presented results clearly demonstrate the remarkable potential of these temperature-sensitive luminescent materials. Among numerous advantages, a key feature is the ability to record emission spectra even in the presence of frost. Moreover, commercial thermal cameras, even high-end ones, typically operate only above -40°C, as shown in **Figure 17a**.

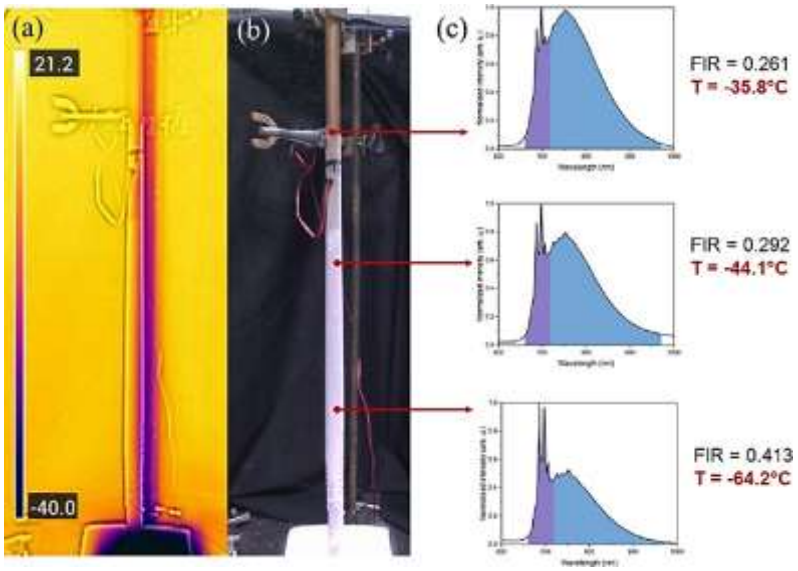

Figure 17. Prototype thermometric setup: (a) thermal image, (b) photograph of the experimental system, and (c) recorded emission spectra for selected points with the corresponding FIR values and determined temperature

Investigated hybrid phosphors exhibit excellent stability during repeated heating and cooling cycles. Performed emission stability measurements confirmed no significant changes in the LIR values, indicating that the materials can be successfully used in thermometric applications. Additionally, the absence of phase transitions within the operational temperature range further supports their thermal stability. What should be pointed out, due to the chemical sensitivity to the environmental conditions, such as humidity, the practical applicability of these materials should be further improved by employing protective strategies, such as resin encapsulation.

7.2 Publication P2

Journal of Materials Chemistry C (2024), 12, 4663-4675

Mechanism of isosymmetric polar order–disorder phase transition in pyroelectric $[CH_3CH_2NH_3]_2NaGa(HCOO)_6$ double perovskite

Maciej Ptak[a],* Adam Kabański[a], Błażej Dziuk[b], Sergejus Balciunas[c], Gediminas Usevicius[c], Jan K. Zaręba[b], Juras Banys[c], Mantas Simenas[c], Adam Sieradzk[d], Dagmara Stefańska[a]

[a]*Institute of Low Temperature and Structure Research, Polish Academy of Sciences, 50-422 Wrocław, Poland*

[a]*Institute of Advanced Materials, Wrocław University of Science and Technology, 50-370 Wrocław, Poland*

[c]*Faculty of Physics, Vilnius University, LT-10257 Vilnius, Lithuania*

[d]*Department of Experimental Physics, Wrocław University of Science and Technology, 50-370 Wrocław, Poland*

The publication **P2** is a continuation of the studies concerning the characteristics of hybrid double perovskites doped with Cr^{3+} ions. The presented publication is also focused on structural, dielectric, electric, optical, and phonon properties of a novel, unreported compound with the general formula $[EA]_2NaGa_{1-x}Cr_x(HCOO)_6$, where x = 0 and 0.931. The investigated materials were synthesized using the hydrothermal method, analogous to the approach used in the **P1** publication.

The performed structural analysis showed that materials crystallize in the non-centrosymmetric and polar *Pn* space group. Performed DSC analysis indicated an order-disorder phase transition to the $P2_1/n$ space group, occurring in the temperature range of 376–379 K. Below the phase transition temperature, the system starts to order, resulting in a modification of the hydrogen-bond network and deformation of the metal-organic framework. The performed scXRD indicated that both phases are assigned to the same *Pn* space group. This is an extremely rare order-disorder polar-polar PT, which has been reported among formate perovskites only for the subgroup of $[MHy]M^{II}(HCOO)_3$ (M^{II} = Fe^{2+}, Mg^{2+}, Mn^{2+}, and Zn^{2+}).

Within the presented publication, a wide range of characterization methods was applied, including electronic paramagnetic resonance (EPR) studies, dielectric analysis, pyrocurrent measurements, electric polarization analysis, as well as energy-dispersive X-ray spectroscopy (EDS). However, within the scope of this dissertation, particular focus should be directed toward optical characteristics – both linear and non-linear. The temperature-dependent second-harmonic generation (SHG) study was performed for an undoped compound by irradiating the sample with femtosecond laser pulses (λ_{exc} = 800 nm) in the 354-403 K temperature range. Both the low-temperature phase (LTP) and high-temperature phase (HTP) phases exhibit measurable

SHG activity, confirming the non-centrosymmetric nature of both phases. A gradual decrease in SHG intensity with increasing temperature was observed in the LTP, with an inflection point near 387 K, above which the SHG intensity remains constant (HTP). Furthermore, the process shows negligible thermal hysteresis between the heating and cooling cycles (**Figure 18**). These features indicate a continuous transition between two acentric phases, consistent with the DSC results.

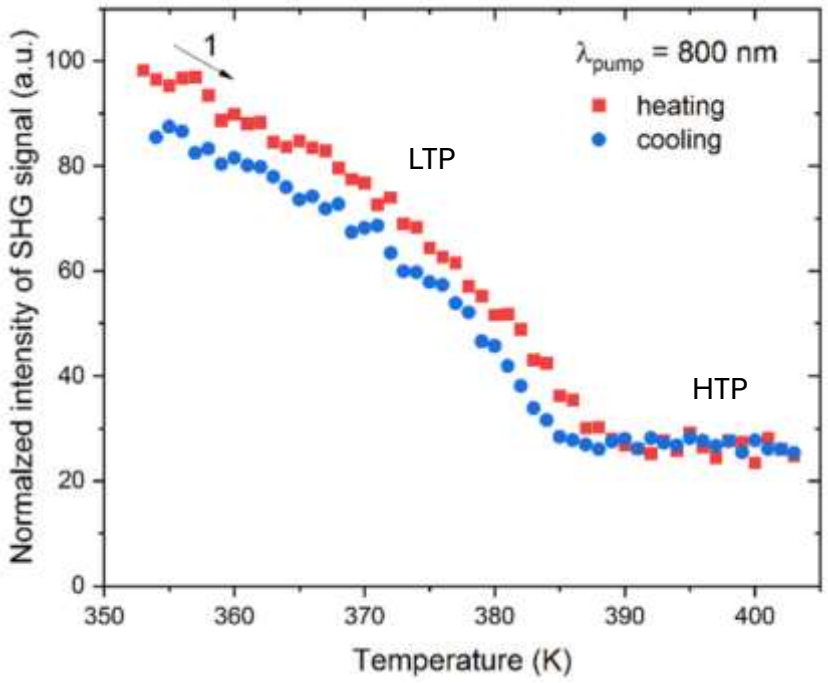

Figure 18. Integral intensities of the SHG signal for heating and cooling runs

The investigated compounds may show a coexistence of nonlinear and linear optical properties. The Cr^{3+}-doped materials exhibit a photoluminescence under excitation with a 405 nm laser beam. At 80 K, the emission spectrum is characterized by narrow and intense emission (around 700 nm), assigned to the $^2E_g \rightarrow {}^4A_{2g}$ transition. However, the presence of the less-intensive broadband emission (720-900 nm), assigned to the $^4T_{2g} \rightarrow {}^4A_{2g}$, is observed. It indicates a medium-to-strong crystal field (**Figure 19a**). This prediction is confirmed by DRS analysis, which provided a *Dq/B* value equal to 2.35. As the temperature increases, the intensity of the emission from the spin-forbidden ^2E_g transition significantly decreases, while the intensity of the broadband emission $^4T_{2g} \rightarrow {}^4A_{2g}$ initially increases (**Figure 19a–c**). The maximum intensity of the broadband emission is observed at approximately 190 K (**Figure 19c**). This phenomenon can be described as a thermally induced energy transfer from the lower ^2E_g level to the higher $^4T_{2g}$ level. Above 190 K, a regular thermal quenching process occurs due to non-radiative crossover between the $^4T_{2g}$ excited state and the $^4A_{2g}$ ground state. This process is illustrated schematically by the energy level diagram of chromium(III) ions (**Figure 19d**).

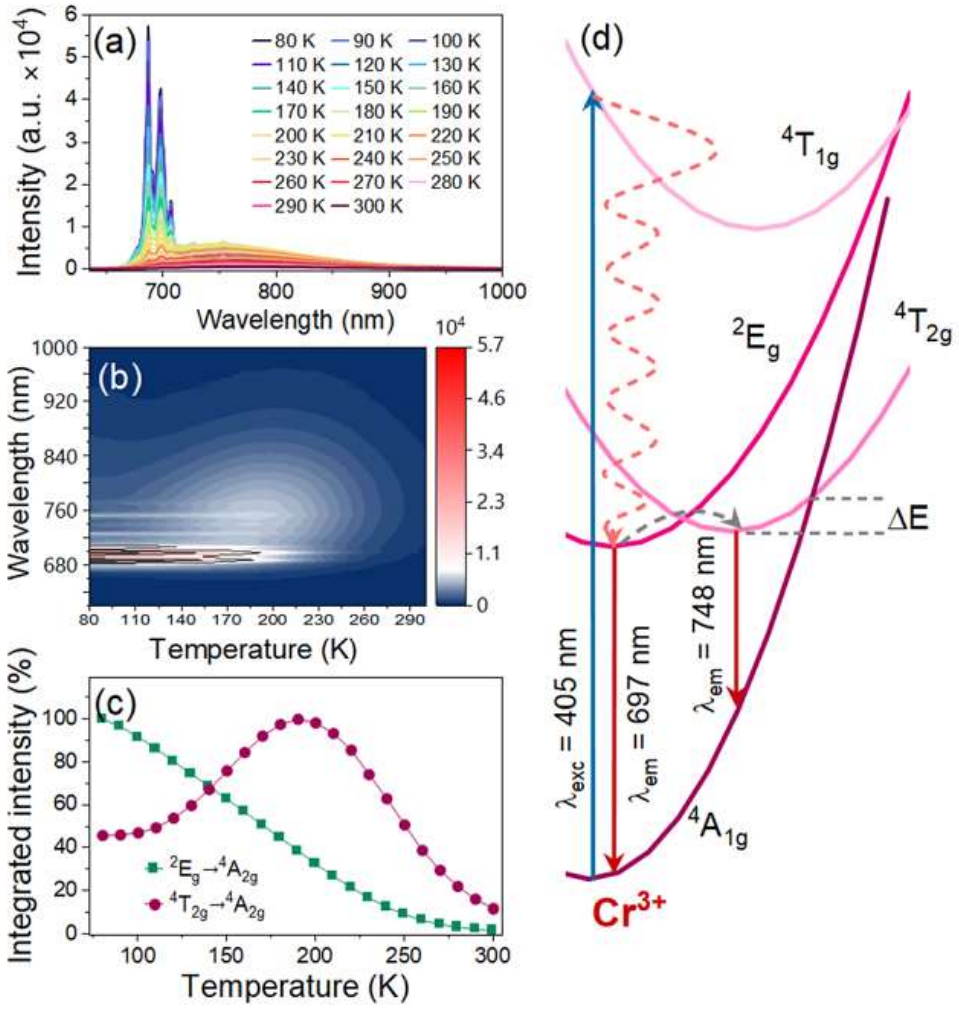

Figure 19. (a) Temperature-dependent emission spectra of $[EA]_2NaGa_{0.069}Cr_{0.931}(HCOO)_6$, (b) thermal evolution of the luminescence, (c) integrated emission intensity of the spin-forbidden $^2E_g \rightarrow {}^4A_{2g}$ and spin-allowed $^4T_{2g} \rightarrow {}^4A_{2g}$ transitions, and (d) the schematic energy level diagram

The significant changes in emission intensities in luminescence spectra provided the basis for developing a luminescent thermometry model utilizing the fluorescence intensity ratio of two bands, assigned to the spin-forbidden (660-718 nm) and spin-allowed (718-970 nm) transitions. The developed model demonstrates a high relative sensitivity of up to 2.11%·K^{-1} at 150 K, which is comparable to other Cr^{3+}-based systems relying on the coexistence of two emission channels presented in **P1**. Moreover, the ability of these materials to exhibit second-harmonic generation opens new perspectives for integrated optical thermometry, combining linear and nonlinear optical functionalities within a single hybrid system.

7.3 Publication P3

Advanced Optical Materials *(2025), 13(25), e01057*

Real-Time Temperature Monitoring with Cr^{3+}-Based Hybrid Formate Perovskites: Insights into the Relation Between Chemical Composition and Thermometric Performance

Adam Kabański[a],* Maciej Ptak[a], Luis Dias Carlos[b], Dagmara Stefańska[a*]

[a]*Institute of Low Temperature and Structure Research, Polish Academy of Sciences, 50-422 Wrocław, Poland*

[b]*Phantom-g, CICECO – Aveiro Institute of Materials, Physics Department, University of Aveiro, 3810-193 Aveiro, Portugal*

The results presented in publications **P1**-**P2** concern the characteristics of double perovskites containing Cr^{3+} ions. However, the group of single perovskites also shows a valuable characteristic, especially from the spectroscopic and thermometric point of view. The publication **P3** describes the developed series of 20 samples with a general formula $[DMA]M^{II}(HCOO)_3$: xCr^{3+}, where $M^{II} = Zn^{2+}$, Mn^{2+}, Mg^{2+}, Ni^{2+}, Co^{2+}, and x = 0, 1, 3, and 5 mol.% of Cr^{3+}, with respect to the M^{II} ion. The slow-diffusion method was applied to prepare the investigated series of hybrid materials, according to the procedure described in **Chapter 6.1**.

The group of $[DMA]M^{II}(HCOO)_3$ compounds shows the trigonal space group $R\bar{3}c$, with the disordered DMA^+ cations located in the cages of the metal-organic network. A decrease in temperature results in ordering of the DMA^+ cations, associated with the decrease of symmetry to the *Cc* space group. This order-disorder phase transition takes place within the 156-270 K range, depending on the type of M^{II} cation. Performed pXRD measurements demonstrated that all obtained crystals are phase-pure and confirmed that an aliovalent doping with chromium(III) ions (up to 5 mol.%) has no effect on the hexagonal $R\bar{3}c$ symmetry. The limitation of the possible Cr^{3+}-doping is most likely linked to the charge mismatch occurring under an increase in the Cr^{3+}/M^{2+} ratio and resulting structural destabilization caused by defects.

To provide a more comprehensive look at the phonon characteristics, ATR and Raman studies were performed. The differences in obtained spectra were observed for different metal ions, mainly changes in intensity or varying component numbers. It originates from differences in crystal lattice parameters, metal-ion radii and electronegativity of M^{II} cations, perovskite cavity size and hydrogen-bond strength. Among the concentration series, the aliovalent doping with Cr^{3+} ions up to 5 mol.% did not significantly affect the obtained spectra. Only shift and broadening (up to 1-2 cm^{-1}) of certain bands were observed, which can be assigned to the increase in substitutional disorder and the creation of defects. Performed phonon studies,

detailed in the described publication **P3**, provides an important insight into the fundamental properties of the obtained hybrid materials.

Considering the broad range of investigated materials, the present study **P3** provides a valuable opportunity for a comparative analysis of compounds that differ not only in the type of metal cation M^{II} but also in the chromium doping level. The conducted DRS measurements revealed the significant influence of the M^{II} cation on the recorded spectra. For the materials containing Zn^{2+} and Mg^{2+} ions, the DRS spectra of the Cr^{3+}-related region show three characteristic bands associated with the main transitions in chromium(III) ions: $^4A_{2g} \rightarrow {}^2E_g$ (~14550 cm^{-1}), $^4A_{2g} \rightarrow {}^4A_{1g}$ (~17200 cm^{-1}), and $^4A_{2g} \rightarrow {}^4A_{2g}$ (~24000 cm^{-1}). The change in the Cr^{3+} ion concentration does not significantly affect the position of the mentioned bands. Within the Mn^{2+}, Ni^{2+}, and Co^{2+}-series, the presence of both types of excitation bands – assigned to originating from given M^{2+} and Cr^{3+} ions – was observed. Exemplary, for the Mn^{2+}-based materials, the presence of transitions from $^6A_1$ to ^4E, $^4T_2$, $^4A_1$, ^4E, and $^4T_1$ energetic levels was recorded (**Figure 20**).

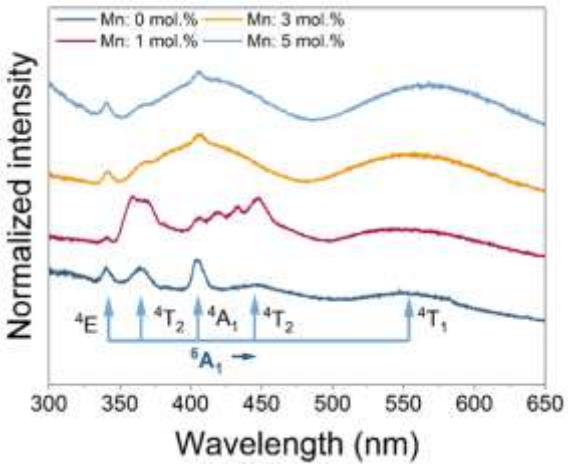

Figure 20. A comparison of excitation spectra of the Mn-series monitored at 699 nm at 80 K

The performed DRS studies were used to determine *Dq/B* and other Racah parameters. By the analysis of the bands' position, the CF strength of Zn- and Mn-based compounds was reported. Zinc-based materials exhibit *Dq/B* values from 2.34 (x = 0.01) via 2.49 (x = 0.03) to 2.36 (x = 0.05), which indicates the intermediate/strong crystal field. Magnesium-based samples exhibit greater diversity of *Dq/B* parameter – from 2.22 (x = 0.01), via 3.42 (x = 0.03), to 3.13 (x = 0.05). Due to the overlap of the absorption bands of Mn^{2+}, Co^{2+}, and Ni^{2+} with the absorption bands of Cr^{3+}, to estimate the general influence of M^{II} cation type on CF strength, the metal-ligand distance was analyzed. Due to the lack of photoluminescence of Ni^{2+} and Co^{2+} derivatives, this analysis was limited to other materials. For the Mg^{2+} sample, the initial (without Cr^{3+} doping) crystal field is 0.0250, and for Zn^{2+}-based compounds — 0.0236. The lowest value of CF is, in turn, observed for Mn^{2+} (0.0199), as it is shown in **Figure 21**. The performed method should not be used for the direct comparison of undoped and doped compounds. However, it proves the general prediction – higher CF strength is observed for Mg^{2+}-based materials. Even though the presented approach is not directly complementary to estimations conducted with the DRS technique, the method based on metal-ligand distance analysis may be a useful tool in the

prediction of the general qualities of Cr^{3+}-doped materials. What is more, due to the overlapping of the absorption bands assigned within the Mn-based series, the determination of the *Dq/B* parameter with the conventional method based on the DRS technique could not be conducted. Thus, this method may provide valuable insights into the dependence of the divalent metal ion on CF strength and resulting spectroscopic properties.

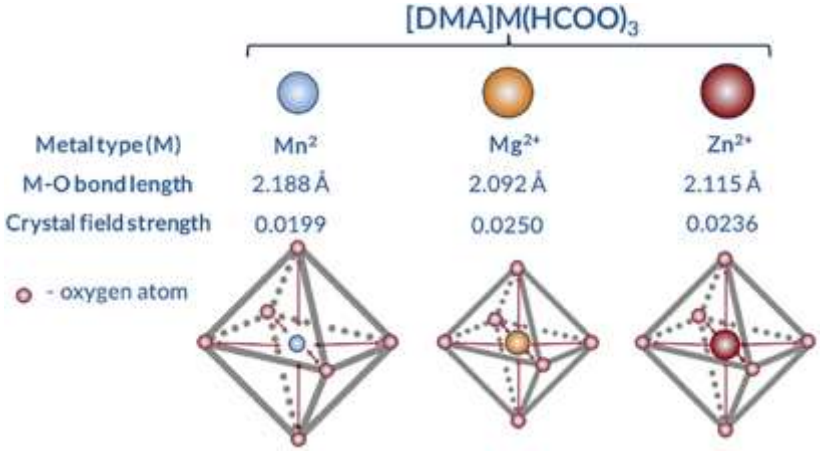

Figure 21. The influence of the metal type on the metal-ligand distance and the following CF strength

Zinc-, manganese-, and magnesium-based compounds exhibit strong photoluminescence related to the presence of Cr^{3+} ions. Materials containing Co^{2+} and Ni^{2+} ions, in turn, did not show detectable luminescence due to efficient non-radiative energy transfer from excited Cr^{3+} ions to Co^{2+} and Ni^{2+} levels. The luminescent measurements were performed under 405 nm excitation, corresponding to the $^4A_{2g} \rightarrow {}^4A_{1g}$ transition. At 80 K, $[DMA]Zn(HCOO)_3$ series of doped compounds shows several narrow emission lines typical of low-temperature Cr^{3+} luminescence. The most intense, called the R_1 line, is localized at 686.1 nm, while additional bands are recorded at 698.3, 706.5, 726.4, and 753.8 nm. Among the zinc series, the strongest emission and highest quantum efficiency (7.8%) were recorded for the sample containing 3 mol.% of Cr^{3+} ions. Lower or higher chromium concentrations lead to a reduction in emission intensity and quantum efficiency. A comparison of representative materials containing 3 mol.% of Cr^{3+} ions indicates that the Zn-based sample exhibits the highest luminescence intensity, while the Mn-derivative exhibits the weakest. The emission spectra are generally similar for all matrices, featuring the R_1 line and accompanying less-energetic bands.

As presented in publications **P1**-**P2**, the temperature has a crucial influence on the luminescent characteristics of Cr^{3+} ions. Within the series described in work **P3**, the increase in temperature induces a reduction in R_1 line intensity. Simultaneously, the significantly less-intensive broadband emission (centered ~796 nm) appears due to the thermally induced population of the $^4T_{2g}$ excited state. The $T_{0.5}$ parameter shows that a cumulative intensity of luminescence is reduced by half at ~154 K. At room temperature, the Zn-based material doped with 3 mol.% Cr^{3+} retains the highest emission intensity. The detectable luminescence around room temperature is a phenomenon that has not been observed for hybrid formates doped with Cr^{3+} ions before.

Temperature-dependent luminescence studies were used to establish a thermometric model based on a ratiometric approach. Due to the notably greater intensity of the $^2E_g \rightarrow {}^4A_{2g}$ emission than the $^4T_{2g} \rightarrow {}^4A_{2g}$ transition, model determination was based on the analysis of the intensity of the R_1-line (680-689 nm) and less-energetical Stokes band (720-732 nm), as it is shown in **Figure 22a**. The change in the LIR value over temperature, combined with the operating range, is presented in **Figure 22b**. For all of the investigated samples, a growth in temperature causes the initial increase of the S_r values, achieving maximum values within the 150–180 K range, depending on the sample composition (**Figure 22c)**. The highest relative sensitivity ($2.5\%\cdot K^{-1}$) is observed for Mn-based compounds doped with 5 mol.% of Cr^{3+} ions. Among Zn- and Mg-based series, the highest S_r values are observed for the samples containing 3 mol.% ($2.4\%\cdot K^{-1}$) and 1 mol.% ($2.2\%\cdot K^{-1}$) of dopant, respectively (**Figure 22d**). The Mg-based materials exhibit the shift of maximal S_r values within the concentration series toward higher temperatures. Such a phenomenon is not observed for other materials in the study. However, an analogous observation has been reported in publication **P1**. The thermometric operating ranges, depending on the material, vary from 80 K to 230 K.

The presented thermometric analysis was performed based on the two temperature-dependent ranges assigned to the spin-forbidden $^2E_g \rightarrow {}^4A_{2g}$ transition. The adopted paradigm of ratiometric thermometric analysis is based on the comparison of two independent temperature-sensitive transitions. Such an approach has been presented in publications **P1** and **P2**, where the calculation of the LIR parameters was based on the ratio of $^2E_g \rightarrow {}^4A_{2g}$ and $^4T_{2g} \rightarrow {}^4A_{2g}$ transitions. In this particular system, the intensity of the spin-allowed $^4T_{2g} \rightarrow {}^4A_{2g}$ transition was not high enough to implement this particular method. The approach presented in publication **P3** is based on a single-transition analysis, which is not a commonly used technique.

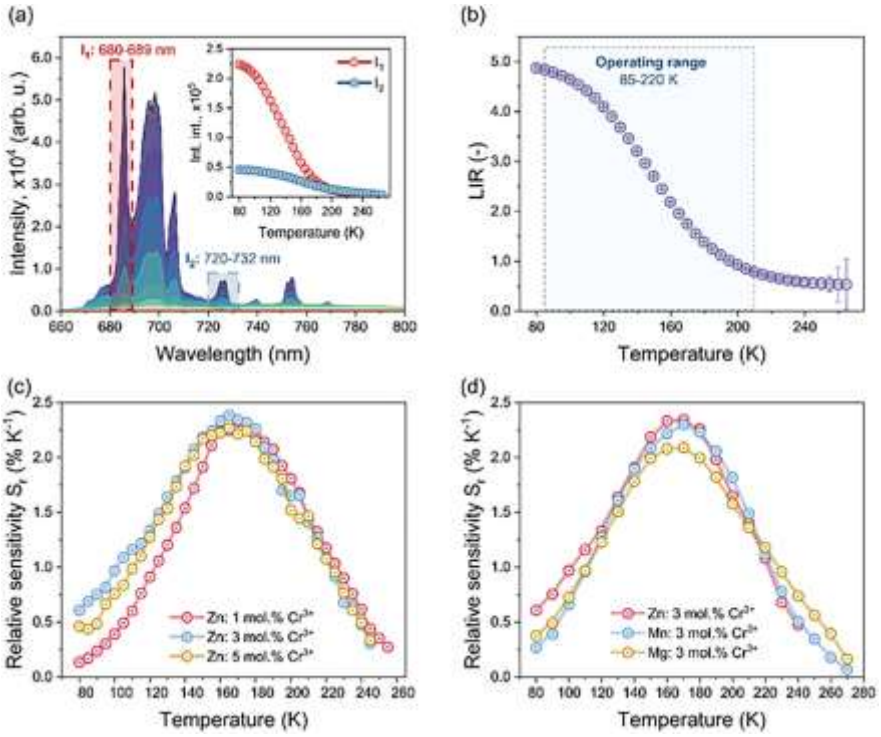

Figure 22. (a) Temperature-dependent emission spectra of Zn-based compound doped with 1 mol.% of Cr^{3+} with I_1 and I_2 markers and changes in: I_1 and I_2 values (inside); (b) luminescence

intensity ratio (LIR) combined with LIR determination error bars and operating range of the thermometer; (c) relative sensitivity (S_r) of zinc-series; (d) comparison of S_r values for series of materials containing 3 mol.% of Cr^{3+} ions and different M^{II} cation

To demonstrate the performance and practicality of the developed luminescent thermometers, an experimental setup, analogous to the system presented in publication **P1**, was constructed (**Figure 23a**). A copper pipe was partially immersed in an insulated container made of extruded polystyrene foam filled with liquid nitrogen. The container remained open to allow natural evaporation. Several crystals of the Mn-based compound doped with 5 mol.% of Cr^{3+} were attached to the pipe surface using silver paste, and their luminescence was continuously monitored. When the luminescence intensity reached its maximum, indicating thermal stabilization, a sequence of luminescence spectra was recorded every 5 s. During the experiment, the sample temperature varied due to nitrogen evaporation (heating) and periodic refilling of the container (inducing a sensor cooling). Each recorded spectrum was processed to calculate LIR values, which were then converted to temperature using a previously calibrated thermometric model. The resulting temperature profile (**Figure 23b**) clearly reflected the dynamic changes in the system: a gradual temperature rise as nitrogen evaporated (range 1), rapid cooling and temporary stabilization after refilling (range 2), a subsequent linear increase (range 3), and a further cooling-heating cycle (ranges 4-5). The final stage (6), when liquid nitrogen was fully removed, produced a distinct and rapid temperature increase. Minor fluctuations were attributed to air circulation and unsteady thermal conditions.

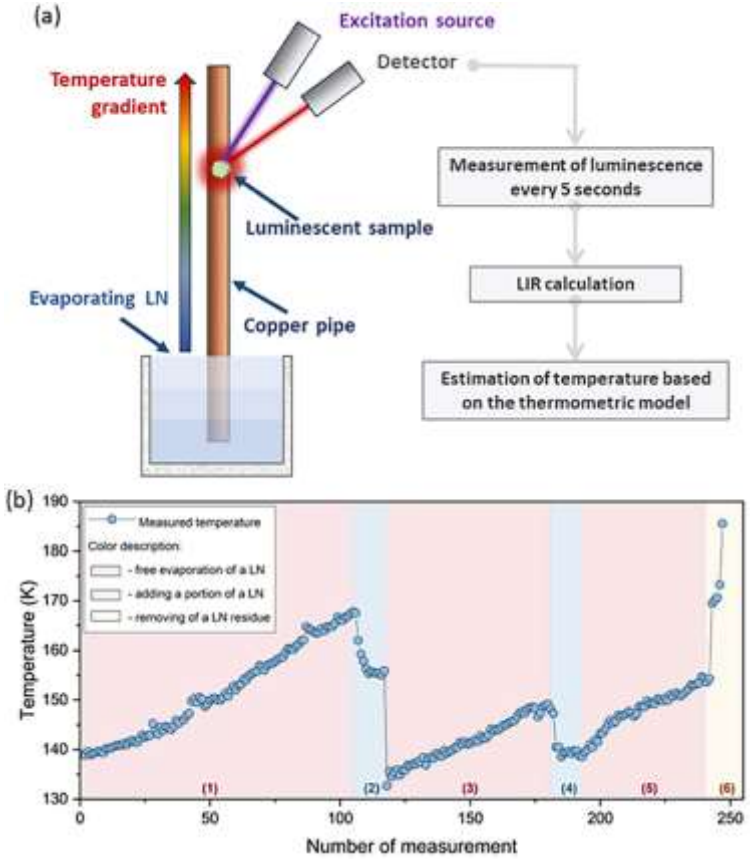

Figure 23. (a) The visualization of the experimental setup and (b) the change in temperature of a sensor during the experiment

This experiment highlights the strong potential of luminescent thermometers for real-time temperature monitoring under nonideal and fluctuating environments. The method effectively monitored both subtle and large temperature variations. These results confirm that formate-based hybrid perovskites possess sufficient characteristics for remote thermometry. The demonstrated Cr^{3+}-based luminescence approach offers a promising perspective toward non-lanthanide optical probes for remote and fast temperature detection.

7.4 Publication P4

Dalton Transactions *(2025), 54, 15899-15908*

High-sensitivity optical thermometry with Cr^{3+}-doped hybrid formate perovskites: comparative analysis of ratiometric and lifetime-based approaches

Adam Kabański[a],* Kacper Caputa, Dagmara Stefańska[a*]

[a]*Institute of Low Temperature and Structure Research, Polish Academy of Sciences, 50-422 Wrocław, Poland*

The continuation of the research on the use of hybrid compounds containing Cr^{3+} ions as luminescent thermometers, presented in papers **P1**–**P3**, is the extension of the analyzed thermometric model by including the analysis of luminescence decay kinetics, as it is presented in paper **P4**. In paper **P4**, similarly to paper **P3**, a series of single perovskite-like materials with the general formula $[EA]Mg(HCOO)_3$: xCr^{3+}, and x = 0, 1, 3, and 5 mol.% of Cr^{3+}, was synthesized using the slow-diffusion method.

The structural and phonon properties of the compound with the $[EA]Mg(HCOO)_3$ formula have already been reported in the literature; therefore, in paper **P4**, particular attention was focused on the spectroscopic and thermometric properties of the series of compounds also containing Cr^{3+} ions. Nevertheless, to provide a comparison with other compounds discussed throughout this dissertation, it should be noted that these materials crystallize in the non-centrosymmetric $Pna2_1$ phase, with a phase transition to the $R\bar{3}$ phase occurring at 316-373 K range. The second phase transition, to the orthorhombic *Imma* space group, takes place within the 415-426 K range. The performed pXRD analysis showed the appearance of additional signals at approximately 18° and 34.5° in the sample containing 5 mol% of chromium(III) ions, which can be attributed to structural defects that destabilize the crystal lattice while trivalent Cr^{3+} is incorporated into the divalent Mg^{2+} site. This phenomenon may be an explanation for the limited achievable Cr^{3+} concentration (up to ~5 mol.%). These results follow the analogous limitation observed within the series of DMA-based compounds presented in **P3**.

Conducted DRS studies showed the presence of characteristic absorption bands assigned to $^4A_{2g}\rightarrow{}^2E_g$, $^4A_{2g}\rightarrow{}^4A_{1g}$, and $^4A_{2g}\rightarrow{}^4A_{2g}$ transitions. The obtained results correspond to those reported in **P1-P3**. According to the DRS spectrum, the *Dq/B* values were determined. Analysed compounds show intermediate-to-strong crystal field with *Dq/B* equal to 2.43, 2.45, and 2.62, for materials containing 1, 3, and 5 mol.% of Cr^{3+} ions. The obtained results of DRS studies, indicating intermediate-to-strong CF, generally correspond to the performed temperature-dependent PL studies. The investigated materials exhibit strong photoluminescence under 405 nm excitation wavelength. At 80 K, several narrow emission bands are observed. The most intense peak at 686.5 nm, identified as the R_1, is attributed to the

spin-forbidden $^2E_g \rightarrow {}^4A_{2g}$ transition. Additional sidebands are observed at 696.8, 726.5, and 754.5 nm. A significantly weaker broadband emission appears in the 720-1000 nm range ($^4T_{2g} \rightarrow {}^4A_{2g}$). Even at 270 K, a weak emission from the $^4T_{2g}$ level remains detectable, although it is approximately 5000 times weaker than the R_1 line intensity recorded at 80 K. Investigated materials show consistent temperature-dependent spectroscopic characteristics with other materials presented in publications **P1**-**P3**.

A notable aspect of publication **P4** is the demonstration of a combination of two thermometric models – ratiometric and lifetime-based. The method based on the analysis of luminescence decay kinetics has not been previously explored within the class of hybrid compounds containing solely Cr^{3+} ions. The ratiometric method, presented also in publications **P1**-**P3**, involves comparing the integral intensities of two selected emission regions - 675-692 nm (I_1) and 710-1000 nm (I_2), assigned to the thermally coupled $^2E_g \rightarrow {}^4A_{2g}$ and $^4T_{2g} \rightarrow {}^4A_{2g}$ transitions, respectively (**Figure 24a-b**). The calculated values of luminescence intensity ratio (LIR) were further used to determine the relative sensitivity of the investigated materials (**Figure 24c**). Maximum S_r values of 2.69%·K^{-1} (120 K), 3.07%·K^{-1} (130 K), and 2.48%·K^{-1} (120 K) were obtained for the samples containing 1, 3, and 5 mol.% of Cr^{3+} ion, respectively. The highest sensitivity, observed for the materials with 3 mol.% of the dopant, results from the most pronounced reduction in LIR parameter with increasing temperature. The operating range of each thermometer was determined based on temperature detection uncertainty analysis. The sample with 3 mol.% of Cr^{3+} ions shows the widest operating range and high thermal resolution (< 0.05 K). Other materials show a sensing range from 80 K to 150 K.

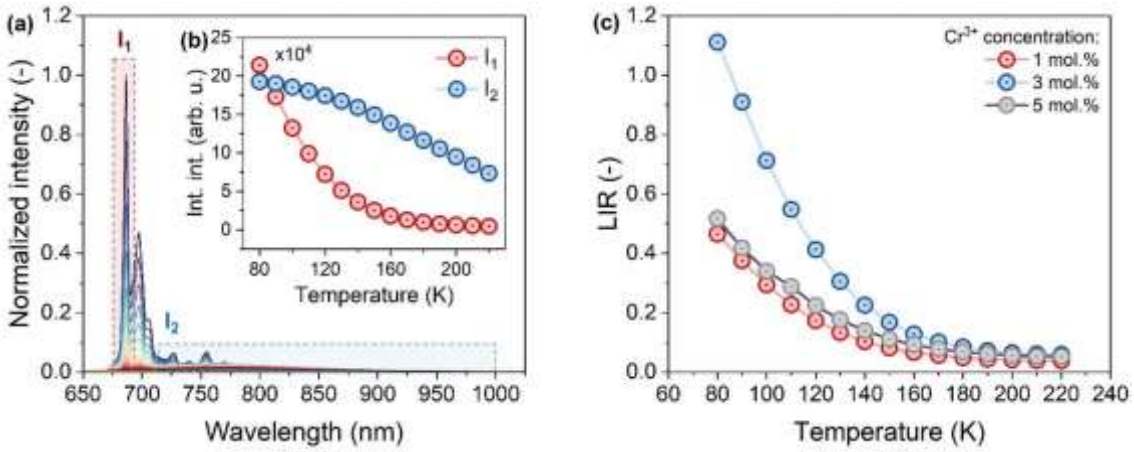

Figure 24. (a) Temperature-dependent luminescence spectra of the materials doped with 3 mol.% of Cr^{3+} ions; (b) thermal quenching of the I_1 and I_2 ranges; (c) the reduction in the LIR parameter over temperature

In the lifetime-based model, the average luminescence lifetime (τ_{avg}) of the emission at 686.5 nm (R_1 line) serves as the thermometric parameter. The change in decay curves in temperature, as shown in **Figure 25a**, is primarily caused by enhanced non-radiative processes and thermal activation to the higher $^4T_{2g}$ state, which results in intensification of spin-allowed emission. At 80 K, τ_{avg} decreases systematically with higher concentration of Cr^{3+} ions, which is consistent with the observations presented in manuscripts **P1**-**P3**. As temperature rises,

decays decrease following a quasi-Arrhenius model (**Figure 25b**). Analogous to the ratiometric method, the S_r parameters were determined. The obtained values of relative sensitivity show that within the Mg-series, the compositional dependence is minimal. The maximum sensitivities reach 2.97%·K^{-1} (140 K) for 1 mol.% sample, 2.90%·K^{-1} (139 K) for 3 mol.%, and 2.94%·K^{-1} (138 K) for 5 mol.% (**Figure 25c**). These high and comparable S_r values indicate that the lifetime-based method may provide a stable and reliable thermometric approach.

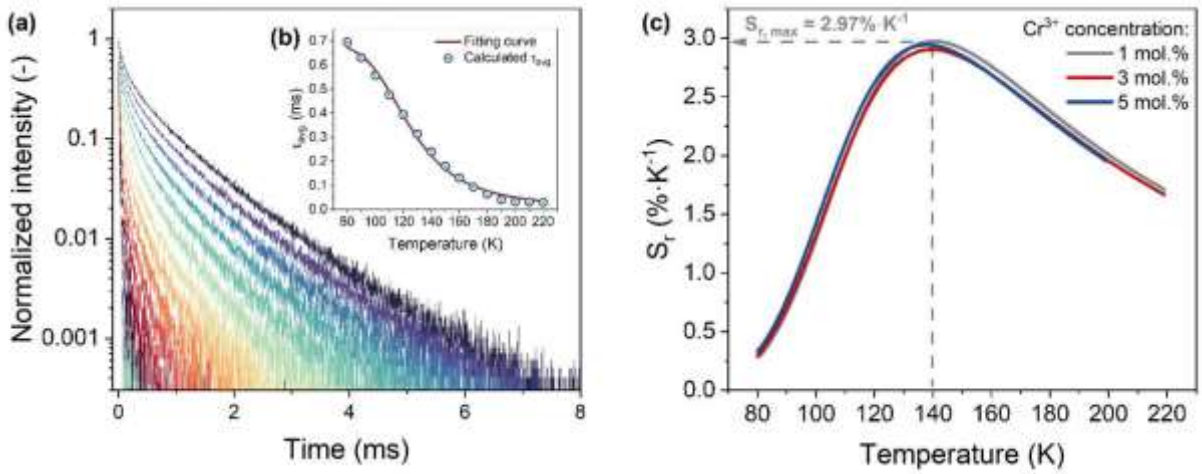

Figure 25. (a) Temperature-dependent decay curves (sample with 3 mol.% of dopant); (b) the τ_{avg} as a function of temperature with fitting function; and (c) the change in S_r values with temperature

These findings demonstrate that lifetime-based thermometry provides sensitivity comparable to ratiometric models. Provided results show that an implementation of a dual-mode thermometric approach, combining both ratiometric and lifetime methods, can significantly enhance precision and versatility in temperature monitoring.

What is more, publication **P4** also discusses the influence of organic cation size on thermometric characteristics. As the size of the amine cation increases ($DMA^+ < EA^+ < GA^+$), the relative sensitivity tends to decrease. Among cations of similar size, such as DMA^+ (272 pm) and EA^+ (274 pm), the molecular geometry becomes an important factor. The more linear structure of EA^+ compared with DMA^+ contributes to the higher sensitivity observed in EA^+-containing compounds. Even though these observations are, at present, primarily phenomenological, they may mark an important step toward the more aware design of advanced luminescent thermometric materials.

7.5 Publication P5

Journal of Materials Chemistry C (2025), 13, 23935-23944 DOI: 10.1039/D5TC02943K

Multimodal temperature sensing in hybrid perovskites doped with Cr^{3+}: a strategy for optimizing luminescent thermometers

Adam Kabański[a],* Kacper Caputa, Dagmara Stefańska[a*]

[a]*Institute of Low Temperature and Structure Research, Polish Academy of Sciences, 50-422 Wrocław, Poland*

An extension of the concept of multiparametric luminescent thermometry in hybrid Cr^{3+}-based materials is presented in study **P5**, in which a series of compounds $[EA]Mn(HCOO)_3$: xCr^{3+}, and x = 0, 1, 3, and 5 mol.% of Cr^{3+}, was investigated. A key aspect of this work is the comparative description of sensing performance obtained from multiple thermometric models, including ratiometric approaches employing various thermometric ranges, as well as the method based on the kinetics of luminescence decay. Although the host material itself - $[EA]Mn(HCOO)_3$ - has been previously described in the literature, its Cr^{3+}-doped derivatives have not yet been investigated, making this study the first attempt to explore them.

The structural characteristics of the undoped analogue, $[EA]Mg(HCOO)_3$, have been described previously; at room temperature, it crystallizes in the noncentrosymmetric $Pna2_1$ space group. The phase transitions have not been reported. To evaluate the quality of the synthesized materials and to understand the effect of incorporating Cr^{3+} ions, pXRD diffractograms were collected and compared with simulated patterns based on single-crystal data. All samples exhibit sufficient quality, which confirms that aliovalent doping with Cr^{3+} ions is possible up to 5 mol.%. This upper limit is consistent with related hybrid materials containing Mn^{2+}, presented in study **P3**, and other single-perovskite materials (**P3**-**P4**)

Performed DRS measurements provided consistent results with other studies (**P1-P4**), especially those focused on Mn^{2+}-based materials presented in publication **P3**. The undoped sample, containing only Mn^{2+} ions, exhibits several low-intensity absorption bands corresponding to electronic transitions originating from the $^6A_{1g}$ energy level of manganese(II) ions (**Figure 26**). After incorporating Cr^{3+} ions into the structure, three characteristic absorption bands become visible at approximately. More intensive Cr^{3+}-related absorption bands almost fully overshadow the less intensive bands assigned to the transitions within Mn^{2+} ions; however, their influence on the shape of the cumulative absorption bands is non-negligible. For this reason, an initial estimation of CF strength was based on metal-ligand distance, as it was proposed in publication **P3**. Comparison with analogous compound $[DMA]Mn(HCOO)_3$ showed a slightly higher distance-related CF parameter ($1/R^5$ = 0.0199) than the EA-based compound (0.0196). Nevertheless, both values are considerably lower than those reported for

Zn^{2+} and Mg^{2+} analogues - 0.0236 and 0.0250, respectively. It may indicate weaker crystal field effects in Mn-based structures.

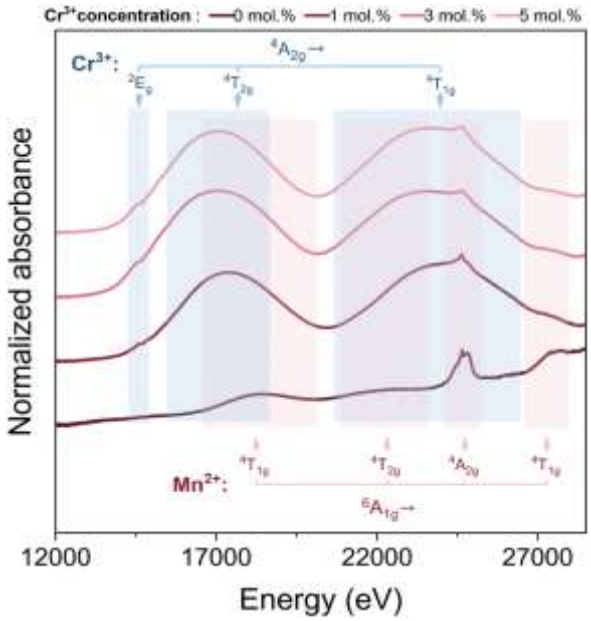

Figure 26. (a) The diffuse reflectance spectra of a series of $[EA]Mn(HCOO)_3$: xCr^{3+}

The undoped $[EA]Mn(HCOO_3$ compound does not exhibit Mn^{2+}-related luminescence due to strong concentration quenching. On the other hand, the Cr^{3+}-doped materials show strong luminescence characteristics to chromium(III) ions in an intermediate-to-strong crystal field. At 80 K, it contains several narrow emission bands, where the most intense peak appears at 685.4 nm (R_1 line). Additional Stokes sidebands are observed at 697.1 nm, 725.4 nm, and 753.1 nm. When the Cr^{3+} concentration increases, a broad emission band emerges between 720-950 nm. The emission is strongly temperature-dependent: as the temperature rises, the overall luminescence intensity decreases, and the spectral profile changes. Thermal quenching is not equally progressive - the R_1 line is quenched the fastest, while the relative contribution of the broadband emission increases.

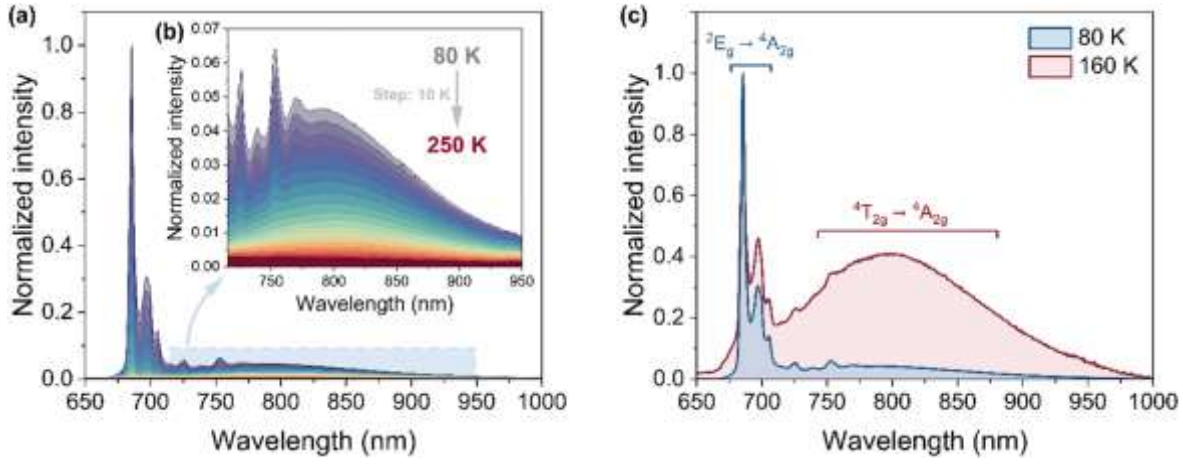

Figure 26. (a) The temperature-dependent luminescence of the sample doped with 3 mol.% of Cr^{3+} ions; (b) the focus on $^4T_{2g} \rightarrow {}^4A_{2g}$ emission range; (c) the normalized luminescence spectra of the compound with 3 mol% of Cr^{3+} ions at 80 K and 160 K

To provide a more comprehensive description of the temperature- and concentration-related spectroscopic characteristics of the investigated materials, the luminescence decay measurements were performed. The R_1 line shows double-exponential decay, attributed to local charge mismatch and structural distortions around Cr^{3+} sites. Increasing dopant concentration shortens the average luminescence lifetime. Among the investigated series, the determined τ_{avg} values were equal to 0.34 ms, 0.40 ms, and 0.78 ms, for materials containing 1, 3, and 5 mol.% of dopant, respectively. The increase in temperature also reduces the average lifetime, which is consistent with other hybrid Cr^{3+}-doped perovskites (**P1-P4**). The temperature-dependent change in luminescence spectra and decay kinetics has been used as a fundamental for thermometric models determination.

In the publication **P5**, the comparison of the performance of two main luminescent thermometric approaches was investigated: ratiometric and the lifetime-based methods. The ratiometric approach is further subdivided into three models, each based on a different determination of the LIR parameter. By examining multiple thermometric ranges, the most effective combination of spectral bands for temperature sensing was identified. What is more, the lifetime-based method was implemented as the second, independent sensing approach. The general idea of the multiparametric analysis is presented in **Figure 27**.

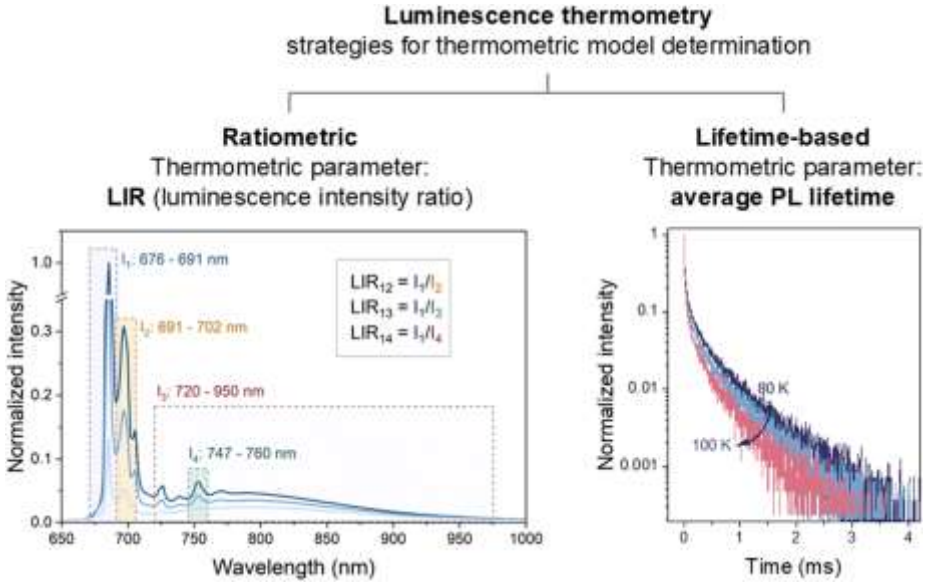

Figure 27. The strategy of multiparametric thermometric analysis

Ranges I_1 and I_2 exhibit nearly identical temperature responses, indicating that both can be assigned to the $^2E_g \rightarrow {}^4A_{2g}$ transition. In contrast, I_3 and I_4 show different quenching characteristics (**Figure 28a**). It leads to a distinct dependency of LIR parameters on temperature (**Figure 28b**). The most progressive reduction is observed for LIR_{14}, which results from the largest contrast in thermal quenching between I_1 and I_4. Less pronounced decreases occur for LIR_{12} and LIR_{13}. Due to the significantly similar temperature-response of I_1 and I_2 ranges, the change in LIR_{12} parameter is the slowest. To evaluate sensing performance, the relative sensitivities were determined.

Among the exemplary compound doped with 3 mol.% of Cr^{3+} ions, the highest sensitivity (3.91%·K^{-1}) is obtained for LIR_{14}, while LIR_{12} yields the lowest value (0.47%·K^{-1}), consistent with its slow thermal evolution (**Figure 28c**). These results are consistent with a purely mathematical understanding of the relative sensitivity, linking high S_r value with the *progressivity* of temperature-based reduction in thermometric parameter. From the practical point of view, the high sensitivity can simultaneously limit the sensing range due to the rapid reduction of the luminescence below the detection and/or accuracy minimum.

The potential of thermometric models based on analysis of the ratio between $^2E_g \rightarrow {}^4A_{2g}$ and $^4T_{2g} \rightarrow {}^4A_{2g}$ transitions has been proved in publications **P1**-**P4**. Within the work **P5**, this statement is additionally confirmed; however, the LIR_{13} model - incorporating phonon sidebands demonstrates strong potential for materials with a strong crystal field, where the $^4T_{2g}$ emission is, in principle, suppressed. In such cases, temperature-sensitive phonon bands offer an alternative route for achieving high sensitivity.

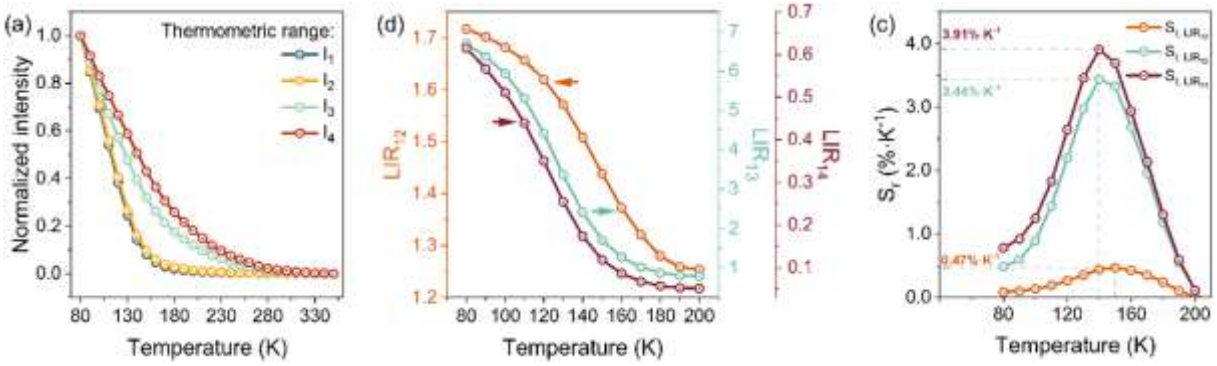

Figure 28. Temperature-induced changes in: (a) thermometric ranges I_1-I_4; (b) LIR parameters; and (c) relative-sensitivities. The results were determined for the sample doped with 3 mol.% of Cr^{3+} ions

To enrich the comparative analysis, the determination of the sensing performance was also performed according to the lifetime-based approach. Within the investigated series, the increasing temperature significantly shortens the average luminescence decay time of the emission assigned to the R_1 line (685.4 nm), as it is presented in **Figures 29a-b**. Obtained results show high sensitivities up to 5.14%·K^{-1} (1 mol.% of Cr^{3+} at 143 K), exceeding those obtained with the ratiometric approach (**Figure 29c**). Other materials show sensitivities equal to 4.23%·K^{-1} and 4.32%·K^{-1}, for materials doped with 1 and 3 mol.% of Cr^{3+} ions.

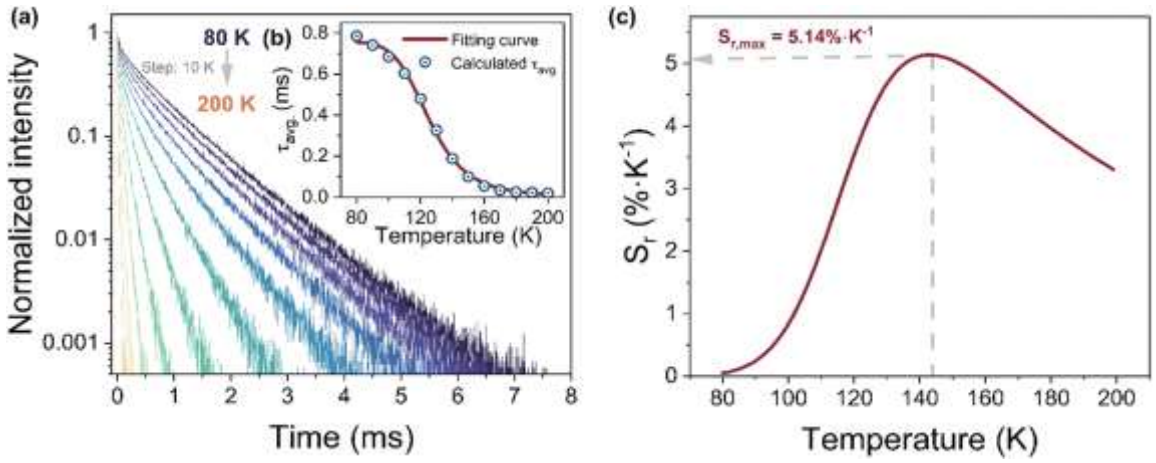

Figure 28. (a) Temperature-dependent decay curves of a sample doped with 1 mol.% of Cr^{3+} ions; (b) the change in the $\tau_{avg}(T)$ value with fitting function; (c) the change in the S_r parameter

Increasing dopant concentration reduces the average lifetime and shifts the temperature of maximum sensitivity to lower temperatures, which is consistent with enhanced population of the thermally coupled $^4T_{2g}$ level. Unlike ratiometric thermometry, lifetime-based sensitivity decreases at higher dopant concentrations, indicating that low Cr^{3+} levels and strong crystal fields are optimal. A comparative thermometric investigation has shown a potential for multiparametric model determination, which may significantly increase the sensing capability.

8. Summary

The presented series of publications **P1-P5,** collectively describes the characteristics of chromium(III)-doped hybrid organic-inorganic formates as well as demonstrates the versatility and high potential for luminescent thermometry**.** The Cr^{3+} ions have been applied as an optical probe whose spectroscopic properties are strongly dependent on the chemical composition of the host material. Observed luminescent characteristics may be influenced by a change in the type of organic cations and the type of metal ions. Within the presented series of publications **P1-P5**, two general groups of materials have been investigated:

- **P1-P2**: double perovskite - $[EA]_2NaM^{III}(HCOO)_6$: xCr^{3+}, where $M^{III} = Al^{3+}$, Ga^{3+}; x = 0-100 mol.% (Al^{3+}) or 0.931 mol.% (Ga^{3+}),
- **P3-P5**: single perovskites - $[A]M^{II}(HCOO)_6$: xCr^{3+}, where $A = DMA^+$, EA^+; $M^{II} = Zn^{2+}$, Mn^{2+}, Mg^{2+}, Ni^{2+}, Co^{2+} (DMA^+) or Mg^{2+}, Mn^{2+} (EA^+); x = 0-5 mol.% (DMA^+, EA^+).

Although the works examine different families of materials - double and single perovskite-like compounds, significant similarities in compositional and structure-related dependences on spectroscopic and further thermometric characteristics have been distinguished.

The specific objectives of the doctoral dissertation that were achieved include:

1. **Development of a synthesis method for hybrid compounds and their further structural investigation (P1-P5)**

   Across all works, synthesis involves solution-based methods to obtain high-quality crystalline materials. The microwave-assisted hydrothermal technique can be successfully implemented for double-perovskite materials preparation, as is presented in publications **P1** and **P2**. On the other hand, for the single-perovskite materials (**P3-P5**), the slow-diffusion method has been chosen as the most prominent one. Within the **P3-P5** publication, presenting single-perovskite materials, the Cr^{3+} replaces M^{2+} metal ions aliovalently and therefore can be introduced only up to about 5 mol.% before structural destabilization, preventing crystallization, occurs. In double-perovskites (**P1-P2**), due to charge neutrality, the M^{3+}/Cr^{3+} ion substitution can be performed across the entire composition range (0–100%). Obtained pXRD patterns confirm the formation of phase-pure crystalline products. While Cr^{3+} incorporation may cause slight peak shifts or broadening, the overall symmetry remains unchanged. The similarities in space groups between the presented materials can be observed. Double perovskite-like materials (**P1-P2**) crystallize in polar *Pn* space group, showing phase transition to high-temperature $P2_1/n$ group (377 K for **P1** and 369-373 K for **P2**). Within the three presented series of single perovskites (**P3-P5**), a higher variety of structural properties can be observed: DMA-based compounds (**P3**) crystallize in $R\bar{3}c$ space group with a phase transition to *Cc* group within the range 156-270 K; EA-based materials with Mg^{2+} cations (**P4**) show $Pna2_1$ phase, which transforms to $R\bar{3}$ (373 K), and further to *Imma* (426 K for heating and 415 K for cooling). The EA-derivative containing Mn^{2+} ions (**P5**), in turn, crystallizes in the $Pna2_1$ phase without reported phase transitions. Moreover, some of the presented perovskites (**P2-P4**) exhibit order-disorder phase transitions associated with the reorientation of the organic cations. Reported phase

transitions do not affect the luminescence-related thermometric performance, due to the non-overlapping temperature of these transitions with the emission temperature range. The summary of the structural parameters is presented in **Table 2**. The conducted analyses constitute a valuable contribution to further research on the influence of chemical composition on structural properties as well as lattice and organic cation dynamics in hybrid compounds.

2. Spectroscopic analysis of the obtained compounds

Diffuse reflectance spectroscopy confirms the presence of Cr^{3+} ions in the hybrid frameworks, enabling assessment of their local coordination environment. In all systems, DRS spectra reveal the characteristic Cr^{3+} absorption bands corresponding to the $^4A_{2g}\rightarrow{}^2E_g$, $^4A_{2g}\rightarrow{}^4A_{1g}$, and $^4A_{2g}\rightarrow{}^4A_{2g}$ transitions, demonstrating successful incorporation of chromium(III) ions into the octahedral metal sites. Within the Mn^{2+}-, Ni^{2+}-, and Co^{2+}-based compounds (**P3** and **P5**), partial overlap of Cr^{3+} and M^{2+} ion-related absorption bands has been observed, which introduces uncertainty in the determination of accurate crystal field and Racah parameters. As a result, the metal-ligand distances were used to estimate crystal field strength. Provided DRS studies, combined with metal-ligand analysis and luminescence studies, have reflected the general trend in presented studies: Mg^{2+}- and Zn^{2+}-based compounds doped with Cr^{3+} ion exhibit stronger crystal fields than Mn^{2+}-derivatives, which is consistent with their longer average metal–oxygen distances. Altogether, DRS measurements provide consistent spectroscopic information concerning Cr^{3+} ions incorporation and show how compositional differences modulate the crystal field strength, which in turn governs the luminescence and thermometric characteristics discussed throughout this dissertation.

Materials presented in a series of publications **P1-P5** exhibit consistent and comparable luminescent characteristics. Under the 405 nm excitation, overlaying the $^4A_{2g}\rightarrow{}^4T_{1g}$ transition, investigated materials, excluding Ni- and Co-containing materials from the DMA-based series, show strong luminescence assigned to the narrow spin-forbidden emission from the ^2E_g excited state. The presence of the less intensive broad spin-allowed transition $^4T_{2g}\rightarrow{}^4A_{2g}$ is observed; however, its initial (at 80 K) intensity is strongly dependent on the host material composition and resulting crystal field strength. Increasing temperature promotes thermal population of the $^4T_{2g}$ state, leading to intensification of broadband emission (**P1-P4**) and progressive quenching of the emission from a ^2E_g state. In the work **P5**, the increase in the intensity of broadband emission was not observed, most likely due to already developed $^4T_{2g}\rightarrow{}^4A_{2g}$ emission at 80 K and its following reduction. The relative contributions of both emission channels vary significantly with host composition. Materials based on Mg^{2+} or Zn^{2+} exhibit a stronger crystal field (stabilizing the ^2E_g state) than Mn^{2+}-based systems, which enhances the creation of a broadband emission band and promotes thermal quenching. The thermally induced quenching in luminescence from ^2E_g and $^4T_{2g}$ excited states is not equally progressive; thus, it may be implemented as an origin of the thermometric model determination. Across presented works, the temperature-dependent ratio between $^2E_g\rightarrow{}^4A_{2g}$ and $^4T_{2g}\rightarrow{}^4A_{2g}$ transitions has been particularly investigated. The relative

intensity of these emissions depends strongly on the crystal field strength. Stronger fields suppress the broadband emission, whereas weaker fields enhance $^4T_{2g}$ emission and intensify thermal quenching, which is especially visible within the full-concentration range of Cr^{3+} doping in publication **P2**. However, this trend occurs consistently across the presented materials, demonstrating a composition-luminescence relationship, particularly significant from the point of metal-ligand distances, depending on the implemented metal ion and Cr^{3+} concentration.

3. **Crystal-field strength determination (P1-P5)**

The crystal field strength values obtained from DRS measurements indicate that the *Dq/B* ratios range from 2.33 to 2.80 (**Table 3**). However, when these values are compared with the luminescence measurements performed at 80 K, it should be noted that the materials exhibit luminescence characteristic of Cr^{3+} ions in a strong crystal field. This is evidenced by the significantly higher intensity of emission from the ^2E_g level relative to that from the $^4T_{2g}$ level. In the series presented in publication **P1**, it is demonstrated that an increase in chromium concentration in the analyzed material leads to a decrease in crystal field strength and an enhancement of emission from the $^4T_{2g}$ level. Taking this into account, it is necessary to clearly emphasize the high importance of the *C/B* parameter, which defines the line between strong and weak crystal field regimes. The materials presented within this dissertation are characterized by *C/B* values ranging from 4.35 to 5.58, indicating that the analysis of crystal field strength should not rely solely on the *Dq/B* ratio, but must also consider the influence of the *C* parameter on the positions of the energy levels in the Tanabe-Sugano diagram.

4. **Thermometric analysis of the obtained compounds (P1-P5)**

The uneven thermal quenching of emissions from ^2E_g and $^4T_{2g}$ levels has been implemented for the thermometric model determination, according to the ratiometric approach. The performed thermometric analysis shows a significant potential of this method within the context of Cr^{3+}-based materials. Within the series of double-perovskite stoichiometry, the highest value of S_r is reported for $[EA]_2NaAl(HCOO)_6$: 21 mol.% Cr^{3+} (2.84%·K^{-1}, 160 K, **P1**), however, the Ga-based analogue (**P1**) shows a comparable magnitude of $S_{r,\,max}$ values – 2.11%·K^{-1} (150 K). The results presented within the work **P2** show that an increase in Cr^{3+} concentration induces the intensification of the relative intensity of broadband $^4T_{2g}\rightarrow{}^4A_{2g}$ emission; however, the clear relationship between this phenomenon and the obtained maximal relative sensitivities has not been observed. On the other hand, increasing concentration of Cr^{3+} ions leads to a change of the $S_{r,\,max}$ toward higher temperature. By tuning the Cr^{3+} concentration, it is possible to modulate the optimal sensing range, which indicates the possibility of the system's optimization according to specific sensing needs. The potential of the ratiometric approach has also been proven within the materials with single-perovskite stoichiometry. Within the DMA-series (**P3**), due to the significantly lower intensity of broadband $^4T_{2g}\rightarrow{}^4A_{2g}$ emission, the ratiometric model was determined according to emission bands assigned to $^2E_g\rightarrow{}^4A_{2g}$ (R_1 line and one of the

accompanying, less-energetic bands). The highest relative sensitivity (2.5%·K^{-1}, 160 K) is observed for the sample doped with 5 mol.% of Cr^{3+} ions. Other materials, differing in M^{2+} cation, show comparable values of $S_{r,\,max}$ parameters - 2.2%·K^{-1} (150 K) and 2.4%·K^{-1} (165 K) for Mg- and Zn-based compounds, respectively. The Mg-based materials exhibit the highest stability of sensitive and shift of maximal S_r values within the concentration series toward higher temperatures, analogous to results presented in publication **P2**. The complementary results have been reported for a series of ethylammonium-based compounds containing Mg^{2+} ion (**P4**). The ratiometric model was determined with a $^2E_g/^4T_{2g}$ ratio, due to a sufficient intensity of spin-allowed transition. The obtained model shows higher relative sensitivity than DMA-derivative — up to 3.07%·K^{-1} (130 K, 3 mol.% of Cr^{3+}).

5. **The development of a multimodal thermometric approach (P4-P5)**
   The notable aspect of the work **P4** is the implementation of the second independent thermometric model based on temperature-dependent luminescence lifetime. This model, based on the decay kinetics of the R_1 line (686.5 nm), shows comparable relative sensitivity, up to 2.97%·K^{-1} (140 K, 1 mol.% of Cr^{3+}). The presented approach demonstrates the potential of investigated materials as highly sensitive luminescent thermometers operating not only according to a ratiometric model, but also shows an alternative strategy of thermometric model determination. The development of an idea of dual-mode thermometry is presented in publication **P5**, in which the series of EA-based compounds containing Mn^{2+} ions were investigated. Performed multiparametric analysis reveals the importance of determining the optimal thermometric ranges. Within the context of the ratiometric method, three LIR parameters were examined. It shows that even around a set of temperature-dependent luminescence spectra of the given sample, the significant modulation of relative sensitivity of the model may be achieved, from the 0.47%·K^{-1} at 150 K (ratio of most intensive lines of $^2E_g \rightarrow {}^4A_{2g}$ transition) up to 3.91%·K^{-1} (140 K) for the ratio between ^2E_g- and $^4T_{2g}$-related emissions. The potential of the method based on R_1 (676–691 nm) and a less intensive band around 747–760 nm (analogous to the approach presented in work **P3**) has been proved – the model shows a $S_{r,\,max}$ value of 3.44%·K^{-1} (140 K). To further investigate the multimodal nature of Cr^{3+}-based luminescent thermometers, a comparison of the obtained results with the lifetime-based model has been provided. It shows that studied materials may exhibit notably high relative sensitivity up to 5.14%·K^{-1} (143 K, 1 mol.% of Cr^{3+}). It clearly demonstrates that high sensitivity (and following thermometric characteristics) may be optimized not only by a change in chemical composition but also by a more aware determination of the thermometric model. The cumulative dataset of spectroscopic parameters is presented in **Table 3**.

6. **The influence of the organic cation on relative sensitivity (P3-P5)**
   According to the obtained thermometric characteristics of the materials presented in a series of publications **P3-P5**, the initial, however important, conclusion concerning the effect of organic cation on luminescent characteristics, and further thermometric

potential, may be established. As the size of the amine cation increases ($DMA^+ < EA^+ < GA^+$), the contribution of the spin-allowed broadband emission at 80 K increases, but overall thermometric performance, described mainly with S_r value, tends to decrease. Among cations of similar size, molecular geometry should be considered. The more linear structure of EA^+ compared with DMA^+ leads to the higher sensitivity observed in ethylammonium-based derivatives. Even though this deliberation is based on a limited group of compounds (**P3-P5)** and a reported series of GA-based compounds,[177] it may have a significant influence on further investigation concerning the implementation of hybrid materials doped with Cr^{3+} ions in the role of highly sensitive luminescent thermometry. To fully understand this objective, more developed amine-dependent studies should be conducted.

7. **The operational potential of investigated luminescent thermometers (P1, P3)**
To better demonstrate the practical potential of investigated materials as luminescent thermometers for the cryogenic temperature range, the prototypic thermometric systems have been presented in publications **P1** (steady-state measurement) and **P3** (time-resolved analysis). The results visualize the robustness and reliability of these materials for cryogenic thermometry, particularly in conditions where conventional thermal imaging devices fail. Applied Cr^{3+}-based compounds show high sensitivity and short response time, which, combined with the remote nature of the measurement itself and the possibility of temperature redout even for the sensor covered with a frost, show an undeniable potential of such a sensing solution.

Table 2. The comparison of structural parameters of undoped materials

Publication	Compound	Space group	T_{PT} (K)	$1/R^5$ ($Å^{-5}$)
P1	$[EA]_2NaAl(HCOO)_6$	*Pn*, $P2_1/n$	369	0.0403
	$[EA]_2NaCr(HCOO)_6$	*Pn*, $P2_1/n$	373	0.0329
P2	$[EA]_2NaGa(HCOO)_6$	*Pn*, $P2_1/n$	369^h-373^c	0.0333
P3	$[DMA]Zn(HCOO)_3$	*Cc*, $R\bar{3}c$	156	0.0236
	$[DMA]Mg(HCOO)_3$	*Cc*, $R\bar{3}c$	270	0.0250
	$[DMA]Mn(HCOO)_3$	*Cc*, $R\bar{3}c$	185	0.0199
	$[DMA]Ni(HCOO)_3$	*Cc*, $R\bar{3}c$	180	0.0248
	$[DMA]Co(HCOO)_3$	*Cc*, $R\bar{3}c$	165	0.0240
P4	$[EA]Mg(HCOO)_3$	$Pna2_1$, $R\bar{3}$, *Imma*	373^h-316^c 426^h -415^c	0.0245
P5	$[EA]Mn(HCOO)_3$	$Pna2_1$	-	0.0196

Symbols: ^{h} – measured during heating; ^{c} – measured during cooling

Table 3. The comparison of spectroscopic parameters of Cr^{3+}-doped materials

Double perovskite stoichiometry: $[A]_2M^IM^{III}(HCOO)_6$

Publication	A	M^I, M^{III}	Cr^{3+} content	*Dq/B*	*C/B*	$S_{r,max}$ (T) (%·K^{-1})
P1	EA^+	Na^+, Al^{3+}	21 mol.%	2.76	5.56	2.84 (160 K)
			30 mol.%	2.74	5.58	2.29 (160 K)
			57 mol.%	2.69	5.52	2.67 (170 K)
			78 mol.%	2.59	5.31	2.02 (160 K)
			100 mol.%	2.33	4.74	2.35 (180 K)
P2	EA^+	Na^+, Ga^{3+}	93.1 mol.%	2.35	4.58	2.11 (150 K)

Single perovskite stoichiometry: $[A]M^{II}(HCOO)_3$

Publication	A	M^{II}	Cr^{3+} content	*Dq/B*	*C/B*	$S_{r,max}$ (T) (%·K^{-1})
P3	DMA^+	Zn^{2+}	1 mol.%	2.34	4.35	2.3 (170 K)
			3 mol.%	2.49	4.66	2.4 (165 K)
			5 mol.%	2.36	4.41	2.3 (165 K)
		Mg^{2+}	1 mol.%	2.77	5.24	2.0 (170 K)
			3 mol.%	2.69	5.13	2.3 (170 K)
			5 mol.%	2.80	5.34	2.5 (160 K)
		Mn^{2+}	1 mol.%	Overlap of the Mn^{2+} and Cr^{3+} absorption bands		2.2 (150 K)
			3 mol.%			2.1 (170 K)
			5 mol.%			2.1 (180 K)
		Ni^{2+}	1 mol.%	Overlap of the Ni^{2+} and Cr^{3+} absorption bands		No detectable emission
			3 mol.%			
			5 mol.%			

		Co^{2+}	1 mol.%	Overlap of the Co^{2+} and Cr^{3+} absorption bands		No detectable emission
			3 mol.%			
			5 mol.%			
P4	EA^{+}	Mg^{2+}	1 mol.%	2.43	4.60	2.69^{RM} (120 K), 2.97^{LT} (140 K)
			3 mol.%	2.45	4.59	3.07^{RM} (130 K), 2.90^{LT} (139 K)
			5 mol.%	2.61	5.06	2.48^{RM} (120 K), 2.94^{LT} (138 K)
P5	EA^{+}	Mn^{2+}	1 mol.%	Overlap of the Mn^{2+} and Cr^{3+} absorption bands		3.34^{RM} (120 K), 5.14^{LT} (143 K)
			3 mol.%			3.91^{RM} (140 K), 4.32^{LT} (128 K) Alternative RM models: 0.47^{a} (150 K), 3.44^{b} (140 K)
			5 mol.%			2.78^{RM} (120 K), 4.23^{LT} (126 K)

Symbols: ^{RM} – ratiometric model; ^{LT} – lifetime-based model; ^{a} – ratiometric model based on $^{2}E_{g}$ components; ^{b} – alternative ratiometric model based on R_1 line (see **Chapter 7.5**)

9. References

(1) Dramićanin, M. D. Trends in Luminescence Thermometry. *J. Appl. Phys.* **2020**, *128* (4), 040902. https://doi.org/10.1063/5.0014825.

(2) Chorąży, S.; Charytanowicz, T.; Wang, J.; Ohkoshi, S.; Sieklucka, B. Hybrid Organic–Inorganic Connectivity of Nd^{III}(Pyrazine-*N*,*N*′-Dioxide)$[Co^{III}(CN)_6]^{3-}$ Coordination Chains for Creating near-Infrared Emissive Nd(III) Showing Field-Induced Slow Magnetic Relaxation. *Dalton Trans.* **2018**, *47* (24), 7870–7874. https://doi.org/10.1039/C8DT01464G.

(3) Kabański, A.; Ptak, M.; Stefańska, D. Metal–Organic Framework Optical Thermometer Based on Cr^{3+} Ion Luminescence. *ACS Appl. Mater. Interfaces* **2023**, *15* (5), 7074–7082. https://doi.org/10.1021/acsami.2c19957.

(4) Morgan, A. B. Hybrid Materials: Synthesis, Characterization, and Applications. *J. Am. Chem. Soc.* **2008**, *130* (3), 1111–1112. https://doi.org/10.1021/ja710637a.

(5) Gomez-Romero, P.; Pokhriyal, A.; Rueda-García, D.; Bengoa, L. N.; González-Gil, R. M. Hybrid Materials: A Metareview. *Chem. Mater.* **2024**, *36* (1), 8–27. https://doi.org/10.1021/acs.chemmater.3c01878.

(6) Zhou, K; Qi, B.; Liu, Z.; Wang, X.; Sun, Y.; Zhang, L.; Advanced Organic–Inorganic Hybrid Materials for Optoelectronic Applications. Adv. Funct. Mater. **2024**, *34* (52), 2411671. https://doi.org/10.1002/adfm.202411671

(7) Absalan, Y.; Gholizadeh, M.; Kim, E.-B.; Ameen, S.; Wang, Y.; Wang, Y.; He, H. Recent Progress on Organic Metal Compound/MOF Hybrids: From Controllable Synthesis to Potential Catalytic Applications. *Coord. Chem. Rev.* **2024**, *515*, 215972. https://doi.org/10.1016/j.ccr.2024.215972.

(8) Kalaj, M.; Bentz, K. C.; Ayala, S. Jr.; Palomba, J. M.; Barcus, K. S.; Katayama, Y.; Cohen, S. M. MOF-Polymer Hybrid Materials: From Simple Composites to Tailored Architectures. *Chem. Rev.* **2020**, *120* (16), 8267–8302. https://doi.org/10.1021/acs.chemrev.9b00575.

(9) Liu, C.; Wang, J.; Wan, J.; Yu, C. MOF-on-MOF Hybrids: Synthesis and Applications. *Coord. Chem. Rev.* **2021**, *432*, 213743. https://doi.org/10.1016/j.ccr.2020.213743.

(10) Runowski, M.; Marcinkowski, D.; Soler-Carracedo, K.; Gorczyński, A.; Ewert, E.; Woźny, P.; Martín, I. R. Noncentrosymmetric Lanthanide-Based MOF Materials Exhibiting Strong SHG Activity and NIR Luminescence of Er^{3+}: Application in Nonlinear Optical Thermometry. *ACS Appl. Mater. Interfaces* **2023**, *15* (2), 3244–3252. https://doi.org/10.1021/acsami.2c22571.

(11) Wyczesany, M.; Zakrzewski, J. J.; Sieklucka, B.; Chorąży, S. Metal-Cyanido Molecular Modulators of the Sensing Range and Performance in Lanthanide-Based Luminescent Thermometers. *J. Mater. Chem. C* **2022**, *10* (33), 12054–12069. https://doi.org/10.1039/D2TC02591D.

(12) Diercks, C. S.; Yaghi, O. M. The Atom, the Molecule, and the Covalent Organic Framework. *Science* **2017**, *355* (6328). https://doi.org/10.1126/science.aal1585.

(13) Zhang, T.; Zhang, G.; Chen, L. 2D Conjugated Covalent Organic Frameworks: Defined Synthesis and Tailor-Made Functions. *Acc. Chem. Res.* **2022**, *55* (6), 795–808. https://doi.org/10.1021/acs.accounts.1c00693.

(14) Jones, C. W. Metal–Organic Frameworks and Covalent Organic Frameworks: Emerging Advances and Applications. *JACS Au* **2022**, *2* (7), 1504–1505. https://doi.org/10.1021/jacsau.2c00376.

(15) Juhi, J.; Saski, M.; Kochaniec, M. K.; Wieczorek, W.; Dominko, R.; Lewiński, J. Exploring Metal Halide Perovskites as Active Architectures in Energy Storage Systems. *J. Mater. Chem. A* **2025**, *13* (45), 38753–38789. https://doi.org/10.1039/D5TA04267D.

(16) Behrens, S. Preparation of Functional Magnetic Nanocomposites and Hybrid Materials: Recent Progress and Future Directions. *Nanoscale* **2011**, *3* (3), 877–892. https://doi.org/10.1039/C0NR00634C.
(17) Vollath, D. Bifunctional Nanocomposites with Magnetic and Luminescence Properties. *Adv. Mater.* **2010**, *22* (39), 4410–4415. https://doi.org/10.1002/adma.201001743.
(18) Cho, J.; Park, C. H.; Ramasami Sundharbaabu, P.; Ju, S.-U.; Shin, D.; Heo, J. H.; Kim, M.; Lee, J. H. Transformative Mechanical and Piezoelectric Properties in Organic–Inorganic Hybrid Materials for Biomedical Applications. *ACS Nano* **2025**, *19* (41), 36035–36081. https://doi.org/10.1021/acsnano.5c07220.
(19) Pan, Y.; Zhao, H.; Huang, W.; Liu, S.; Qi, Y.; Huang, Y. Metal-Protein Hybrid Materials: Unlocking New Frontiers in Biomedical Applications. *Adv. Healthc. Mater.* **2025**, *14* (6), 2404405. https://doi.org/10.1002/adhm.202404405.
(20) Zhang, D.; Chen, Y.; Hao, M.; Xia, Y. Putting Hybrid Nanomaterials to Work for Biomedical Applications. *Angew. Chem. Int. Ed.* **2024**, *63* (16), e202319567. https://doi.org/10.1002/anie.202319567.
(21) Li, Y.; Ji, L.; Liu, R.; Zhang, C.; Mak, C. H.; Zou, X.; Shen, H.-H.; Leu, S.-Y.; Hsu, H.-Y. A Review on Morphology Engineering for Highly Efficient and Stable Hybrid Perovskite Solar Cells. *J. Mater. Chem. A* **2018**, *6* (27), 12842–12875. https://doi.org/10.1039/C8TA04120B.
(22) Katan, C.; Mercier, N.; Even, J. Quantum and Dielectric Confinement Effects in Lower-Dimensional Hybrid Perovskite Semiconductors. *Chem. Rev.* **2019**, *119* (5), 3140–3192. https://doi.org/10.1021/acs.chemrev.8b00417.
(23) Su, T.-S.; Krishna, A.; Zhao, C.; Chu, J.; Zhang, H. Supramolecular Engineering in Hybrid Perovskite Optoelectronics. *Chem. Soc. Rev.* **2025**, *54* (13), 6448–6481. https://doi.org/10.1039/D4CS00924J.
(24) Liu, Y.; Liu, Y.; Guo, J. Organic–inorganic hybrid perovskite materials and their application in transistors. *Mater. Chem. Front.* **2023**, *7*, 5215-5246. https://doi.org/10.1039/D3QM00697B
(25) Egger, D. A.; Rappe, A. M.; Kronik, L. Hybrid Organic–Inorganic Perovskites on the Move. *Acc. Chem. Res.* **2016**, *49* (3), 573–581. https://doi.org/10.1021/acs.accounts.5b00540.
(26) Maufort, A.; Landeghem, M. V.; Deutsch, M.; Banks, P.; Magna, P. L.; Hecke, K. V.; Cerdá, J.; Lutsen, L.; Vanderzande, D.; Quarti, C.; Beljonne, D.; Pillet, S.; Vandewal, K.; Gompel, W. T. M. V. Structural Rigidity, Thermochromism and Piezochromism of Layered Hybrid Perovskites Containing an Interdigitated Organic Bilayer. *Chem. Sci.* **2025**, *16* (13), 5662–5675. https://doi.org/10.1039/D4SC06637E.
(27) Prochowicz, D.; Saski, M.; Yadav, P.; Grätzel, M.; Lewiński, J. Mechanoperovskites for Photovoltaic Applications: Preparation, Characterization, and Device Fabrication. *Acc. Chem. Res.* **2019**, *52* (11), 3233–3243. https://doi.org/10.1021/acs.accounts.9b00454.
(28) Kumar, A.; Chang, D. W.; Baek, J.-B. Current Status and Future of Organic–Inorganic Hybrid Perovskites for Photoelectrocatalysis Devices. *Energy Fuels* **2023**, *37* (23), 17782–17802. https://doi.org/10.1021/acs.energyfuels.3c02680.
(29) Hamdi, I.; Khan, Y.; Aouaini, F.; Seo, J. H.; Koo, H.-J.; Turnbull, M. M.; Walker, B.; Naïli, H. A Copper-Based 2D Hybrid Perovskite Solar Absorber as a Potential Eco-Friendly Alternative to Lead Halide Perovskites. *J. Mater. Chem. C* **2022**, *10* (10), 3738–3745. https://doi.org/10.1039/D1TC05047H.
(30) Chacón-García, A. J.; Baldovi, H. G.; Babaryk, A. A.; Rodríguez-Diéguez, A.; Navalón, S.; Pérez, Y.; García, H.; Horcajada, P. Robust Hybrid Bismuth Perovskites as Potential Photocatalysts for Overall Water Splitting. *Nano Res.* **2024**, *17* (5), 4593–4601. https://doi.org/10.1007/s12274-023-6254-1.

(31) Kiselyova, N. N.; Dudarev, V. A.; Stolyarenko, A. V.; Dokukin, A. A.; Sen'ko, O. V.; Ryazanov, V. V.; Vitushko, M. A.; Pereverzev-Orlov, V. S.; Vaschenko, E. A. Prediction of Space Groups for Perovskite-Like $A_2^{II}B^{III}B'^{V}O_6$ Compounds. *Inorg. Mater. Appl. Res.* **2022**, *13* (2), 277–293. https://doi.org/10.1134/S2075113322020228.
(32) Kunz, S. L.; Haefner, M.; Clemens, O. "Hexagonal" Perovskites: From Stacking Sequence to Space Group Symmetry and New Opportunities. *Chem. Mater.* **2024**, *36* (23), 11341–11358. https://doi.org/10.1021/acs.chemmater.4c01789.
(33) Islam, M. S.; Morikawa, D.; Yamada, S.; Aryal, B.; Tsuda, K.; Terauchi, M. Space Group Determination and First-Principles Structure Optimization of the A-Site Ordered Perovskite-Type Manganite $NdBaMn_2O_6$. *Phys. Rev. B* **2022**, *105* (17), 174114. https://doi.org/10.1103/PhysRevB.105.174114.
(34) *Epitaxial Growth of Complex Metal Oxides*, Edited by: Koster, G.; Hujiben, M.; Rijnders, G.; Woodhead Publishing **2015**, ISBN: 978-1-78242-245-7, https://doi.org/10.1016/C2013-0-16499-9
(35) Shi, Z.; Guo, J.; Chen, Y.; Li, Q.; Pan, Y.; Zhang, H.; Xia, Y.; Huang, W. Lead-Free Organic–Inorganic Hybrid Perovskites for Photovoltaic Applications: Recent Advances and Perspectives. *Adv. Mater.* **2017**, *29* (16), 1605005. https://doi.org/10.1002/adma.201605005.
(36) Zarick, H. F.; Soetan, N.; Erwin, W. R.; Bardhan, R. Mixed Halide Hybrid Perovskites: A Paradigm Shift in Photovoltaics. *J. Mater. Chem. A* **2018**, *6* (14), 5507–5537. https://doi.org/10.1039/C7TA09122B.
(37) Asensio, Y.; Marras, S.; Spirito, D.; Gobbi, M.; Ipatov, M.; Casanova, F.; Mateo-Alonso, A.; Hueso, L. E.; Martín-García, B. Magnetic Properties of Layered Hybrid Organic-Inorganic Metal-Halide Perovskites: Transition Metal, Organic Cation and Perovskite Phase Effects. *Adv. Fun. Mater.* **2022**, *32* (51), 2207988. https://doi.org/10.1002/adfm.202207988.
(38) Asensio, Y.; Olano-Vegas, L.; Mattioni, S.; Gobbi, M.; Casanova, F.; Hueso, L. E.; Martín-García, B. Engineering Magnetism in Hybrid Organic–Inorganic Metal Halide Perovskites. *Mater. Horiz.* **2025**, *12* (8), 2414–2435. https://doi.org/10.1039/D4MH01762E.
(39) Rok, M.; Moskwa, M.; Działowa, M.; Bieńko, A.; Rajnák, C.; Boča, R.; Bator, G. Multifunctional Materials Based on the Double-Perovskite Organic–Inorganic Hybrid $(CH_3NH_3)_2[KCr(CN)_6]$ Showing Switchable Dielectric, Magnetic, and Semiconducting Behaviour. *Dalton Trans.* **2019**, *48* (44), 16650–16660. https://doi.org/10.1039/C9DT03553B.
(40) Mączka, M.; Nowok, A.; Zaręba, J. K.; Stefańska, D.; Gągor, A.; Trzebiatowska, M.; Sieradzki, A. Near-Infrared Phosphorescent Hybrid Organic–Inorganic Perovskite with High-Contrast Dielectric and Third-Order Nonlinear Optical Switching Functionalities. *ACS Appl. Mater. Interfaces* **2022**, *14* (1), 1460–1471. https://doi.org/10.1021/acsami.1c20557.
(41) Zhang, M.; Jin, L.; Zhang, T.; Jiang, X.; Li, M.; Guan, Y.; Fu, Y. Two-Dimensional Organic-Inorganic Hybrid Perovskite Quantum-Well Nanowires Enabled by Directional Noncovalent Intermolecular Interactions. *Nat Commun* **2025**, *16* (1), 2997. https://doi.org/10.1038/s41467-025-58166-x.
(42) Burger, S.; Ehrenreich, M. G.; Kieslich, G. Tolerance Factors of Hybrid Organic–Inorganic Perovskites: Recent Improvements and Current State of Research. *J. Mater. Chem. A* **2018**, *6* (44), 21785–21793. https://doi.org/10.1039/C8TA05794J.
(43) Goldschmidt, V. M. Die Gesetze der Krystallochemie. *Naturwissenschaften* **1926**, *14* (21), 477–485. https://doi.org/10.1007/BF01507527.

(44) Travis, W.; Glover, E. N. K.; Bronstein, H.; Scanlon, D. O.; Palgrave, R. G. On the Application of the Tolerance Factor to Inorganic and Hybrid Halide Perovskites: A Revised System. *Chem. Sci.* **2016**, *7* (7), 4548–4556. https://doi.org/10.1039/C5SC04845A.

(45) Benkatlane, A.; Rached, D.; Caid, M.; Rached, H.; Deligöz, E.; Rached, Y.; Ozisik, H.; Mansour, H.; Benkhettou, N.-E. Lead-Free $Cs_2(Cd/Sn)BeCl_6$ Halide Double Perovskites: A Comprehensive First-Principles Study of Structural, Optoelectronic, and Thermoelectric Properties for Sustainable Energy Applications. *Phys. Status Solidi B* **2025**, *263* (1), 2500019. https://doi.org/10.1002/pssb.202500019.

(46) Rowińska, M. N.; Korolevych, O.; Kabański, A.; Stefańska, D.; Bednarchuk, T.; Piecha-Bisiorek, A.; Gągor, A. Hybrid Bismuth(III)-Halide Double Perovskite-Derived Ferroelastic $(Pip)_2[KBiBr_6]$ with Excitonic and Bi(III) Luminescence Due to Electronic Confinement along Inorganic Pillars. *Chem. Mater.* **2025**, *37* (18), 7125–7135. https://doi.org/10.1021/acs.chemmater.5c01183.

(47) Zanetta, A.; Larini, V.; Vikram; Toniolo, F.; Vishal, B.; Elmestekawy, K. A.; Du, J.; Scardina, A.; Faini, F.; Pica, G.; Pirota, V.; Pitaro, M.; Marras, S.; Ding, C.; Yildirim, B. K.; Babics, M.; Ugur, E.; Aydin, E.; Ma, C.-Q.; Doria, F.; Loi, M. A.; De Bastiani, M.; Herz, L. M.; Portale, G.; De Wolf, S.; Islam, M. S.; Grancini, G. Vertically Oriented Low-Dimensional Perovskites for High-Efficiency Wide Band Gap Perovskite Solar Cells. *Nat Commun* **2024**, *15* (1), 9069. https://doi.org/10.1038/s41467-024-53339-6.

(48) Rok, M.; Zarychta, B.; Bator, G.; Piecha-Bisiorek, A. Screening Order–Disorder Phase Transition in 1-D Perovskite-like Crystals of [Azetidinium]$CdBr_3$. *J. Phys. Chem. C* **2022**, *126* (44), 18876–18884. https://doi.org/10.1021/acs.jpcc.2c05577.

(49) Rok, M.; Zarychta, B.; Trojan-Piegza, J.; Bil, A.; Piecha-Bisiorek, A.; Zaręba, J. K.; Medycki, W.; Jakubas, R. A One-Dimensional Perovskite with Ferroelectric and Switchable Nonlinear Optical Properties: [Azetidinium]$CdCl_3$. *J. Mater. Chem. C* **2022**, *10* (8), 3036–3047. https://doi.org/10.1039/D1TC05355H.

(50) Guo, Y.-Y.; Yang, L.-J.; Biberger, S.; McNulty, J. A.; Li, T.; Schötz, K.; Panzer, F.; Lightfoot, P. Structural Diversity in Layered Hybrid Perovskites, A_2PbBr_4 or $AA'PbBr_4$, Templated by Small Disc-Shaped Amines. *Inorg. Chem.* **2020**, *59* (17), 12858–12866. https://doi.org/10.1021/acs.inorgchem.0c01807.

(51) Mao, L.; Teicher, S. M. L.; Stoumpos, C. C.; Kennard, R. M.; DeCrescent, R. A.; Wu, G.; Schuller, J. A.; Chabinyc, M. L.; Cheetham, A. K.; Seshadri, R. Chemical and Structural Diversity of Hybrid Layered Double Perovskite Halides. *J. Am. Chem. Soc.* **2019**, *141* (48), 19099–19109. https://doi.org/10.1021/jacs.9b09945.

(52) Leguy, A. M. A.; Frost, J. M.; McMahon, A. P.; Sakai, V. G.; Kockelmann, W.; Law, C.; Li, X.; Foglia, F.; Walsh, A.; O'Regan, B. C.; Nelson, J.; Cabral, J. T.; Barnes, P. R. F. The Dynamics of Methylammonium Ions in Hybrid Organic–Inorganic Perovskite Solar Cells. *Nat Commun* **2015**, *6* (1), 7124. https://doi.org/10.1038/ncomms8124.

(53) Minns, J. L.; Zajdel, P.; Chernyshov, D.; van Beek, W.; Green, M. A. Structure and Interstitial Iodide Migration in Hybrid Perovskite Methylammonium Lead Iodide. *Nat Commun* **2017**, *8* (1), 15152. https://doi.org/10.1038/ncomms15152.

(54) He, X.; Guo, P.; Wu, J.; Tu, Y.; Lan, Z.; Lin, J.; Huang, M. Hybrid Perovskite by Mixing Formamidinium and Methylammonium Lead Iodides for High-Performance Planar Solar Cells with Efficiency of 19.41%. *Sol. Energy* **2017**, *157*, 853–859. https://doi.org/10.1016/j.solener.2017.09.014.

(55) Liu, X.; Xu, M.; Hao, Y.; Fu, J.; Wang, F.; Zhang, B.; Bennett, S.; Sellin, P.; Jie, W.; Xu, Y. Solution-Grown Formamidinium Hybrid Perovskite ($FAPbBr_3$) Single Crystals for α-Particle and γ-Ray Detection at Room Temperature. *ACS Appl. Mater. Interfaces* **2021**, *13* (13), 15383–15390. https://doi.org/10.1021/acsami.1c00174.

(56) Akbulatov, A. F.; Frolova, L. A.; Anokhin, D. V.; Gerasimov, K. L.; Dremova, N. N.; Troshin, P. A. Hydrazinium-Loaded Perovskite Solar Cells with Enhanced Performance and Stability. *J. Mater. Chem. A* **2016**, *4* (47), 18378–18382. https://doi.org/10.1039/C6TA08215G.
(57) Yu, S.; Liu, H.; Wang, S.; Zhu, H.; Dong, X.; Li, X. Hydrazinium Cation Mixed $FAPbI_3$-Based Perovskite with 1D/3D Hybrid Dimension Structure for Efficient and Stable Solar Cells. *Chem. Eng. J.***2021**, *403*, 125724. https://doi.org/10.1016/j.cej.2020.125724.
(58) Mahapatra, A.; Runjhun, R.; Nawrocki, J.; Lewiński, J.; Kalam, A.; Kumar, P.; Trivedi, S.; Tavakoli, M. M.; Prochowicz, D.; Yadav, P. Elucidation of the Role of Guanidinium Incorporation in Single-Crystalline $MAPbI_3$ Perovskite on Ion Migration and Activation Energy. *Phys. Chem. Chem. Phys.* **2020**, *22* (20), 11467–11473. https://doi.org/10.1039/D0CP01119C.
(59) Tan, C. S. Transition Metal Ions in Methylammonium Chloride Perovskites. *ACS Omega* **2022**, *7* (1), 1412–1419. https://doi.org/10.1021/acsomega.1c06088.
(60) Chaykun, K.; Febriansyah, B.; Nguyen, T. T.; Lekina, Y.; Li, Y.; Li, S.; Teng, J.; Tan, Z.-K.; Mathews, N.; Shen, Z. Intercalation of Transition-Metal Complexes into 2D Hybrid Perovskites for Tailored Dual-Band Emission. *Angew. Chem. Int. Ed.* **2025**, *64* (22), e202503957. https://doi.org/10.1002/anie.202503957.
(61) Walker, B.; Kim, G.-H.; Kim, J. Y. Pseudohalides in Lead-Based Perovskite Semiconductors. *Adv. Mater.* **2019**, *31* (20), 1807029. https://doi.org/10.1002/adma.201807029.
(62) Mączka, M.; Zienkiewicz, J. A.; Ptak, M. Comparative Studies of Phonon Properties of Three-Dimensional Hybrid Organic–Inorganic Perovskites Comprising Methylhydrazinium, Methylammonium, and Formamidinium Cations. *J. Phys. Chem. C* **2022**, *126* (8), 4048–4056. https://doi.org/10.1021/acs.jpcc.1c09671.
(63) García-Ben, J.; McHugh, L. N.; Bennett, T. D.; Bermúdez-García, J. M. Dicyanamide-Perovskites at the Edge of Dense Hybrid Organic–Inorganic Materials. *Coord. Chem. Rev.* **2022**, *455*, 214337. https://doi.org/10.1016/j.ccr.2021.214337.
(64) Svane, K. L.; Forse, A. C.; Grey, C. P.; Kieslich, G.; Cheetham, A. K.; Walsh, A.; Butler, K. T. How Strong Is the Hydrogen Bond in Hybrid Perovskites? *J. Phys. Chem. Lett.* **2017**, *8* (24), 6154–6159. https://doi.org/10.1021/acs.jpclett.7b03106.
(65) Wu, Y.; Shaker, S.; Brivio, F.; Murugavel, R.; Bristowe, P. D.; Cheetham, A. K. $[Am]Mn(H_2POO)_3$: A New Family of Hybrid Perovskites Based on the Hypophosphite Ligand. *J. Am. Chem. Soc.* **2017**, *139* (47), 16999–17002. https://doi.org/10.1021/jacs.7b09417.
(66) Wang, M.; Yuan, S.; Jiang, D.; Wong, W. P. D.; Choi, H. S.; Yang, H.; Zhang, C.; Zhang, X.; Wang, Y.; Hu, W.; Loh, K. P. Two-Dimensional Mixed Tetrahedral–Octahedral Hybrid Perovskites with Coexisting Ferroelectricity and Intralayer Antiferromagnetism. *Nat. Synth* **2025**, 1–10. https://doi.org/10.1038/s44160-025-00942-0.
(67) Wu, Y.; Halat, D. M.; Wei, F.; Binford, T.; Seymour, I. D.; Gaultois, M. W.; Shaker, S.; Wang, J.; Grey, C. P.; Cheetham, A. K. Mixed X-Site Formate–Hypophosphite Hybrid Perovskites. *Chem. Eur. J.* **2018**, *24* (44), 11309–11313. https://doi.org/10.1002/chem.201803061.
(68) Ji, L.-J.; Sun, S.-J.; Qin, Y.; Li, K.; Li, W. Mechanical Properties of Hybrid Organic-Inorganic Perovskites. *Coord. Chem. Rev.* **2019**, *391*, 15–29. https://doi.org/10.1016/j.ccr.2019.03.020.
(69) Nowok, A.; Sobczak, S.; Roszak, K.; Szeremeta, A. Z.; Mączka, M.; Katrusiak, A.; Pawlus, S.; Formalik, F.; Barros dos Santos, A. J.; Paraguassu, W.; Sieradzki, A. Temperature and Volumetric Effects on Structural and Dielectric Properties of Hybrid

Perovskites. *Nat Commun* **2024**, *15* (1), 7571. https://doi.org/10.1038/s41467-024-51396-5.

(70) Peksa, P.; Zaręba, J. K.; Ptak, M.; Mączka, M.; Gągor, A.; Pawlus, S.; Sieradzki, A. Revisiting a Perovskite-like Copper-Formate Framework $NH_4[Cu(HCOO)_3]$: Order–Disorder Transition Influenced by Jahn-Teller Distortion and above Room-Temperature Switching of the Nonlinear Optical Response between Two SHG-Active States. *J. Phys. Chem. C* **2020**, *124* (34), 18714–18723. https://doi.org/10.1021/acs.jpcc.0c06141.

(71) Scatena, R.; Johnson, R. D.; Manuel, P.; Macchi, P. Formate-Mediated Magnetic Superexchange in the Model Hybrid Perovskite $[(CH3)_2NH_2]Cu(HCOO)_3$. *J. Mater. Chem. C* **2020**, *8* (37), 12840–12847. https://doi.org/10.1039/D0TC03913F.

(72) Novendra, N.; Nagabhushana, G. P.; Navrotsky, A. Thermodynamics of Hybrid Manganese Formate Perovskites. *RSC Adv.* **2024**, *14* (40), 29301–29307. https://doi.org/10.1039/D4RA03700F.

(73) Abdelhadi, A. B.; Ouarsal, R.; Poupon, M.; Dusek, M.; Andrés González, J. P.; Lezama, L.; Bali, B. E.; Lachkar, M.; Douhal, A. A Novel Layered Cu-Based Perovskite Metal–Organic Framework with 1,2-Diaminoethane Cations: Synthesis, Crystal Structure, and Thermal and Magnetic Properties. *Mater. Adv.* **2024**, *5* (15), 6154–6161. https://doi.org/10.1039/D4MA00222A.

(74) Wang, X.-Y.; Gan, L.; Zhang, S.-W.; Gao, S. Perovskite-like Metal Formates with Weak Ferromagnetism and as Precursors to Amorphous Materials. *Inorg. Chem.* **2004**, *43* (15), 4615–4625. https://doi.org/10.1021/ic0498081.

(75) Bulled, J. M.; Willis, A.; Faure Beaulieu, Z.; Cassidy, S. J.; Bruckmoser, J.; Boström, H. L. B.; Goodwin, A. L. Percolation-Induced Ferrimagnetism from Vacancy Order in $[Gua]Mn_{1-X}Fe_{2x/3}(HCOO)_3$ Hybrid Perovskites. *J. Am. Chem. Soc.* **2024**, *146* (20), 13714–13718. https://doi.org/10.1021/jacs.4c03407.

(76) Ptak, M.; Zarychta, B.; Stefańska, D.; Ciupa, A.; Paraguassu, W. Novel Bimetallic MOF Phosphors with an Imidazolium Cation: Structure, Phonons, High- Pressure Phase Transitions and Optical Response. *Dalton Trans.* **2018**, *48* (1), 242–252. https://doi.org/10.1039/C8DT04246B.

(77) Sobczak, S.; Katrusiak, A. Environment-Controlled Postsynthetic Modifications of Iron Formate Frameworks. *Inorg. Chem.* **2019**, *58* (17), 11773–11781. https://doi.org/10.1021/acs.inorgchem.9b01817.

(78) Piskorska-Hommel, E.; Ciupa-Litwa, A. Local Structure Study of the Fe Ions in Mixed-Valence Iron(II)-Iron(III) Metal Formate Frameworks. *Polyhedron* **2022**, *223*, 115963. https://doi.org/10.1016/j.poly.2022.115963.

(79) Liu, S.; Huang, Y.; He, Y.; Zhu, Y.; Wang, Z.; Liu, S.; Huang, Y.; He, Y.; Zhu, Y.; Wang, Z. Review of Development and Comparison of Surface Thermometry Methods in Combustion Environments: Principles, Current State of the Art, and Applications. *Processes* **2022**, *10* (12). https://doi.org/10.3390/pr10122528.

(80) Childs, P. R. N.; Greenwood, J. R.; Long, C. A. Review of Temperature Measurement. *Rev. Sci. Instrum.* **2000**, *71* (8), 2959–2978. https://doi.org/10.1063/1.1305516.

(81) Ximendes, E.; Marin, R.; Carlos, L. D.; Jaque, D. Less Is More: Dimensionality Reduction as a General Strategy for More Precise Luminescence Thermometry. *Light Sci Appl* **2022**, *11* (1), 237. https://doi.org/10.1038/s41377-022-00932-3.

(82) Brites, C. D. S.; Marin, R.; Suta, M.; Carneiro Neto, A. N.; Ximendes, E.; Jaque, D.; Carlos, L. D. Spotlight on Luminescence Thermometry: Basics, Challenges, and Cutting-Edge Applications. *Adv. Mater.* **2023**, *35* (36), 2302749. https://doi.org/10.1002/adma.202302749.

(83) *An Introduction to the Optical Spectroscopy of Inorganic Solids* by Garcia Sole, J.; Busa, L.E.; Jaque, D., John Wiley & Sons, Ltd **2005**, ISBN:9780470868850, https://doi.org/10.1002/0470016043
(84) Zhang, Y.; Yuan, S.; Day, G.; Wang, X.; Yang, X.; Zhou, H.-C. Luminescent Sensors Based on Metal-Organic Frameworks. *Coord. Chem. Rev.* **2018**, *354*, 28–45. https://doi.org/10.1016/j.ccr.2017.06.007.
(85) Parker, D.; Fradgley, J. D.; Wong, K.-L. The Design of Responsive Luminescent Lanthanide Probes and Sensors. *Chem. Soc. Rev.* **2021**, *50* (14), 8193–8213. https://doi.org/10.1039/D1CS00310K.
(86) Antoniak, M. A.; Zelewski, S. J.; Oliva, R.; Żak, A.; Kudrawiec, R.; Nyk, M. Combined Temperature and Pressure Sensing Using Luminescent $NaBiF_4$: Yb,Er Nanoparticles. *ACS Appl. Nano Mater.* **2020**, *3* (5), 4209–4217. https://doi.org/10.1021/acsanm.0c00403.
(87) Marciniak, L.; Woźny, P.; Szymczak, M.; Runowski, M. Optical Pressure Sensors for Luminescence Manometry: Classification, Development Status, and Challenges. *Coord. Chem. Rev.* **2024**, *507*, 215770. https://doi.org/10.1016/j.ccr.2024.215770.
(88) Wei, Y.; Zhou, Q.; Zhang, C.; Li, L.; Li, X.; Li, F. Fluorescence Pressure Sensors: Calibration of Ruby, Sm^{2+}: SrB_4O_7, and Sm^{3+}: YAG to 55 GPa and 850 K. *J. Appl. Phys.* **2024**, *135* (10), 105902. https://doi.org/10.1063/5.0178597.
(89) Runowski, M.; Woźny, P.; Stopikowska, N.; Guo, Q.; Lis, S. Optical Pressure Sensor Based on the Emission and Excitation Band Width (Fwhm) and Luminescence Shift of Ce^{3+}-Doped Fluorapatite — High-Pressure Sensing. *ACS Appl. Mater. Interfaces* **2019**, *11* (4), 4131–4138. https://doi.org/10.1021/acsami.8b19500.
(90) Forman, R. A.; Piermarini, G. J.; Barnett, J. D.; Block, S. Pressure Measurement Made by the Utilization of Ruby Sharp-Line Luminescence. *Science* **1972**, *176* (4032), 284–285. https://doi.org/10.1126/science.176.4032.284.
(91) Stacy, B. J.; Nagasaki, K.; Korgel, B. A. Luminescent Silicon Nanocrystals as Metal Ion Sensors. *ACS Nano* **2024**, *18* (24), 15744–15753. https://doi.org/10.1021/acsnano.4c02309.
(92) Mehta, S. K.; Salaria, K.; Umar, A. Highly Sensitive Luminescent Sensor for Cyanide Ion Detection in Aqueous Solution Based on PEG-Coated ZnS Nanoparticles. *Spectrochim. Acta Part A* **2013**, *105*, 516–521. https://doi.org/10.1016/j.saa.2012.12.068.
(93) Zhang, Z.; Zhang, H.; Tian, D.; Phan, A.; Seididamyeh, M.; Alanazi, M.; Ping Xu, Z.; Sultanbawa, Y.; Zhang, R. Luminescent Sensors for Residual Antibiotics Detection in Food: Recent Advances and Perspectives. *Coord. Chem. Rev.* **2024**, *498*, 215455. https://doi.org/10.1016/j.ccr.2023.215455.
(94) Gao, Y.-J.; Romolini, G.; Huang, H.; Jin, H.; Saha, R. A.; Ghosh, B.; Ras, M. D.; Wang, C.; Steele, J. A.; Debroye, E.; Hofkens, J.; Roeffaers, M. B. J. Ultrasensitive Turn-on Luminescence Humidity Sensor Based on a Perovskite/Zeolite Composite. *J. Mater. Chem. C* **2022**, *10* (34), 12191–12196. https://doi.org/10.1039/D2TC02498E.
(95) Papkovsky, D. B.; Ponomarev, G. V.; Chernov, S. F.; Ovchinnikov, A. N.; Kurochkin, I. N. Luminescence Lifetime-Based Sensor for Relative Air Humidity. *Sens. Actuators B Chem.***1994**, *22* (1), 57–61. https://doi.org/10.1016/0925-4005(94)01261-X.
(96) Chorąży, S.; Zakrzewski, J. J.; Reczyński, M.; Nakabayashi, K.; Ohkoshi, S.; Sieklucka, B. Humidity Driven Molecular Switch Based on Photoluminescent $Dy^{III}Co^{III}$ Single-Molecule Magnets. *J. Mater. Chem. C* **2019**, *7* (14), 4164–4172. https://doi.org/10.1039/C8TC06630B.
(97) Xu, X.; Lu, J.; Wang, J.; Wang, K.; Miao, P. Fluorescence Sensor for pH Tracing Based on Hydrogen-Bonded Organic Frameworks. *Langmuir* **2025**, *41* (44), 30007–30014. https://doi.org/10.1021/acs.langmuir.5c04716.

(98) Knöbl, Y. J.; Bedoya, M.; Farquharson, A.; Courtney, P.; Orellana, G. Wide Range Luminescence Lifetime-Based pH Sensing with Covalently Immobilized Multi-Protonatable Ru(II) Complexes. *Sens. Actuators B Chem.* **2025**, *425*, 136960. https://doi.org/10.1016/j.snb.2024.136960.
(99) Dereń, P. J.; Malinowski, M.; Stręk, W. Site Selection Spectroscopy of Cr^{3+} in $MgAl_2O_4$ Green Spinel. *J. Lumin* **1996**, *68* (2), 91–103. https://doi.org/10.1016/0022-2313(96)00020-8.
(100) Głuchowski, P.; Pązik, R.; Hreniak, D.; Stręk, W. Luminescence Properties of Cr^{3+}:$Y_3Al_5O_{12}$ Nanocrystals. *J. Lumin.* **2009**, *129* (5), 548–553. https://doi.org/10.1016/j.jlumin.2008.12.012.
(101) Brik, M. G.; Srivastava, A. M. Critical Review — A Review of the Electronic Structure and Optical Properties of Ions with d3 Electron Configuration (V^{2+}, Cr^{3+}, Mn^{4+}, Fe^{5+}) and Main Related Misconceptions. *ECS J. Solid State Sci. Technol.* **2017**, *7* (1), R3079. https://doi.org/10.1149/2.0041801jss.
(102) *Atoms, Molecules and Photons: An Introduction to Atomic-, Molecular- and Quantum Physics* by Demtroder, W. Springer **2010** ISBN: 978-3-642-10298-1. https://doi.org/10.1007/978-3-642-10298-1.
(103) *Atomic Physics* by Ewart, P. Morgan & Claypool Publishers **2019**, ISBN: 978-1-64327-404-1. https://doi.org/10.1088/2053-2571/aaf801
(104) Wongkokua, W.; Pongkrapan, S.; Dararutana, P.; T-Thienprasert, J.; Wathanakul, P. X-Ray Absorption near-Edge Structure of Chromium Ions in α-Al_2O_3. *J. Phys.: Conf. Ser.* **2009**, *185* (1), 012054. https://doi.org/10.1088/1742-6596/185/1/012054.
(105) Imbusch, G. F. Energy Transfer in Heavily-Doped Ruby. *J. Lumin.* **1992**, *53* (1), 465–467. https://doi.org/10.1016/0022-2313(92)90199-J.
(106) Kabański, A.; Caputa, K.; Stefańska, D. Multimodal Temperature Sensing in Hybrid Perovskites Doped with Cr^{3+}: A Strategy for Optimizing Luminescent Thermometers. *J. Mater. Chem. C* **2025**. https://doi.org/10.1039/D5TC02943K.
(107) Głuchowski, P.; Chaika, M. Crystal-Field Strength Variations and Energy Transfer in Cr^{3+}-Doped GGG Transparent Nanoceramics. *J. Phys. Chem. C* **2024**, *128* (23), 9641–9651. https://doi.org/10.1021/acs.jpcc.4c01658.
(108) Adachi, S. Racah Parameters and Tanabe−Sugano Energy-Level Diagram: Effects of the Different Host-Lattice Cation Species on the Crystal-Field Strength Parameters. *J. Lumin.* **2025**, *281*, 121194. https://doi.org/10.1016/j.jlumin.2025.121194.
(109) Henderson, B.; Imbusch, G. Optical Spectroscopy of Inorganic Solids. J. Mod. Opt. **1990**, *37* (10), 1688. https://doi.org/10.1080/09500349014551901
(110) *Modern Luminescence Spectroscopy of Minerals and Materials* by Gaft, M.; Reisfeld, R.; Panczer, G. Springer Mineralogy **2015**, ISBN: 978-3-319-24765-6 https://doi.org/10.1007/978-3-319-24765-6.
(111) Kabański, A.; Ptak, M.; Carlos, L. D.; Stefańska, D. Real-Time Temperature Monitoring with Cr^{3+}-Based Hybrid Formate Perovskites: Insights into the Relation Between Chemical Composition and Thermometric Performance. *Adv. Opt. Mater.* **2025**, *13* (25), e01057. https://doi.org/10.1002/adom.202501057.
(112) Adachi, S. Spectroscopy of Cr^{3+} Activator: Tanabe−Sugano Diagram and Racah Parameter Analysis. *J. Lumin.* **2021**, *232*, 117844. https://doi.org/10.1016/j.jlumin.2020.117844.
(113) Adachi, S. Racah Parameter Ratio *C/B* for the $3d^3$-Configuration Ions Like Mn^{4+} and Cr^{3+} in the Tanabe-Sugano Diagram. *ECS J. Solid State Sci. Technol.* **2020**, *9* (6), 066003. https://doi.org/10.1149/2162-8777/aba679.
(114) Shi, M.; Yao, L.; Yu, S.; Dong, Y.; Shao, Q. Enhancing the Temperature Sensitivity of Cr^{3+} Emissions by Modification of the Host's Composition for Fluorescence

Thermometry Applications. *Dalton Trans.* **2022**, *51* (2), 587–593. https://doi.org/10.1039/D1DT03480D.
(115) Szymczak, M.; Antuzevics, A.; Rodionovs, P.; Runowski, M.; Rodríguez-Mendoza, U. R.; Szymanski, D.; Kinzhybalo, V.; Marciniak, L. Bifunctional Luminescent Thermometer-Manometer Based on Cr^{3+}–Cr^{3+} Pair Emission. *ACS Appl. Mater. Interfaces* **2024**, *16* (47), 64976–64987. https://doi.org/10.1021/acsami.4c11806.
(116) Liu, S.; Du, J.; Song, Z.; Ma, C.; Liu, Q. Intervalence Charge Transfer of Cr^{3+}-Cr^{3+} Aggregation for NIR-II Luminescence. *Light Sci Appl* **2023**, *12* (1), 181. https://doi.org/10.1038/s41377-023-01219-x.
(117) Rajendran, V.; Fang, M.-H.; Huang, W.-T.; Majewska, N.; Lesniewski, T.; Mahlik, S.; Leniec, G.; Kaczmarek, S. M.; Pang, W. K.; Peterson, V. K.; Lu, K.-M.; Chang, H.; Liu, R.-S. Chromium Ion Pair Luminescence: A Strategy in Broadband Near-Infrared Light-Emitting Diode Design. *J. Am. Chem. Soc.* **2021**, *143* (45), 19058–19066. https://doi.org/10.1021/jacs.1c08334.
(118) Dereń, P. J.; Watras, A.; Gągor, A.; Pązik, R. Weak Crystal Field in Yttrium Gallium Garnet (YGG) Submicrocrystals Doped with Cr^{3+}. *Cryst. Growth Des.* **2012**, *12* (10), 4752–4757. https://doi.org/10.1021/cg300435t.
(119) Mao, N.; Liu, S.; Song, Z.; Yu, Y.; Liu, Q. A Broadband Near-Infrared Phosphor $Ca_3Y_2Ge_3O_{12}$: Cr^{3+} with Garnet Structure. *J. Alloys Compd.* **2021**, *863*, 158699. https://doi.org/10.1016/j.jallcom.2021.158699.
(120) Zou, W.; Lou, B.; Kurboniyon, M. S.; Buryi, M.; Rahimi, F.; Srivastava, A. M.; Brik, M. G.; Wang, J.; Ma, C.; Zou, W.; Lou, B.; Kurboniyon, M. S.; Buryi, M.; Rahimi, F.; Srivastava, A. M.; Brik, M. G.; Wang, J.; Ma, C. Unraveling Broadband Near-Infrared Luminescence in Cr^{3+}-Doped $Ca_3Y_2Ge_3O_{12}$ Garnets: Insights from First-Principles Analysis. *Materials* **2024**, *17* (7). https://doi.org/10.3390/ma17071709.
(121) Ma, Y.; Li, S.; Wei, J.; Liao, W.; Quan, B.; Molokeev, M. S.; Cheng, M.; Chen, X.; Zhou, Z.; Xia, M. Spectroscopically Enhanced Far-Red Phosphor $Li_2Mg_3TiO_6$: Cr^{3+} and Its Application Prospects to the Cold Resistance of Rice. *Mater. Adv.* **2023**, *4* (22), 5808–5816. https://doi.org/10.1039/D3MA00654A.
(122) Wang, Y.; Chen, B.; Wang, F. Overcoming Thermal Quenching in Upconversion Nanoparticles. *Nanoscale* **2021**, *13* (6), 3454–3462. https://doi.org/10.1039/D0NR08603G.
(123) Wegh, R. T.; van Klinken, W.; Meijerink, A. High-Energy $^2G(2)_{9/2}$ Emission and $4f^25d \rightarrow 4f^3$ Multiphonon Relaxation for Nd^{3+} in Orthoborates and Orthophosphates. *Phys. Rev. B* **2001**, *64* (4), 045115. https://doi.org/10.1103/PhysRevB.64.045115.
(124) Szalkowski, M.; Kotulska, A.; Dudek, M.; Korczak, Z.; Majak, M.; Marciniak, L.; Misiak, M.; Prorok, K.; Skripka, A.; Schuck, P. J.; Chan, E. M.; Bednarkiewicz, A. Advances in the Photon Avalanche Luminescence of Inorganic Lanthanide-Doped Nanomaterials. *Chem. Soc. Rev.* **2025**, *54* (2), 983–1026. https://doi.org/10.1039/D4CS00177J.
(125) Lv, X.; Xiao, R.; Liu, J.; Yang, C.; Xin, Y.; Guo, N. Recent Progress on Modulating Luminescence Thermal Quenching Properties of Bi^{3+}-Activated Phosphors. *Inorganic Chemistry Frontiers* **2024**, *11* (6), 1668–1682. https://doi.org/10.1039/D3QI02588H.
(126) Yang, J.; Yuan, L.; Qian, D.; Wu, H.; Jin, Y. Highly Thermal-Stable Broadband near-Infrared Emission of Cr^{3+} Doped Spinel $CdGa_2O_4$ Phosphors. *J. Lumin.* **2024**, *275*, 120825. https://doi.org/10.1016/j.jlumin.2024.120825.
(127) Pukhov, K. K.; Basiev, T. T.; Orlovskii, Yu. V.; Glasbeek, M. Multiphonon Relaxation of the Electronic Excitation Energy of Rare-Earth Ions in Laser Crystals. *J. Lumin.***1998**, *76–77*, 586–590. https://doi.org/10.1016/S0022-2313(97)00294-9.

(128) Yu, D.; Ballato, J.; Riman, R. E. Temperature-Dependence of Multiphonon Relaxation of Rare-Earth Ions in Solid-State Hosts. *J. Phys. Chem. C* **2016**, *120* (18), 9958–9964. https://doi.org/10.1021/acs.jpcc.6b01466.
(129) Pistor, P.; Ruiz, A.; Cabot, A.; Izquierdo-Roca, V. Advanced Raman Spectroscopy of Methylammonium Lead Iodide: Development of a Non-Destructive Characterisation Methodology. *Sci Rep* **2016**, *6* (1), 35973. https://doi.org/10.1038/srep35973.
(130) Mączka, M.; Gagor, A.; Stefanska, D.; Hanuza, J.; Kucharska, E.; Zareba, J. K. Divalent Methylhydrazinium─An Ultrasmall Organic Cation for Construction of Hybrid Perovskites. *Chem. Mater.* **2025**, *37* (14), 5195–5205. https://doi.org/10.1021/acs.chemmater.5c00919.
(131) Ptak, M.; Mączka, M.; Gągor, A.; Sieradzki, A.; Bondzior, B.; Dereń, P.; Pawlus, S. Phase Transitions and Chromium(III) Luminescence in Perovskite-Type $[C_2H_5NH_3][Na_{0.5}Cr_xAl_{0.5-x}(HCOO)_3]$ (x = 0, 0.025, 0.5), Correlated with Structural, Dielectric and Phonon Properties. *Phys. Chem. Chem. Phys.* **2016**, *18* (42), 29629–29640. https://doi.org/10.1039/C6CP05151K.
(132) Mączka, M.; Ptak, M.; Gągor, A.; Stefańska, D.; Zaręba, J. K.; Sieradzki, A. Methylhydrazinium Lead Bromide: Noncentrosymmetric Three-Dimensional Perovskite with Exceptionally Large Framework Distortion and Green Photoluminescence. *Chem. Mater.* **2020**, *32* (4), 1667–1673. https://doi.org/10.1021/acs.chemmater.9b05273.
(133) Wright, A. D.; Verdi, C.; Milot, R. L.; Eperon, G. E.; Pérez-Osorio, M. A.; Snaith, H. J.; Giustino, F.; Johnston, M. B.; Herz, L. M. Electron–Phonon Coupling in Hybrid Lead Halide Perovskites. *Nat Commun* **2016**, *7* (1), 11755. https://doi.org/10.1038/ncomms11755.
(134) Xin, L.; Fan, Z.; Li, G.; Zhang, M.; Han, Y.; Wang, J.; Ong, K. P.; Qin, L.; Zheng, Y.; Lou, X. Growth of Centimeter-Sized $[(CH_3)_2NH_2][Mn(HCOO)_3]$ Hybrid Formate Perovskite Single Crystals and Raman Evidence of Pressure-Induced Phase Transitions. *New J. Chem.* **2016**, *41* (1), 151–159. https://doi.org/10.1039/C6NJ02798A.
(135) Pato-Doldán, B.; Sánchez-Andújar, M.; Gómez-Aguirre, L. C.; Yáñez-Vilar, S.; López-Beceiro, J.; Gracia-Fernández, C.; Haghighirad, A. A.; Ritter, F.; Castro-García, S.; Señarís-Rodríguez, M. A. Near Room Temperature Dielectric Transition in the Perovskite Formate Framework $[(CH_3)_2NH_2][Mg(HCOO)_3]$. *Phys. Chem. Chem. Phys.* **2012**, *14* (24), 8498–8501. https://doi.org/10.1039/C2CP40564D.
(136) Straus, D. B.; Hurtado Parra, S.; Iotov, N.; Gebhardt, J.; Rappe, A. M.; Subotnik, J. E.; Kikkawa, J. M.; Kagan, C. R. Direct Observation of Electron–Phonon Coupling and Slow Vibrational Relaxation in Organic–Inorganic Hybrid Perovskites. *J. Am. Chem. Soc.* **2016**, *138* (42), 13798–13801. https://doi.org/10.1021/jacs.6b08175.
(137) Schlipf, M.; Poncé, S.; Giustino, F. Carrier Lifetimes and Polaronic Mass Enhancement in the Hybrid Halide Perovskite $CH_3NH_3PbI_3$ from Multiphonon Frohlich Coupling. *Phys. Rev. Lett.* **2018**, *121* (8), 086402. https://doi.org/10.1103/PhysRevLett.121.086402.
(138) Wright, W. F. Early Evolution of the Thermometer and Application to Clinical Medicine. *J. Therm. Biol.* **2016**, *56*, 18–30. https://doi.org/10.1016/j.jtherbio.2015.12.003.
(139) Loyson, P. Galilean Thermometer Not So Galilean. *J. Chem. Educ.* **2012**, *89* (9), 1095–1096. https://doi.org/10.1021/ed200793g.
(140) Angelini, E.; Grassini, S.; Parvis, M.; Parvis, L.; Gori, A. Body Temperature Measurement from the 17th Century to the Present Days. In *2020 IEEE International Symposium on Medical Measurements and Applications (MeMeA)*; **2020**. 1–6. https://doi.org/10.1109/MeMeA49120.2020.9137339.

(141) *Understanding Fever and Body Temperature: A Cross-disciplinary Approach to Clinical Practice* by Grodzinsky, E., Sund Levander, M. Springer International Publishing: Cham **2020**; 23–35. ISBN: 978-3030218850 https://doi.org/10.1007/978-3-030-21886-7_3.
(142) Hill, K. D.; Steele, A. G. The International Temperature Scale: Past, Present, and Future. *NCSLI Measure* **2014**, *9* (1), 60–67. https://doi.org/10.1080/19315775.2014.11721675.
(143) Dramićanin Far, L.; Dramićanin, M. D. Luminescence Thermometry with Nanoparticles: A Review. *Nanomaterials* **2023**, *13* (21). https://doi.org/10.3390/nano13212904.
(144) Stryczniewicz, W.; Fronc, K.; Chojnacki, M.; Sobczak, K.; Szajna, E.; Leśniewska-Matys, K.; Kozłowska, A.; Kamińska, I. Upconverting Thermal History Paint for Investigations of Short Thermal Events. *Sens. Actuators, A. Phys.* **2024**, *379*, 115980. https://doi.org/10.1016/j.sna.2024.115980.
(145) Li, L.; Zhou, Y.; Qin, F.; Miao, J.; Zheng, Y.; Zhang, Z. Eu^{3+}-Based Luminescence Ratiometric Thermometry. *RSC Adv.* **2020**, *10* (16), 9444–9449. https://doi.org/10.1039/D0RA00170H.
(146) Kabański, A.; Caputa, K.; Stefańska, D. High-Sensitivity Optical Thermometry with Cr^{3+}-Doped Hybrid Formate Perovskites: Comparative Analysis of Ratiometric and Lifetime-Based Approaches. *Dalton Trans.* **2025**, *54* (42), 15899–15908. https://doi.org/10.1039/D5DT01748C.
(147) Basore, E.; Huajun, W.; Xiao, W.; Zheng, G.; Liu, X.; Qiu, J. High-Power Broadband NIR LEDs Enabled by Highly Efficient Blue-to-NIR Conversion. *Advanced Optical Materials* **2021**, *9*, 2001660. https://doi.org/10.1002/adom.202001660.
(148) Mikenda. W. N-lines in the luminescence spectra of Cr^{3+}-doped spinels (III) partial spectra. J. Lumin. **1981**, *26* (1-2), 85-98, https://doi.org/10.1016/0022-2313(81)90171-X
(149) Li, R.; Wu, X.; Chen, Y.; Zeng, Q.; Deng, T.; Yu, T. Developing Luminescent Ratiometric Thermometers Based on Dual-Emission of $NaMgF_3$: Eu^{3+}/Carbon Dot Nanocomposites. *ACS Appl. Nano Mater.* **2024**, *7* (13), 15288–15297. https://doi.org/10.1021/acsanm.4c02103.
(150) Bednarkiewicz, A.; Marciniak, L.; Carlos, L. D.; Jaque, D. Standardizing Luminescence Nanothermometry for Biomedical Applications. *Nanoscale* **2020**, *12* (27), 14405–14421. https://doi.org/10.1039/D0NR03568H.
(151) Li, C.; Wang, L.; Tu, D.; Shang, X.; Yang, M.; Gong, J.; Wen, F.; Xing, Y.; Xie, Z.; Jiang, J.; Yu, S.; Chen, X. Luminescence Lifetime Thermometers Based on Hybrid Cuprous Halides with Exceptional Water Resistance and Giant Thermal Expansion. *Light Sci Appl* **2025**, *14* (1), 224. https://doi.org/10.1038/s41377-025-01910-1.
(152) Gálico, D. A.; Murugesu, M. Lifetime Thermometry with an Ytterbium(III)–Terbium(III) Molecular Upconverter. *J. Mater. Chem. C* **2024**, *12* (38), 15413–15417. https://doi.org/10.1039/D4TC03204G.
(153) dos Santos, L. F.; Galindo, J. A. O.; de O. Lima, K.; Pessoa, A. R.; Amaral, A. M.; de S. Menezes, L.; Gonçalves, R. R. Lifetime-Based Luminescence Thermometry from Yb^{3+}/Er^{3+} Codoped Nanoparticles Suspended in Water. *J. Lumin.* **2023**, *262*, 119946. https://doi.org/10.1016/j.jlumin.2023.119946.
(154) Bai, B.; Dang, P.; Huang, D.; Lian, H.; Lin, J. Broadband Near-Infrared Emitting $Ca_2LuScGa_2Ge_2O_{12}$: Cr^{3+} Phosphors: Luminescence Properties and Application in Light-Emitting Diodes. *Inorg. Chem.* **2020**, *59* (18), 13481–13488. https://doi.org/10.1021/acs.inorgchem.0c01890.
(155) Adaszyński, M.; Adamczak, K.; Kabański, A.; Jerzykiewicz, M.; Stefańska, D. Blue-to-NIR Energy Transfer for Bifunctional Application in Indoor Agriculture and High-Temperature Luminescent Thermometry. *J. Alloys Compd.* **2025**, *1039*, 183250. https://doi.org/10.1016/j.jallcom.2025.183250.

(156) Gu, S.; Liu, B.; Si, S.; Wang, J. Laser-Driven NIR Light Source Based on MgO: Cr^{3+},Ni^{2+} Phosphor-in-Glass Film for NIR Spectroscopy Application. *J. Mater. Chem. C* **2023**, *11* (26), 9014–9022. https://doi.org/10.1039/D3TC00457K.
(157) Elzbieciak-Piecka, K.; Marciniak, L. Optical Heating and Luminescence Thermometry Combined in a Cr^{3+}-Doped $YAl_3(BO_3)_4$. *Sci Rep* **2022**, *12* (1), 16364. https://doi.org/10.1038/s41598-022-20821-4.
(158) Ćirić, A.; Ristić, Z.; Periša, J.; Antić, Ž.; Dramićanin, M. D. $MgAl_2O_4$: Cr^{3+} Luminescence Thermometry Probe in the Physiological Temperatures Range. *Ceram. Int.* **2021**, *47* (19), 27151–27156. https://doi.org/10.1016/j.ceramint.2021.06.131.
(159) Wang, S.; Sun, M.; Fan, X.; Liu, B.; Qiao, C.; Jing, S.; Zhou, X.; Li, W.; Wang, Y.; Li, H. Dual-Modal Optical Thermometry Based on near-Infrared Emission of Cr^{3+} with High Relative Sensitivities over a Wide Temperature Range. *Ceram. Int.* **2025**, *51* (21), 33527–33537. https://doi.org/10.1016/j.ceramint.2025.05.083.
(160) Back, M.; Ueda, J.; Nambu, H.; Fujita, M.; Yamamoto, A.; Yoshida, H.; Tanaka, H.; Brik, M. G.; Tanabe, S. Boltzmann Thermometry in Cr^{3+}-Doped Ga_2O_3 Polymorphs: The Structure Matters! *Adv. Opt. Mater.* **2021**, *9* (9), 2100033. https://doi.org/10.1002/adom.202100033.
(161) Li, R.; Wei, G.; Wang, Z.; Wang, Y.; Li, J.; He, S.; Li, L.; Suo, H.; Ding, W.; Li, P. Cr^{3+}-Facilitated Ultra-Sensitive Luminescence Ratiometric Thermometry at Cryogenic Temperature. *Laser Photonics Rev.* **2023**, *17* (3), 2200589. https://doi.org/10.1002/lpor.202200589.
(162) Dantelle, G.; Reita, V.; Ibanez, A.; Ledoux, G.; Dujardin, C. Luminescent Nd^{3+}, Cr^{3+} Codoped YAG Nanocrystals for Thermal Sensing: Influence of the Excitation Wavelength. *Phys. B Condens. Matter* **2022**, *628*, 413622. https://doi.org/10.1016/j.physb.2021.413622.
(163) Piotrowski, W. M.; Maciejewska, K.; Dalipi, L.; Fond, B.; Marciniak, L. Cr^{3+} Ions as an Efficient Antenna for the Sensitization and Brightness Enhancement of Nd^{3+}, Er^{3+}-Based Ratiometric Thermometer in $GdScO_3$ Perovskite Lattice. *J. Alloys Compd.* **2022**, *923*, 166343. https://doi.org/10.1016/j.jallcom.2022.166343.
(164) Piotrowski, W.; Kniec, K.; Marciniak, L. Enhancement of the Ln^{3+} Ratiometric Nanothermometers by Sensitization with Transition Metal Ions. *J. Alloys Compd.* **2021**, *870*, 159386. https://doi.org/10.1016/j.jallcom.2021.159386.
(165) Mykhaylyk, V. B.; Kraus, H.; Bulyk, L.-I.; Lutsyuk, I.; Hreb, V.; Vasylechko, L.; Zhydachevskyy, Y.; Wagner, A.; Suchocki, A. Al_2O_3 Co-Doped with Cr^{3+} and Mn^{4+}, a Dual-Emitter Probe for Multimodal Non-Contact Luminescence Thermometry. *Dalton Trans.* **2021**, *50* (41), 14820–14831. https://doi.org/10.1039/D1DT02836G.
(166) Mullins, A. L.; Ćirić, A.; Zeković, I.; Williams, J. A. G.; Dramićanin, M. D.; Evans, I. R. Dual-Emission Luminescence Thermometry Using $LaGaO_3$: Cr^{3+}, Nd^{3+} Phosphors. *J. Mater. Chem. C* **2022**, *10* (28), 10396–10403. https://doi.org/10.1039/D2TC02011D.
(167) Zhu, B.; Li, N.; Ren, S.; Liu, Y.; Zhang, D.; Wang, Q.; Shi, Q.; Wang, Q.; Li, S.; Zhang, B.; Wang, W.; Liu, C. Mn^{2+} Ions Substitution Inducing Improvement of Optical Performances in $ZnAl_2O_4$: Cr^{3+} Phosphors: Energy Transfer and Ratiometric Optical Thermometry. *Spectrochim Acta A Mol Biomol Spectrosc* **2022**, *264*, 120321. https://doi.org/10.1016/j.saa.2021.120321.
(168) Zhang, Y.; Gao, Z.; Li, Y.; Wang, H.; Zhao, S.; Shen, Y.; Deng, D.; Xu, S.; Yu, H. Energy-Transfer-Enhanced Cr^{3+}/Ni^{2+} Co-Doped Broadband Near-Infrared Phosphor for Fluorescence Thermometers and Near-Infrared Window Imaging. *ACS Appl. Mater. Interfaces* **2024**, *16* (42), 57316–57324. https://doi.org/10.1021/acsami.4c10476.
(169) Ptak, M.; Dziuk, B.; Stefańska, D.; Hermanowicz, K. The Structural, Phonon and Optical Properties of $[CH_3NH_3]M_{0.5}Cr_xAl_{0.5-x}(HCOO)_3$ (M = Na, K; x = 0, 0.025, 0.5) Metal–

Organic Framework Perovskites for Luminescence Thermometry. *Phys. Chem. Chem. Phys.* **2019**, *21* (15), 7965–7972. https://doi.org/10.1039/C9CP01043B.
(170) Ptak, M.; Zarychta, B.; Stefańska, D.; Ciupa, A.; Paraguassu, W. Novel Bimetallic MOF Phosphors with an Imidazolium Cation: Structure, Phonons, High- Pressure Phase Transitions and Optical Response. *Dalton Trans.* **2018**, *48* (1), 242–252. https://doi.org/10.1039/C8DT04246B.
(171) Back, M.; Ueda, J.; Brik, M. G.; Tanabe, S. Pushing the Limit of Boltzmann Distribution in Cr^{3+}-Doped $CaHfO_3$ for Cryogenic Thermometry. *ACS Appl. Mater. Interfaces* **2020**, *12* (34), 38325–38332. https://doi.org/10.1021/acsami.0c08965.
(172) Shan, X.; Back, M.; Chen, D.; Miao, S.; Shi, R.; Liang, Y. A Reliable and Stable Ratiometric Luminescence Thermometer Based on Dual Near-Infrared Emission in a Cr^{3+}-Doped $LaSr_2Ga_{11}O_{20}$ Phosphor. *J. Mater. Chem. C* **2023**, *11* (26), 8952–8960. https://doi.org/10.1039/D3TC01232H.
(173) Qiu, L.; Wang, P.; Mao, J.; Liao, Z.; Chi, F.; Chen, Y.; Wei, X.; Yin, M. Cr^{3+}-Doped $InTaO_4$ Phosphor for Multi-Mode Temperature Sensing with High Sensitivity in a Physiological Temperature Range. *Inorg. Chem. Front.* **2022**, *9* (13), 3187–3199. https://doi.org/10.1039/D2QI00660J.
(174) Stefańska, D.; Bondzior, B.; Vu, T. H. Q.; Grodzicki, M.; Dereń, P. J. Temperature Sensitivity Modulation through Changing the Vanadium Concentration in a $La_2MgTiO_6:V^{5+}$, Cr^{3+} Double Perovskite Optical Thermometer. *Dalton Trans.* **2021**, *50* (28), 9851–9857. https://doi.org/10.1039/D1DT00911G.
(175) Piotrowski, W. M.; Szymczak, M.; Rodríguez, E. M.; Marin, R.; Henklewska, M.; Poźniak, B.; Dramićanin, M.; Marciniak, L. Step by Step Optimization of Luminescence Thermometry in $MgTiO_3$: Cr^{3+}, Nd^{3+}@SiO_2 Nanoparticles towards Bioapplications. *Mater. Chem. Phys.* **2024**, *312*, 128623. https://doi.org/10.1016/j.matchemphys.2023.128623.
(176) Wang, Q.; Liang, Z.; Luo, J.; Yang, Y.; Mu, Z.; Zhang, X.; Dong, H.; Wu, F. Ratiometric Optical Thermometer with High Sensitivity Based on Dual Far-Red Emission of Cr^{3+} in $Sr_2MgAl_{22}O_{36}$. *Ceramics International* **2020**, *46* (4), 5008–5014. https://doi.org/10.1016/j.ceramint.2019.10.241.
(177) Stefańska, D.; Kabański, A.; Vu, T. H. Q.; Adaszyński, M.; Ptak, M.; Stefańska, D.; Kabański, A.; Vu, T. H. Q.; Adaszyński, M.; Ptak, M. Structure, Luminescence and Temperature Detection Capability of $[C(NH_2)_3]M(HCOO)_3$ (M = Mg^{2+}, Mn^{2+}, Zn^{2+}) Hybrid Organic–Inorganic Formate Perovskites Containing Cr^{3+} Ions. *Sensors* **2023**, *23* (14). https://doi.org/10.3390/s23146259.

10. Copies of publications P1-P5

10.1 Publication P1

ACS APPLIED MATERIALS & INTERFACES

www.acsami.org

Research Article

Metal–Organic Framework Optical Thermometer Based on Cr^{3+} Ion Luminescence

Adam Kabański,* Maciej Ptak, and Dagmara Stefańska*

Cite This: https://doi.org/10.1021/acsami.2c19957

Read Online

ACCESS | Metrics & More | Article Recommendations | Supporting Information

ABSTRACT: Metal–organic frameworks with perovskite structures have recently attracted increasing attention due to their structural, optical, and phonon properties. Herein, we report the structural and luminescence studies of a series of six heterometallic perovskite-type metal–organic frameworks with the general formula $[EA]_3NaCr_xAl_{1-x}(HCOO)_6$, where x = 1, 0.78, 0.57, 0.30, 0.21, and 0. The diffuse reflectance spectral analysis provided valuable information, particularly on crystal field strength (Dq/B) and energy band gap (E_g). We showed that the Dq/B varies in the 2.33–2.76 range depending on the composition of the sample. Performed Raman, XRD, and lifetime decay analyses provided information on the relationship between those parameters and the chemical composition. We also performed the temperature-dependent luminescence studies within the 80–400 K range, which was the first attempt to use an organic–inorganic framework luminescence thermometer based solely on the luminescence of Cr^{3+} ions. The results showed a strong correlation between the surrounding temperature, composition, and spectroscopic properties, allowing one to design a temperature sensing model. The temperature-dependent luminescence of the Cr^{3+} ions makes the investigated materials promising candidates for noncontact thermometers.

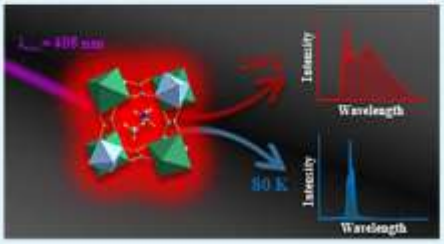

KEYWORDS: *hybrid perovskite, luminescence, thermometry, chromium(III) ions, temperature sensing, noncontact optical thermometer*

INTRODUCTION

Over the past few years, perovskite materials with the general formula ABX_3 have become a significant object of study. One of the most noteworthy groups of these materials is hybrid compounds containing organic cations A (e.g., ammonium and methylammonium), divalent metal ions B (e.g., Pb^{2+} and Sn^{2+}), and halide ligands X (e.g., I^- and Cl^-).[1,2] Hybrid compounds have been particularly useful in thin-film photovoltaic devices.[3,4] Due to their specific properties, such as ferroelectricity,[5−7] colossal magnetoresistance,[8,9] magnetocaloric effect,[10,11] and unique optical properties,[1,12,13] they can be implemented in various applications. The characteristics of the perovskite-like materials can be significantly tuned by replacing the A and B ions and X linkers.[14−16]

Formate-based metal–organic frameworks (MOFs) with perovskite structures have attracted a lot of attention due to their various properties, such as multiferroicity, ferroelectricity, luminescence, and magnetic effects.[17−21] The bimetallic compounds with the general formula $[A]_3M^{I}M^{III}(HCOO)_6$, where A = EA^+ (ethylammonium), DMA^+ (dimethylammonium), M^{I} = Na^+ and K^+, and M^{III} = Cr^{3+}, Al^{3+}, and Fe^{3+}, exhibit unique, especially temperature-induced properties.[14,16,19] The origin of this phenomenon is related to order–disorder phase transitions and changes in energy level populations caused by the change in temperature.

Bimetallic perovskite-like MOFs also exhibit interesting luminescence properties.[14,22−24] Particularly, the subgroup of chromium-based phosphors is noteworthy due to its strong temperature sensitivity and weak concentration quenching.[22,23] The heterometallic MOFs containing chromium ions exhibit temperature-dependent luminescence properties and may be used for noncontact temperature detection.[14]

The spectroscopic properties of the transition metal (TM) ions, such as Cr^{3+}, are strongly dependent on the local environment, particularly the type of crystal field and temperature.[14,25−27] Trivalent chromium ions exhibit two main emission bands: narrow spin-forbidden $^2E_g \rightarrow {}^4A_{2g}$ transitions around 700 nm and broad spin-allowed $^4T_{2g} \rightarrow {}^4A_{2g}$ transitions near 750 nm. The narrow emission occurs in a strong crystal field, whereas broad emission takes place when the material exhibits a weak crystal field.[28,29] The materials with intermediate crystal field strength exhibit both types of emissions. Furthermore, the change of temperature strongly affects the intensities of bands, which was reported as a

Received: November 6, 2022
Accepted: January 19, 2023

potentially useful feature for temperature sensing.[27] The concentration of the Cr^{3+} ions affects not only the intensity of emission but also may influence the dominant emission band due to the change of the crystal structure.[26]

Luminescence noncontact thermometry is a novel scientific approach for temperature measurements that has attracted a lot of attention.[30−36] Noncontact temperature sensing has a high potential for application in industrial, scientific, biomedical, and technological fields due to a variety of advantages, such as micro- and nanosized implementation possibility, high accuracy, and fast response. The general measurement mechanism is mainly based on thermally induced changes in the quality of luminescence spectra, such as peak intensities, positions, or decay lifetimes.[31,37] The most promising approach is based on the examination of the parameters known as fluorescence intensity ratio (FIR or Δ), which is calculated by comparing intensities of two emission peaks.[27] FIR-based methods are particularly useful due to the minimalization of an influence of measurement conditions.[27,36]

The temperature calculation can be based on the emissions originating from individual dopants or codopants incorporated into the structure of the material. Luminescent materials used for temperature sensing can be divided into several groups according to their size (nano- and microthermometers), change of the wavelength (down- and up-converting materials), and number of emission centers (single and dual emission centers). Another subgroup of thermometric materials is compounds containing rare-earth (RE) metal ions.[27,38]

The application of host materials exhibiting luminescence properties enables the analysis based on the emission peaks of both host and dopant. The vast majority of research involves inorganic host materials containing RE metal ions as dopants.[13,39−41] Thermal sensing solutions based on transition metal ions are not so popular; however, promising results have been reported for double perovskites codoped with vanadium ions.[13]

Another noteworthy approach is the incorporation of trivalent chromium ions, which can be a valuable direction for RE-free luminescence thermometer design.[42−44] The potential of implementation of Cr^{3+} ions for high thermal sensing has been reported for several inorganic materials.[13,45,46] However, up to date, such solutions based on MOFs have not been proposed.[13,43,44] Another promising approach is using mixed systems containing chromium ions as well as lanthanide ions.[30,47]

Herein, we report the preparation and structural and optical characteristics of the first MOF-type luminescence thermometers based solely on spectroscopic properties of the Cr^{3+} ions, i.e., $[EA]_2NaCr_xAl_{1-x}(HCOO)_6$, where x = 1, 0.78, 0.57, 0.30, 0.21, and 0. The investigated materials exhibit significant temperature-dependent emission, simultaneously related to chromium ion concentration. In this work, we attempt to describe the effect of the composition of the material and the strength of the crystal field on the spectroscopic properties. Particular attention is given to the possibility of the implementation of investigated materials as noncontact luminescence thermometers. To achieve this purpose, we performed spectroscopic analysis in a broad temperature range.

EXPERIMENTAL SECTION

Materials and Instrumentation. All precursors (analytical grade) were commercially available and were used without further purification. The synthesis was performed on an Ertec Magnum II microwave reactor with a standard Teflon vessel. The powder X-ray diffraction (XRD) patterns were obtained on an X'Pert Pro X-ray diffraction system equipped with a PIXcel detector, a focusing mirror, and Soller slits for CuKα radiation (λ = 1.54056 Å). The Raman spectra were measured using a Bruker MultiRAM spectrometer with 2 cm^{-1} resolution. A 1064 nm wavelength YAG:Nd laser was used as an excitation source. The diffuse reflectance spectra were obtained using a Varian Cary 5E UV−VIS−NIR spectrometer. The temperature-dependent emission spectra were obtained with a Hamamatsu PMA-12 photonic multichannel analyzer combined with a BT-CCD sensor. As an excitation source, a 405 nm laser diode was used. The temperature was controlled by a Linkam THMS600 stage. For lifetime measurements, a Ti-sapphire laser pumped with Nd:YAG was used as the excitation source. To record decay profiles, the digital oscilloscope Tektronix MDO3052 was used. The compositions of samples were determined with energy-dispersive X-ray spectroscopy (EDS) measurement using a FEI NOVA NanoSEM 140 scanning electron microscope.

Synthesis. A series of $[EA]_2NaCr_xAl_{1-x}(HCOO)_6$, where x = 1, 0.78, 0.57, 0.30, 0.21, and 0, were prepared using the microwave-assisted solvothermal method. Exemplarily, to grow $[EA]_2NaCr_{0.78}Al_{0.22}(HCOO)_6$ crystals, 3.2 mmol (0.8526 g) of $CrCl_3{\cdot}6H_2O$, 0.8 mmol (0.3900 g) of $Al(ClO_4)_3{\cdot}9H_2O$, 4 mmol of EA·HCl (0.3262 g), and 8.8 mmol of HCOONa (0.5985 g) were dissolved in 15 mL of water. Afterward, 25 mL of *N*-ethylformamide and 5 mL of 98% HCOOH were added to the prepared solution. The mixture was subsequently transferred to a microwave reactor containing a Teflon vessel. The reaction was maintained at 140 °C for 16 h and then cooled to room temperature. The solution was kept undisturbed for 24 h. Next, obtained crystals were separated from the mother liquid and dried at 50 °C. The obtained crystals of the $[EA]_2NaAl(HCOO)_6$ sample were colorless. In contrast, crystals of materials containing Cr^{3+} ions were purple or dark purple depending on the chromium concentration. The exact quantities of precursors used for the preparation together with nominal and experimentally determined compositions of each sample are listed in Table S1. The performed EDS analysis provided information about the real concentration of Cr^{3+} ions, which is used in the further part of the paper.

RESULTS AND DISCUSSION

Structural Properties. Both $[EA]_2NaCr(HCOO)_6$ (EA-NaCr) and $[EA]_2NaAl(HCOO)_6$ (EANaAl) crystallize in the monoclinic, polar space group *Pn*. Previously published results have shown that the space group transformation into a $P2_1/n$ space group occurs at around 373 K for EANaCr and 369 K for EtANaAl.[6] The crystal structure in both phases exhibits a perovskite-like topology composed of alternatively distributed octahedral units of CrO_6/AlO_6 and NaO_6. A 3D metal-formate framework comprises voids occupied by EA^+ cations (see Figure 1). In the high-temperature $P2_1/n$ phase, organic cations are dynamically disordered over two independent positions that are occupied with roughly 50% probability. In the low-temperature *Pn* phase, due to the strengthening of hydrogen bonds, the metal-formate framework distorts, voids shrink, and the thermal motions of EA^+ cations are suppressed. The arrangement of EA^+ dipole moments in the ordered *Pn* phase is responsible for the polar properties of EANaCr and EANaAl.[6]

The cell volume in the $[EA]_2NaCr_xAl_{1-x}(HCOO)_6$ series is dependent on the type of metal ion; the decrease in volume was reported, while the Cr^{3+} ions were replaced with Al^{3+} ions. Such a phenomenon is related to the different ionic radii of Cr^{3+} and Al^{3+} (0.615 and 0.535 Å, respectively).[6] The unit cell volumes of the investigated series change within the range from 1065.6 to 1078.9 $Å^3$. Detailed unit cell parameters are

https://doi.org/10.1021/acsami.2c19957
ACS Appl. Mater. Interfaces XXXX, XXX, XXX−XXX

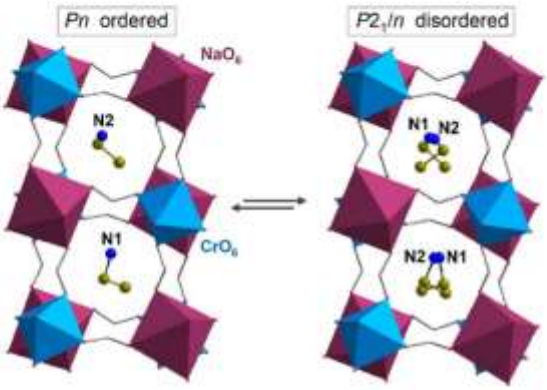

Figure 1. Crystal structure of EANaCr in the high-temperature $P2_1/n$ and low-temperature Pn phases. H atoms are omitted for clarity.

presented in Table S2 and Figure S1. The comprehensive structural and vibrational studies on both EANaCr and EANaAl have been published previously.[6,7]

The phase purity of prepared materials was confirmed by XRD measurements. The collation of obtained patterns measured for the series of samples is presented in Figure S2. The increasing concentration of Cr^{3+} ions leads to a change in XRD patterns, where the most visible change takes place in a range of 20.5−21.5°. No additional diffraction lines were detected, which indicates that the Cr^{3+} ions can be substituted by the Al^{3+} ions within the full range of concentrations. The similar structural properties of the investigated materials significantly expand the field of their possible implementation.

Raman Studies. Raman spectra of investigated compounds contain bands related to internal vibrations of $HCOO^-$ and EA^+ ions as well as lattice vibrations. The specific assignments of observed Raman bands, as well as more complex structural description for combined hybrid materials containing EA^+ and $HCOO^-$ ions of isostructural compounds, were described in the literature; thus, no particular attention will be given to this matter.[6,7]

The collation of the room-temperature Raman spectra for a series of $[EA]_2NaCr_xAl_{1-x}(HCOO)_6$ compounds is presented in Figure S3a. As one can see, the change of the composition parameter x affects qualitatively the spectra. The disappearance of some peaks and/or changes in intensity is accompanied by an increase in Cr^{3+} concentration. For instance, the increasing amount of Cr^{3+} causes a decrease in the intensity of bands at 227, 290, 308, 630, 936, 1352, and 1682 cm^{-1} followed by the emergence of bands at 245, 1340, 1383, and 1672 cm^{-1}. Some of them strongly change the relative intensity (Figure S3b,c). These subtle differences are related to the slightly different phonon properties of the Cr^{3+}/Al^{3+}−O bonds and the changes in the local environments in the samples composed of the mixed CrO_6/AlO_6 octahedra. Additionally, a particular change is observed around 1352 cm^{-1} (Figure 2a). The variety of the peak intensities might be implemented to estimate the concentration of the Cr^{3+} ions in the sample. The exemplary intensity as a function of concentration is presented in Figure 2b. Due to the high accessibility and measurement simplicity of the Raman spectra, the calculation of the ion concentration may be a useful analytical tool for material science.[48−50] Therefore, this topic may be an interesting subject for further investigation.

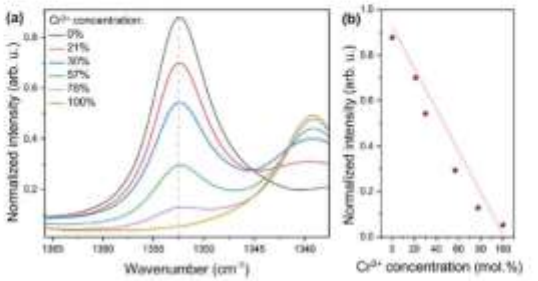

Figure 2. (a) Change of the normalized Raman spectra for a 1352 cm^{-1} peak corresponding to the C−H in-plane bending mode (υ_5); (b) relation between 1352 cm^{-1} peak intensity and Cr^{3+} concentration with linear fitting.

Diffuse Reflectance Spectra. The comparison of the diffuse reflectance spectra of the prepared compounds is presented in Figure 3a. A series of obtained spectra contain

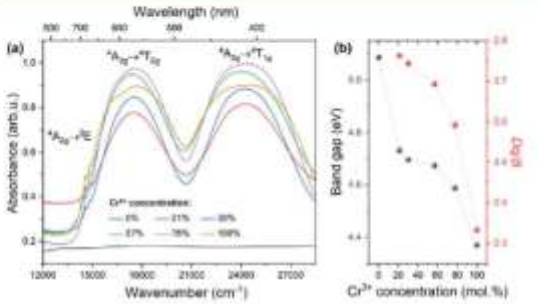

Figure 3. (a) Diffuse reflectance spectra of a series of $[EA]_2NaCr_xAl_{1-x}(HCOO)_6$ (x = 1, 0.78, 0.57, 0.30, 0.21, and 0) compounds measured at 300 K; (b) change of the energy band gap (E_g) and Dq/B parameters as a function of Cr^{3+} ion concentration.

two main broad bands localized at about 17,452 cm^{-1} (573 nm) and 24,213 cm^{-1} (413 nm) corresponding to spin-allowed $^4A_{2g} \rightarrow {}^4T_{1g}$ and $^4A_{2g} \rightarrow {}^4T_{2g}$ transitions, respectively. Low-intensity and narrow lines at around 14,577 cm^{-1} (686 nm) are attributed to the spin-forbidden transition from the $^4A_{2g}$ ground state to the ^2E excited level. The intensity of the DRS spectrum is related to several factors, e.g., size and position of crystallites. Thus, performed measurements are used in a qualitative rather than quantitative manner. The change in the spectrum shape is caused by the decrease in spectrum components' overlapping. In fact, each part of the spectrum assigned to $^4A_{2g} \rightarrow {}^4T_{1g}$ and $^4A_{2g} \rightarrow {}^4T_{2g}$ transitions contains two bands, in which overlapping creates the final shape of the band, which is particularly visible for a sample containing 100 mol % chromium ions.

The $[EA]_2NaAl(HCOO)_6$ sample does not exhibit absorption in the given range due to a lack of optically active chromium ions. The comprehensive description of absorption spectrum deconvolution has been described by Strek et al.[51]

In addition, spectral changes like band broadening or maximum peak shift were observed at the absorption spectra (Figure S4).

The Kubelka−Munk function was used to calculate the energy of band gaps (E_g) in the examined materials.[52] This

https://doi.org/10.1021/acsami.2c19957
ACS Appl. Mater. Interfaces XXXX, XXX, XXX−XXX

determination is based on the graphical examination of the following function:

$$F(R) = \frac{(1-R)^2}{2R} \quad (1)$$

where R denotes the measured diffuse reflectance. The comparison of the prepared graphical analysis is presented in Figure S5a–f. The estimated values of band gaps are presented in Figure 3b. The nonlinear decrease in E_g value is observed across the entire range of Cr^{3+} concentrations due to the substitution of the smaller Al^{3+} ion (0.535) by the larger Cr^{3+} (0.615) one. The sample containing only Al^{3+} ions exhibits the maximum value of the band gap energy (5.09 eV), whereas the compound based only on Cr^{3+} ions shows a minimum value of 4.38 eV. The reduction of the E_g value due to an increase in Cr^{3+} ion concentration has been reported for similar compounds containing a methylammonium cation.[14]

The obtained diffuse reflectance spectra were used to determine the crystal field (Dq), as well as the Racah parameters (B and C). The calculations were conducted following the previously reported methodology.[16,22] The detailed procedure of crystal field parameter determination is presented in Instruction 1 (Supporting Information). The summary of the calculation values is presented in the Supporting Information (Table S3). The analysis of the Dq/B ratio allows the determination of the crystal field strength. According to the Tanabe–Sugano diagram, the ^2E_g and $^4T_{2g}$ levels are overlapped for the Dq/B ratio equal to 2.3, which separates strong ($Dq/B > 2.3$) and weak ($Dq/B < 2.3$) crystal fields. Additionally, samples exhibiting a Dq/B value close to 2.3 can be assigned to the so-called intermediate crystal field. The sample containing the lowest concentration of Cr^{3+} ions (21 mol %) exhibits the strongest crystal field ($Dq/B = 2.76$). The increasing concentration of Cr^{3+} ions leads to a reduction of the Dq/B value (Figure 3b). The lowest value of the Dq/B parameter (2.33) was calculated for the sample containing 100 mol % chromium ions. Thus, the series of investigated compounds can be mainly described as exhibiting strong crystal fields. However, the sample containing 100% Cr^{3+} ions exhibits an intermediate crystal field. The comparison of two samples containing 21 and 100 mol % Cr^{3+} with energy diagrams and representative emission spectra is presented in Figure 4. The obtained results confirm the crystal field strength reduction by increasing the chromium concentration, which was reported previously.[14]

Luminescence and Temperature Dependency. The emission spectra of the obtained compounds were measured within the range of 80–400 K with 10 K steps. The used excitation wavelength was 405 nm since this energy corresponds well with the $^4A_{2g} \rightarrow {}^4T_{1g}$ transition. The collation of the excitation and emission spectra of $[EA]_2NaCr_{0.78}Al_{0.22}(HCOO)_6$ is presented in Figure S6. Due to fast nonradiative relaxation, the energy transfer from $^4T_{1g}$ to $^4T_{2g}$ and ^2E_g levels occurs.[6] The emission spectra of investigated compounds are strongly sensitive to the environmental temperature. At low temperatures, several narrow bands are present, where the strongest one is located at 686.4 nm (named the R_1 line). Moreover, the band at 684.2 nm (named R_2) can be observed. There are also additional Stokes bands localized at 696.8, 706.5, 727.2, and 752.3 nm. At higher temperatures, the intensities of the R_1 and R_2 bands significantly decrease. The intensities of bands at 727.2 and 752.3 nm also simultaneously decrease, although this process is not as progressive as a reduction of more intensive bands.

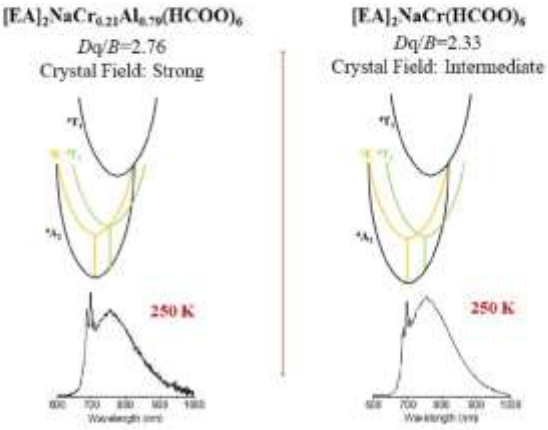

Figure 4. Comparison of the Dq/B values of two samples containing 21 and 100 mol % Cr^{3+} ions as well as energy diagrams of Cr^{3+} ions with the obtained emission spectra (normalized).

As the temperature increases, the emission spectra expand and create a wide band with a maximum at 752.3 nm. A progressive increase in temperature leads to a reduction of the emission intensity. The maximum intensities of this band occur at 210, 190, 185, and 150 K for samples containing 100, 78, 57, and 21 mol % chromium ions, respectively.

This emission is assigned to the spin-allowed $^4T_{2g} \rightarrow {}^4A_{2g}$ transitions. The formation of this broad band depends on the concentration of the Cr^{3+} ions. Therefore, the sample of $[EA]_2NaCr_{0.21}Al_{0.79}(HCOO)_6$ does not exhibit such a property and, on the other hand, the sample of $[EA]_2NaCr(HCOO)_6$ shows the strongest emission from the $^4T_{2g}$ level.

The luminescence properties of transition metal ions, such as Cr^{3+}, originate from d–d electronic transitions, which are not shielded by the outer orbitals, unlike the 4f orbitals in trivalent lanthanide ions.[53] Consequently, the spectroscopic characteristics of Cr^{3+} ions are strongly affected by the crystal field strength of the matrix material; thus, the emission type, range, and thermal quenching rate can be tuned by changing the matrix type.[53−56] The sensitivity of spectroscopic properties to the change of crystal field parameters plays a particular role in research on TM-based luminescence thermometers.[13,14,57] The irradiation with 405 nm wavelength excites a higher $^4T_{1g}$ level. The nonradiative energy transfer causes the increase in the population of the lowest vibrational level of ^2E_g. At low temperatures, the $^2E_g \rightarrow {}^4A_{2g}$ transition is dominant. An increase in temperature leads to a thermal population of the $^4T_{2g}$ level, which causes the occurrence of the broad spin-allowed $^4T_{2g} \rightarrow {}^4A_{2g}$ transition. The emission of the Cr^{3+} ions may be influenced by the local ion's symmetry changes, which causes a distortion of the excited state parabola.[58] Due to the occurrence of the crossing point between ground and excitation state parabolas, the increasing temperature may cause the depopulation of the excitation states via nonradiative transitions.

The same behavior was previously reported in methylammonium-based materials exhibiting different crystal field properties, particularly the Dq/B parameter.[14] The overall emission of prepared compounds quenches rapidly due to an

https://doi.org/10.1021/acsami.2c19957
ACS Appl. Mater. Interfaces XXXX, XXX, XXX−XXX

increase in temperature to around 300 K. The concentration of Cr^{3+} ions affects the maximal temperature when any emission is detectable, which is 270 and 330 K for samples containing 21 and 100 mol % Cr^{3+} ions, respectively.

It is worth noting that the sample of $[EA]_2NaCr(HCOO)_6$ exhibits low intensity and a very broad band within a range of 770 to 870 nm at a low temperature (80−130 K). This behavior was not detected in samples containing a lower concentration of Cr^{3+} ions. Such an occurrence of the additional band may indicate surface defects that can be related to a high concentration of chromium ions. A similar additional emission peak was reported for hybrid perovskites, e.g., $CH_3NH_3PbCl_3$ or $MHyPbCl_3$, and it has been assigned to the recombination of photoexcited carriers in defects.[59,60]

Additionally, the decay profiles for samples containing 21−100 mol % Cr^{3+} were measured (Figure 5a). To calculate the time components of the decay (τ_1 and τ_2 parameters), double exponential fitting was performed with the following equation:

$$I = I_0 + A_1 e^{-(t/\tau_1)} + A_2 e^{-(t/\tau_2)} \quad (2)$$

where I_0 is the initial luminescence intensity, A_1 and A_2 are the pre-exponential coefficients, τ_1 and τ_2 are first and second time components, respectively, and t is the time.

The influence of the chromium ions on the decay curve shape is observed. The highest values of τ_1 and τ_2 were calculated for the $[EA]_2NaCr_{0.21}Al_{0.79}(HCOO)_6$ sample and were equal to 1.35 and 2.26 ms, respectively. The increase in chromium ion concentration leads to the nonlinear reduction of the τ_1 and τ_2 parameters (Figure 5b). The most significant decrease occurs between 21 and 30 mol % Cr^{3+} ion concentrations, and then the change of the time parameters is closer to linear. The lowest values of τ_1 (0.069 ms) and τ_2 (0.176 ms) were calculated for the $[EA]_2NaCr(HCOO)_6$ sample. The values of the time parameters for all of the measured samples are listed in Table S4.

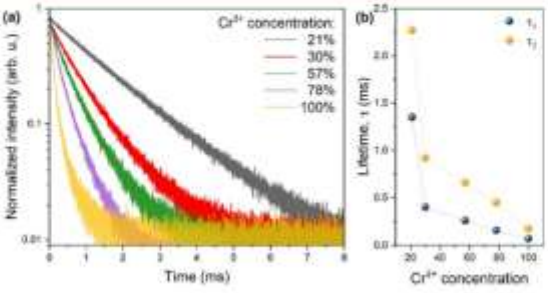

Figure 5. (a) Decay profiles of $[EA]_2NaCr_xAl_{1-x}(HCOO)_6$ (x = 1, 0.78, 0.57, 0.30, and 0.21) measured at 77 K; (b) change of time parameters as a function of Cr^{3+} concentration.

Luminescence Thermometry. The observed changes in the intensity and character of the emission in the aftermath of temperature change make the investigated metal−organic frameworks interesting materials for luminescence thermometry. It was recently suggested that hybrid materials with a perovskite-type architecture containing Cr^{3+} ions exhibit a sufficient optical response and physicochemical properties to be implemented into noncontact temperature sensing solutions.[13,45,46,57,61]

Temperature sensing originates from the coexistence of at least two temperature-dependent transitions. In the case of $[EA]_2NaCr_xAl_{1-x}(HCOO)_6$ compounds, the change in intensities of two bands, assigned to $^4T_{2g} \rightarrow {}^4A_{2g}$ and $^2E_g \rightarrow {}^4A_{2g}$, serves as the basis for temperature estimation. The thermal

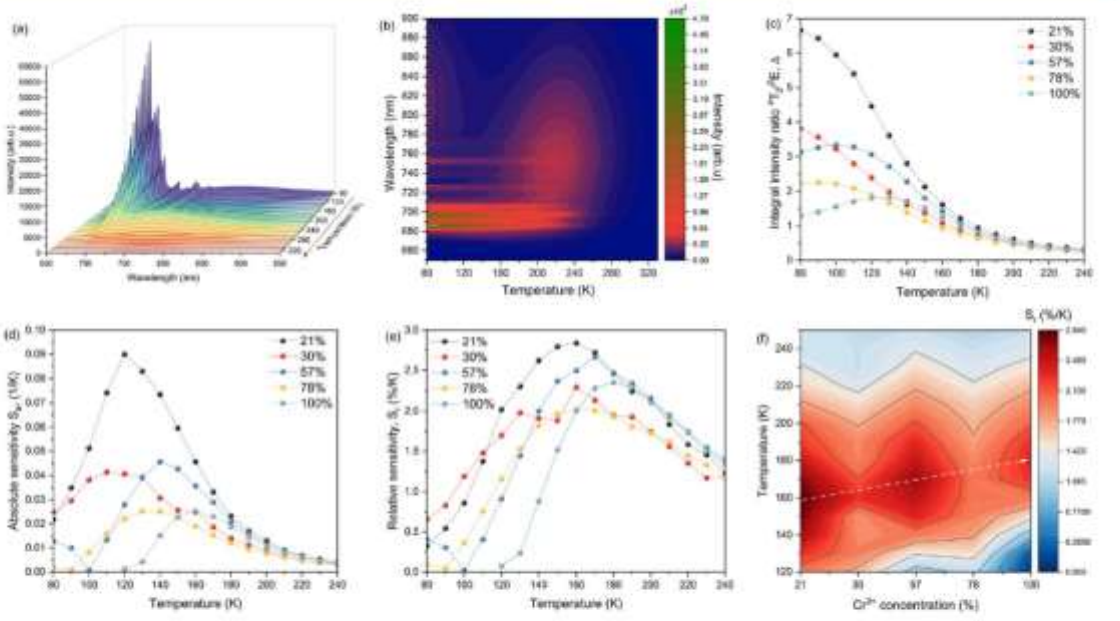

Figure 6. (a) Temperature-dependent emission spectra and (b) thermal evolution of the intensity measured for the $[EA]_2NaCr(HCOO)_6$ sample; (c) thermometric parameter (Δ); (d) absolute sensitivity (S_a); (e) relative sensitivity (S_r) and (f) influence of the Cr^{3+} ion concentration and temperature on the relative sensitivity.

https://doi.org/10.1021/acsami.2c19957
ACS Appl. Mater. Interfaces XXXX, XXX, XXX−XXX

evolution of the emission spectra for the sample containing 100 mol % Cr^{3+} is presented in Figure 6a,b. The results for the remaining samples are presented in Figure S7. To demonstrate the temperature sensing performance, the thermometric parameter Δ (FIR) was calculated. It is described as the ratio of the integrated intensities of the considered bands. For the calculations, two regions were chosen, namely, 660−718 nm for $^2E_g \rightarrow {}^4A_{2g}$ (denoted as I_1) and 718−970 nm for $^4T_{2g} \rightarrow {}^4A_{2g}$ (denoted as I_2). The comparison of the Δ value as a function of the temperature for a series of investigated materials is presented in Figure 6c.

The increase in temperature causes the general reduction of Δ; however, for samples containing 100 and 57 mol % Cr^{3+} ions, the increase in the calculated value is observed within ranges of 80−130 and 80−100 K, respectively. The highest initial value of Δ was calculated for a sample containing 21 mol % Cr^{3+}. Within a range of 200−300 K, the calculated values of the thermometric parameters for all samples are comparable. The slightly different shape of the initial part of the plot for the material containing 100% Cr^{3+} ions may be related to the additional, low-intensity broad band associated with a possible self-trapped exciton (STE), whose existence was reported for a wide variety of perovskite materials.[62−64] The observed emission decreases rapidly due to the increase in temperature.

To further demonstrate the luminescence thermometry performance, the absolute (S_a) and relative (S_r) sensitivities were calculated. The parameters are described by the following equations:[13]

$$S_a = \left|\frac{d\Delta}{dT}\right| \quad (3)$$

and

$$S_r = \frac{1}{\Delta}\left|\frac{d\Delta}{dT}\right| \quad (4)$$

where dΔ represents the change of thermometer parameter Δ (Figure 6c) at temperature change dT. The collations of absolute sensitivities for a series of investigated materials are presented in Figure 6d. The absolute sensitivities initially increase with the growth of temperature. The maximum value of S_a is 0.09 K^{-1} at 120 K for a sample containing 21 mol % Cr^{3+} ions. A progressive increase in temperature causes a significant decrease in S_a value. Similarly, the relative sensitivity values increase with temperature (Figure 6e). The maximum value of S_r is 2.84% K^{-1} and is reached again for a sample containing 21% chromium ions at a temperature of 160 K. The calculated temperature measurement uncertainty (δT) for the $[EA]_2NaCr_{0.21}Al_{0.79}(HCOO)_6$ sample at 160 K was 0.40 K. An increasing temperature leads to a simultaneous decrease in S_r parameter. The final value of relative sensitivity for most of the samples is 1.04−1.33% K^{-1}. In addition, the dependency of chromium ion concentration on the useful temperature sensing range and relative sensitivity can be observed. The increasing concentration of Cr^{3+} ions causes the change of the maximal relative sensitivity toward a higher temperature (Figure 6f). The possible modulation of the optimal sensing range by tuning the Cr^{3+} concentration significantly expands the possibility of system optimization.

To initially demonstrate a practical potential of luminescence thermometry, the exemplary thermometric solution based on one of presented compounds has been prepared (Figure 7). The obtained materials were investigated as

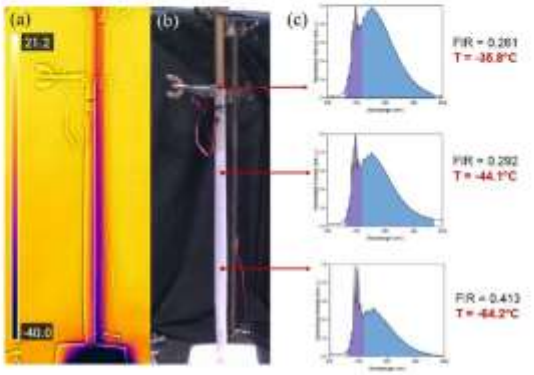

Figure 7. Exemplary thermometric system: (a) thermal image and (b) picture of the experimental setup; (c) recorded emission spectra for individual points with calculated FIR.

luminescence thermometers for low-temperature (T < −30 °C) systems. Luminescence thermometers have to be cooled by contact with an object, whose temperature is to be measured. The very first tests were performed with the system based on the temperature gradient present in a copper pipe, one of which end is submerged in liquid nitrogen (Figure 7a,b). Crystals of $[EA]_2NaCr(HCOO)_6$ were attached to the surface of the pipe with a thermal paste.

Thermometric calculations were performed with the model determined with presented temperature-dependent luminescence properties. The obtained photoluminescence spectra ($\lambda_{exc.}$ = 405 nm) were used to calculate the integrated intensity ratio (FIR parameter) and then compared to the model temperature relation (Figure 7c).

The presented result shows the undeniable potential of temperature-sensitive luminescent materials. Among various advantages, one of the most significant is the possibility to record the spectrum even in a presence of hoar frost. In addition, even expensive commercially available thermal imaging cameras are able to operate mainly in a temperature regime above −40 °C. The implementation of functional and durable luminescence thermometers is a significant matter for more developed investigation. Investigated organic−inorganic phosphors exhibit sufficient stability during heating−cooling intervals (Figure S8). Performed measurements consist of several consecutive heating and cooling processes. A significant change in the FIR value has not been observed, so the materials can be reused in thermometric systems. Measured materials do not exhibit phase transitions within the thermometric range, which additionally improves the stability in nonconstant temperature conditions. It is worth noting that possible practical usefulness may be significantly improved by protecting solutions, such as resin impregnation.

The obtained results, especially considering the luminescence thermometry performance, are remarkable and provide valuable information about the relationship between the composition, crystal field strength, and optical properties. Achieved values of relative sensitivity, up to 2.84% K^{-1}, are comparable to conventional inorganic lanthanide-doped materials.[13,65−67] The comparison of the S_r parameters of some reported luminescence thermometers is shown in Table 1.

https://doi.org/10.1021/acsami.2c19957
ACS Appl. Mater. Interfaces XXXX, XXX, XXX−XXX

Table 1. Collation of Exemplary Luminescence Thermometers with Relative Sensitivity (S_r) at a Given Temperature (T)[a]

compound	S_r(% K^{-1})	T (K)	ref.
$Sr_3MgAl_{12}O_{20}:Cr^{3+}$	1.7	310	46
$La_2MgTiO_6:Cr^{3+}$, V^{4+}	1.96	165	13
$La_2MgTiO_6:Eu^{3+}$	3.0	77	65
$SrGdLiTeO_6:Mn^{4+}$, Eu^{3+}	4.9	550	68
$Li_2Zn_4Al_5Ge_9O_{30}:Mn^{2+}$	8.489	323	69
$Sr_2GeO_4:Pr^{3+}$	9.0	22	70
$ZnGa_2O_4:Cr^{3+}$	2.8	310	45
$[EA]_2NaCr_{0.21}Al_{0.79}(HCOO)_6$	2.84	160	this work
Tb0.9Eu0.1(pia)	3.27	300	71
$Tb_{0.95}Eu_{0.05}$(btb)	2.85	14	72
$Tb_{0.957}Eu_{0.043}$cpda	16.0	300	73
FIR-8⊂DMASM	2.98	341	74

[a]H2pia, 5-(pyridin-4-yl)isophthalic acid; H3btb, 3,5-tris(4-carboxyphenyl)benzene; H3cpda, 5-(4-carboxyphenyl)-2,6-pyridinedicarboxylic acid; DMASM, 4-[*p*-(dimethylamino)styryl]-1-methylpyridinium.

The results show that formate-based hybrid compounds with the perovskite-like architecture $[EA]_2NaCr_xAl_{1-x}(HCOO)_6$ are promising materials for luminescence thermometry. The performed analysis shows that low-concentration chromium-doped materials may be promising compounds for highly sensitive and lanthanide-free temperature sensors.

CONCLUSIONS

The microwave-assisted solvothermal method was used to successfully synthesize a series of MOFs with the general formula $[EA]_2NaCr_xAl_{1-x}(HCOO)_6$, where x = 1, 0.78, 0.57, 0.30, 0.21, and 0. XRD measurements confirmed the phase purity and the ability to obtain mixed structures across the whole concentration range. The Raman spectra confirmed the expected composition of the prepared materials and provided preliminary information on how the phonon properties change as the Cr^{3+} concentration increases. The emission properties of synthesized compounds were found to be strongly temperature-dependent below 250 K. This feature and the coexistence of temperature-sensitive bands, spin-forbidden $^2E_g \rightarrow {}^4A_{2g}$ and spin-allowed $^4T_{2g} \rightarrow {}^4A_{2g}$, let one to perform calculations in order to evaluate the possible implementation of investigated materials as luminescence thermometers. The relative and absolute sensitivities of the studied compounds are satisfactory and are comparable to those of known inorganic materials. The highest relative sensitivity (2.84% K^{-1}, δT = 0.40 K) was achieved for a sample of $[EA]_2NaCr_{0.21}Al_{0.79}(HCOO)_6$ at 160 K. The results also showed that the concentration of Cr^{3+} ions has a big impact on luminescence outputs. The temperature sensing range and temperature of the maximal relative sensitivity can be precisely tuned by modifying the sample composition, substantially increasing the utility of the developed luminescence thermometer. According to the results of the investigation, chromium-based organic−inorganic perovskites could be promising materials for noncontact temperature sensing. The presented practical implementation of the investigated compounds shows the potential of this particular type of sensor. The development of thermosensitive materials containing transition metal ions could pave the way for lanthanide-free, low-cost, and efficient contactless luminescence thermometry solutions.

ASSOCIATED CONTENT

Supporting Information

The Supporting Information is available free of charge at https://pubs.acs.org/doi/10.1021/acsami.2c19957.

Quantities of precursors; unit cell parameters; crystal field parameters and electron transition energies; time parameters of decays; change of unit cell parameters; XRD; Raman spectra; normalized DRS spectra; band gap determined with the Kubelka−Munk function; excitation−emission spectra; temperature dependence on the luminescence spectra; thermometric stability in 100−160 K intervals for the representative sample; thermal stability and crystal field parameter calculation (PDF)

AUTHOR INFORMATION

Corresponding Authors

Adam Kabański − *Institute of Low Temperature and Structure Research, Polish Academy of Sciences, Wroclaw 50-422, Poland*; Email: a.kabanski@intibs.pl

Dagmara Stefańska − *Institute of Low Temperature and Structure Research, Polish Academy of Sciences, Wroclaw 50-422, Poland*; orcid.org/0000-0002-1051-3761; Email: d.stefanska@intibs.pl

Author

Maciej Ptak − *Institute of Low Temperature and Structure Research, Polish Academy of Sciences, Wroclaw 50-422, Poland*

Complete contact information is available at: https://pubs.acs.org/10.1021/acsami.2c19957

Notes

The authors declare no competing financial interest.

Experimental data: The Raman and diffuse reflectance spectra, band gap and crystal field strength, decay profiles and lifetimes, temperature-dependent luminescence and emission maps, thermometric parameters, exemplary system's luminescence characteristics, unit cell characteristics, powder XRD data, Kubelka−Munk function with band gap estimation, excitation and emission spectra, and stability of PL are available at 10.5281/zenodo.7505524.

ACKNOWLEDGMENTS

This research was founded in whole by the National Science Centre, Poland, under project no. UMO- 2020/39/D/ST5/01289. For the purpose of open access, the author has applied a CC-BY public copyright license to any Author Accepted Manuscript (AAM) version arising from this submission.

REFERENCES

(1) Ptak, M.; Sieradzki, A.; Šimėnas, M.; Mączka, M. Molecular Spectroscopy of Hybrid Organic−Inorganic Perovskites and Related Compounds. *Coord. Chem. Rev.* **2021**, *448*, No. 213180.

(2) Fan, Z.; Sun, K.; Wang, J. Perovskites for Photovoltaics: A Combined Review of Organic-Inorganic Halide Perovskites and Ferroelectric Oxide Perovskites. *J. Mater. Chem. A* **2015**, *3*, 18809−18828.

(3) Prochowicz, D.; Franckevičius, M.; Cieslak, A. M.; Zakeeruddin, S. M.; Gratzel, M.; Lewinski, J. Mechanosynthesis of the Hybrid Perovskite $CH_3NH_3PbI_3$: Characterization and the Corresponding Solar Cell Efficiency. *J. Mater. Chem. A* **2015**, *3*, 20772−20777.

(4) Kim, J. Y.; Lee, J. W.; Jung, H. S.; Shin, H.; Park, N. G. High-Efficiency Perovskite Solar Cells. *Chem. Rev.* **2020**, *120*, 7867−7918.
(5) Huang, C. R.; Luo, X.; Chen, X. G.; Song, X. J.; Zhang, Z. X.; Xiong, R. G. A Multiaxial Lead-Free Two-Dimensional Organic-Inorganic Perovskite Ferroelectric. *Natl. Sci. Rev.* **2021**, *8*, 1−7.
(6) Ptak, M.; Mączka, M.; Gągor, A.; Sieradzki, A.; Bondzior, B.; Dereń, P.; Pawlus, S. Phase Transitions and Chromium(III) Luminescence in Perovskite-Type $[C_2H_5NH_3][Na_{0.5}Cr_xAl_{0.5-x}(HCOO)_3]$ (x = 0, 0.025, 0.5), Correlated with Structural, Dielectric and Phonon Properties. *Phys. Chem. Chem. Phys.* **2016**, *18*, 29629−29640.
(7) Ptak, M.; Mączka, M.; Gągor, A.; Sieradzki, A.; Stroppa, A.; di Sante, D.; Perez-Mato, J. M.; MacAlik, L. Experimental and Theoretical Studies of Structural Phase Transition in a Novel Polar Perovskite-like $[C_2H_5NH_3][Na_{0.5}Fe_{0.5}(HCOO)_3]$ Formate. *Dalton Trans.* **2016**, *45*, 2574−2583.
(8) Wang, Z. C.; Rogers, J. D.; Yao, X.; Nichols, R.; Atay, K.; Xu, B.; Franklin, J.; Sochnikov, I.; Ryan, P. J.; Haskel, D.; Tafti, F. Colossal Magnetoresistance without Mixed Valence in a Layered Phosphide Crystal. *Adv. Mater.* **2021**, *33*, 2005755−2005762.
(9) Zhang, J.; Ji, W.-J.; Xu, J.; Geng, X.-Y.; Zhou, J.; Gu, Z.-B.; Yao, S.-H.; Zhang, S.-T. Giant Positive Magnetoresistance in Half-Metallic Double-Perovskite Sr_2CrWO_6 Thin Films. *Sci. Adv.* **2017**, *3*, 1−7.
(10) Dhahri, A.; Dhahri, E.; Hlil, E. K. Large Magnetocaloric Effect in Manganese Perovskite $La_{0.67-x}Bi_xBa_{0.33}MnO_3$ near Room Temperature. *RSC Adv.* **2019**, *9*, 5530−5539.
(11) Kadim, G.; Masrour, R.; Jabar, A.; Hlil, E. K. Room-Temperature Large Magnetocaloric, Electronic and Magnetic Properties in $La_{0.75}Sr_{0.25}MnO_3$ Manganite: Ab Initio Calculations and Monte Carlo Simulations. *Phys. A* **2021**, *573*, No. 125936.
(12) Chen, C. W.; Hsiao, S. Y.; Chen, C. Y.; Kang, H. W.; Huang, Z. Y.; Lin, H. W. Optical Properties of Organometal Halide Perovskite Thin Films and General Device Structure Design Rules for Perovskite Single and Tandem Solar Cells. *J. Mater. Chem. A* **2015**, *3*, 9152−9159.
(13) Stefańska, D.; Bondzior, B.; Vu, T. H. Q.; Grodzicki, M.; Dereń, P. J. Temperature Sensitivity Modulation through Changing the Vanadium Concentration in a $La_2MgTiO_6:V^{5+},Cr^{3+}$ Double Perovskite Optical Thermometer. *Dalton Trans.* **2021**, *50*, 9851−9857.
(14) Ptak, M.; Dziuk, B.; Stefańska, D.; Hermanowicz, K. The Structural, Phonon and Optical Properties of $[CH_3NH_3]M_{0.5}Cr:XAl_{0.5-x}(HCOO)_3$ (M = Na, K; X = 0, 0.025, 0.5) Metal-Organic Framework Perovskites for Luminescence Thermometry. *Phys. Chem. Chem. Phys.* **2019**, *21*, 7965−7972.
(15) Zhu, H.; Fu, Y.; Meng, F.; Wu, X.; Gong, Z.; Ding, Q.; Gustafsson, M. V.; Trinh, M. T.; Jin, S.; Zhu, X. Y. Lead Halide Perovskite Nanowire Lasers with Low Lasing Thresholds and High Quality Factors. *Nat. Mater.* **2015**, *14*, 636−642.
(16) Ptak, M.; Stefańska, D.; Gągor, A.; Svane, K. L.; Walsh, A.; Paraguassu, W. Heterometallic Perovskite-Type Metal−Organic Framework with an Ammonium Cation: Structure, Phonons, and Optical Response of $[NH_4]Na_{0.5}CrxAl_{0.5-x}(HCOO)_3$ (X= 0, 0.025 and 0.5). *Phys. Chem. Chem. Phys.* **2018**, *20*, 22284−22295.
(17) Zhang, Y.; Liao, W. Q.; Fu, D. W.; Ye, H. Y.; Liu, C. M.; Chen, Z. N.; Xiong, R. G. The First Organic-Inorganic Hybrid Luminescent Multiferroic: (Pyrrolidinium)$MnBr_3$. *Adv. Mater.* **2015**, *27*, 3942−3946.
(18) Shang, R.; Xu, G. C.; Wang, Z. M.; Gao, S. Phase Transitions, Prominent Dielectric Anomalies, and Negative Thermal Expansion in Three High Thermally Stable Ammonium Magnesium-Formate Frameworks. *Chem. − Eur. J.* **2014**, *20*, 1146−1158.
(19) Mączka, M.; Ptak, M.; Pawlus, S.; Paraguassu, W.; Sieradzki, A.; Balciunas, S.; Simenas, M.; Banys, J. Temperature- and Pressure-Dependent Studies of Niccolite-Type Formate Frameworks of $[NH_3(CH_2)_4NH_3][M_3(HCOO)_6]$ (M = Zn, Co, Fe). *Phys. Chem. Chem. Phys.* **2016**, *18*, 27613−27622.
(20) Xu, X. Y.; Yan, B. An Efficient and Sensitive Fluorescent PH Sensor Based on Amino Functional Metal-Organic Frameworks in Aqueous Environment. *Dalton Trans.* **2016**, *45*, 7078−7084.
(21) Cui, Y.; Zhu, F.; Chen, B.; Qian, G. Metal-Organic Frameworks for Luminescence Thermometry. *Chem. Commun.* **2015**, *51*, 7420−7431.
(22) Mączka, M.; Bondzior, B.; Dereń, P.; Sieradzki, A.; Trzmiel, J.; Pietraszko, A.; Hanuza, J. Synthesis and Characterization of $[(CH_3)_2NH_2][Na_{0.5}Cr_{0.5}(HCOO)_3]$: A Rare Example of Luminescent Metal-Organic Frameworks Based on Cr(III) Ions. *Dalton Trans.* **2015**, *44*, 6871−6879.
(23) Ptak, M.; Zarychta, B.; Stefańska, D.; Ciupa, A.; Paraguassu, W. Novel Bimetallic MOF Phosphors with an Imidazolium Cation: Structure, Phonons, High- Pressure Phase Transitions and Optical Response. *Dalton Trans.* **2019**, *48*, 242−252.
(24) Charroux, B.; Daian, F.; Royet, J. Drosophila Aversive Behavior toward Erwinia carotovora carotovora Is Mediated by Bitter Neurons and Leukokinin. *iScience* **2020**, 23, No. 101152.
(25) Dereń, P. J.; Malinowski, M.; Stręk, W. Site Selection Spectroscopy of Cr^{3+} in MgA1204 Green Spinel. *J. Lumin.* **1996**, *68*, 91−103.
(26) Deren, P. J.; Watras, A.; Gagor, A.; Pazik, R. Weak Crystal Field in Yttrium Gallium Garnet (YGG) Submicrocrystals Doped with Cr 3+. *Cryst. Growth Des.* **2012**, *12*, 4752−4757.
(27) Wang, Q.; Liao, M.; Lin, Q.; Xiong, M.; Mu, Z.; Wu, F. A Review on Fluorescence Intensity Ratio Thermometer Based on Rare-Earth and Transition Metal Ions Doped Inorganic Luminescent Materials. *J. Alloys Compd.* **2021**, *850*, No. 156744.
(28) Yuan, J.; Zhang, Y.; Xu, J.; Tian, T.; Luo, K.; Huang, L. Novel Cr^{3+}-Doped Double-Perovskite Ca_2MNbO_6 (M = Ga, Al) Phosphor: Synthesis, Crystal Structure Photoluminescence and Thermoluminescence Properties. *J. Alloys Compd.* **2020**, *815*, No. 152656.
(29) Lin, H.; Bai, G.; Yu, T.; Tsang, M. K.; Zhang, Q.; Hao, J. Site Occupancy and Near-Infrared Luminescence in $Ca_3Ga_2Ge_3O_{12}$: Cr^{3+} Persistent Phosphor. *Adv. Opt. Mater.* **2017**, *5*, No. 1700227.
(30) Marciniak, L.; Bednarkiewicz, A. Nanocrystalline NIR-to-NIR Luminescent Thermometer Based on Cr^{3+}, Yb^{3+} Emission. *Sens. Actuators, B* **2017**, *243*, 388−393.
(31) Maturi, F. E.; Brites, C. D. S.; Ximendes, E. C.; Mills, C.; Olsen, B.; Jaque, D.; Ribeiro, S. J. L.; Carlos, L. D. Going Above and Beyond: A Tenfold Gain in the Performance of Luminescence Thermometers Joining Multiparametric Sensing and Multiple Regression. *Laser Photonic Rev.* **2021**, *15*, No. 2100301.
(32) Yin, H. Q.; Yin, X. B. Metal-Organic Frameworks with Multiple Luminescence Emissions: Designs and Applications. *Acc. Chem. Res.* **2020**, 53, 485−495.
(33) Wu, S.; Min, H.; Shi, W.; Cheng, P. Multicenter Metal−Organic Framework-Based Ratiometric Fluorescent Sensors. *Adv. Mater.* **2020**, No. e1805871.
(34) N'Dala-Louika, I.; Ananias, D.; Latouche, C.; Dessapt, R.; Carlos, L. D.; Serier-Brault, H. Ratiometric Mixed Eu-Tb Metal-Organic Framework as a New Cryogenic Luminescent Thermometer. *J. Mater. Chem. C* **2017**, *5*, 10933−10937.
(35) del Rosal, B.; Ximendes, E.; Rocha, U.; Jaque, D. In Vivo Luminescence Nanothermometry: From Materials to Applications. *Adv. Opt. Mater.* **2017**, *5*, No. 1600508.
(36) Dramićanin, M. D. Trends in Luminescence Thermometry. *J. Appl. Phys.* **2020**, *128*, No. 040902.
(37) Brites, C. D. S.; Millán, A.; Carlos, L. D.Lanthanides in Luminescent Thermometry. In *Handbook on the Physics and Chemistry of Rare Earths*; Elsevier B.V., 2016; Vol. *49*, pp. 339−427. DOI: 10.1016/bs.hpcre.2016.03.005.
(38) Rocha, J.; Brites, C. D.; Carlos, L. D. Lanthanide Organic Framework Luminescent Thermometers. *Chem. − Eur. J.* **2016**, *22*, 14782−14795.
(39) Kolesnikov, I. E.; Afanaseva, E. V.; Kurochkin, M. A.; Kolesnikov, E. Y.; Lähderanta, E. Mixed-Valent $MgAl_2O_4:Eu^{2+}/Eu^{3+}$ Phosphor for Ratiometric Optical Thermometry. *Phys. B* **2022**, *624*, No. 413456.
(40) Trojan-Piegza, J.; Brites, C. D. S.; Ramalho, J. F. C. B.; Wang, Z.; Zhou, G.; Wang, S.; Carlos, L. D.; Zych, E. $La_{0.4}Gd_{1.6}Zr_2O_7$:0.1%

https://doi.org/10.1021/acsami.2c19957
ACS Appl. Mater. Interfaces XXXX, XXX, XXX−XXX

Pr Transparent Sintered Ceramic - a Wide-Range Luminescence Thermometer. *J. Mater. Chem. C* **2020**, *8*, 7005−7011.
(41) Gavrilović, T. V.; Jovanović, D. J.; Lojpur, V.; Dramićanin, M. D. Multifunctional Eu^{3+}- and Er^{3+}/Yb^{3+}-Doped $GdVO_4$ Nanoparticles Synthesized by Reverse Micelle Method. *Sci. Rep.* **2014**, *4*, 4209.
(42) Mykhaylyk, V.; Kraus, H.; Zhydachevskyy, Y.; Tsiumra, V.; Luchechko, A.; Wagner, A.; Suchocki, A. Multimodal Non-Contact Luminescence Thermometry with Cr-Doped Oxides. *Sensors* **2020**, *20*, 1−22.
(43) Glais, E.; Pellerin, M.; Castaing, V.; Alloyeau, D.; Touati, N.; Viana, B.; Chanéac, C. Luminescence Properties of $ZnGa_2O_4$:Cr^{3+}, Bi^{3+} Nanophosphors for Thermometry Applications. *RSC Adv.* **2018**, *8*, 41767−41774.
(44) Elzbieciak, K.; Marciniak, L. The Impact of Cr^{3+} Doping on Temperature Sensitivity Modulation in Cr^{3+} Doped and Cr^{3+}, Nd^{3+} Co-Doped $Y_3Al_5O_{12}$, $Y_3Al_2Ga_3O_{12}$, and $Y_3Ga_5O_{12}$ Nanothermometers. *Front. Chem.* **2018**, *6*, 1−8.
(45) Ueda, J.; Back, M.; Brik, M. G.; Zhuang, Y.; Grinberg, M.; Tanabe, S. Ratiometric Optical Thermometry Using Deep Red Luminescence from $^4T_2$ and ^2E States of Cr^{3+} in $ZnGa_2O_4$ Host. *Opt. Mater.* **2018**, *85*, 510−516.
(46) Wang, Q.; Liang, Z.; Luo, J.; Yang, Y.; Mu, Z.; Zhang, X.; Dong, H.; Wu, F. Ratiometric Optical Thermometer with High Sensitivity Based on Dual Far-Red Emission of Cr^{3+} in $Sr_2MgAl_{22}O_{36}$. *Ceram. Int.* **2020**, *46*, 5008−5014.
(47) Mullins, A. L.; Ćirić, A.; Zeković, I.; Williams, J. A. G.; Dramićanin, M. D.; Evans, I. R. Dual-Emission Luminescence Thermometry Using $LaGaO_3$:Cr^{3+}, Nd^{3+} Phosphors. *J. Mater. Chem. C* **2022**, *10*, 10396−10403.
(48) Li, Z.; Xu, S. C.; Zhang, C.; Liu, X. Y.; Gao, S. S.; Hu, L. T.; Guo, J.; Ma, Y.; Jiang, S. Z.; Si, H. P. High-Performance SERS Substrate Based on Hybrid Structure of Graphene Oxide/AgNPs/Cu Film@pyramid Si. *Sci. Rep.* **2016**, *6*, 1.
(49) Liu, T.; Kim, D.; Han, H.; bin Mohd Yusoff, A. R.; Jang, J. Fine-Tuning Optical and Electronic Properties of Graphene Oxide for Highly Efficient Perovskite Solar Cells. *Nanoscale* **2015**, *7*, 10708−10718.
(50) Lipiäinen, T.; Fraser-Miller, S. J.; Gordon, K. C.; Strachan, C. J. Direct Comparison of Low- and Mid-Frequency Raman Spectroscopy for Quantitative Solid-State Pharmaceutical Analysis. *J. Pharm. Biomed. Anal.* **2018**, *149*, 343−350.
(51) Stręk, W.; Dereń, P.; Jeżowska-Trzebiatowska, B. Optical Properties of Cr^{3+} in $MgAl_2O_4$. *Phys. B* **1988**, *152*, 3790384.
(52) López, R.; Gómez, R. Band-Gap Energy Estimation from Diffuse Reflectance Measurements on Sol-Gel and Commercial TiO_2: A Comparative Study. *J. Sol-Gel Sci. Technol.* **2012**, *61*, 1−7.
(53) Marciniak, L.; Kniec, K.; Elżbieciak-Piecka, K.; Trejgis, K.; Stefańska, J.; Dramićanin, M. Luminescence Thermometry with Transition Metal Ions. *A Review. Coord. Chem. Rev.* **2022**, *469*, No. 214671.
(54) Adachi, S. Review - Photoluminescence Properties of Cr^{3+}-Activated Fluoride Phosphors. *ECS J. Solid State Sci. Technol.* **2021**, *10*, No. 036001.
(55) Marciniak, L.; Szalkowski, M.; Bednarkiewicz, A.; Elżbieciak-Piecka, K. A Cr^{3+} Luminescence Based Ratiometric Optical Laser Power Meter. *J. Mater. Chem. C* **2022**, *10*, 11040−11047.
(56) Adachi, S. Luminescence Spectroscopy of Cr^{3+} in an Oxide: A Strong or Weak Crystal-Field Phosphor? *J. Lumin.* **2021**, *234*, No. 117965.
(57) Elżbieciak-Piecka, K.; Drabik, J.; Jaque, D.; Marciniak, L. Cr^{3+}-based Nanocrystalline Luminescent Thermometers Operating in a Temporal Domain. *Phys. Chem. Chem. Phys.* **2020**, *22*, 25949−25962.
(58) Marciniak, L.; Bednarkiewicz, A.; Strek, W. The Impact of Nanocrystals Size on Luminescent Properties and Thermometry Capabilities of Cr, Nd Doped Nanophosphors. *Sens. Actuators, B* **2017**, *238*, 381−386.
(59) Mączka, M.; Gągor, A.; Zareba, J. K.; Stefańska, D.; Drozd, M.; Balciunas, S.; Simenas, M.; Banys, J.; Sieradzki, A. Three-Dimensional Perovskite Methylhydrazinium Lead Chloride with Two Polar Phases and Unusual Second-Harmonic Generation Bistability above Room Temperature. *Chem. Mater.* **2020**, *32*, 4072−4082.
(60) Hsu, H. P.; Li, L. C.; Shellaiah, M.; Sun, K. W. Structural, Photophysical, and Electronic Properties of $CH_3NH_3PbCl_3$ Single Crystals. *Sci. Rep.* **2019**, *9*, 13311.
(61) Otto, S.; Scholz, N.; Behnke, T.; Resch-Genger, U.; Heinze, K. Thermo-Chromium: A Contactless Optical Molecular Thermometer. *Chem. − Eur. J.* **2017**, *23*, 12131−12135.
(62) Gautier, R.; Paris, M.; Massuyeau, F. Exciton Self-Trapping in Hybrid Lead Halides: Role of Halogen. *J. Am. Chem. Soc.* **2019**, *141*, 12619−12623.
(63) Kumar, V.; Luo, Z. A Review on X-ray Excited Emission Decay Dynamics in Inorganic Scintillator Materials. *Photonics* **2021**, *8*, 1−27.
(64) Smith, M. D.; Jaffe, A.; Dohner, E. R.; Lindenberg, A. M.; Karunadasa, H. I. Structural Origins of Broadband Emission from Layered Pb-Br Hybrid Perovskites. *Chem. Sci.* **2017**, *8*, 4497−4504.
(65) Bondzior, B.; Stefańska, D.; Vũ, T. H. Q.; Miniajluk-Gawel, N.; Dereń, P. J. Red Luminescence with Controlled Rise Time in La_2MgTiO_6: Eu^{3+}. *J. Alloys Compd.* **2021**, *852*, No. 157074.
(66) Kniec, K.; Ledwa, K.; Marciniak, L. Enhancing the Relative Sensitivity of V^{2+}, V^{4+} and V^{3+} Based Luminescent Thermometer by the Optimization of the Stoichiometry of $Y_3Al_{5-x}Ga_xO_{12}$ Nanocrystals. *Nanomaterials* **2019**, *9*, 1375.
(67) Stefańska, D.; Stefanski, M.; Dereń, P. J. Unusual Emission Generated from Ca2Mg0.5AlSi1.5O7:Eu2+ and Its Potential for UV-LEDs and Non-Contact Optical Thermometry. *J. Alloys Compd.* **2021**, *863*, 1375.
(68) Li, L.; Tian, G.; Deng, Y.; Wang, Y.; Cao, Z.; Ling, F.; Li, Y.; Jiang, S.; Xiang, G.; Zhou, X. Constructing Ultra-Sensitive Dual-Mode Optical Thermometers: Utilizing FIR of Mn^{4+}/Eu^{3+} and Lifetime of Mn^{4+} Based on Double Perovskite Tellurite Phosphor. *Opt. Express* **2020**, *28*, 33747.
(69) Wang, Q.; Liao, M.; Mu, Z.; Zhang, X.; Dong, H.; Liang, Z.; Luo, J.; Yang, Y.; Wu, F. Ratiometric Optical Thermometer with High Sensitivity Based on Site-Selective Occupancy of Mn^{2+} Ions in $Li_5Zn_8Al_5Ge_9O_{36}$ under Controllable Synthesis Atmosphere. *J. Phys. Chem. C* **2020**, *124*, 886−895.
(70) Brites, C. D. S.; Fiaczyk, K.; Ramalho, J. F. C. B.; Sójka, M.; Carlos, L. D.; Zych, E. Widening the Temperature Range of Luminescent Thermometers through the Intra- and Interconfigurational Transitions of Pr^{3+}. *Adv. Opt. Mater.* **2018**, *6*, No. 1701318.
(71) Rao, X.; Song, T.; Gao, J.; Cui, Y.; Yang, Y.; Wu, C.; Chen, B.; Qian, G. A Highly Sensitive Mixed Lanthanide Metal-Organic Framework Self-Calibrated Luminescent Thermometer. *J. Am. Chem. Soc.* **2013**, *135*, 15559−15564.
(72) Ananias, D.; Brites, C. D. S.; Carlos, L. D.; Rocha, J. Cryogenic Nanothermometer Based on the MIL-103(Tb,Eu) Metal-Organic Framework. *Eur. J. Inorg. Chem.* **2016**, *2016*, 1967−1971.
(73) Cui, Y.; Zou, W.; Song, R.; Yu, J.; Zhang, W.; Yang, Y.; Qian, G. A Ratiometric and Colorimetric Luminescent Thermometer over a Wide Temperature Range Based on a Lanthanide Coordination Polymer. *Chem. Commun.* **2014**, *50*, 719−721.
(74) Wan, Y.; Yu, L.; Xia, T. A Dye-Loaded Nonlinear Metal-Organic Framework as Self-Calibrated Optical Thermometer. *Dyes Pigm.* **2022**, *202*, No. 110234.

https://doi.org/10.1021/acsami.2c19957
ACS Appl. Mater. Interfaces XXXX, XXX, XXX−XXX

Supporting information

Metal-organic framework optical thermometer based on Cr^{3+} ions luminescence

Adam Kabański[a,*], Maciej Ptak[a], Dagmara Stefańska[a*],

[a]Institute of Low Temperature and Structure Research, Polish Academy of Sciences, Box 1410, 50-950 Wrocław 2, Poland

[*]E-mail: a.kabanski@intibs.pl, d.stefanska@intibs.pl

Table S1. Quantities of precursors used for the synthesis of the series of $[EA]_2NaCr_xAl_{1-x}(HCOO)_6$

Real x	Nominal x	Amount of the substrate [g]					
		$CrCl_3 \cdot 6H_2O$	$Al(ClO_4)_3 \cdot 9H_2O$	EA·HCl	HCOONa	*N*-ethylformamide	HCOOH
1.00	1.00	1.0658	-	0.3264	0.5985	25 ml	5 ml
0.78	0.80	0.8530	0.3905	0.3267	0.5985		
0.57	0.60	0.6396	0.7803	0.3266	0.5987		
0.30	0.40	0.3739	1.1710	0.3265	0.5992		
0.21	0.20	0.2139	1.5604	0.3267	0.5989		
0.00	0.00	-	1.9502	0.3264	0.5987		

Table S2. The parameters of the unit cells of the series of $[EA]_2NaCr_xAl_{1-x}(HCOO)_6$

Parameter	x					
	0	0.21	0.30	0.57	0.78	1
a (Å)	8.038	8.051	8.065	8.079	8.092	8.102
b (Å)	9.263	9.260	9.260	9.262	9.265	9.268
c (Å)	14.311	14.321	14.338	14.346	14.359	14.368
β (°)	123.226	123.204	123.194	123.152	123.113	123.100
V (Å^3)	1065.564	1067.598	1070.759	1073.424	1076.531	1078.881

Table S3. The collation of crystal field parameters and energies of electron transitions of the investigated series of $[EA]_2NaCr_xAl_{1-x}(HCOO)_6$

Parameter	x				
	0.21	0.30	0.57	0.78	1
$^4A_{2g} \rightarrow {}^2E$ (cm^{-1})	14549	14550	14550	14551	14555
$^4A_{2g} \rightarrow {}^4T_{2g}$ (cm^{-1})	16610	16453	16285	16112	15715
$^4A_{2g} \rightarrow {}^4T_{1g}$ (cm^{-1})	22764	22581	22440	22383	22329
*D*q (cm^{-1})	1661	1645	1628	1611	1572
B (cm^{-1})	601	600	605	622	674
*D*q/B	2.76	2.74	2.69	2.59	2.33
C (cm^{-1})	3341	3346	3337	3302	3198
C/*B*	5.56	5.58	5.52	5.31	4.74

Table S4. The collation of lifetime time-parameters for a series of $[EA]_2NaCr_xAl_{1-x}(HCOO)_6$

Parameter	x				
	0.21	0.30	0.57	0.78	1
τ_1 [ms]	1.35	0.403	0.261	0.159	0.069
τ_2 [ms]	2.27	0.920	0.660	0.452	0.176

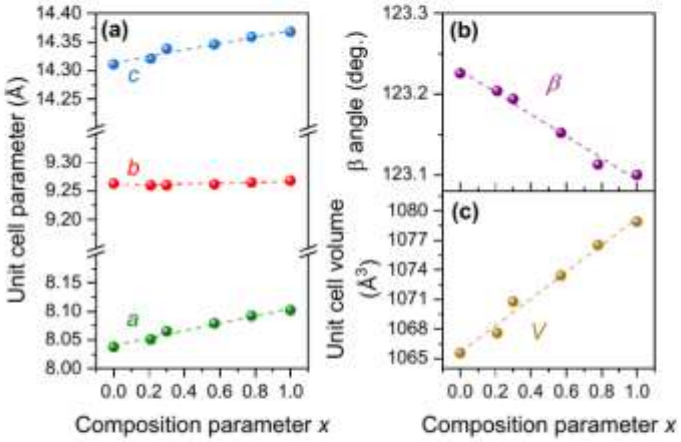

Figure S1. Influence of the composition parameter x on the unit cell parameters of the series of $[EA]_2NaCr_xAl_{1-x}(HCOO)_6$: (a) change of *a*, *b*, and *c* parameters; (b) change of the *β* angle; (c) unit cell volumes.

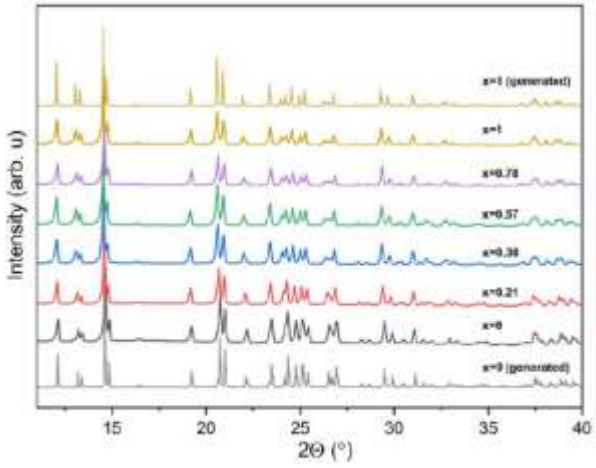

Figure S2. XRD patterns for a series of $[EA]_2NaCr_xAl_{1-x}(HCOO)_6$

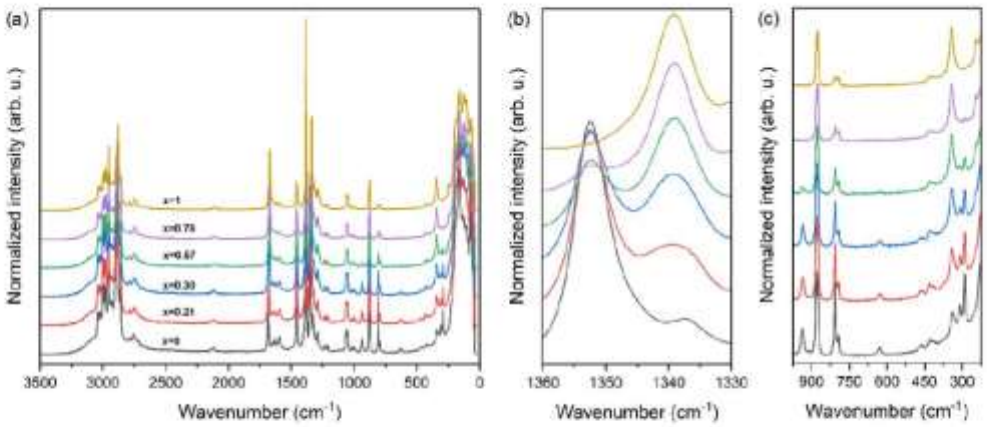

Figure S3. (a) Raman spectra for the obtained series of $[EA]_2NaCr_xAl_{1-x}(HCOO)_6$; (b) enlargement of a range within 1330-1360 cm^{-1}; (c) enlargement of a range within 225-975 cm^{-1}.

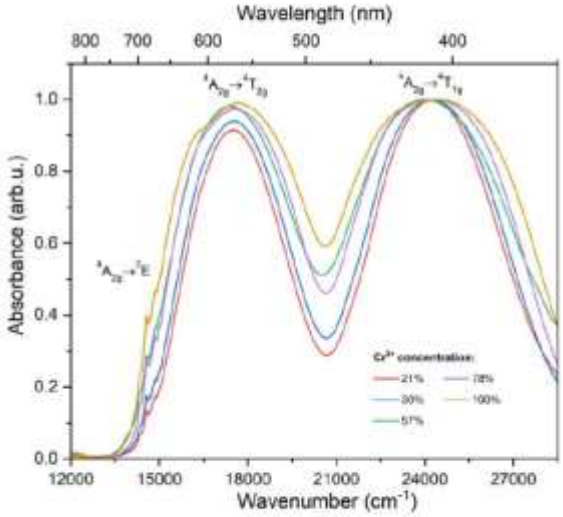

Figure S4. Normalized diffuse reflectance spectra of the series of $[EA]_2NaCr_xAl_{1-x}(HCOO)_6$ (x=1, 0.78, 0.57, 0.30, 0.21, and 0) compounds measured at 300 K

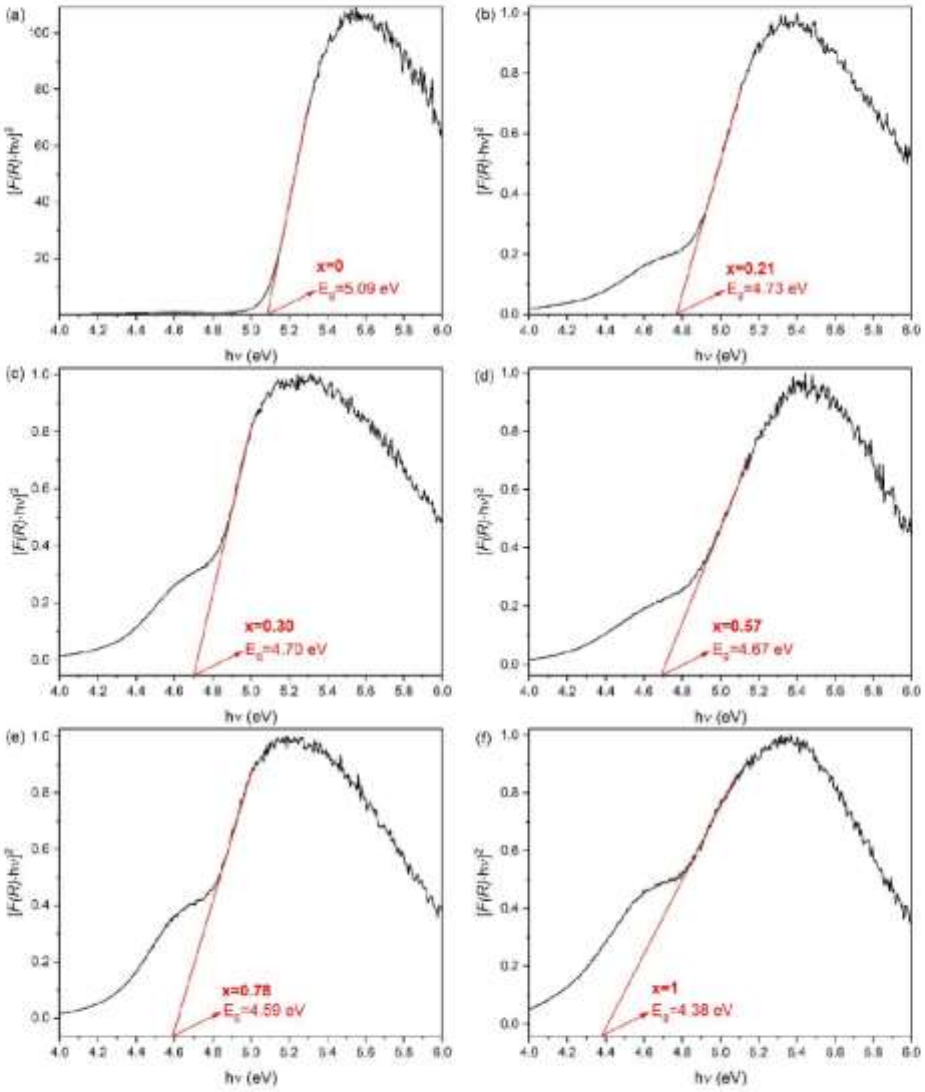

Figure S5. (a-f) The energy of band gaps determined with Kubelka-Munk function for the investigated series of $[EA]_2NaCr_xAl_{1-x}(HCOO)_6$. The composition of the individual material is presented in the graph.

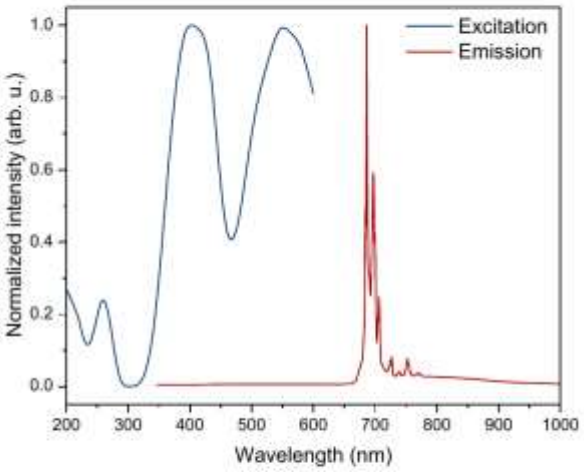

Figure S6. The collation of excitation and emission spectra of $[EA]_2NaCr_{0.78}Al_{0.22}(HCOO)_6$ ($\lambda_{exc.}$=405 nm).

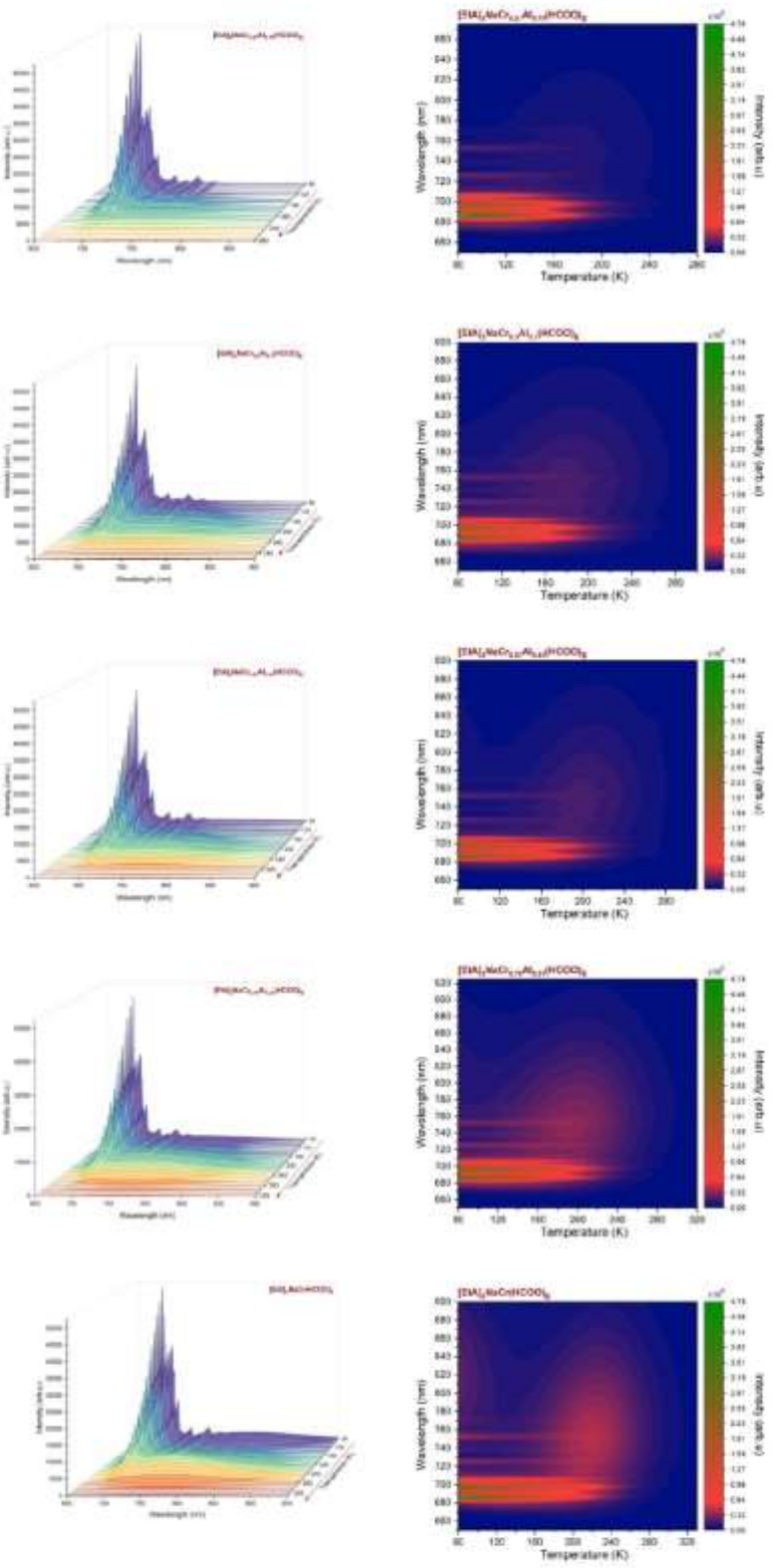
Wavelength (nm)
Temperature (K)

Figure S7. The collation of temperature-dependent emission spectra of the investigated materials with evolution map. The composition of the individual material is presented in the graphs.

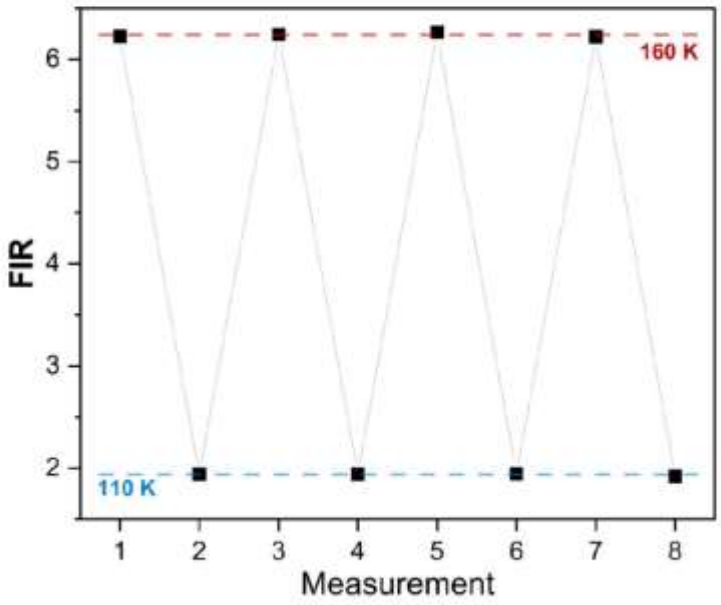

Figure S8. Thermometric stability in 110-160 K intervals for $[EA]_2NaCr_{0.21}Al_{0.79}(HCOO)_6$ sample.

Instruction 1. – crystal field parameters calculation[1,2]

1. The first step was the DRS spectrum deconvolution within the individual ranges of $^4A_{2g} \rightarrow {}^4T_{2g}$ as well as $^4A_{2g} \rightarrow {}^4T_{1g}$. The obtained values of the less-energetic component of each transition range were presented in Table S3. The energies of $^4A_{2g} \rightarrow {}^2E$ transition for each sample were taken directly from the individual spectra. Having regard to the readability of the instruction, the energy parameters were implemented:
   - *E1* – energy of the $^4A_{2g} \rightarrow {}^2E$ transition;
   - *E2* – energy of the $^4A_{2g} \rightarrow {}^4T_{2g}$ transition;
   - *E3* – energy of the $^4A_{2g} \rightarrow {}^4T_{1g}$ transition.

2. The calculations of the crystal field (Dq) were performed as follows:

$$Dq = \frac{E2_i}{10}, \#(1)$$

   where *i* stands for the individual sample (e.g. $E2_{21\ mol.\%} = 16610\ cm^{-1}$)

3. The Racah parameters (B and C) were calculated according to the following formulas:

$$x = \frac{E1_i - E2_i}{Dq}, \#(2)$$

$$B = \frac{Dq}{15(x-8)(x^2-10x)}, \#(3)$$

$$C = \frac{E3_i - 7.9B + \frac{1.8B^2}{Dq}}{3.05} \#(4)$$

4. The crystal field strength is described by the radio of crystal field and the Racah parameter – ***Dq*/*B*.**

The detailed results of the calculations are presented in Table S3.

[1] B. Henderson and G.F. Imbush, *Optical Spectroscopy of Inorganic Solids*, Clarendon Press, Oxford, 1989, ISBN: 0-19-851372-0

[2] B. Henderson and R.H. Bartram, *Crystal-Field Engineering of Solid-State Laser Materials*, Cambridge: Cambridge University Press, 2000, ISBN 0-521-59349-2

10.2 Publication P2

Journal of Materials Chemistry C

ROYAL SOCIETY OF CHEMISTRY

PAPER

View Article Online
View Journal

Cite this: DOI: 10.1039/d3tc04529c

Mechanism of isosymmetric polar order–disorder phase transition in pyroelectric $[CH_3CH_2NH_3]_2NaGa(HCOO)_6$ double perovskite†

Maciej Ptak, *[a] Adam Kabański, [a] Błażej Dziuk, [b] Sergejus Balciunas, [c] Gediminas Usevicius, [c] Jan K. Zaręba, [b] Juras Banys, [c] Mantas Simenas, *[c] Adam Sieradzki [d] and Dagmara Stefańska [a]

Recently, hybrid double-perovskite structures have attracted attention due to their versatile multifunctional properties originating from the variety of different constituent units in these materials. Here, we report the synthesis and comprehensive multitechnique characterization of a novel hybrid double-perovskite formate-based material $[CH_3CH_2NH_3]_2NaGa(HCOO)_6$. The heat capacity measurements indicate that this compound has a structural phase transition at 379 K. In the low-temperature phase, the compound crystallizes in the non-centrosymmetric polar *Pn* structure, which exhibits a long-range order of ethylammonium (EA^+) cations. Surprisingly, the *Pn* space group is not affected by the transition to the high-temperature disordered phase, which indicates that the transitions are isosymmetric making this compound a unique member of the formate-based double-perovskite family. The presence of the second-harmonic generation response in both phases confirms their non-centrosymmetric nature, while the dielectric spectroscopy experiments reveal that the transitions have a continuous order–disorder character. The observation of the pyroelectric current, but the absence of the electric polarization switching indicate that this compound is not properly ferroelectric. The electron paramagnetic resonance experiments of a compound slightly doped with paramagnetic Fe^{3+} impurities confirm the continuous character of the transition and allow us to probe the EA^+ cation and framework dynamics in this system. The vibrational spectroscopy data confirm that the phase transition is primarily driven by the progressive ordering of EA^+ cations and the resulting changes in the hydrogen bond strength. The temperature-dependent luminescence studies show that the $[EA]_2NaCr_{0.931}Ga_{0.069}(HCOO)_6$ perovskite is a promising material for noncontact temperature monitoring.

Received 9th December 2023,
Accepted 22nd February 2024

DOI: 10.1039/d3tc04529c

rsc.li/materials-c

Introduction

Recently, three-dimensional (3D) hybrid organic–inorganic perovskite materials with the formula $AM^{II}X_3$ (A^+ denotes a protonated amine, M^{II} – a divalent metal ion, and X^- –a small organic linker) have gained significant attention due to their structure-based multifunctionalities.[1–5] In some hybrid perovskites, a few intriguing physical phenomena can simultaneously coexist making them appealing for a wide range of applications.[2,5–7] In particular, the simplest halide 3D lead-based perovskites comprising the smallest organic cations, including methylammonium (MA^+),[8–10] fluoromethylammonium (FMA^+),[11] formamidinium (FA^+),[12–14] methylhydrazinium (MHy^+),[15,16] and aziridinium (AZR^+),[17] exhibit excellent optical properties for optoelectronic photovoltaic, light emitting, and lasing applications, including tuneable bandgaps, second-harmonic generation (SHG), excitonic emission, long carrier diffusion lengths, high mobility, and high absorption coefficients.[1,5,18,19] Due to a

[a] Institute of Low Temperature and Structure Research, Polish Academy of Sciences, 50-422 Wroclaw, Poland. E-mail: m.ptak@intibs.pl
[b] Institute of Advanced Materials, Wroclaw University of Science and Technology, 50-370 Wroclaw, Poland
[c] Faculty of Physics, Vilnius University, LT-10257 Vilnius, Lithuania
[d] Department of Experimental Physics, Wroclaw University of Science and Technology, 50-370 Wroclaw, Poland

† Electronic supplementary information (ESI) available: Fig S1–S16: powder XRD, DSC curve, asymmetric parts and packing diagrams, SHG traces, dielectric permittivity, current density, room-temperature Raman spectra, temperature-dependent IR spectra, thermal evolution of selected IR bands, absorption spectra, Tauc plots, emission spectra, FIR ratio; Tables S1–S6: XRD experimental data, selected geometric and hydrogen bond parameters, and assignment of Raman bands. See DOI: https://doi.org/10.5281/zenodo.10624656 (link will be given upon acceptance). CCDC 2254366 and 2254367. For ESI and crystallographic data in CIF or other electronic format see DOI: https://doi.org/10.1039/d3tc04529c

rather scarce choice of molecular cations forming 3D lead halide perovskites and lead toxicity, perovskites with other metal ions and longer organic linkers, such as formates, hypophosphites, azides, cyanides, and dicyanamides, are of considerable relevance.[6,20]

Order–disorder phase transitions (PT) are a common feature in these materials, and they are usually connected with the emergence of phenomena related to the loss of the inversion centre.[21–26] The organic cation A^+ is often involved in the ordering due to the interaction with the 3D framework *via* a network of N–H···X hydrogen bonds (HBs).[20,21,23]

Because of their remarkable ferroelectric, multiferroic, dielectric, magnetic, and optical properties, formate perovskites containing divalent metal ions M^{II} are the most researched group.[6,20–26] Only formates, azides, and cyanides are capable of forming the $A_2M^IM^{III}X_6$ double-perovskite structure, which is comprised of an equimolar ratio of monovalent (M^I) and trivalent (M^{III}) metal ions arranged into an alternately propagating 3D framework of ligand-connected octahedra.[27,28]

There are several members of the $A_2M^IM^{III}(HCOO)_6$ family, where A^+ = ammonium (AM^+), hydrazinium (Hy^+), MA^+, dimethylammonium (DMA^+), ethylammonium (EA^+), imidazolium (IM^+), and guanidinium (GA^+) cations, $M^I = Na^+$, K^+, and $M^{III} = Al^{3+}$, Cr^{3+}, and Fe^{3+}.[27–32] Order–disorder PTs have only been reported for DMA^+ and EA^+ analogues, and the latter compounds have received significant attention due to the density functional theory (DFT) calculations and experimental findings suggesting the presence of ferroelectricity[29] and polarization enhancement under high pressure.[33,34] Its existence, however, has never been proven experimentally for double-perovskite formates.

All known $[EA]_2NaM^{III}(HCOO)_6$ members ($M^{III} = Al^{3+}$, Cr^{3+}, and Fe^{3+}) exhibited PT in the 361–369 K range when heated from the low-temperature (LT) non-centrosymmetric and polar phase *Pn* to the high-temperature (HT) centrosymmetric phase $P2_1/n$. In the HT phase, the EA^+ cations are disordered, and the arrangement of dipole moments prevents the occurrence of polar order.[28–30] Furthermore, the presence of Cr^{3+} ions in the structure predisposes the aforementioned materials to be used as luminescent thermometers, with the crystal field strength being dependent on the applied metal ion ratio.[27] We recently demonstrated $[EA]_2NaCr(HCOO)_6$ as a sensitive thermometer with low operating temperatures.[27]

This work is focused on the structural, dielectric, electric, optical, and phonon properties of a novel analogue, $[EA]_2NaGa(HCOO)_6$. We show that, despite various similarities, the physicochemical properties of this compound stand out in the group, primarily because the HT phase is also polar. As an outcome, the compound displays an extremely rare order–disorder polar–polar PT, which has been reported among formate perovskites only for the subgroup of $[MHy][M^{II}(HCOO)_3]$ (M^{II} = Fe, Mg, Mn, and Zn).[35] The mechanism of this unusual PT is discussed. The investigated perovskite can be used as a non-linear optical switch and a luminescent thermometer.

Experimental

Materials and synthesis

The crystals of $[EA]_2NaGa(HCOO)_6$ (**1**) were synthesized using the solvothermal method described earlier for $[EA]_2NaCr_xAl_{1-x}(HCOO)_6$.[27] All chemicals were purchased and used without further purification. To synthesize **1**, a mixture of *ca.* 4 mmol (*ca.* 1.5 g) of $Ga(NO_3)_3{\cdot}XH_2O$ (Sigma Aldrich, 99.9%), 4 mmol (0.3262 g) of ethylamine hydrochloride (Sigma Aldrich, 98%), and 8 mmol (0.5441 g) of sodium formate (Sigma Aldrich, 99%) was dissolved in 10 mL of distilled water. Next, 25 mL of *N*-ethylformamide (Sigma Aldrich, 99%) and 5 mL of concentrated formic acid (Avantor Poland, 98–100%) were added. The solution was sealed in a Teflon-line autoclave and heated at 140 °C for 24 hours. The obtained liquid was then allowed to slowly evaporate at room temperature (RT). After two days, the crystals were separated, washed with 10 mL of anhydrous methanol (Sigma-Aldrich, 99.8%), and dried in air.

Despite attempts to synthesize a mixed sample with a composition of 25 mol% Cr^{3+} and 75 mol% Ga^{3+}, a sample with much more chromium crystallized. The EDS tests confirmed that we were only able to synthesize a sample composed of *ca.* 6.9 mol% Ga^{3+} and 93.1 mol% Cr^{3+} ions, namely $[EA]_2NaCr_{0.931}Ga_{0.069}(HCOO)_6$ (**2**).

To get more information on the framework contribution to the mechanism of PT, an additional sample comprising a small amount (*ca.* 0.01 mol%) of paramagnetic Fe^{3+} ions (**3**) was prepared in the same manner.

X-ray diffraction

The single crystal of **1** was mounted on a CCD Xcalibur diffractometer (graphite monochromatic, MoKα radiation, λ = 0.71073 Å) at 293(2) K and 391(2) K. The corrections to the Lorentz and polarization factors were applied to the reflection intensities. The structures were solved by direct methods applying the SHELX program. The H atoms were determined from the geometric concepts and refined in a riding model with isotropic temperature factors 1.2 times the U_{eq} value of the parent atom. All non-hydrogen atoms were located from difference Fourier synthesis and refined by the least squares method in the full-matrix anisotropic approximation. The crystallographic data for **1** and details of the X-ray experiment are collected in Table S1 (ESI†). The structure drawings in the ESI† were prepared by using OLEX program.[36]

The CCDC deposits 2254366 (293 K) and 2254367 (391 K) contain the supplementary crystallographic data for **1**.† These data can be obtained free of charge at **https://www.ccdc.cam.ac.uk/structures**.

Powder X-ray diffraction patterns of **1**, **2**, and **3** were collected using an X'Pert Pro X-ray diffraction system fitted with a PIXcel detector, a focusing mirror, and Soller slits for CuKα radiation (λ = 1.54056 Å). Fig. S1 (ESI†) presents a comparison of experimental patterns with a simulated pattern based on structure refinement for **1** at 293 K.

Differential scanning calorimetry (DSC)

The heat capacity of **1** was measured from RT to 400 K using a Mettler Toledo DSC-1 calorimeter with a high resolution of 0.4 μW. Nitrogen was used as a purging gas, and the heating and cooling rates were 5 K min^{-1}. The mass of the measured sample was 6.1 mg. The excess heat capacity associated with the PT was calculated by subtracting from the data a baseline representing the system variation in the absence of PTs.

Second harmonic generation (SHG)

SHG properties were studied using a laser system Coherent Astrella Ti:Sapphire regenerative amplifier providing femtosecond laser pulses (800 nm, 75 fs) at a 1 kHz repetition rate. The laser fluence at the sample was set to 0.28 mJ cm^{-2}. The single crystals of **1** were crushed with a spatula and sieved through an Aldrich mini-sieve set, collecting a microcrystal size fraction of 88–125 μm. Next, size-graded sample of **1** was fixed in-between microscope glass slides to form a tightly packed layer, sealed, and mounted to the horizontally aligned sample holder. No refractive index matching oil was used. The employed measurement setup operates in the reflection mode. Specifically, the laser beam was directed onto the sample at 45 degrees to its surface. Emission collecting optics consisted of a Ø25.0 mm plano-convex lens of focal length 25.4 mm mounted on the 400 μm 0.22 NA glass optical fiber and was placed along the normal to the sample surface. The distance between the collection lens and the sample was equal to 30 mm. The spectra of SHG responses were recorded using an Ocean Optics Flame T XR fiber-coupled CCD spectrograph with 200 μm entrance slit. Scattered pumping radiation was suppressed with the use of a Thorlabs 700 nm hard-coated short-pass dielectric filter. The temperature-dependent SHG study was performed in the 353–403 K range using a Linkam LTS420 Heating/Freezing Stage. Temperature stability was equal to 0.1 K. Kurtz–Perry powder tests were performed at 293 K, using potassium hydrogen phosphate of the same particle size as the SHG reference.

Electronic paramagnetic resonance (EPR) studies

The X-band (9.5 GHz) EPR experiments of the sample **3** were performed using a Bruker ELEXSYS E580 EPR spectrometer. For the EPR measurements, the crystal samples of $[EA]_2NaGa(HCOO)_6$:Fe were ground into a fine powder. For the continuous-wave (CW) EPR experiments, we used 8 G and 100 kHz field modulation. The microwave power was adjusted to avoid saturation of the EPR signal. The pulsed EPR experiments were performed using 32 ns π-pulse duration. The echo-detected field sweep (EDFS) spectra were recorded using a Hahn echo pulse sequence ($\pi/2$–τ–π–τ–echo) with an interpulse delay τ of 200 ns and two-step phase cycling. The three-pulse electron spin echo envelope (ESEEM) time traces were obtained by integrating the echo obtained using the stimulated echo pulse sequence ($\pi/2$–τ–$\pi/2$–τ'–$\pi/2$–τ–echo) with the four-step phase cycling, where the interpulse delay τ' was incremented by a time step of 8 ns. A stretched exponential function was used for background correction.

Dielectric measurements

Dielectric spectroscopy experiments of single crystal and pressed pellet samples of **1** were performed in the 20–10^6 Hz frequency range using an HP4284A LCR meter. The flat capacitor model was used to calculate the complex dielectric permittivity from the measured capacitance and dielectric loss tangent. Silver paste was used for sample electrodes. Temperature-dependent dielectric spectra were measured on cooling at a rate of 1 K min^{-1}.

Pyrocurrent measurements

For the pyrocurrent measurements, the pellet sample of **1** was poled with 50 VDC and cooled down through the PT from 400 K to RT. Afterwards, the poling voltage was removed and the sample was shorted. The pyrocurrent was measured using a 6514 Keithley electrometer during heating at a rate of 1 K min^{-1}.

Electric polarization measurements

An Aixact instrument was used to measure the electric field-dependent electric polarization of a pellet sample of **1**. A periodic triangular signal with a frequency of 100 Hz was used for the measurements. A high voltage was obtained using a Trek 609E6 voltage amplifier.

Vibrational measurements

RT Raman spectra in the range of 3600–80 cm^{-1} of **1** and **2** were measured using a Bruker FT-Raman RFS 100/S spectrometer with a 1064 nm excitation line (YAG:Nd).

The temperature-dependent IR spectra of **1** in the 3250–675 cm^{-1} range were measured using a Nicolet iN10 FTIR microscope and a Linkam THMS600 stage equipped with ZnSe windows.

Optical measurements

The diffuse reflectance spectra of **1** and **2** were collected in the back-scattering geometry using an Agilent Cary 5000 spectrophotometer.

A Hamamatsu PMA-12 photonic multichannel analyzer paired with a BT-CCD sensor was employed to obtain temperature-dependent emission spectra of **2**. As an excitation source, a 405 nm laser diode was used. A Linkam THMS600 stage was employed to regulate the temperature.

Energy-dispersive X-ray spectroscopy (EDS)

The chemical composition of **2** was determined using a FEI NOVA NanoSEM 140 scanning electron microscope.

Results and discussion

Thermal properties

The acquired DSC curve, shown in Fig. S2 (ESI†), demonstrates that **1** undergoes PT at T_C = 379 and 376 K during heating and cooling, respectively. A small temperature hysteresis of 2 K as well as the lambda-shaped change in ΔC_p and a gradual change

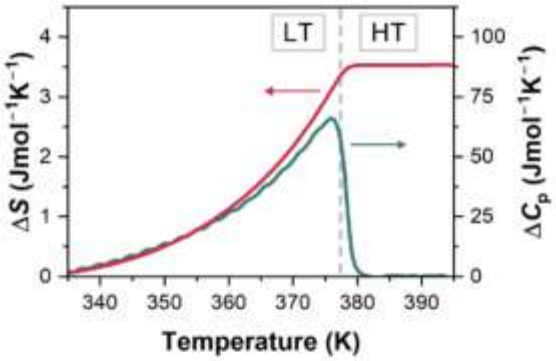

Fig. 1 (a) Temperature dependence of the excess heat capacity (ΔC_p) and change in entropy (ΔS) obtained for **1**.

in ΔS associated with this PT shown in Fig. 1 imply that this transformation has a second-order (continuous) nature. The estimated value of change in entropy ΔS (3.5 J mol^{-1} K^{-1}) is similar to that reported for the $[EA]_2NaM^{III}(HCOO)_6$ (M^{III} = Al^{3+}, Cr^{3+}, Fe^{3+}) analogues (2.0–5.0 J mol^{-1} K^{-1}),[29,30] indicating a similar order–disorder mechanism of PTs (see the comparison of thermal parameters in Table S2, ESI†).

Assuming that $\Delta S = R \ln N$, where R denotes the gas constant, and N specifies the ratio of disordered states in the HT and LT phases, respectively, the calculated N for **1** is 1.6. This value is slightly lower than that obtained from our X-ray diffraction data (see below), revealing that EA^+ cations in **1** display two-fold disorder in the HT phase and become ordered below the T_C (N = 2). This mismatch indicates that the deformation of the metal-formate framework triggered by the ordering of EA^+ cations is equally significant.

Single-crystal X-ray diffraction

The structure of **1** has been determined at 293 and 391 K. Both, the HT and LT phases belong to the monoclinic system, non-centrosymmetric and polar space group *Pn* at 293 and 391 K. Table S1 (ESI†) contains the experimental data regarding the single-crystal structure determination. Table S3 (ESI†) provides the geometrical parameters for both phases.

In the HT phase, the asymmetric part of the unit cell consists of two metal ions (Ga^{3+} and Na^+) surrounded by six formate ($HCOO^-$) linkers and two protonated EA^+ cations (see Fig. 2 and Fig. S3, ESI†). The metal centres are connected through formate linkers in the anti–anti mode configuration forming a 3D network with pseudo-cubic voids. The cavities are occupied by EA^+ cations joined to the framework by stronger N–H···O and weaker C–H···O HBs (Table S4, ESI†). The organic cations are dynamically disordered in two positions (Fig. 2a and Fig. S3 and S4, ESI†). The crystal structure is very similar to previously studied $[EA]_2NaM^{III}(HCOO)_6$ (M^{III} = Al^{3+}, Cr^{3+}, Fe^{3+}) members with disordered HT phases, in which dipole moment alignment leads to the disappearance of polar properties in the HT centrosymmetric $P2_1/n$ phase.[29,30] In contrast, the HT phase of **1** remains non-centrosymmetric despite the similar disorder of EA^+ cations.

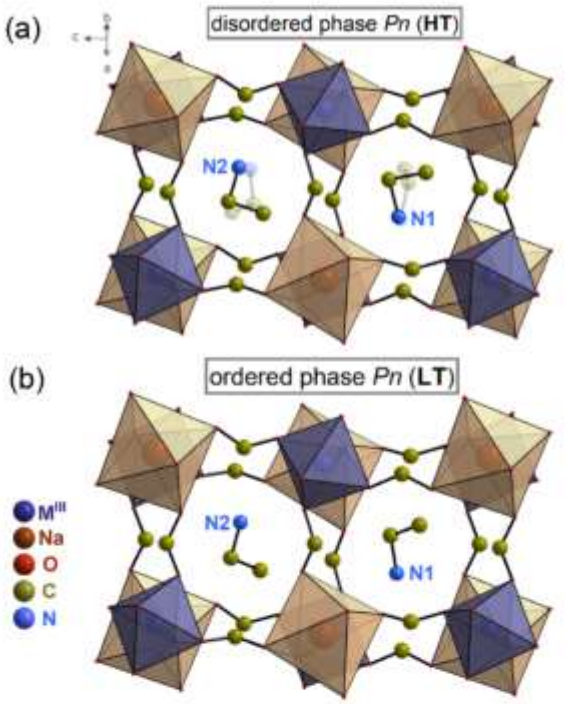

Fig. 2 Structures of **1** at (a) 391 K (disordered phase) and (b) 293 K (ordered phase). The M^{III} label stands for Ga^{3+}/Fe^{3+}/Cr^{3+}.

Lowering the temperature below 377 K causes the organic cations to order. The asymmetric unit in the LT phase has remained mostly unaltered. However, the PT strongly affects the HB network, as the donor–acceptor distances (D···A) are in the 2.865(5)–3.277(5) Å range for the LT phase and 2.85(4)–3.444(19) Å range for the HT phase (see Table S4, ESI†).

The distortion of octahedral coordination in both phases is depicted in bond lengths and valence angles (see Tables S2 and S3, ESI†). At 293 K, the Ga–O distances range from 1.965(3) Å to 1.987(3) Å, while the Na–O from 2.385(5)–2.531(4) Å, resulting in the bond length distortion indexes Δ of 0.0040 and 0.0196 for the GaO_6 and NaO_6 octahedra, respectively. The corresponding bond angle variances σ^2 are equal to 1.77 and 17.04 deg^2, respectively, implying that the NaO_6 octahedra are more distorted in the LT phase compared to the GaO_6 ones. The increase of temperature to 391 K results in a decrease of Δ (0.0027) and σ^2 (1.42 deg^2) for GaO_6, making it less distorted. In contrast, for NaO_6 the Δ parameter slightly increases to 0.0231, while σ^2 is decreased to 12.06 deg^2. Taking into account the Δ and σ^2 parameters for all members of the $[EA]_2NaM^{III}(HCOO)_6$ family, the crystals of **1** are composed of the most distorted NaO_6 and $M^{III}O_6$ octahedra (Table S2, ESI†).

Second harmonic generation

Temperature-dependent SHG study was performed by illumination of **1** with 800 nm femtosecond laser pulses in the 354–403 K temperature range. The temperature plot of integral intensities of

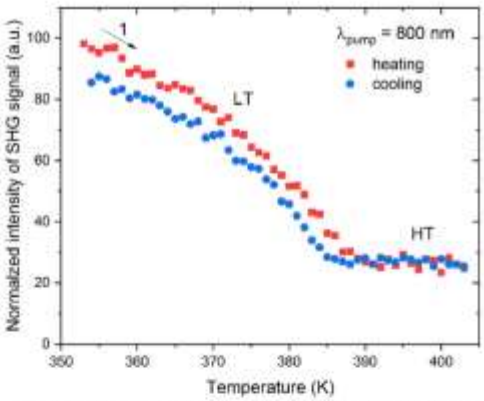

Fig. 3 Integral intensities of the SHG signal of **1** for heating (red squares) and cooling (blue squares) runs.

the SHG signal of **1** is shown in Fig. 3, while the experimental spectra are provided in Fig. S5 (ESI†). It is apparent that both LT and HT phases show the SHG response, confirming a non-centrosymmetric nature of these phases. Moreover, one also sees a gradual decrease in the SHG intensity with increasing temperature (LT phase) with an inflection at around 387 K, above which the SHG response stays flat (HT phase). There is also a negligible temperature hysteresis for heating and cooling runs. These features indicate the continuous character of the transition between the two acentric phases, in line with the DSC studies. From the quantitative perspective, the amplitude of the SHG response is rather moderate. A Kurtz–Perry powder test[37] using a size-graded sample of **1** at 293 K shows that the SHG response is 0.01 *versus* a KDP reference of the same particle size, see Fig. S6 (ESI†).

Dielectric properties

The temperature dependence of the real ε' and imaginary ε'' parts of the complex dielectric permittivity ($\varepsilon^* = \varepsilon' - i\varepsilon''$) a single crystal sample of **1** is presented in Fig. 4. A sharp anomalous increase of ε^* can be observed at 380 K (Fig. 4) due to the isosymmetric phase transition in good agreement with the DSC and SHG results. A similar anomalous behaviour is also observed for the pressed pellet sample (see Fig. S7a, ESI†). Note that we did not observe any additional dielectric anomalies, which can be associated with the phase transitions down to 5 K temperature (Fig. S7b, ESI†). The overall dielectric response is similar to that of the related $[EA]_2NaFe(HCOO)_6$ compound.[29]

We analysed the dielectric anomaly using the Curie–Weiss law $\varepsilon' = C/(T - T_C)$, where C is the Curie–Weiss constant and T_C denotes the phase transition temperature.[38] It follows from this equation that $1/\varepsilon'$ should linearly depend on temperature, which is indeed observed in our dielectric data (see inset in Fig. 4a). The values of the determined Curie–Weiss constants in the ordered and disordered phases are 101 K and 195 K, respectively. Both values are close to the value of the transition temperature confirming the order–disorder nature of the

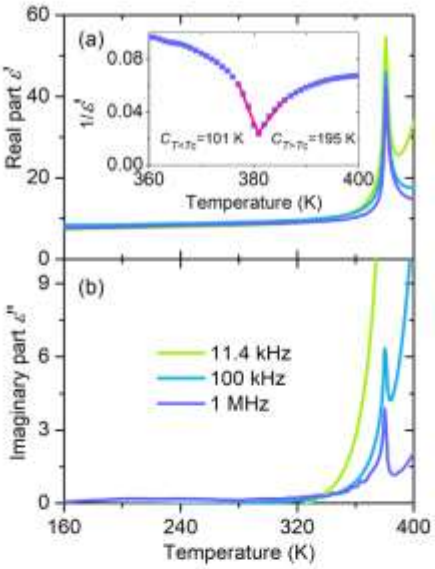

Fig. 4 Temperature dependence of the (a) real and (b) imaginary parts of the complex dielectric permittivity of a single crystal sample of **1** obtained at selected frequencies. The inset in (a) shows the $1/\varepsilon'$ *vs.* temperature plot, where the linear fits (solid lines) correspond to the Curie–Weiss fits above and below the phase transition point.

transition.[38] In addition, the ratio of the Curie–Weiss constants $C(T > T_C)/C(T < T_C)$ is very close to 2 indicating a second-order (continuous) phase transition in agreement with the DSC and SHG results.[38]

Pyrocurrent and polarization measurements

The temperature-dependent pyrocurrent density of a pellet sample of **1** obtained after the background correction (see Fig. S8, ESI†) is presented in Fig. 5a. A clear maximum at the phase transition point can be observed, which indicates the pyroelectric nature of the compound. The corresponding electric polarization is also presented in Fig. 5a showing a typical behaviour at the phase transition point observed in other formate-based hybrid perovskites.[39–41]

The pyrocurrent response shows that the studied system is pyroelectric, but it is not sufficient to prove the ferroelectric behaviour. A ferroelectric compound should exhibit a ferroelectric hysteresis loop, *i.e.* switching of the electric polarization with the external electric field.[38] The obtained electric field dependent polarization of a pellet sample of **1** at 296 and 360 K is presented in Fig. 5b showing typical 'banana' loops of a slightly conducting compound[42] and the absence of ferroelectric switching. This indicates that the studied compound is not ferroelectric or that the moderate amplitude of the driving field (22 kV cm^{-1}) is insufficient to switch the polarization.

EPR

We further employed CW and pulsed EPR spectroscopy on the sample doped with a small amount of paramagnetic Fe^{3+} ions

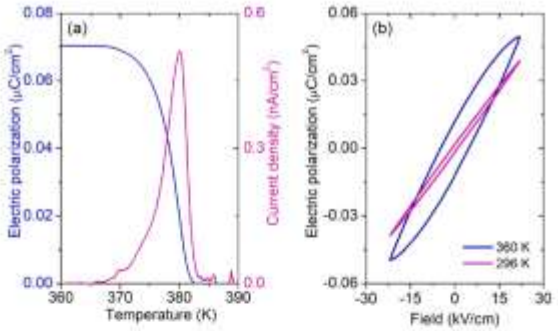

Fig. 5 (a) Temperature dependence of the pyrocurrent and corresponding electric polarization of a pellet sample of **1**. (b) Electric field dependence of the electric polarization of **1** pellet sample obtained at 296 and 360 K.

to further probe the phase transition and dynamic properties of $[EA]_2NaGa(HCOO)_6$. The measured EDFS (10 K) and CW EPR spectra a sample of **3** show a typical powder pattern of high-spin Fe^{3+} ions[43] (Fig. 6a). The Fe^{3+} centre has $3d^5$ electronic configuration and, in the high-spin state, it has five unpaired electrons leading to the total electron spin of $S = 5/2$. In a non-cubic environment, this ion is expected to have a substantial zero-field splitting providing a complicated fine structure pattern observed in the measured spectra of **3**.

The temperature dependence of the CW EPR linewidth of Fe^{3+} centres in **3** is presented in Fig. 6b. Upon temperature increase in the low-temperature phase, the linewidth exhibits a significant broadening and peaks at 377 K indicating the structural phase transition in agreement with other methods. Similar behaviour of the EPR linewidth was observed in a number of different systems (including hybrid perovskites) exhibiting ferroelectric and related structural phase transitions, and it was assigned to the critical dynamics of the order parameter fluctuations.[44–47] The measured anomaly also indicates that the Fe^{3+} ions are susceptible to the local changes of the $[EA]_2NaGa(HCOO)_6$ lattice occurring during the phase transition, which confirms the successful incorporation of these ions in this material.

We analysed the temperature dependence of the CW EPR linewidth in the low-temperature phase in more detail assuming that the broadening process follows the Arrhenius law: $\Gamma - \Gamma_0 = \Gamma_\infty e^{-E_a/kT}$. Here, E_a is the activation energy of a dynamic process, k is the Boltzmann constant, and Γ_0 and Γ_∞ denote the linewidth in the low and high temperature limits, respectively. Using Γ_0 = 1.2 mT (low temperature limit), our analysis provides E_a = 204(12) meV (see the inset in Fig. 6b), which is in the range of typical values for molecular cation motion observed in different hybrid perovskites such as $[DMA]Zn(HCOO)_3$ (266 meV)[48] and $MAPbI_3$ (80 meV).[49] Thus, the broadening of the Fe^{3+} signal with increasing temperature may be related to the enhanced EA^+ cation motion, as it directly couples to the inorganic framework *via* the H-bonds.

We used pulsed EPR spectroscopy to further investigate the local Fe^{3+} ion environment in **3**. The magnetic field dependence of the three-pulse ESEEM spectrum in the low-frequency region is presented in Fig. 7 revealing a well-resolved peak with frequency linearly dependent on the magnetic field. Such a signal belongs to a nucleus with non-zero nuclear spin in close vicinity of the Fe^{3+} centre. The slope of the signal occurring corresponds to the gyromagnetic ratio of ^{23}Na nucleus. ^{38}We have not detected any ESEEM signals from ^{69}Ga and ^{71}Ga isotopes indicating that Ga^{3+} ions are significantly more distant than Na^+ from the iron impurity. Based on the crystal structure of **1**, these results confirm that Fe^{3+} substitutes Ga^{3+} in the lattice and forms FeO_6 octahedra.

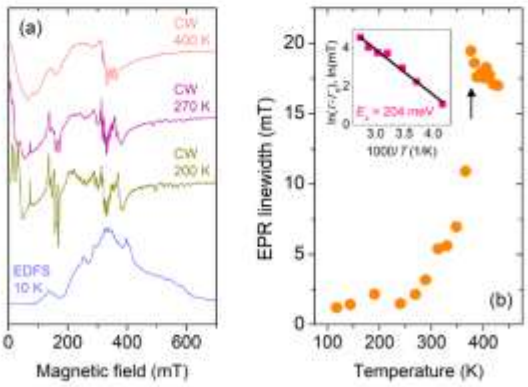

Fig. 6 (a) EDFS (10 K) and CW (200, 270, and 400 K) EPR spectra of the Fe^{3+} centres in **3**. (b) Temperature dependence of the CW EPR linewidth (at 70 mT) of the Fe^{3+} centres in **3** indicating the phase transition at 377 K (arrow). Inset in (b) shows the Arrhenius-type temperature dependence of the EPR linewidth. Error bars in (b) are about the size of the data points.

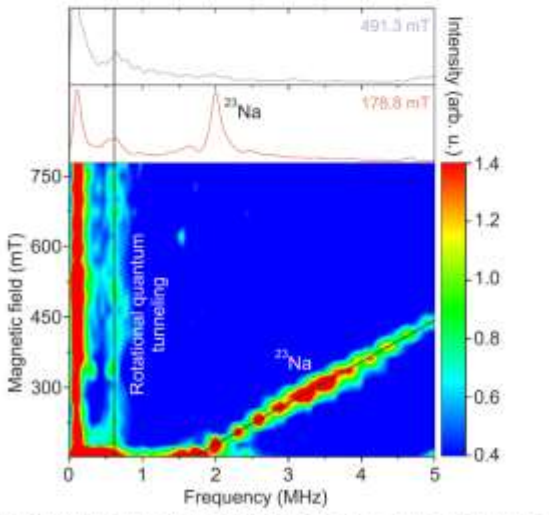

Fig. 7 Colour plot of the three-pulse ESEEM spectrum *vs.* magnetic field of **3** obtained at 10 K and τ = 130 ns. The field-dependent signal of ^{23}Na is indicated in the plot. The field-independent signal at about 0.6 MHz is assigned to methyl group quantum rotational tunnelling of the EA^+ cation.

Fig. 7 also shows a couple of ESEEM signals below 1 MHz, which are independent of the magnetic field. The origin of the weaker signal at about 0.61 MHz can be assigned to the quantum rotational tunneling of methyl groups of the EA^+ molecular cation. Note that such a field-independent ESEEM effect has recently been observed in Mn- and Co-doped $[DMA]Zn(HCOO)_3$,[50,51] and Mn-doped $[DMA]Cd(N_3)_3$[50] hybrid perovskites, as well as nitroxide radicals.[52] The current work provides the first signatures of this effect detected with a paramagnetic Fe^{3+} centre. The stronger signal occurring at much lower frequency of 0.1 MHz may originate from the NH_3 group tunneling, as, due to the stronger H-bonds, these groups are expected to have a higher rotational barrier (lower tunneling frequency) compared to the CH_3 groups. Note that we also cannot rule out that the origin of this low frequency signal is imperfect background correction of the time-domain ESEEM data. The EPR measurements of the samples containing partially deuterated EA^+ cations are needed to unambiguously determine the origin of these field-independent signals.

The frequency at which the tunnelling signal appears can be used to estimate the rotation barrier of the CH_3 and NH_3 groups in $[EA]_2NaGa(HCOO)_6$ by diagonalizing the rotational Hamiltonian on the basis of the free quantum rotor.[53] The obtained barrier for the CH_3 group is 12.1 kJ mol^{-1}, which is similar in value to the energies obtained for methyl group rotation in DMA-containing hybrid perovskites.[50,51] Assuming that the low-frequency signal originates from the NH_3 groups, a rough estimate for the NH_3 group rotational barrier gives $\sim$18 kJ mol^{-1}. In the calculations, we used rotational constants $B(CH_3)$ = 0.655 meV and $B(NH_3)$ = 0.782 meV.[54]

Phonon properties

We further used vibrational spectroscopy to study the phonon properties of $[EA]_2NaGa(HCOO)_6$. Fig. S9 (ESI†) compares the Raman spectra of **1** and **2** obtained at room temperature. Table S5 (ESI†) includes Raman band assignment based on published data for $[EA]_2NaM^{III}(HCOO)_6$ (M^{III} = Al^{3+}, Cr^{3+}, and Fe^{3+}).[29,30] Because the doping level of Ga^{3+} in **2** is as low as 6.9 mol%, the Raman spectrum is roughly comparable to that reported earlier for the pure $[EA]_2NaCr(HCOO)_6$ compound.[30]

When Cr^{3+} ions are replaced with Ga^{3+} ions, a number of bands move due to differences in weights and electronegativity; gallium ions are approximately 34% heavier at almost the same ionic radius, and Ga–O bonds are more ionic than Cr–O bonds. The most significant change among internal vibrations is 5 cm^{-1}, whereas the highest shift among the lattice modes involving M^{III} translations is up to 12 cm^{-1}.

IR spectra were obtained as a function of temperature to better understand the mechanism of the PT occurring in **1** (see Fig. 8 and Fig. S10, ESI†). The assignments of IR bands at 80 and 400 K are summarized in Table S6 (ESI†). As shown by the results, the number of observed bands at 80 K is significantly higher than those at room temperature and at temperatures corresponding to the HT phase (above 380 K). Since for both phases, the space group symmetry of the cell does not vary, the number of expected phonon modes for the crystal **1**

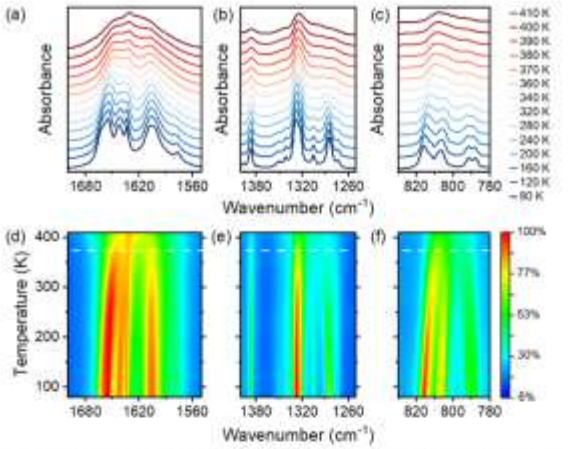

Fig. 8 Temperature-dependent IR spectra measured for **1** (a)–(c) and the corresponding contour maps of intensity (d)–(f). Horizontal dashed lines in (d)–(f) correspond to the PT temperature.

also remains the same. Thus, the large number of bands at low temperatures can only be attributable to strong narrowing and better separation of closely laid bands. Such narrowing is a common effect observed for order–disorder transformations, and it confirms the nature of the observed PT.[55,56]

Fig. 8a and d present the temperature evolution of bands corresponding to bending modes of NH_3 groups that coincide with antisymmetric OCO stretching. In the HT phase, all bands in this range merge into a very broad contour. The map presented in Fig. 8d exhibits that the intensity decreases quicker above the PT temperature. The disorder of HBs in the HT phase also contributes to the severe half-width of the bands. Similar substantial broadening is also observed for IR bands in the 1250–1400 cm^{-1} range, which correspond to alkyl chain bending modes and formate ligand stretching vibrations. (Fig. 8b).

Fig. 8c and f present the thermal evolution of bands that result from the OCO bending vibrations. Fig. S11a (ESI†) depicts the fitting of those bands. The abrupt shifts and the disappearance of bands in the HT phase are caused by the fitting procedure, in which the usage of the same number of bands in both phases fails to produce satisfactory results. Nonetheless, significant shifts in maxima and differences in the intensity of band contours imply a more deformed metal-formate framework in the LT phase.

The structural, thermal, dielectric, and EPR data demonstrate that the spectral changes are continuous (Fig. 8 and Fig. S10 and S11, ESI†). As a result, cation ordering does not occur abruptly but rather is a gradual process that still occurs below the PT temperature. This behavior can be demonstrated by thermal changes in bands corresponding to rocking modes of protonated amine groups and alkyl chain vibrations (Fig. S11b, ESI†). They remain quite broad (Fig. S11c, ESI†) at the PT temperature, and their narrowing upon cooling is still observed down to 80 K. The corresponding intensity changes

are also continuous over the entire range of measured temperatures (Fig. S11d, ESI†).

Optical properties

Finally, we investigated the optical properties of $[EA]_2NaGa(HCOO)_6$. Fig. S12 (ESI†) presents the absorption spectra of crystals of **1** and **2**. As can be seen, the spectrum of the sample containing Cr^{3+} ions consists of two broad bands centered at around 17 265 cm^{-1} (579 nm) and 24 035 cm^{-1} (416 nm) attributed to spin-allowed $^4A_{2g} \rightarrow {}^4T_{2g}$ and $^4A_{2g} \rightarrow {}^4T_{1g}$ transitions, respectively. The low intense and narrow band localized at 14 571 cm^{-1} (686 nm) is characteristic of the R_1 line of the spin-forbidden $^4A_{2g} \rightarrow {}^2T_{2g}$ transition. The sample of **1** does not contain any absorption bands in the given range.

Using the diffuse reflectance spectrum, it is possible to determine the energy band gap (E_g) of investigated samples by applying the Kubelka–Munk relation.[57] The E_g for **1** equals 5.04 eV and is comparable with the band gap (5.09 eV) of the recently reported $[EA]_2NaAl(HCOO)_6$ (Fig. S13, ESI†).[27] The analogue comprising Cr^{3+} ions **2** has a much lower E_g of 4.71 eV. The decreasing energy band gap with increasing concentrations of Cr^{3+} has been reported lately for similar compounds.[27,58]

In sample **2**, Cr^{3+} ions are positioned in the octahedral sites. The low-temperature (80 K) emission spectrum contains a few sharp and narrow bands that span from 679 nm to 778 nm (Fig. S14, ESI†). The most intense line centered at 686 nm (14 577 cm^{-1}) is attributed to the spin-forbidden $^2E_g \rightarrow {}^4A_{2g}$ transition and is called the R line.[32,58,59] The band localized at 697 nm (14 347 cm^{-1}) belongs to the N line and can be assigned to the Cr^{3+}–Cr^{3+} pair line.[30,32,59] Moreover, some anti-Stokes phonon side bands of the R line are visible in the range of 707–778 nm.[60] Similar behavior has been reported recently for other formate analogues with Cr^{3+} ions.[32,58,59] Careful analysis shows a less intense and wide emission band extending up to 1000 nm, which can be attributed to the spin-allowed $^4T_{2g} \rightarrow {}^4A_{2g}$ transition (Fig. S14, ESI†).

Based on the absorption and emission spectra, the crystal field (D_q) and Racah parameters (B and C) were calculated according to the previously applied methodology.[30,59,61] The calculated values are presented in Table 1. The ratio of D_q/B = 2.35 indicates that Cr^{3+} ions are positioned in a strong crystal field. This value is very close to the 2.3 point on the Tanabe–Sugano diagram for the d^3 configuration, where the ^2E_g and $^4T_{2g}$ levels overlap and separate the areas of $D_q/B < 2.3$ and $D_q/B > 2.3$ corresponding to weak and strong crystal fields, respectively. The obtained values as well as the experimental data show that the ^2E_g energy level is located below the $^4T_{2g}$ state (Fig. 9a and b), and the energy separation between these

Table 1 Energy band gap and crystal field parameters of the investigated formate perovskites

Sample	E_g (eV)	D_q/B	B (cm^{-1})	C (cm^{-1})	C/B
1	5.04	—	—	—	—
2	4.71	2.35	689	3157	4.6

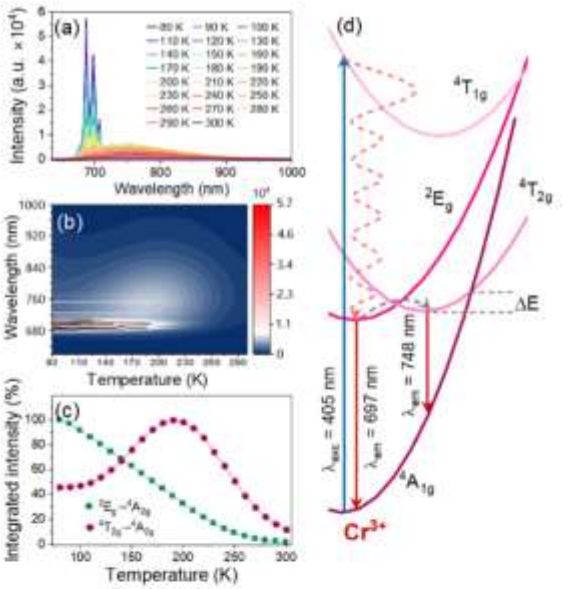

Fig. 9 (a) Temperature-dependent emission spectra of **2**. (b) thermal evolution of the measured intensity at various temperatures, (c) integrated emission intensity of the spin-forbidden and spin-allowed transitions, and (d) the schematic energy level diagram of Cr^{3+} ions.

two levels is not large. It was mentioned that even at 80 K, residual emission from the $^4T_{2g}$ level is visible and becomes stronger upon heating. Careful analysis showed that the intensity of the spin-forbidden transition decreases significantly with rising temperature, while the broad emission associated with the $^4T_{2g} \rightarrow {}^4A_{2g}$ transition becomes stronger up to 190 K (Fig. 9a–c). This phenomenon is related to the temperature-stimulated energy transfer from the lower ^2E_g level to the $^4T_{2g}$ higher state. Above 190 K, the regular temperature quenching process occurs *via* the intercrossing of the $^4T_{2g}$ excited state with the $^4A_{2g}$ ground state parabolas (Fig. 9d).

The significant changes in the emission intensity of both spin-forbidden and spin-allowed transitions can be an attractive feature for luminescence thermometry applications. Recently, the potential of hybrid organic–inorganic compounds with a perovskite-type architecture containing Cr^{3+} ions for temperature detection based on the fluorescence intensity ratio (FIR) of two emission bands was reported.[27,62] In the investigated Cr^{3+}-doped perovskite, FIR parameter Δ can be defined as a ratio of the $^2E_g \rightarrow {}^2A_{2g}$ (660–718 nm) to the $^4T_{2g} \rightarrow {}^4A_{2g}$ (718–970 nm) (Fig. S15, ESI†) transitions of the Cr^{3+} ions. It is not surprising that FIR decreases with an increase in temperature (Fig. S16, ESI†). To further compare the luminescence thermometry performance, the absolute (S_a) and relative (S_r) sensitivities, as well as the temperature uncertainty (δT) were calculated as follows: $S_a = |\partial\Delta/\partial T|$, $S_r = 1/\Delta|\partial\Delta/\partial T|$, and $\delta T = 1/S_r|\delta\Delta/\Delta|$, where $\partial\Delta$ symbolizes the changes of Δ at ∂T temperature change.

The fluorescence intensity ratio curve was fitted using the following equation: $\Delta T = A/(1 + \alpha\exp(-\Delta E/k_B T)$ (Fig. S15, ESI†).

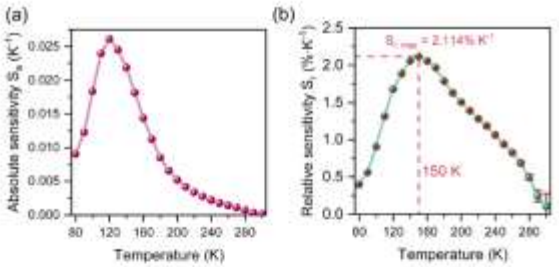

Fig. 10 (a) The absolute sensitivity (S_a) and (b) relative sensitivity (S_r) of optical thermometer **2**. The temperature uncertainty (δT) is presented on the graph (b) as error bars.

Table 2 Comparison of the highest relative sensitivity (S_r) at operating temperature (T) of selected luminescent thermometers

Compound	S_r (% K^{-1})	T (K)	Ref.
Coordination polymers			
$[EA]_2NaCr_{0.21}Al_{0.79}(HCOO)_6$	2.84	160	27
2	2.11	150	
$[GA]Mg(HCOO)_3$:1% Cr^{3+}	2.08	90	62
$[GA]Mn(HCOO)_3$:3% Cr^{3+}	1.20	100	62
$[GA]Zn(HCOO)_3$:1% Cr^{3+}	1.08	90	62
Inorganic compounds			
$ZnGa_2O_4$:Cr^{3+}	2.8	310	65
La_2MgTiO_6:Cr^{3+}, V^{4+}	1.96	165	66
La_3MgTiO_6:Cr^{3+}, Mn^{4+}	1.74	220	67
$Sr_2MgAl_{22}O_{36}$:Cr^{3+}	1.7	310	68
$Bi_2Al_4O_9$:Cr^{3+}	1.24	290	69
$MgTiO_3$:Mn^{4+}	1.2	93	70
$SrAl_{12}O_{19}$:Mn^{4+}	0.27	393	71

The temperature dependencies of S_a and S_r are presented in Fig. 10. First, upon heating, the sensitivity increases with temperature and reaches the maximum S_r value of 2.11% K^{-1} at 150 K (Fig. 10b). Then capability of temperature readout decreases as the temperature increases. However, the sensitivity above 0.5% K^{-1} can be achieved in the broad temperature range from 90 to 280 K. The sensitivity of perovskite **2** is comparable with the S_r parameter obtained for other formate analogues with the EA^+ and GA^+ cations.[27,62] The summary of the S_r parameters of various luminescent thermometers is shown in Table 2.

The thermometric performance of the Cr^{3+}-based materials might also be extended by combining the presented approach with the SHG signal. Such a strategy of temperature sensing has been successfully used for lanthanide-based nanoparticles and MOFs.[63,64] However, due to the overlap of the SHG excitation wavelength with Cr^{3+} emission bands, this particular method has not been applied in this study.

Conclusions

A solvothermal method has been employed to successfully synthesize a novel double perovskite $[CH_3CH_2NH_3]_2NaGa(HCOO)_6$. Our multitechnique characterization approach revealed that this compound exhibits a phase transition at about 379 K. We also synthesized its analogues doped with approximately 0.1 mol% Fe^{3+} ions to study the effects of phase transition on the metal-formate framework and those doped with roughly 93.1 mol% Cr^{3+} to estimate the usefulness for non-contact temperature sensing. The powder X-ray diffraction, Raman and EPR studies confirmed the phase purity and that the dopant ions are located at expected sites in the crystal structure.

The single-crystal X-ray diffraction studies of $[CH_3CH_2NH_3]_2NaGa(HCOO)_6$ revealed that the high-temperature phase comprises disordered EA^+ cations in two different positions. Below the phase transition temperature, they start to order, resulting in a modification of the H-bond network and deformation of the metal-formate framework. According to the XRD results, both phases are represented by a non-centrosymmetric and polar *Pn* monoclinic space group. Such an isosymmetric order–disorder polar phase transition is extremely unusual among formates. The SHG measurement confirmed the continuous character of the transition and the acentric nature of both phases.

The dielectric spectroscopy experiments revealed that the phase transition is of the order–disorder character. The pyrocurrent and electric polarization loop measurements demonstrated that $[CH_3CH_2NH_3]_2NaGa(HCOO)_6$ is pyroelectric, but not a proper ferroelectric, as we did not observe polarization switching (polarization hysteresis). We note that such a behavior is rather typical for formate-based perovskites.

We also employed EPR spectroscopy to probe the phase transition and dynamic effects in $[CH_3CH_2NH_3]_2NaGa(HCOO)_6$ enriched with a tiny amount of paramagnetic Fe^{3+} ions. Our CW EPR experiments confirmed the continuous character of the phase transition and allowed us to probe the dynamics of the inorganic framework. The pulsed EPR ESEEM experiments confirmed that the iron ions were successfully incorporated at the Ga^{3+} sites in the lattice. We also observed ESEEM signals independent of the magnetic field, which were assigned to the quantum rotational tunneling dynamics of the CH_3 and NH_3 groups of the EA^+ cation. This allowed us to estimate the rotational barriers of these rotors in $[CH_3CH_2NH_3]_2NaGa(HCOO)_6$.

IR investigations confirmed the nature of the observed phase transition and helped to clarify that the EA^+ cation ordering does not occur abruptly but rather is a gradual process that still occurs below the phase transition temperature. The narrowing of IR bands corresponding to vibrations of atoms involved in H-bonding demonstrated that there is still some degree of disorder at 80 K.

The linear optical results revealed that $[CH_3CH_2NH_3]_2NaGa(HCOO)_6$ has a wide bandgap of 5.04 eV. The analogue, composed mainly of Cr^{3+} ions, exhibited a substantially lower bandgap value of 4.71 eV. The estimated Racah parameters showed that Cr^{3+} ions are positioned in a strong crystal field, which was applied to evaluate the utility of the Cr-doped material for non-contact temperature monitoring. Based on the temperature-dependent luminescence, the maximum relative sensitivity (2.11% K^{-1}) was reached at 150 K, and this value is comparable to other hybrid and inorganic materials.

Author contributions

Conceptualization, M. P., A. K., and M. S.; formal analysis, M. P., A. K., B. D., S. B., G. U., M. S., and D. S.; funding acquisition, D. S. and M. S.; investigation, M. P., A. K., B. D., S. B., G. U., J. K. Z., M. S., and A. S.; methodology, M. P. and M. S.; project administration, D. S. and M. S.; resources, M. S., D. S.; supervision, J. B., D. S., and M. S.; validation, M. P., M. S., and D. S.; visualization, M. P., A. K., B. D., S. B., G. U., M. S., and D. S.; writing – original draft, M. P., A. K., B. D., S. B., G. U., J. K. Z., M. S., A. S., and D. S.; writing – review & editing, M. P. and M. S.

Conflicts of interest

There are no conflicts to declare.

Acknowledgements

This research was founded by the National Science Centre, Poland, under project no. UMO-2020/39/D/ST5/01289. This project was funded by the Research Council of Lithuania (LMTLT) (agreement no. S-MIP-22-73). The authors would like to thank Dr Damian Szymański for performing the EDS tests, Ewa Bukowska for measurements of powder XRD patterns, and Dr Bogusław Macalik for measurements of diffuse reflectance spectra. JKZ acknowledges support from *Academia Iuvenum*, Wroclaw University of Science and Technology. For the purpose of open access, the author has applied a CC-BY public copyright license to any Author Accepted Manuscript (AAM) version arising from this submission.

References

1 X. Zhao, J. D. A. Ng, R. H. Friend and Z. K. Tan, Opportunities and Challenges in Perovskite Light-Emitting Devices, *ACS Photonics*, 2018, **5**, 3866–3875, DOI: **10.1021/acsphotonics.8b00745**.

2 B. Saparov and D. B. Mitzi, Organic-Inorganic Perovskites: Structural Versatility for Functional Materials Design, *Chem. Rev.*, 2016, **116**, 4558–4596, DOI: **10.1021/acs.chemrev.5b00715**.

3 W. Li, Z. Wang, F. Deschler, S. Gao, R. H. Friend and A. K. Cheetham, Chemically Diverse and Multifunctional Hybrid Organic-Inorganic Perovskites, *Nat. Rev. Mater.*, 2017, **2**, 1–18, DOI: **10.1038/natrevmats.2016.99**.

4 J. Y. Kim, J. W. Lee, H. S. Jung, H. Shin and N. G. Park, High-Efficiency Perovskite Solar Cells, *Chem. Rev.*, 2020, **120**, 7867–7918, DOI: **10.1021/acs.chemrev.0c00107**.

5 F. Wang, Y. Cao, C. Chen, Q. Chen, X. Wu, X. Li, T. Qin and W. Huang, Materials toward the Upscaling of Perovskite Solar Cells: Progress, Challenges, and Strategies, *Adv. Funct. Mater.*, 2018, **28**, 1803753, DOI: **10.1002/adfm.201803753**.

6 H. L. B. Boström, M. S. Senn and A. L. Goodwin, Recipes for Improper Ferroelectricity in Molecular Perovskites, *Nat. Commun.*, 2018, **9**(1), 1–7, DOI: **10.1038/s41467-018-04764-x**.

7 J. Huang, Y. Yuan, Y. Shao and Y. Yan, Understanding the Physical Properties of Hybrid Perovskites for Photovoltaic Applications, *Nat. Rev. Mater.*, 2017, **2**, 1–19, DOI: **10.1038/natrevmats.2017.42**.

8 A. Capitaine and B. Sciacca, Monocrystalline Methylammonium Lead Halide Perovskite Materials for Photovoltaics, *Adv. Mater.*, 2021, **33**, 1–38, DOI: **10.1002/adma.202102588**.

9 Y. He, K. Zheng, P. F. Henry, T. Pullerits and J. Chen, Direct Observation of Size-Dependent Phase Transition in Methylammonium Lead Bromide Perovskite Microcrystals and Nanocrystals, *ACS Omega*, 2022, **7**, 39970–39974, DOI: **10.1021/acsomega.2c04503**.

10 K. Schötz, A. M. Askar, A. Köhler, K. Shankar and F. Panzer, Investigating the Tetragonal-to-Orthorhombic Phase Transition of Methylammonium Lead Iodide Single Crystals by Detailed Photoluminescence Analysis, *Adv. Opt. Mater.*, 2020, **17**, 1–9, DOI: **10.1002/adom.202000455**.

11 S. Huang, P. Huang, L. Wang, J. Han, Y. Chen and H. Zhong, Halogenated-Methylammonium Based 3D Halide Perovskites, *Adv. Mater.*, 2019, **31**, 1–5, DOI: **10.1002/adma.201903830**.

12 Z. A. Nan, L. Chen, Q. Liu, S. H. Wang, Z. X. Chen, S. Y. Kang, J. B. Ji, Y. Y. Tan, Y. Hui, J. W. Yan, Z. X. Xie, W. Z. Liang, B. W. Mao and Z. Q. Tian, Revealing Phase Evolution Mechanism for Stabilizing Formamidinium-Based Lead Halide Perovskites by a Key Intermediate Phase, *Chem*, 2021, **7**, 2513–2526, DOI: **10.1016/j.chempr.2021.07.011**.

13 S. Jiang, Y. Luan, J. I. Jang, T. Baikie, X. Huang, R. Li, F. O. Saouma, Z. Wang, T. J. White and J. Fang, Phase Transitions of Formamidinium Lead Iodide Perovskite under Pressure, *J. Am. Chem. Soc.*, 2018, **140**, 13952–13957, DOI: **10.1021/jacs.8b09316**.

14 N. Pellet, P. Gao, G. Gregori, T. Y. Yang, M. K. Nazeeruddin, J. Maier and M. Grätzel, Mixed-Organic-Cation Perovskite Photovoltaics for Enhanced Solar-Light Harvesting, *Angew. Chem., Int. Ed.*, 2014, **53**, 3151–3157, DOI: **10.1002/anie.201309361**.

15 M. Maczka, M. Ptak, D. L. M. Vasconcelos, L. Giriunas, P. T. C. Freire, M. Bertmer, J. Banys and M. Simenas, NMR and Raman Scattering Studies of Temperature-and Pressure-Driven Phase Transitions in $CH_3NH_2NH_2PbCl_3$ Perovskite, *J. Phys. Chem. C*, 2020, **124**, 26999–27008, DOI: **10.1021/acs.jpcc.0c07886**.

16 M. Maczka, M. Ptak, A. Gagor, D. Stefanska, J. K. Zareba and A. Sieradzki, Methylhydrazinium Lead Bromide: Noncentrosymmetric Three-Dimensional Perovskite with Exceptionally Large Framework Distortion and Green Photoluminescence, *Chem. Mater.*, 2020, **32**, 1667–1673, DOI: **10.1021/acs.chemmater.9b05273**.

17 H. R. Petrosova, O. I. Kucheriv, S. Shova and I. A. Gural'skiy, Aziridinium Cation Templating 3D Lead Halide Hybrid Perovskites, *Chem. Commun.*, 2022, **58**, 5745–5748, DOI: **10.1039/d2cc01364a**.

18 M. Pitaro, E. K. Tekelenburg, S. Shao and M. A. Loi, Tin Halide Perovskites: From Fundamental Properties to Solar

Cells, *Adv. Mater.*, 2022, **34**, 1–47, DOI: **10.1002/adma.202105844**.

19 M. Maczka, A. Gagor, J. K. Zareba, D. Stefanska, M. Drozd, S. Balciunas, M. Simenas, J. Banys and A. Sieradzki, Three-Dimensional Perovskite Methylhydrazinium Lead Chloride with Two Polar Phases and Unusual Second-Harmonic Generation Bistability above Room Temperature, *Chem. Mater.*, 2020, **32**, 4072–4082, DOI: **10.1021/acs.chemmater.0c00973**.

20 M. Ptak, A. Sieradzki, M. Simėnas and M. Maczka, Molecular Spectroscopy of Hybrid Organic–Inorganic Perovskites and Related Compounds, *Coord. Chem. Rev.*, 2021, **448**, 1–51, DOI: **10.1016/j.ccr.2021.214180**.

21 P. Jain, V. Ramachandran, R. J. Clark, D. Z. Hai, B. H. Toby, N. S. Dalal, H. W. Kroto and A. K. Cheetham, Multiferroic Behavior Associated with an Order-Disorder Hydrogen Bonding Transition in Metal-Organic Frameworks (MOFs) with the Perovskite ABX3 Architecture, *J. Am. Chem. Soc.*, 2009, **131**, 13625–13627, DOI: **10.1021/ja904156s**.

22 M. Sanchez-Andujar, S. Presedo, S. Ya Nez-Vilar, S. Castro-Garcia, J. Shamir and M. A. Senaris-Rodriguez, Characterization of the Order-Disorder Dielectric Transition in the Hybrid Organic-Inorganic Perovskite-like Formate $Mn(HCOO)_3[(CH_3)_2NH_2]$, *Inorg. Chem.*, 2010, **49**, 1510–1516, DOI: **10.1021/ic901872g**.

23 Y. Imai, B. Zhou, Y. Ito, H. Fijimori, A. Kobayashi, Z. M. Wang and H. Kobayashi, Freezing of Ring-Puckering Molecular Motion and Giant Dielectric Anomalies in Metal-Organic Perovskites, *Chem. – Asian J.*, 2012, **7**, 2786–2790, DOI: **10.1002/asia.201200673**.

24 W. Li, Z. Zhang, E. G. Bithell, A. S. Batsanov, P. T. Barton, P. J. Saines, P. Jain, C. J. Howard, M. A. Carpenter and A. K. Cheetham, Ferroelasticity in a Metal-Organic Framework Perovskite; Towards a New Class of Multiferroics, *Acta Mater.*, 2013, **61**, 4928–4938, DOI: **10.1016/j.actamat.2013.04.054**.

25 Z. Wang, B. Zhang, T. Otsuka, K. Inoue, H. Kobayashi and M. Kurmoo, Anionic NaCl-Type Frameworks of $[MnII(HCOO)_3]$, Templated by Alkylammonium, Exhibit Weak Ferromagnetism, *Dalton Trans.*, 2004, 2209–2216, DOI: **10.1039/B404466E**.

26 S. Chen, R. Shang, K. L. Hu, Z. M. Wang and S. Gao, $[NH_2NH_3][M(HCOO)_3]$ (M = Mn^{2+}, Zn^{2+}, Co^{2+} and Mg^{2+}): Structural Phase Transitions, Prominent Dielectric Anomalies and Negative Thermal Expansion, and Magnetic Ordering, *Inorg. Chem. Front.*, 2014, **1**, 83–98, DOI: **10.1039/c3qi00034f**.

27 A. Kabanski, M. Ptak and D. Stefanska, Metal-Organic Framework Optical Thermometer Based on Cr^{3+} Ion Luminescence, *ACS Appl. Mater. Interfaces*, 2023, **15**, 7074–7082, DOI: **10.1021/acsami.2c19957**.

28 Y. Yu, R. Shang, S. Chen, B. W. Wang, Z. M. Wang and S. Gao, A Series of Bimetallic Ammonium AlNa Formates, *Chem. – Eur. J.*, 2017, **23**, 9857–9871, DOI: **10.1002/chem.201701099**.

29 M. Ptak, M. Mączka, A. Gagor, A. Sieradzki, A. Stroppa, D. Di Sante, J. M. Perez-Mato and L. Macalik, Experimental and Theoretical Studies of Structural Phase Transition in a Novel Polar Perovskite-like $[C_2H_5NH_3][Na_{0.5}Fe_{0.5}(HCOO)_3]$ Formate, *Dalton Trans.*, 2016, **45**, 2574–2583, DOI: **10.1039/c5dt04536c**.

30 M. Ptak, M. Maczka, A. Gagor, A. Sieradzki, B. Bondzior, P. Deren and S. Pawlus, Phase Transitions and Chromium(III) Luminescence in Perovskite-Type $[C_2H_5NH_3]$-$[Na_{0.5}Cr_xAl_{0.5-x}(HCOO)_3]$ (x = 0, 0.025, 0.5), Correlated with Structural, Dielectric and Phonon Properties, *Phys. Chem. Chem. Phys.*, 2016, **18**, 29629–29640, DOI: **10.1039/c6cp05151k**.

31 M. Ptak, A. Gagor, A. Sieradzki, B. Bondzior, P. Deren, A. Ciupa, M. Trzebiatowska and M. Maczka, The Effect of K^+ Cations on the Phase Transitions, and Structural, Dielectric and Luminescence Properties of $[Cat][K_{0.5}Cr_{0.5}(HCOO)_3]$, Where Cat Is Protonated Dimethylamine or Ethylamine, *Phys. Chem. Chem. Phys.*, 2017, **19**, 12156–12166, DOI: **10.1039/c7cp01336a**.

32 M. Ptak, B. Zarychta, D. Stefanska, A. Ciupa and W. Paraguassu, Novel Bimetallic MOF Phosphors with an Imidazolium Cation: Structure, Phonons, High- Pressure Phase Transitions and Optical Response, *Dalton Trans.*, 2019, **48**, 242–252, DOI: **10.1039/C8DT04246B**.

33 M. Ptak, I. E. Collings, K. L. Svane, A. Sieradzki, W. Paraguassu and M. Maczka, Pressure-Enhanced Ferroelectric Polarisation in a Polar Perovskite-like $[C_2H_5 NH_3]Na_{0.5}$-$Cr_{0.5}(HCOO)_3$ Metal-Organic Framework, *J. Mater. Chem. C*, 2019, **7**, 8660–8668, DOI: **10.5281/zenodo.2608304**.

34 D. Di Sante, A. Stroppa, P. Jain and S. Picozzi, Tuning the Ferroelectric Polarization in a Multiferroic Metal-Organic Framework, *J. Am. Chem. Soc.*, 2013, **135**, 18126–18130, DOI: **10.1021/ja408283a**.

35 M. Maczka, A. Gagor, M. Ptak, W. Paraguassu, T. A. Da Silva, A. Sieradzki and A. Pikul, Phase Transitions and Coexistence of Magnetic and Electric Orders in the Methylhydrazinium Metal Formate Frameworks, *Chem. Mater.*, 2017, **29**, 2264–2275, DOI: **10.1021/acs.chemmater.6b05249**.

36 O. V. Dolomanov, L. J. Bourhis, R. J. Gildea, J. A. K. Howard and H. Puschmann, OLEX2: A Complete Structure Solution, Refinement and Analysis Program, *J. Appl. Crystallogr.*, 2009, **42**, 339–341, DOI: **10.1107/S0021889808042726**.

37 S. K. Kurtz and T. T. Perry, A Powder Technique for the Evaluation of Nonlinear Optical Materials, *J. Appl. Phys.*, 1968, **39**, 3798–3813, DOI: **10.1063/1.1656857**.

38 M. E. Lines and A. M. Glass, *Principles and Applications of Ferroelectrics and Related Materials*, Clarendon Press, Oxford, 1977, ISBN: 9780198507789.

39 M. Simenas, S. Balciunas, M. Maczka, J. Banys and E. E. Tornau, Structural Phase Transition in Perovskite Metal-Formate Frameworks: A Potts-Type Model with Dipolar Interactions, *Phys. Chem. Chem. Phys.*, 2016, **18**, 18528–18535, DOI: **10.1039/c6cp03414d**.

40 W. Wang, L. Q. Yan, J. Z. Cong, Y. L. Zhao, F. Wang, S. P. Shen, T. Zou, D. Zhang, S. G. Wang, X. F. Han and Y. Sun, Magnetoelectric Coupling in the Paramagnetic State of a Metal-Organic Framework, *Sci. Rep.*, 2013, **3**, 1–5, DOI: **10.1038/srep02024**.

41 Y. Tian, A. Stroppa, Y. Chai, L. Yan, S. Wang, P. Barone, S. Picozzi and Y. Sun, Cross Coupling between Electric and Magnetic Orders in a Multiferroic Metal-Organic Framework, *Sci. Rep.*, 2014, **4**, 1–5, DOI: **10.1038/srep06062**.

42 J. F. Scott, Ferroelectrics Go Bananas, *J. Phys. Condens. Matter*, 2008, **20**, 1–3, DOI: **10.1088/0953-8984/20/02/021001**.

43 F. Gheorghiu, M. Simenas, C. E. Ciomaga, M. Airimioaei, V. Kalendra, J. Banys, M. Dobromir, S. Tascu and L. Mitoseriu, Preparation and Structural Characterization of Fe-Doped $BaTiO_3$ Diluted Magnetic Ceramics, *Ceram. Int.*, 2017, **43**, 9998–10005, DOI: **10.1016/j.ceramint.2017.05.013**.

44 W. C. Phillips, W. C. Phillips, R. J. Weiss, P. B. Rev, T. Paakori, S. Manninen, O. Inkinen, R. Currat, P. D. DeCicco, A. Harvey, W. A. Rachinger, J. Sci, R. E. Watson, T. von Waldkirch, K. A. Muller and W. Berlinger, Fluctuations in $SrTi0_3$ near the 105-K Phase Transition, *Phys. Rev. B: Solid State*, 1972, **7**, 1052–1066, DOI: **10.1103/PhysRevB.7.1052**.

45 K. Nishimura and T. Hashimoto, ESR Investigation of TGS Doped with Cr^{3+} Ions, *J. Phys. Soc. Japan*, 1973, **35**, 1699–1703, DOI: **10.1143/JPSJ.35.1699**.

46 M. Simenas, A. Ciupa, G. Usevicius, K. Aidas, D. Klose, G. Jeschke, M. Maczka, G. Volkel, A. Poppl and J. Banys, Electron Paramagnetic Resonance of a Copper Doped $[(CH_3)_2NH_2][Zn(HCOO)_3]$ Hybrid Perovskite Framework, *Phys. Chem. Chem. Phys.*, 2018, **20**, 12097–12105, DOI: **10.1039/c8cp01426d**.

47 M. Simenas, A. Ciupa, M. Mączka, G. Volkel, A. Poppl and J. Banys, EPR of Structural Phase Transition in Manganese- and Copper-Doped Formate Framework of $[NH_3(CH_2)_4NH_3][Zn(HCOO)_3]_2$, *J. Phys. Chem. C*, 2016, **120**, 19751–19758, DOI: **10.1021/acs.jpcc.6b07389**.

48 M. Simenas, S. Balciunas, A. Ciupa, L. Vilciauskas, D. Jablonskas, M. Kinka, A. Sieradzki, V. Samulionis, M. Maczka and J. Banys, Elucidation of Dipolar Dynamics and the Nature of Structural Phases in the $[(CH_3)_2NH_2][Zn(HCOO)_3]$ Hybrid Perovskite Framework, *J. Mater. Chem. C*, 2019, **7**, 6779–6785, DOI: **10.1039/c9tc01275c**.

49 M. Simenas, S. Balciunas, J. N. Wilson, S. Svirskas, M. Kinka, A. Garbaras, V. Kalendra, A. Gagor, D. Szewczyk, A. Sieradzki, M. Maczka, V. Samulionis, A. Walsh, R. Grigalaitis and J. Banys, Suppression of Phase Transitions and Glass Phase Signatures in Mixed Cation Halide Perovskites, *Nat. Commun.*, 2020, **11**, 5103, DOI: **10.1038/s41467-020-18938-z**.

50 M. Simenas, D. Klose, M. Ptak, K. Aidas, M. Mączka, J. Banys, A. Poppl and G. Jeschke, Magnetic Excitation and Readout of Methyl Group Tunnel Coherence, *Sci. Adv.*, 2020, **6**, 1–7.

51 G. Usevicius, A. Eggeling, I. Pocius, V. Kalendra, D. Klose, M. Mączka, A. Poppl, J. Banys, G. Jeschke and M. Simenas, Probing Methyl Group Tunneling in $[(CH_3)_2NH_2][Zn(HCOO)_3]$ Hybrid Perovskite Using Co^{2+} EPR, *Molecules*, 2023, **28**, 1–13, DOI: **10.3390/molecules28030979**.

52 J. Soetbeer, L. F. Ibanez, Z. Berkson, Y. Polyhach and G. Jeschke, Regularized Dynamical Decoupling Noise Spectroscopy-a Decoherence Descriptor for Radicals in Glassy Matrices, *Phys. Chem. Chem. Phys.*, 2021, **23**, 21664–21676, DOI: **10.1039/d1cp03103a**.

53 R. M. Dimeo, Visualization and Measurement of Quantum Rotational Dynamics, *Am. J. Phys.*, 2003, **71**, 885–893, DOI: **10.1119/1.1538575**.

54 M. Prager and A. Heidemann, Rotational Tunneling and Neutron Spectroscopy: A Compilation, *Chem. Rev.*, 1997, **97**, 2933–2966, DOI: **10.1021/cr9500848**.

55 M. Maczka, A. Pietraszko, B. Macalik and K. Hermanowicz, Structure, Phonon Properties, and Order-Disorder Transition in the Metal Formate Framework of $[NH_4][Mg(HCOO)_3]$, *Inorg. Chem.*, 2014, **53**, 787–794, DOI: **10.1021/ic4020702**.

56 M. Trzebiatowska-Gusowska and A. Gagor, The Order-Disorder State of Diaminoalkanes in Cu-Based Metal-Organic Materials, *J. Coord. Chem.*, 2017, **70**, 1536–1547, DOI: **10.1080/00958972.2017.1305109**.

57 P. Kubelka and F. Munk, Ein Beitrag Zur Optik Der Farbanstriche, *Z. Tech. Phys.*, 1931, **12**, 593–601.

58 M. Ptak, B. Dziuk, D. Stefanska and K. Hermanowicz, The Structural, Phonon and Optical Properties of $[CH_3NH_3][M_{0.5}Cr_xAl_{0.5-x}(HCOO)_3]$ (M = Na, K; X = 0, 0.025, 0.5) Metal-Organic Framework Perovskites for Luminescence Thermometry, *Phys. Chem. Chem. Phys.*, 2019, **21**, 7965–7972, DOI: **10.1039/c9cp01043b**.

59 M. Maczka, B. Bondzior, P. Deren, A. Sieradzki, J. Trzmiel, A. Pietraszko and J. Hanuza, Synthesis and Characterization of $[(CH_3)_2NH_2][Na_{0.5}Cr_{0.5}(HCOO)_3]$: A Rare Example of Luminescent Metal-Organic Frameworks Based on Cr(III) Ions, *Dalton Trans.*, 2015, **44**, 6871–6879, DOI: **10.1039/c5dt00060b**.

60 W. Dai, F. Chi, B. Lou, X. Wei, J. Cheng, S. Liu and M. Yin, Temperature-Dependent Luminescent Properties of Cr^{3+} Doped $ZnGa_2O_4$ Far-Red Emitting Phosphor, *Opt. Mater.*, 2021, **116**, 1–8, DOI: **10.1016/j.optmat.2021.111104**.

61 M. Ptak, D. Stefanska, A. Gagor, K. L. Svane, A. Walsh and P. Waldeci, Heterometallic Perovskite-Type Metal–Organic framework with an Ammonium Cation: Structure, Phonons, and Optical Response of $[NH_4]Na_{0.5}Cr_xAl_{0.5-x}(HCOO)_3$ (X = 0, 0.025 and 0.5), *Phys. Chem. Chem. Phys.*, 2018, **20**, 22284–22295, DOI: **10.1039/c8cp03788d**.

62 D. Stefańska, A. Kabański, T. H. Q. Vu, M. Adaszyński and M. Ptak, Structure, Luminescence and Temperature Detection Capability of $[C(NH_2)_3]M(HCOO)_3$ (M = Mg^{2+}, Mn^{2+}, Zn^{2+}) Hybrid Organic–Inorganic Formate Perovskites Containing Cr^{3+} Ions, *Sensors*, 2023, **23**, 6259, DOI: **10.3390/s23146259**.

63 M. Runowski, P. Woźny, I. R. Martín, K. Soler-Carracedo, T. Zheng, H. Hemmerich, F. Rivera-López, J. Moszczyński, P. Kulpiński and S. Feldmann, Multimodal Optically Nonlinear Nanoparticles Exhibiting Simultaneous Higher Harmonics Generation and Upconversion Luminescence for Anticounterfeiting and 8-Bit Optical Coding, *Adv. Funct. Mater.*, 2023, **34**, 2307791, DOI: **10.1002/adfm.202307791**.

64 M. Runowski, D. Marcinkowski, K. Soler-Carracedo, A. Gorczyński, E. Ewert, P. Woźny and I. R. Martín, Noncentrosymmetric Lanthanide-Based MOF Materials

Exhibiting Strong SHG Activity and NIR Luminescence of Er^{3+}: Application in Nonlinear Optical Thermometry, *ACS Appl. Mater. Interfaces*, 2023, **15**, 3244–3252, DOI: **10.1021/acsami.2c22571**.

65 J. Ueda, M. Back, M. G. Brik, Y. Zhuang, M. Grinberg and S. Tanabe, Ratiometric Optical Thermometry Using Deep Red Luminescence from 4T2 and 2E States of Cr^{3+} in $ZnGa_2O_4$ Host, *Opt. Mater.*, 2018, **85**, 510–516, DOI: **10.1016/j.optmat.2018.09.013**.

66 D. Stefanska, B. Bondzior, T. H. Q. Vu, M. Grodzicki and P. J. Deren, Temperature Sensitivity Modulation through Changing the Vanadium Concentration in a La2MgTiO6: V5 +, Cr3+ Double Perovskite Optical Thermometer, *Dalton Trans.*, 2021, **50**, 9851–9857, DOI: **10.1039/d1dt00911g**.

67 D. Stefanska, T. H. Q. Vu and P. J. Deren, Multiple Ways for Temperature Detection Based on La_2MgTiO_6 Double Perovskite Co-Doped with Mn^{4+} and Cr^{3+} Ions, *J. Alloys Compd.*, 2023, **938**, 1–10, DOI: **10.1016/j.jallcom.2022.168653**.

68 Q. Wang, Z. Liang, J. Luo, Y. Yang, Z. Mu, X. Zhang, H. Dong and F. Wu, Ratiometric Optical Thermometer with High Sensitivity Based on Dual Far-Red Emission of Cr^{3+} in $Sr_2MgAl_{22}O_{36}$, *Ceram. Int.*, 2020, **46**, 5008–5014, DOI: **10.1016/j.ceramint.2019.10.241**.

69 M. Back, J. Ueda, J. Xu, K. Asami, M. G. Brik and S. Tanabe, Effective Ratiometric Luminescent Thermal Sensor by Cr^{3+} -Doped Mullite $Bi_2Al_4O_9$ with Robust and Reliable Performances, *Adv. Opt. Mater.*, 2020, **8**, 1–10, DOI: **10.1002/adom.202000124**.

70 E. Glais, V. Dordevic, J. Papan, B. Viana and M. D. Dramicanin, $MgTiO_3:Mn^{4+}$ a Multi-Reading Temperature Nanoprobe, *RSC Adv.*, 2018, **8**, 18341–18346, DOI: **10.1039/c8ra02482k**.

71 S. H. Yang, Y. C. Lee and Y. C. Hung, Thermometry of Red Nanoflaked $SrAl_{12}O_{19}:Mn^{4+}$ Synthesized with Boric Acid Flux, *Ceram. Int.*, 2018, **44**, 11665–11673, DOI: **10.1016/j.ceramint.2018.03.242**.

Electronic Supplementary Information
for

Mechanism of isosymmetric polar order-disorder phase transition in pyroelectric $[CH_3CH_2NH_3]_2NaGa(HCOO)_6$ double perovskite

Maciej Ptak,*[a] Adam Kabański,[a] Błażej Dziuk,[b] Sergejus Balciunas,[c] Gediminas Usevicius,[c] Jan K. Zaręba,[b] Juras Banys,[c] Mantas Simenas,*[c] Adam Sieradzki [d] and Dagmara Stefańska [a]

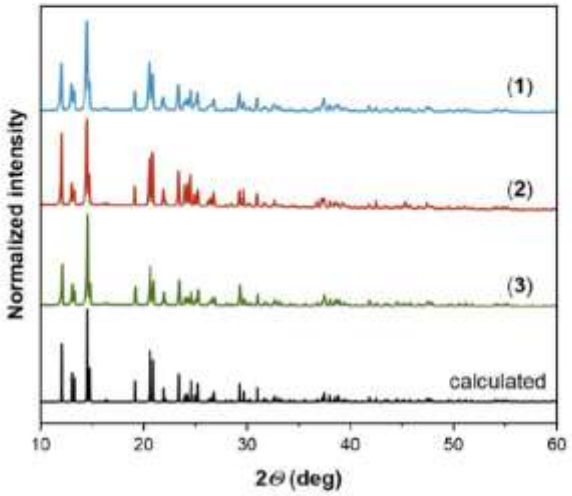

Fig. S1. Powder XRD patterns of (**1**), (**2**), and (**3**) compared to the simulated pattern based on the single crystal data obtained for (1) at 293 K; (**1**), $[CH_3CH_2NH_3]_2NaGa(HCOO)_6$; (**2**), $[CH_3CH_2NH_3]_2NaGa_{0.069}Cr_{0.931}(HCOO)_6$; (**3**), $[CH_3CH_2NH_3]_2NaGa_{0.99}Fe_{0.01}(HCOO)_6$;

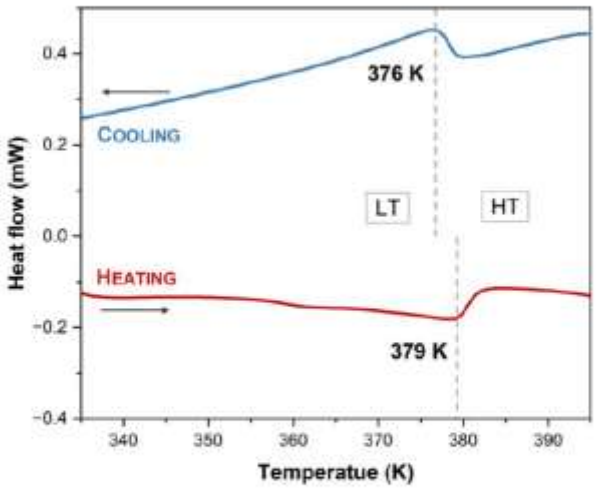

Fig. S2. The DSC curve recorded for (**1**), $[CH_3CH_2NH_3]_2NaGa(HCOO)_6$.

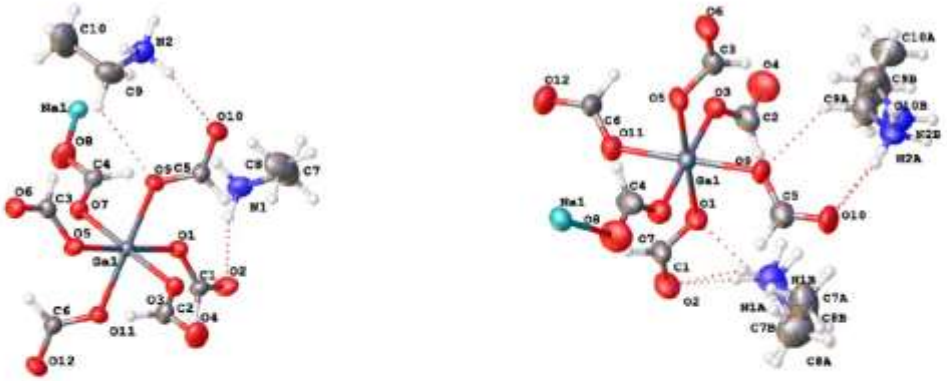

Fig. S3. Asymmetric part of unit cell for (**1**), $[CH_3CH_2NH_3]_2NaGa(HCOO)_6$, at (a) 293 K and (b) 391 K. Displacement ellipsoids are drawn at the 50% probability level.

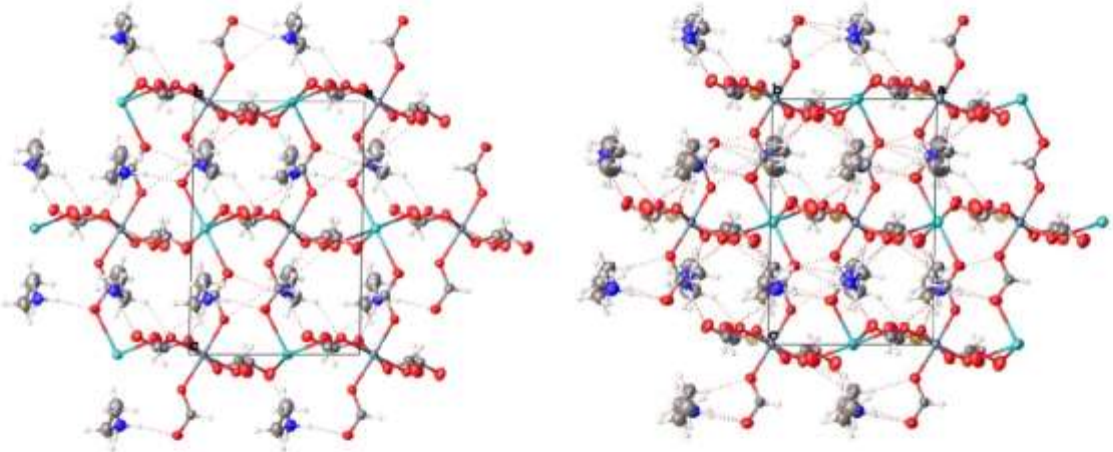

Fig. S4. Packing diagrams along the *b* axis for (**1**), $[CH_3CH_2NH_3]_2NaGa(HCOO)_6$, at (a) 293 K and (b) 391 K. Displacement ellipsoids are drawn at the 50% probability level.

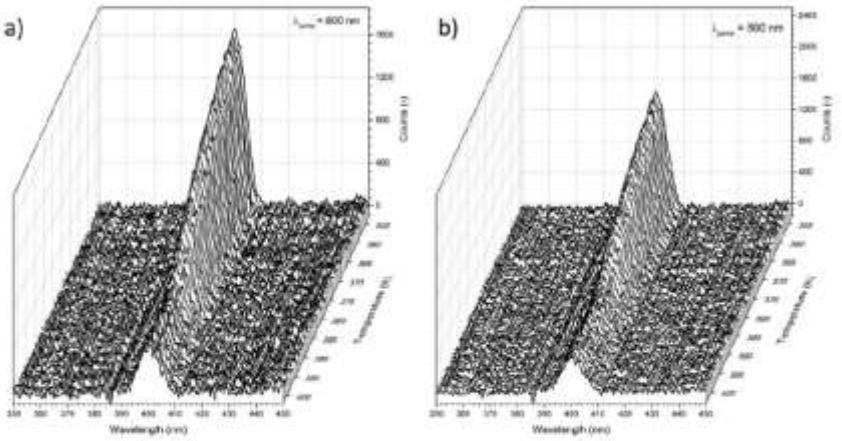

Fig. S5. SHG traces collected for (1) during (a) heating run, and (b) cooling run.

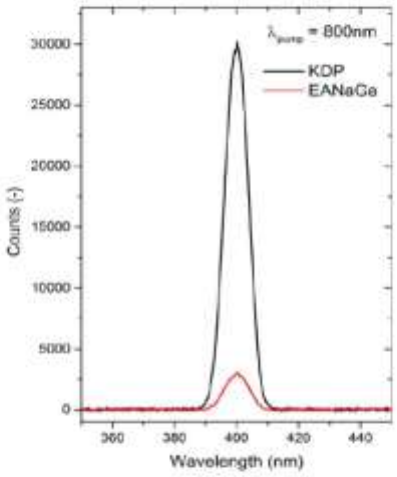

Fig. S6. Overlay of SHG traces obtained for (1) and KDP. Note that signal collection times were 6000 ms and 500 ms for (1) and KDP, respectively. Relative SHG efficiency of (1) is about 0.01 that of KDP.

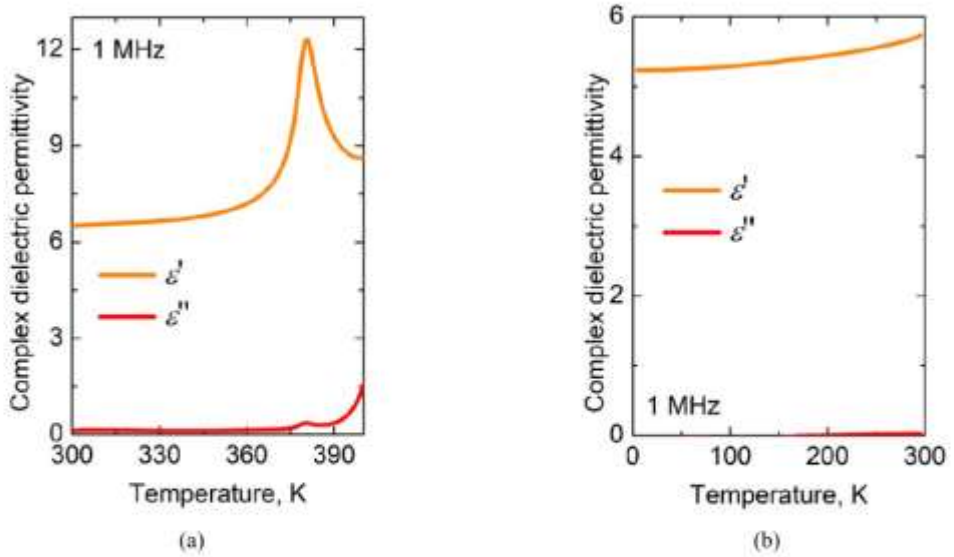

Fig. S7. Temperature dependence of the complex dielectric permittivity of pellet sample (**1**), $[CH_3CH_2NH_3]_2NaGa(HCOO)_6$, measured at 1 MHz above (a) and below RT (b). A clear phase transition anomaly can be observed at 380 K (a).

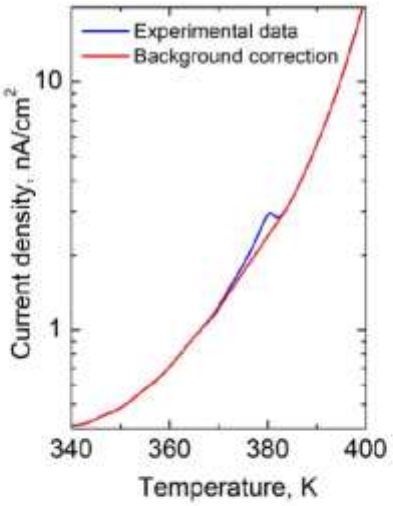

Fig. S8. Temperature dependence of the thermally stimulated current of the pellet sample (**1**), $[CH_3CH_2NH_3]_2NaGa(HCOO)_6$, prior the background correction. The red curve indicates the background correction employed to extract the pyrocurrent due to the phase transition.

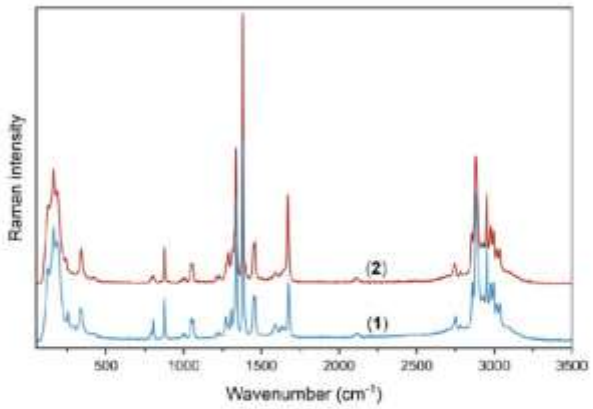

Fig. S9. Comparison of RT Raman spectra of (**1**), $[CH_3CH_2NH_3]_2NaGa(HCOO)_6$ and (**2**), $[CH_3CH_2NH_3]_2NaGa_{0.069}Cr_{0.931}(HCOO)_6$.

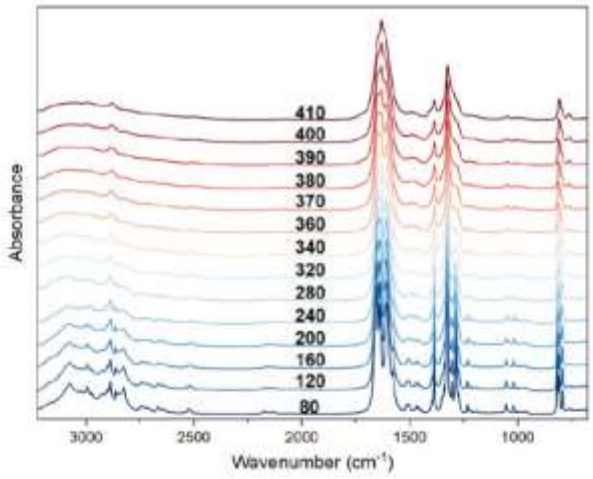

Fig. S10. Temperature-dependent IR spectra of (**1**), $[CH_3CH_2NH_3]_2NaGa(HCOO)_6$.

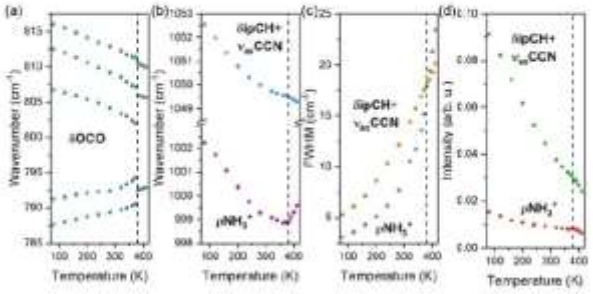

Fig. S11. Thermal evolution of selected IR bands for (**1**), $[CH_3CH_2NH_3]_2NaGa(HCOO)_6$.

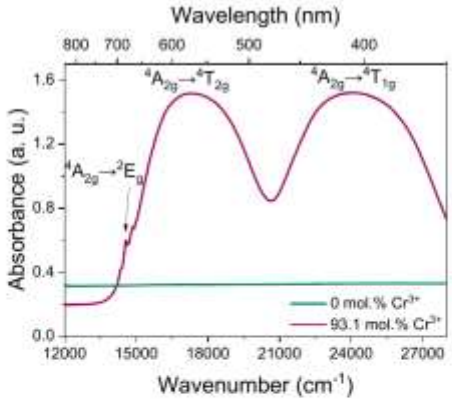

Fig. S12. Room temperature absorption spectra of (**1**), $[CH_3CH_2NH_3]_2NaGa(HCOO)_6$ and (**2**), $[CH_3CH_2NH_3]_2NaGa_{0.069}Cr_{0.931}(HCOO)_6$.

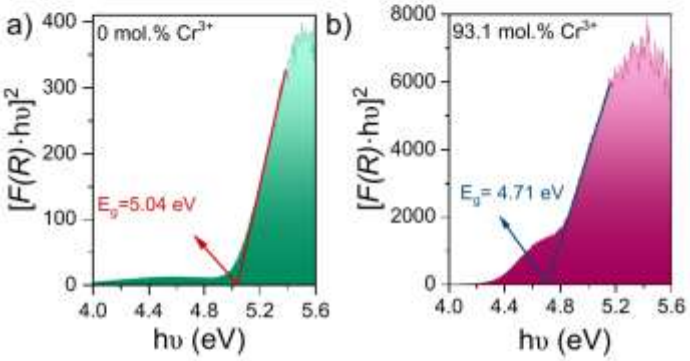

Fig. S13. Energy band gap of investigated samples estimated by x-axis intersection point of the linear fit of the Tauc plot. Using the diffuse reflectance spectrum, it is possible to determine the energy band gap (E_g) of investigated samples by applying the Kubelka-Munk relation (Z. Technol. Phys. 1931, 12, 593−599): $F(R) = (1 - R)^2 / 2R$, where R is reflectance. The modification of this method proposed by Tauc in 1966 (Status Solidi B 1966, 15, 627−637) assumed that the E_g can be determined based on the graphical examination of the following function: $[F(R \cdot h\nu]^n = B(h\nu - E_g)$, where h denotes the Planck constant, ν is the photon's frequency, and B is a constant. The n factor is related to the type of electron transition and takes a 1/2 or 2 value for the direct and indirect transition band gaps, respectively (J. Sol-Gel Sci. Technol. 2012, 61, 1–7, *J. Phys. Chem. Lett*. 2018, 9, 23, 6814–6817).

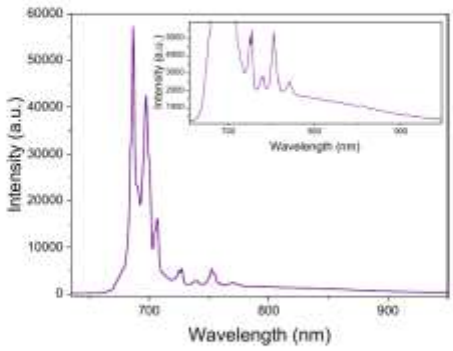

Fig. S14. The low-temperature (80 K) emission spectrum of (**2**), $[EA]_2NaCr_{0.931}Ga_{0.069}(HCOO)_6$, in the inset magnification of the spectrum, shows the broad emission from the $^4T_{2g}$ emission level.

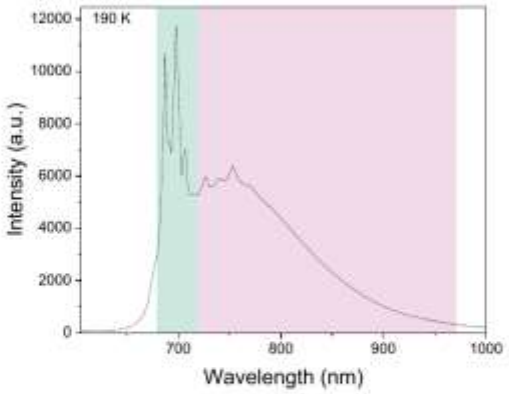

Fig. S15. The emission spectra of (**2**), $[EA]_2NaCr_{0.931}Ga_{0.069}(HCOO)_6$, at 190 K presented spectral ranges used to determine FIR.

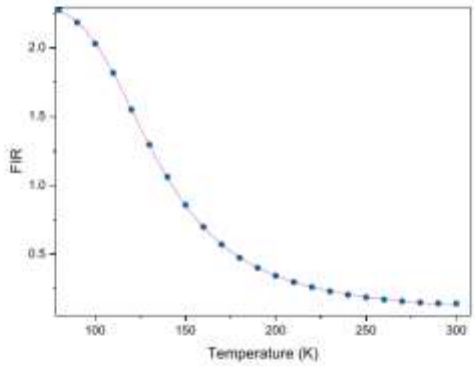

Fig. S16. Changes of FIR ratio with the temperature of (**2**), $[EA]_2NaCr_{0.931}Ga_{0.069}(HCOO)_6$.

Tab. S1. Experimental data for (**1**), $[CH_3CH_2NH_3]_2NaGa(HCOO)_6$, at 293 and 391 K.

Crystal data		
Chemical formula	$(C_2H_5NH_3)_2GaNa(HCOO)_6$ (**1**)	
M_r	455.00	
Crystal system, space group	Monoclinic, *Pn*	
Temperature (K)	293(2)	391(2)
***a*, *b*, *c* (Å)**	8.1127 (5), 9.2570 (6), 12.0281 (8)	8.1080 (6), 9.3326 (7), 12.0697 (10)
α, β, γ (°)	90.000 (0), 91.084 (5), 90.000 (0)	90.000, 90.940 (7), 90.000
V (Å^3)	903.14 (10)	913.18 (12)
Z	2	
Radiation type	Mo $K\alpha$	
μ (mm^{-1})	1.61	1.59
Crystal size (mm)	0.30 x 0.20 x 0.10	
Data collection		
No. of measured, independent and observed [$I > 2\sigma(I)$] reflections	6130, 3505, 3362	4249, 2831, 2678
R_{int}	0.019	0.025
(sin θ/λ_{max} (Å^{-1})	0.651	0.617
Refinement		
$R[F^2 > 2\sigma(F^2)]$, $wR(F^2)$, S	0.025, 0.056, 1.05	0.034, 0.083, 1.08
No. of reflections	3505	2831
No. of parameters	241	292
$\Delta\rho_{max}$, $\Delta\rho_{min}$ (e Å^{-3})	0.29, −0.27	0.34, −0.37

Tab. S2. Comparison of thermal and structural parameters for $[EA]_2NaM^{III}(HCOO)_6$ double perovskites.

M^{III}	T_C (K) [a]	ΔS (Jmol^{-1}K^{-1}) [b]	σ^2 (deg^2) [c]		$\Delta \times 10^2$ [d]	
			NaO_6	$M^{III}O_6$	NaO_6	$M^{III}O_6$
Ga^{3+} (**1**)	379/376	3.7	17.04 [e] / 12.06 [f]	1.77 [e] / 1.43 [f]	1.96 [e] / 2.31 [f]	0.40 [e] / 0.27 [f]
Al^{3+}	369/364	2.0	18.03 [g] / 7.99 [h]	0.91 [g] / 0.47 [h]	1.82 [g] / 1.96 [h]	0.37 [g] / 0.25 [h]
Cr^{3+}	373/370	4.0	14.94 [i] / 7.33 [j]	1.16 [i] / 0.73 [j]	1.88 [i] / 2.19 [j]	0.20 [i] / 0.09 [j]
Fe^{3+}	361/359	5.0	12.84 [i] / 5.06 [k]	1.50 [i] / 0.65 [k]	1.72 [i] / 1.92 [k]	0.33 [i] / 0.16 [k]

[a] heating/cooling; [b] estimated for the $[EA]_2NaM^{III}(HCOO)_6$ ($Z = 2$) formula; [c] bond angle variance for HT/LT phase; [d] distortion index for HT/LT phase; [e] 293 K; [f] 391 K; [g] 270 K; [h] 375 K; [i] 297 K; [j] 400 K; [k] 377 K. Literature data for $M^{III} = Al^{3+}$, Cr^{3+}, and Fe^{3+} were taken from: 10.1039/C6CP05151K and 10.1039/C5DT04536C. The bond angle variance and distortion indexes were calculated using Vesta software (10.1107/S0021889808012016).

Tab. S3. Selected geometric parameters (Å, °) for (**1**), $[CH_3CH_2NH_3]_2NaGa(HCOO)_6$, at 293 and 391 K.

293 K			
Ga1—O1	1.966 (4)	O12—C6	1.238 (5)
Ga1—O3	1.964 (2)	C1—H1	0.9300
Ga1—O5	1.971 (3)	C2—H2	0.9300
Ga1—O7	1.985 (2)	C3—H3	0.9300
Ga1—O9	1.987 (3)	C4—H4	0.9300
Ga1—O11	1.977 (2)	C5—H5	0.9300
Na1—O2^{i}	2.437 (5)	C6—H6	0.9300
Na1—O4^{ii}	2.418 (4)	N1—H1A	0.8900
Na1—O6^{iii}	2.441 (5)	N1—H1B	0.8900
Na1—O8	2.385 (4)	N1—H1C	0.8900
Na1—O10^{iv}	2.526 (3)	N1—C7	1.470 (6)
Na1—O12^{v}	2.531 (3)	C7—H7A	0.9700
O1—C1	1.275 (7)	C7—H7B	0.9700
O2—Na1^{vi}	2.437 (5)	C7—C8	1.490 (7)
O2—C1	1.228 (7)	C8—H8A	0.9600
O3—C2	1.274 (5)	C8—H8B	0.9600
O4—Na1^{vii}	2.418 (4)	C8—H8C	0.9600
O4—C2	1.215 (5)	N2—H2A	0.8900
O5—C3	1.261 (7)	N2—H2B	0.8900
O6—Na1^{viii}	2.441 (5)	N2—H2C	0.8900
O6—C3	1.220 (7)	N2—C9	1.468 (6)
O7—C4	1.289 (5)	C9—H9A	0.9700
O8—C4	1.215 (5)	C9—H9B	0.9700
O9—C5	1.268 (5)	C9—C10	1.466 (8)
O10—Na1^{ix}	2.526 (3)	C10—H10A	0.9600
O10—C5	1.234 (5)	C10—H10B	0.9600
O11—C6	1.256 (5)	C10—H10C	0.9600
O12—Na1^{x}	2.531 (3)		
O1—Ga1—O5	178.28 (16)	O5—C3—H3	117.3
O1—Ga1—O7	89.94 (12)	O6—C3—O5	125.5 (5)
O1—Ga1—O9	88.93 (13)	O6—C3—H3	117.3
O1—Ga1—O11	91.12 (13)	O7—C4—H4	118.2
O3—Ga1—O1	89.18 (12)	O8—C4—O7	123.6 (4)
O3—Ga1—O5	92.49 (12)	O8—C4—H4	118.2
O3—Ga1—O7	178.87 (12)	O9—C5—H5	117.5
O3—Ga1—O9	90.64 (11)	O10—C5—O9	125.0 (4)
O3—Ga1—O11	88.89 (11)	O10—C5—H5	117.5
O5—Ga1—O7	88.38 (11)	O11—C6—H6	116.7
O5—Ga1—O9	90.66 (13)	O12—C6—O11	126.6 (4)
O5—Ga1—O11	89.30 (13)	O12—C6—H6	116.7
O7—Ga1—O9	88.63 (11)	H1A—N1—H1B	109.5
O11—Ga1—O7	91.85 (11)	H1A—N1—H1C	109.5
O11—Ga1—O9	179.53 (12)	H1B—N1—H1C	109.5
O2^{i}—Na1—O6^{iii}	171.68 (14)	C7—N1—H1A	109.5
O2^{i}—Na1—O10^{iv}	84.11 (13)	C7—N1—H1B	109.5
O2^{i}—Na1—O12^{v}	96.89 (13)	C7—N1—H1C	109.5
O4^{ii}—Na1—O2^{i}	86.61 (15)	N1—C7—H7A	109.4
O4^{ii}—Na1—O6^{iii}	89.65 (15)	N1—C7—H7B	109.4
O4^{ii}—Na1—O10^{iv}	89.02 (10)	N1—C7—C8	111.3 (4)
O4^{ii}—Na1—O12^{v}	91.69 (14)	H7A—C7—H7B	108.0
O6^{iii}—Na1—O10^{iv}	88.40 (12)	C8—C7—H7A	109.4

O6^{iii}—Na1—O12^{v}	90.64 (14)	C8—C7—H7B	109.4
O8—Na1—O2^{i}	91.58 (15)	C7—C8—H8A	109.5
O8—Na1—O4^{ii}	174.61 (15)	C7—C8—H8B	109.5
O8—Na1—O6^{iii}	92.79 (16)	C7—C8—H8C	109.5
O8—Na1—O10^{iv}	95.85 (15)	H8A—C8—H8B	109.5
O8—Na1—O12^{v}	83.48 (11)	H8A—C8—H8C	109.5
O10^{iv}—Na1—O12^{v}	178.80 (19)	H8B—C8—H8C	109.5
C1—O1—Ga1	127.3 (4)	H2A—N2—H2B	109.5
C1—O2—Na1^{vi}	117.3 (4)	H2A—N2—H2C	109.5
C2—O3—Ga1	128.3 (3)	H2B—N2—H2C	109.5
C2—O4—Na1^{vii}	123.5 (3)	C9—N2—H2A	109.5
C3—O5—Ga1	126.0 (4)	C9—N2—H2B	109.5
C3—O6—Na1^{viii}	119.7 (3)	C9—N2—H2C	109.5
C4—O7—Ga1	124.6 (3)	N2—C9—H9A	109.3
C4—O8—Na1	130.5 (3)	N2—C9—H9B	109.3
C5—O9—Ga1	127.2 (3)	H9A—C9—H9B	107.9
C5—O10—Na1^{ix}	120.0 (3)	C10—C9—N2	111.7 (5)
C6—O11—Ga1	127.6 (3)	C10—C9—H9A	109.3
C6—O12—Na1^{x}	120.1 (3)	C10—C9—H9B	109.3
O1—C1—H1	117.9	C9—C10—H10A	109.5
O2—C1—O1	124.2 (6)	C9—C10—H10B	109.5
O2—C1—H1	117.9	C9—C10—H10C	109.5
O3—C2—H2	117.4	H10A—C10—H10B	109.5
O4—C2—O3	125.1 (4)	H10A—C10—H10C	109.5
O4—C2—H2	117.4	H10B—C10—H10C	109.5
Ga1—O1—C1—O2	169.6 (4)	Na1^{vi}—O2—C1—O1	177.7 (4)
Ga1—O3—C2—O4	−179.2 (3)	Na1^{vii}—O4—C2—O3	−179.8 (3)
Ga1—O5—C3—O6	−178.8 (3)	Na1^{viii}—O6—C3—O5	179.5 (3)
Ga1—O7—C4—O8	179.2 (3)	Na1—O8—C4—O7	−165.7 (3)
Ga1—O9—C5—O10	178.9 (3)	Na1^{ix}—O10—C5—O9	172.5 (3)
Ga1—O11—C6—O12	177.5 (3)	Na1^{x}—O12—C6—O11	−170.9 (3)
391 K			
Ga1—O1	1.967 (10)	N1A—C7A	1.47 (8)
Ga1—O3	1.977 (5)	C7A—H7AA	0.9700
Ga1—O5	1.968 (9)	C7A—H7AB	0.9700
Ga1—O7	1.977 (5)	C7A—C8A	1.16 (5)
Ga1—O9	1.984 (5)	C8A—H8AA	0.9600
Ga1—O11	1.981 (6)	C8A—H8AB	0.9600
Na1—O2^{viii}	2.436 (15)	C8A—H8AC	0.9600
Na1—O4^{vii}	2.386 (11)	N2A—H2AA	0.8900
Na1—O6^{vi}	2.439 (15)	N2A—H2AB	0.8900
Na1—O8	2.435 (12)	N2A—H2AC	0.8900
Na1—O10^{x}	2.547 (8)	N2A—C9A	1.49 (3)
Na1—O12^{ix}	2.558 (8)	C9A—H9AA	0.9700
O1—C1	1.259 (18)	C9A—H9AB	0.9700
O2—Na1^{iii}	2.436 (15)	C9A—C10A	1.56 (2)
O2—C1	1.237 (19)	C10A—H10A	0.9600
O3—C2	1.291 (11)	C10A—H10B	0.9600
O4—Na1^{ii}	2.386 (11)	C10A—H10C	0.9600
O4—C2	1.200 (11)	N1B—H1BA	0.8900
O5—C3	1.270 (18)	N1B—H1BB	0.8900
O6—Na1^{i}	2.439 (15)	N1B—H1BC	0.8900
O6—C3	1.208 (19)	N1B—C7B	1.53 (6)
O7—C4	1.260 (10)	C7B—H7BA	0.9700

O8—C4	1.217 (11)	C7B—H7BB	0.9700
O9—C5	1.272 (11)	C7B—C8B	1.64 (3)
O10—Na1^{v}	2.547 (8)	C8B—H8BA	0.9600
O10—C5	1.222 (11)	C8B—H8BB	0.9600
O11—C6	1.263 (10)	C8B—H8BC	0.9600
O12—Na1^{iv}	2.558 (8)	N2B—H2BA	0.8900
O12—C6	1.226 (10)	N2B—H2BB	0.8900
C1—H1	0.9300	N2B—H2BC	0.8900
C2—H2	0.9300	N2B—C9B	1.37 (5)
C3—H3	0.9300	C9B—H9BA	0.9700
C4—H4	0.9300	C9B—H9BB	0.9700
C5—H5	0.9300	C9B—C10B	1.38 (4)
C6—H6	0.9300	C10B—H10D	0.9600
N1A—H1AA	0.8900	C10B—H10E	0.9600
N1A—H1AB	0.8900	C10B—H10F	0.9600
N1A—H1AC	0.8900		
O1—Ga1—O3	90.3 (3)	N1A—C7A—H7AA	103.2
O1—Ga1—O5	178.5 (5)	N1A—C7A—H7AB	103.2
O1—Ga1—O7	89.4 (3)	H7AA—C7A—H7AB	105.2
O1—Ga1—O9	89.0 (3)	C8A—C7A—N1A	136 (5)
O1—Ga1—O11	91.3 (3)	C8A—C7A—H7AA	103.2
O3—Ga1—O9	88.8 (2)	C8A—C7A—H7AB	103.2
O3—Ga1—O11	91.8 (2)	C7A—C8A—H8AA	109.5
O5—Ga1—O3	88.4 (3)	C7A—C8A—H8AB	109.5
O5—Ga1—O7	91.9 (3)	C7A—C8A—H8AC	109.5
O5—Ga1—O9	90.3 (3)	H8AA—C8A—H8AB	109.5
O5—Ga1—O11	89.4 (3)	H8AA—C8A—H8AC	109.5
O7—Ga1—O3	179.2 (3)	H8AB—C8A—H8AC	109.5
O7—Ga1—O9	90.5 (2)	H2AA—N2A—H2AB	109.5
O7—Ga1—O11	89.0 (3)	H2AA—N2A—H2AC	109.5
O11—Ga1—O9	179.3 (3)	H2AB—N2A—H2AC	109.5
O2^{viii}—Na1—O6^{vi}	175.6 (4)	C9A—N2A—H2AA	109.5
O2^{viii}—Na1—O10^{x}	85.6 (4)	C9A—N2A—H2AB	109.5
O2^{viii}—Na1—O12^{ix}	94.8 (4)	C9A—N2A—H2AC	109.5
O4^{vii}—Na1—O2^{viii}	91.5 (4)	N2A—C9A—H9AA	110.2
O4^{vii}—Na1—O6^{vi}	91.2 (5)	N2A—C9A—H9AB	110.2
O4^{vii}—Na1—O8	176.2 (5)	N2A—C9A—C10A	107.4 (15)
O4^{vii}—Na1—O10^{x}	95.8 (4)	H9AA—C9A—H9AB	108.5
O4^{vii}—Na1—O12^{ix}	84.4 (2)	C10A—C9A—H9AA	110.2
O6^{vi}—Na1—O10^{x}	90.6 (3)	C10A—C9A—H9AB	110.2
O6^{vi}—Na1—O12^{ix}	89.0 (4)	C9A—C10A—H10A	109.5
O8—Na1—O2^{viii}	87.0 (5)	C9A—C10A—H10B	109.5
O8—Na1—O6^{vi}	90.6 (4)	C9A—C10A—H10C	109.5
O8—Na1—O10^{x}	87.6 (2)	H10A—C10A—H10B	109.5
O8—Na1—O12^{ix}	92.3 (4)	H10A—C10A—H10C	109.5
O10^{x}—Na1—O12^{ix}	179.6 (6)	H10B—C10A—H10C	109.5
C1—O1—Ga1	126.3 (10)	H1BA—N1B—H1BB	109.5
C1—O2—Na1^{iii}	118.9 (9)	H1BA—N1B—H1BC	109.5
C2—O3—Ga1	126.2 (5)	H1BB—N1B—H1BC	109.5
C2—O4—Na1^{ii}	130.4 (7)	C7B—N1B—H1BA	109.5
C3—O5—Ga1	127.4 (9)	C7B—N1B—H1BB	109.5
C3—O6—Na1^{i}	119.3 (9)	C7B—N1B—H1BC	109.5
C4—O7—Ga1	127.8 (6)	N1B—C7B—H7BA	111.4
C4—O8—Na1	125.9 (6)	N1B—C7B—H7BB	111.4

C5—O9—Ga1	128.5 (6)	N1B—C7B—C8B	102 (2)
C5—O10—Na1^{v}	120.1 (6)	H7BA—C7B—H7BB	109.3
C6—O11—Ga1	127.7 (5)	C8B—C7B—H7BA	111.4
C6—O12—Na1^{iv}	119.9 (6)	C8B—C7B—H7BB	111.4
O1—C1—H1	117.8	C7B—C8B—H8BA	109.5
O2—C1—O1	124.4 (14)	C7B—C8B—H8BB	109.5
O2—C1—H1	117.8	C7B—C8B—H8BC	109.5
O3—C2—H2	117.4	H8BA—C8B—H8BB	109.5
O4—C2—O3	125.2 (9)	H8BA—C8B—H8BC	109.5
O4—C2—H2	117.4	H8BB—C8B—H8BC	109.5
O5—C3—H3	117.5	H2BA—N2B—H2BB	109.5
O6—C3—O5	125.1 (13)	H2BA—N2B—H2BC	109.5
O6—C3—H3	117.5	H2BB—N2B—H2BC	109.5
O7—C4—H4	117.4	C9B—N2B—H2BA	109.5
O8—C4—O7	125.1 (8)	C9B—N2B—H2BB	109.5
O8—C4—H4	117.4	C9B—N2B—H2BC	109.5
O9—C5—H5	116.9	N2B—C9B—H9BA	108.1
O10—C5—O9	126.2 (9)	N2B—C9B—H9BB	108.1
O10—C5—H5	116.9	N2B—C9B—C10B	117 (3)
O11—C6—H6	117.1	H9BA—C9B—H9BB	107.3
O12—C6—O11	125.9 (8)	C10B—C9B—H9BA	108.1
O12—C6—H6	117.1	C10B—C9B—H9BB	108.1
H1AA—N1A—H1AB	109.5	C9B—C10B—H10D	109.5
H1AA—N1A—H1AC	109.5	C9B—C10B—H10E	109.5
H1AB—N1A—H1AC	109.5	C9B—C10B—H10F	109.5
C7A—N1A—H1AA	109.5	H10D—C10B—H10E	109.5
C7A—N1A—H1AB	109.5	H10D—C10B—H10F	109.5
C7A—N1A—H1AC	109.5	H10E—C10B—H10F	109.5
Ga1—O1—C1—O2	172.5 (8)	Na1^{iii}—O2—C1—O1	178.2 (7)
Ga1—O3—C2—O4	179.2 (7)	Na1^{ii}—O4—C2—O3	−171.2 (7)
Ga1—O5—C3—O6	−176.6 (8)	Na1^{i}—O6—C3—O5	−179.5 (7)
Ga1—O7—C4—O8	−176.6 (7)	Na1—O8—C4—O7	178.1 (7)
Ga1—O9—C5—O10	−179.5 (6)	Na1^{v}—O10—C5—O9	173.3 (7)
Ga1—O11—C6—O12	178.1 (7)	Na1^{iv}—O12—C6—O11	−175.0 (8)

Symmetry code(s): (i) $x-1/2, -y+1, z-1/2$; (ii) $x-1, y+1, z$; (iii) $x-1/2, -y+1, z+1/2$; (iv) $x, y+1, z$; (v) $x-1, y, z$; (vi) $x+1/2, -y+1, z+1/2$; (vii) $x+1, y-1, z$; (viii) $x+1/2, -y+1, z-1/2$; (ix) $x, y-1, z$; (x) $x+1, y, z$.

Tab. S4. Selected hydrogen-bond parameters for (**1**), $[CH_3CH_2NH_3]_2NaGa(HCOO)_6$, at 293 and 391 K.

D—H···*A*	*D*—H (Å)	H···*A* (Å)	*D*···*A* (Å)	*D*—H···*A* (°)
293 K				
C2—H2···O5	0.93	2.55	3.041 (5)	113.0
C4—H4···O1	0.93	2.49	2.953 (6)	110.7
N1—H1A···O7^{i}	0.89	2.09	2.974 (4)	176.0
N1—H1A···O8^{i}	0.89	2.55	3.158 (5)	125.9
N1—H1B···O12^{ii}	0.89	1.98	2.865 (5)	170.6
N1—H1C···O2	0.89	2.01	2.869 (5)	162.5
C7—H7A···O8^{i}	0.97	2.53	3.056 (6)	113.8
N2—H2A···O10	0.89	1.99	2.865 (4)	167.7
N2—H2B···O3^{iii}	0.89	2.13	2.971 (4)	156.4
N2—H2B···O4^{iii}	0.89	2.45	3.209 (5)	144.0
N2—H2C···O5^{ii}	0.89	2.58	3.277 (5)	135.7
N2—H2C···O6^{ii}	0.89	2.13	2.967 (5)	155.7
C9—H9B···O9	0.97	2.52	3.189 (6)	126.4
391 K				
C2—H2···O1	0.93	2.49	2.970 (13)	112.2
C4—H4···O5	0.93	2.57	3.031 (12)	111.4
N1A—H1AA···O12^{ii}	0.89	2.07	2.88 (9)	150.4
N1A—H1AB···O2	0.89	1.97	2.85 (8)	166.7
N1A—H1AC···O3^{iv}	0.89	2.18	3.02 (8)	157.7
N1A—H1AC···O4^{iv}	0.89	2.48	3.25 (7)	145.1
C7A—H7AB···O11^{ii}	0.97	2.41	3.15 (4)	132.9
N2A—H2AA···O7^{v}	0.89	2.29	3.11 (2)	152.8
N2A—H2AA···O8^{v}	0.89	2.52	3.31 (2)	148.3
N2A—H2AB···O5^{ii}	0.89	2.57	3.28 (3)	137.3
N2A—H2AB···O6^{ii}	0.89	2.20	3.00 (3)	149.7
N2A—H2AC···O10	0.89	1.86	2.74 (2)	168.1
C9A—H9AA···O9	0.97	2.39	3.127 (16)	132.5
C10A—H10A···O11^{vi}	0.96	2.64	3.442 (18)	141.1
N1B—H1BA···O12^{ii}	0.89	2.00	2.88 (6)	169.8
N1B—H1BB···O2	0.89	2.13	2.95 (5)	152.0
N1B—H1BC···O3^{iv}	0.89	2.05	2.93 (5)	173.9
N1B—H1BC···O4^{iv}	0.89	2.57	3.12 (4)	120.6
C7B—H7BA···O4^{iv}	0.97	2.42	2.98 (2)	116.3
C8B—H8BB···O1	0.96	2.55	3.40 (2)	148.2
C8B—H8BC···O11^{ii}	0.96	2.64	3.444 (19)	141.3
N2B—H2BA···O7^{v}	0.89	1.98	2.85 (4)	167.6
N2B—H2BA···O8^{v}	0.89	2.40	3.01 (4)	126.1
N2B—H2BB···O10	0.89	2.26	3.09 (4)	154.0
N2B—H2BC···O6^{ii}	0.89	2.04	2.91 (5)	165.0

Symmetry code(s): (i) $x-1/2, -y+1, z+1/2$; (ii) $x-1, y, z$; (iii) $x-1/2, -y, z-1/2$; (iv) $x-1/2, -y+2, z+1/2$; (v) $x-1/2, -y+1, z-1/2$; (vi) $x-1/2, -y+2, z-1/2$.

Tab. S5. Proposed assignment of Raman bands for **(1)**, $[CH_3CH_2NH_3]_2NaGa(HCOO)_6$ and **(2)**, $[CH_3CH_2NH_3]_2NaGa_{0.069}Cr_{0.931}(HCOO)_6$.

(1) (cm^{-1})	**(2)** (cm^{-1})	Assignment
3102_{vw}	3102_{vw}	$\nu(NH_3^+)$
3036_m, 3018_w, 2996_w, 2979_s, 2952_s, 2927_m	3035_m, 3017_w, 2995_w, 2978_s, 2952_s, 2927_m	$\nu(CH_3)+\nu(CH_2)$
2898_{vs}, 2885_{vs}, 2861_{vs}	2893_{vs}, 2880_{vs}, 2857_{vs}	$\nu(CH)$
2784_{vw}, 2753_w, 2120_{vw}	2785_{vw}, 2746_w, 2111_{vw}	ov+cb
1676_w, 1649_{vw}, 1628_{vw}	1671_w, 1648_{vw}, 1627_{vw}	$\delta_{as}(NH_3^+)+\nu_{as}(OCO)$
1588_{vw}	1589_{vw}	$\nu_{as}(OCO)$
1502_{vw}	1497_{vw}	$\delta_s(NH_3^+)$
1459_w, 1451_w	1458_w, 1451_w	$\delta(CH_3)+\delta(CH_2)$
1385_m, 1370_{sh}, 1340_m	1382_m, 1372_{sh}, 1338_m	$\delta_{ip}(CH)$
1326_w, 1320_{sh}, 1304_w	1328_w, 1318_{sh}, 1307_w	$\nu_s(OCO)$
1288_w, 1274_{vw}	1288_w, 1277_{vw}	$\rho(CH_2)+\nu_s(OCO)$
1229_{vw}, 1211_w	1230_{vw}, 1210_w	$\rho(CH_2)$
1058_w, 1049_w	1056_w, 1050_w	$\delta_{ip}(CH)+\nu_{as}(CCN)$
1012_{vw}, 999_{vw}	1011_{vw}, 997_{vw}	$\rho(NH_3^+)$
878_{sh}, 875_w	878_{sh}, 875_w	$\nu_s(CCN)$
804_w, 790_w	804_w, 790_w	$\delta(OCO)$
427_w	428_w	$\delta(CCN)$
338_w	341_w	$T'(Na^+)$
294_w, 255_w	243_w	$T'(Na^+)+T'(M^{III})+T'(HCOO^-)$
189_m, 163_m, 146_{sh}, 126_m, 109_{sh}	187_m, 163_m, 146_{sh}, 128_m, 108_{sh}	$L(HCOO^-)$

Key: s, strong; m, medium; w, weak; vw, very weak; sh, shoulder; ν, stretching vibration (s, symmetric; as, antisymmetric); δ, bending vibration (ip, in-plane; op, out-of-plane); ρ, rocking vibration; T', translation; L, libration.

Ta. S6. Proposed assignment of IR bands for **(1)**, $[CH_3CH_2NH_3]_2NaGa(HCOO)_6$, at 80 and 400 K.

(1) (cm^{-1}) 80 K	**(1)** (cm^{-1}) 400 K	Assignment
3163_{vw}, 3074_w, 3052_w,	$3068_{vw,b}$	$\nu(NH_3^+)$
3026_{vw}, 3019_{vw}, 3012_{vw}, 2993_w, 2972_{vw}, 2948_{vw}, 2924_{vw}, 2905_{vw}	3030_{vw}, 2997_{vw}, 2978_s, 2984_{vw}, 2951_{vw}	$\nu(CH_3)+\nu(CH_2)$
2898_w, 2887_w, 2861_{vw}, 2841_{vw}, 2824_w	2880_{vw}, $2816_{vw,b}$	$\nu(CH)$
2757_{vw}, 2741_{vw}, 2723_{vw}, 2710_{vw}, 2666_{vw}, 2647_{vw}, 2636_{vw}, 2525_{vw}, 2516_{vw}	2753_{vw}, 2706_{vw}, 2655_{vw}, 2498_{vw}	ov+cb
1661_{sh}, 1655_{vs}, 1642_{vs}, 1634_{vs}, 1606_{vs}, 1603_{vs}	1644_{sh}, 1631_{vs}, 1611_{sh}	$\delta_{as}(NH_3^+)+\nu_{as}(OCO)$
1576_w	1589_{vw}	$\nu_{as}(OCO)$
1515_{vw}, 1505_{vw}	1500_{vw}	$\delta_s(NH_3^+)$
1472_{vw}, 1468_{vw}, 1461_{vw}, 1446_{vw}	1471_{vw}	$\delta(CH_3)+\delta(CH_2)$
1395_{vw}, 1387_w, 1377_{vw}, 1350_{vw}, 1340_w	1398_{sh}, 1386_w, 1344_{sh}	$\delta_{ip}(CH)$
1327_{vs}, 1324_{sh}, 1305_w	1325_s	$\nu_s(OCO)$
1284_s, 1273_{vw}	1297_{sh}, 1282_w	$\rho(CH_2)+\nu_s(OCO)$
1233_{vw}, 1213_{vw}, 1186_{vw}	1227_{vw}, 1207_{vw}	$\rho(CH_2)$
1053_{vw}	1048_{vw}, 1050_w	$\delta_{ip}(CH)+\nu_{as}(CCN)$

1019_{vw}, 1002_{vw}	1007_{vw}	$\rho(NH_3^+)$
816_w, 812_{sh}, 807_w, 791_{vw}, 787_{vw}	810_w, 806_{sh}, 793_{vw}	δ(OCO)

Key: s, strong; m, medium; w, weak; vw, very weak; sh, shoulder; b, broad; ν, stretching vibration (s, symmetric; as, antisymmetric); δ, bending vibration (ip, in-plane; op, out-of-plane); ρ, rocking vibration; T', translation; L, libration.

10.3 Publication P3

RESEARCH ARTICLE

ADVANCED OPTICAL MATERIALS
www.advopticalmat.de

Real-Time Temperature Monitoring with Cr^{3+}-Based Hybrid Formate Perovskites: Insights into the Relation Between Chemical Composition and Thermometric Performance

Adam Kabański, Maciej Ptak, Luís Dias Carlos, and Dagmara Stefańska**

Metal–organic frameworks (MOFs) exhibiting perovskite-like structures have become a significant object of study due to their structural, phonon, and optical features. Temperature-dependent luminescence is a valuable property within the context of luminescence thermometry. Herein, we report structural and spectroscopic studies of a series of $[DMA]M^{II}_{1-x}Cr_x(HCOO)_3$, where DMA = dimethylammonium cation, x = 0, 0.01, 0.03, and 0.05, while $M^{II} = Zn^{2+}$, Mn^{2+}, Mg^{2+}, Co^{2+}, and Ni^{2+}. The influence of the metal type on crystal field strength (Dq/B) is determined with diffuse reflectance spectroscopy. Additionally, the estimation of the crystal field strength is performed with the analysis of the metal-oxygen distance. Conducted Raman, IR, and XRD analysis provide information on the relationship between structural properties and chemical composition. To investigate the thermometric potential of obtained materials the temperature-dependent luminescence measurements (80–300 K) are implemented. Obtained results show the extraordinary potential of hybrid compounds for luminescence thermometry (relative senitivity (S_r)up to 2.49%•K^{-1} at 160 K). The exemplary system based on luminescent thermometers for remote temperature measurements in dynamic systems has been additionally proposed. The presented results show a significant relationship between the surrounding temperature, chemical composition, and spectroscopic properties, allowing to design of a temperature sensing model for time-resolved measurements.

1. Introduction

Hybrid perovskites with the general formula ABX_3, which contain organic cations A, divalent metal ions B, and halide ligands X, have become an important area of research in recent years due to their multifunctional properties and uncomplicated synthesis procedure.[1,2] Perovskite-like metal-organic frameworks have been extensively investigated thanks to their ferroelectric, multiferroic, magnetic, and luminescent properties.[1,3–5] Among several subgroups of hybrid compounds, particular attention has been gained to compounds based on formate anions at the X site with the general formula $[A][M(HCOO)_3]_n$. Materials containing dimethylammonium (DMA^+) cations have been extensively studied, especially those with the metals Mn, Zn, Ni, Co, and Fe.[6–8] All of them crystallize in the trigonal space group $R\bar{3}c$, where DMA^+ cations are positioned in three equivalent but disordered sites. The first metal-organic formate containing DMA^+ (DMANaFe) was obtained in 2014 by Mączka et al.[9] Subsequent studies have shown that the incorporation of Cr^{3+} ions in the Fe^{3+} site significantly suppresses the phase transition and that low temperature freezes the rotation of DMA^+ around the trigonal axis.[10] The structural order-disorder phase transition in these perovskite-type formates is mainly driven by DMA^+ cation dynamics and framework deformation. It was found that the temperature of the order-disorder phase transition depends on the type of metal center, with a transition temperature of 155–185 K.[3,6,11–16] The loss of DMA^+ threefold symmetry coincides with the observed phase transitions, and the strengthening of hydrogen bonds at lower temperatures often results in the ordering of DMA^+ cations, framework distortion, and the appearance of long-range electric order.[17,18] The structural and luminescence properties of $[DMA]Na_{0.5}Cr_{0.5}(HCOO)_3$ and $[DMA]K_{0.5}Cr_{0.5}(HCOO)_3$ have been recently studied.[10,19] In $[DMA]K_{0.5}Cr_{0.5}(HCOO)_3$, the dopant ions exhibit a narrow, spin-forbidden transition from the ^2E_g excited level to the $^4A_{2g}$ ground state at low temperature (5 K). The emission of Cr^{3+} ions was significantly quenched with temperature and almost disappeared at 150 K. However, the emission of chromium ions in the Na^+ compound is much more stable. At 10 K, as in the case of K^+ analog, only emission from the ^2E_g state is observed, but as the temperature increases, the $^4T_{2g}$ state becomes thermally

A. Kabański, M. Ptak, D. Stefańska
Institute of Low Temperature and Structure Research
Polish Academy of Sciences
Wroclaw 50–422, Poland
E-mail: a.kabanski@intibs.pl; d.stefanska@intibs.pl
L. D. Carlos
Phantom-g
CICECO – Aveiro Institute of Materials
Physics Department
University of Aveiro
Aveiro 3810-193, Portugal
The ORCID identification number(s) for the author(s) of this article can be found under https://doi.org/10.1002/adom.202501057

DOI: 10.1002/adom.202501057

populated and emission lines from both the ^2E_g and the $^4T_{2g}$ levels were recorded.[19]

The spectroscopic properties of chromium ions, such as their two main emission bands, depend on the local environment and temperature. The co-existence of two types of emission (spin-allowed from the $^4T_{2g}$ level and spin-forbidden from the ^2E_g level) can be used to detect temperature, which is a promising approach for remote temperature measurements.[1,20–24] Remote temperature sensing has numerous advantages, including the ability to implement it at the micro- and nanoscale, as well as high accuracy and fast response times.[25–27] Luminescent materials used for temperature sensing can be divided into several groups, including those containing rare-earth metal ions[28–30] transition metal ions,[21,31] and compounds with mixed systems containing chromium and lanthanide ions.[32,33] The potential of trivalent chromium ions for high thermal sensing has been reported for several inorganic materials, but solutions based on metal–organic frameworks are a fairly new area.

Research efforts have focused on improving the performance of chromium ions as temperature sensors. Various approaches have been explored, including the development of new host materials, optimization of doping concentrations, and the investigation of luminescence dynamics. New host materials can be used to improve the luminescence efficiency of Cr^{3+} ions and to reduce the influence of external factors on temperature sensitivity. The doping concentration can be optimized to improve the signal-to-noise ratio and to better understand the temperature-dependent quenching mechanisms, as well as develop new strategies to improve the performance of chromium ions as temperature sensors.[1,20,24,34–40]

In the present study, the effect of divalent metal cation M^{II} (Mn^{2+}, Mg^{2+}, Zn^{2+}, Co^{2+}, Ni^{2+}) on the structural and luminescence properties of $[DMA]M^{II}_{1-x}Cr_x(HCOO)_3$ (where x = 0.01, 0.03, 0.05) was investigated applying various techniques such as powder XRD, Raman and IR spectroscopy, as well as absorption and linear optical spectroscopy. The synthesized compounds exhibited a strong correlation between temperature and the type of observed luminescence. Special attention was focused on the possibility of applying obtained hybrid organic-inorganic formate perovskites as luminescent thermometers. For this purpose, we proposed an exemplary sensor setup that allows temperature time-resolved monitoring in the cryogenic temperature range.

2. Results

2.1. Structural Properties

The crystal structure of $[DMA]M^{II}(HCOO)_3$ (M^{II} = Zn^{2+}, Mn^{2+}, Mg^{2+}, Co^{2+}, Ni^{2+}) compounds has been studied in detail over the past few years.[14,16,41,42] Therefore, they are described briefly, with an emphasis on the most important features that characterize this type of material. In the structure of $[DMA]M^{II}(HCOO)_3$, metal ions are connected by formate linkers in three directions, forming a 3D coordination polymeric network consisting of $M^{II}O_6$ octahedra (**Figure 1**). Such a framework creates voids filled with DMA^+ cations, balancing the negative charge of the metal-formate framework. The DMA^+ cations are bound by hydrogen N–H···O bonds that, at low temperatures, are strong enough to freeze the dynamics of the cation. Upon heating to 156–270 K,

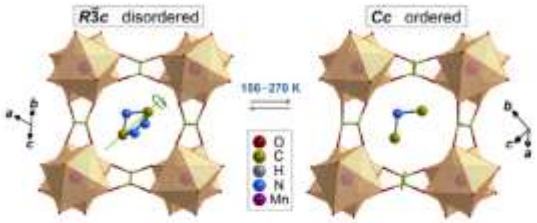

Figure 1. Schematic illustration of $[DMA]M^{II}(HCOO)_3$ crystal structure in the disordered (left) and ordered phase (right). Above the arrow are the temperatures at which the phase transition occurs.

depending on M^{II}, $[DMA]M^{II}(HCOO)_3$ compounds undergo an order-disorder phase transition, which results in the release of cation three-fold disorder around the trigonal axis (Figure 1).[14,16] According to the literature data, this phase transition to the high-temperature $R\bar{3}c$ phase is accompanied by reducing octahedral deformation.[14,16,41]

To confirm the quality of the obtained crystals and the influence of Cr^{3+} ions on the structure, the powder X-ray diffraction patterns were measured and compared to the simulated ones based on the single-crystal data.[6,14,16,41,43,44] Figure S1 presents diffractograms recorded for each sample and demonstrates that all obtained crystals are phase-pure and that the aliovalent doping with Cr^{3+} ions up to 5 mol% has no effect on the hexagonal $R\bar{3}c$ symmetry. Investigated materials can be doped up to 5 mol.% of chromium(III) ions. This limitation is most likely linked to the charge mismatch occurring under an increase in the Cr^{3+}/M^{2+} ratio and resulting structural destabilization caused by defects.

2.2. Phonon Properties

To further understand the fundamental properties of the obtained crystals, Raman and IR spectra were collected. The ATR and Raman spectra of all samples (Figure S2, Supporting Information) are highly comparable to those obtained during previous studies,[16,45,46] demonstrating that all crystals adopt the hexagonal phase at ambient temperature. Table S1 (Supporting Information) presents the assignments of the observed IR and Raman bands based on the previous detailed studies.[16,45,46] The differences in the spectra observed for different metal ions (**Figure 2**), i.e., down- or up-shifts, changes in intensity, or various numbers of components, are caused by differences in the crystal lattice structural parameters, the size of the ionic radii of the metal ions, their electronegativity, the size of the perovskite cavities in which the organic cation is located, and the strength of the hydrogen bonds.

Aliovalent doping with Cr^{3+} ions at concentrations ranging from 1 to 5 mol% results in no notable changes in the recorded spectra. With higher doping, certain bands shift or broaden up to 1–2 cm^{-1}, which is related to an increase in substitutional disorder and the creation of defects. This effect is demonstrated as a function of tolerance factor (TF) for three selected bands, namely symmetric OCO stretching, ν_{sCOO}, OCO bending, δ_{OCO}, and symmetric CNC stretching, ν_{sCNC} (Figure S3). The TF values were calculated for each sample composition using the methodology introduced by Kieslich et al. for hybrid

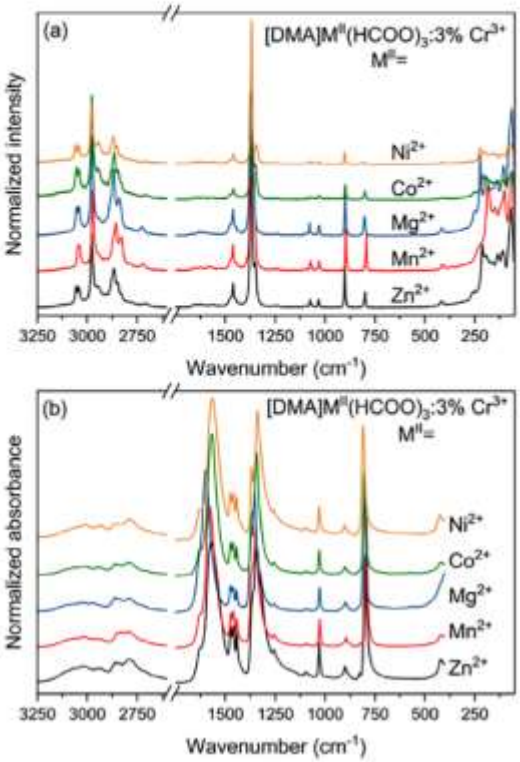

Figure 2. Comparison of Raman (a) and IR (b) spectra of [DMA]M^{II}(HCOO)$_3$ (M^{II} = Zn^{2+}, Mn^{2+}, and Mg^{2+}, Co^{2+}, and Ni^{2+}) doped with 3 mol.% Cr^{3+} ions.

formate-based perovskites.[47,48] The ν_{sCOO} vibrations are the most susceptible to the Cr^{3+} substitution, which is expected due to the direct bonding of oxygen atoms with M^{II}/Cr^{3+} ions. In the studied concentration range of 0–5 mol.%, the observed upshifts with increased doping levels reach 0.2-2.0 cm^{-1}. The upshifts observed for δ_{OCO} are weaker (0-0.95 cm^{-1}) and the vibrations originating from the organic cation are less sensitive to metal ion substitutions, with maximum upshifts of 0.6 cm^{-1}.

2.3. Diffuse Reflectance Spectroscopy

To investigate the presence of the Cr^{3+} ions and crystal field parameters, the room-temperature diffuse reflectance spectroscopy (DRS) has been used. **Figure 3a** presents the representative collation of the diffuse reflectance spectra of the [DMA]Zn$_{1-x}$Cr$_x$(HCOO)$_3$ (x = 0.01, 0.03, 0.05). Main bands are localized at about 17233 cm^{-1} (580 nm) and 23940 cm^{-1} (nm), representing the allowed $^4A_{2g}\rightarrow{}^4T_{1g}$ and $^4A_{2g}\rightarrow{}^4T_{2g}$ transitions, respectively. Additionally, the low-intensity lines around 15550 cm^{-1} are present and can be attributed to the $^4A_{2g}\rightarrow{}^2E_g$ spin-forbidden transition. Within the investigated series, the change in the Cr^{3+} ion concentration does not significantly affect the position of the absorption bands. The presence of the specific absorption bands is also visible in representative Mn- and Mg-related results (Figure 3b). A more comprehensive description of diffuse reflectance spectra of chromium-based perovskites has recently been reported.[1] The comparison of DRS spectra of [DMA]M$^{II}_{0.97}$Cr$_{0.03}$(HCOO)$_3$ (M^{II} = Zn^{2+}, Mg^{2+}) is presented in Figure S4 (Supporting Information). The series of DMA with Zn and Mg ions exhibit symmetric absorption spectra, which is characteristic of Cr^{3+} ions.[1,49] For the representative samples with Mg ions, the excitation spectra monitored at the R line were recorded at 80 K (Figure S5a, Supporting Information). The Cr^{3+} bands' positions agree with the results from DRS. However, the analysis of the excitation spectrum of Mn-based compounds shows the presence of both types of excitation bands – originating from Mn^{2+} and Cr^{3+} (Figure S5b, Supporting Information). The sample of the material containing solely Mn^{2+} ions exhibits several excitation bands assigned to transitions from $^6A_1$ to ^4E, $^4T_2$, $^4A_1$, ^4E, and $^4T_1$ energetical levels. On the other hand, Co- and Ni-derivatives show significantly changed absorption spectra (Figure S6, Supporting Information). For cobalt-based materials, a broad absorption origin from $^4T_{1g}\rightarrow{}^4A_{2g}$ and $^4T_{1g}\rightarrow{}^4T_{2g}$ is observed. The sample of Ni-based compound without Cr^{3+} ion shows a series of specific absorption bands assigned to the transition from $^3A_{2g}$ ground state to the $^3T_{1g}$, $^3T_{2g}$, $^1A_{1g}$, and ^1E_g.[50]

The obtained results have been used to determine the crystal field (CF) and Racah parameters (*D*q, B, and C). The procedure of the crystal field parameters determination has been precisely described in the literature.[1] As can be seen in Figures S5 and S6 (Supporting Information), the absorption bands of Mn^{2+}, Co^{2+}, and Ni^{2+} overlapped with the absorption peaks of Cr^{3+}. For this reason, direct estimation of the crystal field parameters and thus further analysis of the influence of the CF strength on the luminescence properties will be mainly limited to Mg- and Zn-based materials. Calculated *D*q, B, and C values as well as *D*q/B are listed in Table S2 (Supporting Information). Analysis of the *D*q/B ratio allows for determining crystal field (CF) strength. According to the Tunabe-Sugano diagram, at the *D*q/B = 2.3 the ^2E_g and $^4T_{2g}$ levels overlap. This point categorizes weak (*D*q/B < 2.3) and strong (*D*q/B > 2.3) crystal fields, however, this division is arbitrary. Thus, materials with *D*q/B value near 2.3 might be assigned as intermediate crystal field strength. The influence of the Cr^{3+} ion concentration on crystal field strength is diverse and nonlinear. Zinc-based materials exhibit *D*q/B values from 2.34 (x = 0.01, weak CF), via 2.49 (x = 0.03, strong CF) to 2.36 (x = 0.05, strong CF), which indicates the intermediate and strong crystal field. Magnesium-based samples exhibit greater diversity of *D*q/B parameter – from 2.22 (x = 0.01, weak CF), via 3.42 (x = 0.03, strong CF), to 3.13 (x = 0.05, strong CF).

To compare the obtained results to the initial CF of host materials, the determination of the crystal field strength based on the metal-ligand distance has been performed. The crystal field strength can be calculated with the following formula:

$$CF \propto \frac{1}{R^5} \quad (1)$$

where R is a metal-oxygen distance obtained from the crystallographic information files (CIFs, Mn: *ICSD 194 126*, Mg: CCDC *696 736*, Zn: *ICSD 184 621*). The metal-ligand distance is strongly dependent on the ionic radii of the metal ion. The change in ionic

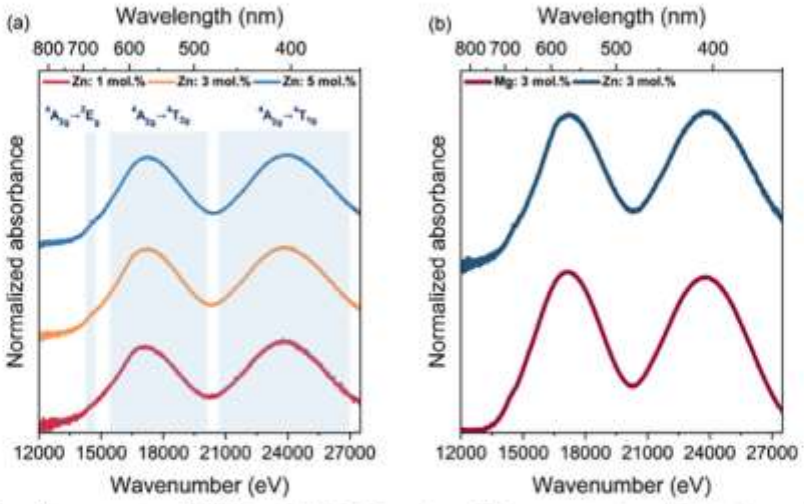

Figure 3. (a) The diffuse reflectance spectra of $[DMA]Zn_{1-x}Cr_x(HCOO)_3$ for various Cr^{3+} ion concentrations; (b) The influence of the metal type on the DRS of $[DMA]M^{II}{}_{1-x}Cr_x(HCOO)_3$ ($M^{II} = Zn^{2+}$, Mg^{2+}).

radii as well as the corresponding M-O distance and CF strength is presented in **Figure 4**.

The presented approach enables us to compare the CF strength in host materials within the undoped series differing in chemical composition. For the Mg^{2+} sample, the initial (without Cr^{3+} doping) crystal field is 0.0250, and for Zn^{2+}-based compounds – 0.0236. The lowest value of CF is, in turn, observed for Mn^{2+} (0.0199). The performed method can not be used for direct comparison of undoped and doped compounds. However, the performed calculation of CF strength in compounds containing Cr^{3+} ions proves the general prediction – higher CF strength is observed for Mg^{2+}-based materials. Even though the presented approach is not directly complementary to estimations conducted with the DRS technique, the method based on M-O distance analysis may be a useful tool in the prediction of the general qualities of Cr^{3+}-doped materials, particularly within the series of host materials differing in chemical composition. What is more, due to the overlapping of the absorption bands assigned to Mn^{2+} and Cr^{3+} ions, the determination of CF strength with the conventional DRS method could not be performed. Thus, this method provides valuable insights into the dependence of the divalent metal ion on CF strength and resulting spectroscopic properties.

2.4. Optical Properties

Zinc-, manganese- and magnesium-based structures exhibit strong Cr^{3+} photoluminescence (PL) properties, while Co- and Ni-based compounds do not show any luminescence. This is due

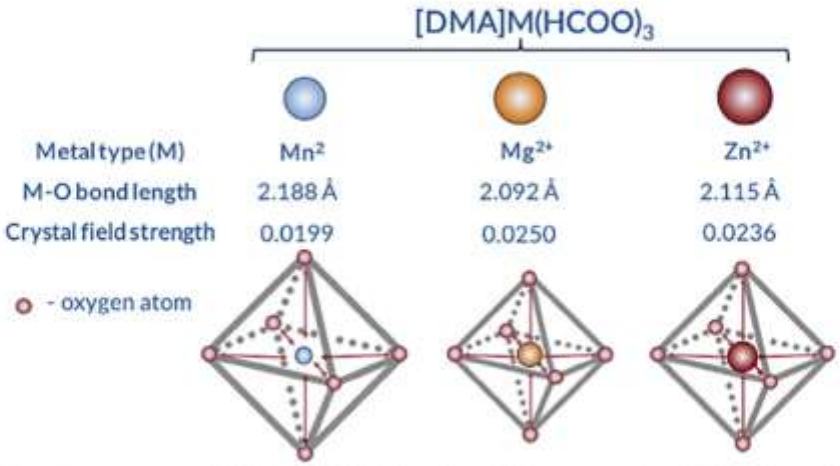

Figure 4. (a) The diffuse reflectance spectra of $[DMA]Zn_{1-x}Cr_x(HCOO)_3$ for various Cr^{3+} ion concentrations; (b) The influence of the metal type on the DRS of $[DMA]M^{II}{}_{1-x}Cr_x(HCOO)_3$ ($M^{II} = Zn^{2+}$, Mg^{2+}).

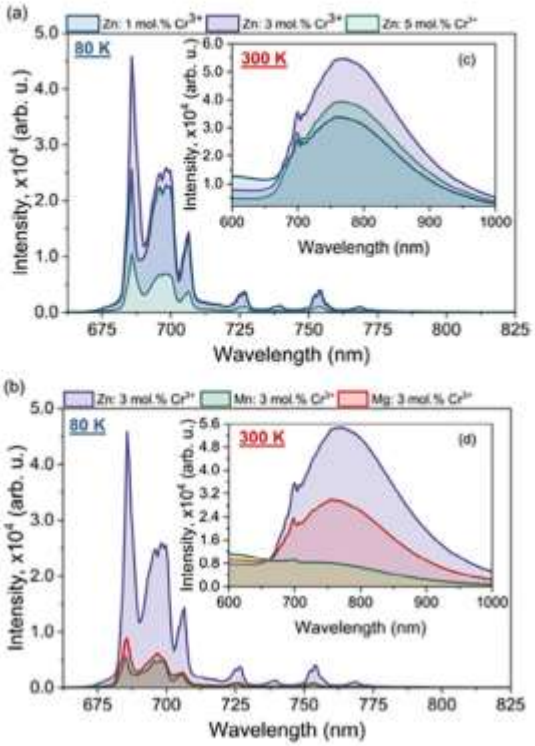

Figure 5. (a) Comparison of emission intensity at 80 K: (a) $[DMA]Zn_{1-x}Cr_x(HCOO)_3$, where x = (0.01, 0.03, 0.05) and (b) $[DMA]M^{II}_{0.97}Cr_{0.03}(HCOO)_3$, where M^{II} = (Zn^{2+}, Mn^{2+}, Mg^{2+}); The insets show comparison of emission intensity at 300 K: (c) $[DMA]Zn_{1-x}Cr_x(HCOO)_3$, where x = (0.01, 0.03, 0.05) and (d) $[DMA]M^{II}_{0.97}Cr_{0.03}(HCOO)_3$, where M^{II} = (Zn^{2+}, Mn^{2+}, Mg^{2+}).

to the strong overlap of Cr^{3+} emission with Co^{2+} and Ni^{2+} absorption bands and the efficient energy transfer to excited Co^{2+} and Ni^{2+} levels. However, due to high concentration of these ions, electrons recombine in a non-radiative way without PL generation. Thus, in this part, particular attention is not paid to Ni- and Co-based materials. Other investigated materials exhibit strong luminescent properties, while the luminescence is under 405 nm excitation. The chosen excitation source corresponds to the $^4A_{2g} \rightarrow {}^4T_{1g}$ transition in Cr^{3+} ions. Spectroscopic characteristics of measured materials are strongly sensitive to the temperature of the environment. At 80 K (**Figure 5a**), the emission spectrum of $[DMA]Zn_{1-x}Cr_x(HCOO)_3$ contains several narrow bands, where the most intensive is observed for 686.1 nm (named R_1 line). Additional Stokes bands localized at 698.3, 706.5, 726.4, and 753.8 nm. The obtained results are typical for low-temperature Cr^{3+} luminescence, especially in hybrid perovskites.[51,52] The rich number of emission bands and their asymmetry may result from a charge mismatch occurring in the Cr^{3+}/M^{2+} MOF structure. This translates into two different optical sites of Cr^{3+} ions and a slight contribution of the emission from the defected Cr^{3+} site. Among the zinc concentration series, the highest emission intensity and quantum efficiency (7.8%) were observed for a sample containing 3 mol.% of Cr^{3+} ions. Presented luminescence measurements were performed comparatively while maintaining the uniformity and stability of experimental conditions. Thus, the obtained results can be directly compared. For the sample containing 1 mol.% of chromium ions, the intensities of the R_1 line, as well as the additional peak at 698.3 nm are reduced. On the other hand, other Stokes bands do not change their intensities. For the sample doped with 5 mol.% of Cr^{3+} ions the highest reduction of the emission, for both the R_1 line and accompanying bands, is noticeable. The quantum efficiency for samples containing 1% and 5% Cr^{3+} ions is slightly lower and amounts to 1.6% and 7.1%, respectively. Comparisons of low-temperature emission spectra of Mn- and Mg-based materials are presented in Figure S7a,b (Supporting Information). For the Mn-based materials, the increase of Cr^{3+} ions induces the reduction of luminescence intensity. Series containing magnesium, in turn, exhibit the weakest luminescence for a sample doped with 1 mol.% of Cr^{3+} ions. On the other hand, the greatest intensity is observed for the 3 mol.% sample. Further increase of chromium trivalent ion concentration leads to about a two-time reduction of the intensity. The change of the main metal type significantly affects the luminescence intensity, which is presented in Figure 5b. For a representative sample containing 3 mol.% of Cr^{3+} ions, the highest intensity of luminescence is observed for Zn-based material while intensities for Mn- and Mg-based samples are approximately nine- and five times weaker, respectively. It is also not surprising that the QE of the manganese and magnesium samples is much lower (3.5% and 1.7%) than that of the Zn-sample. The shape of emission spectra is similar – the most intensive peak is localized at 686.1 nm (R_1 line) as well as bands localized at 698.3, 706.5, 726.4, and 753.8 nm. Measurements within the temperature series were performed in the same conditions thus results presented in Figure 5 and Figure S7 (Supporting Information) can be compared directly, which shows that Zn-based material exhibits the greatest luminescent intensity. An increase in temperature induces a significant reduction of R_1-line intensity. Moreover, the creation of a wide band with a maximum at 769.3 nm is observed (Figure 5c,d). At 300 K, the Zn-based materials containing 3 mol.% of Cr^{3+} ions exhibit the highest intensity, while the weakest emission was recorded for the sample with 1 mol.% of Cr^{3+} ions. Comparisons of emission spectra at 300 K of Mn- and Mg-based samples are presented in Figure S7c,d (Supporting Information).

In the case of materials containing Mn^{2+} ions, the increase in chromium concentration leads to the reduction of luminescence. On the other hand, Mg-samples exhibit the highest emission intensity for the material containing 3 mol.% of Cr^{3+} ions while the weakest emission is observed for the sample with 1 mol.%. The luminescence of the 5 mol.% material is slightly weaker than the 3 mol.% sample. Among materials containing 3 mol.% of chromium trivalent ions, similarly to the measurements at 80 K, the highest luminescence intensity is observed for the Zn-based material and the weakest for the Mn-based one (Figure 5d). Positions of the described broad band and some residues of narrow emission bands remain unchanged. Due to the presence of unshielded *d-d* electronic transitions, characteristic of transition metal ions such as Cr^{3+} ions, its luminescent properties are significantly affected by the crystal field strength of the matrix. The influence of the Dq/B parameter on the spectroscopic

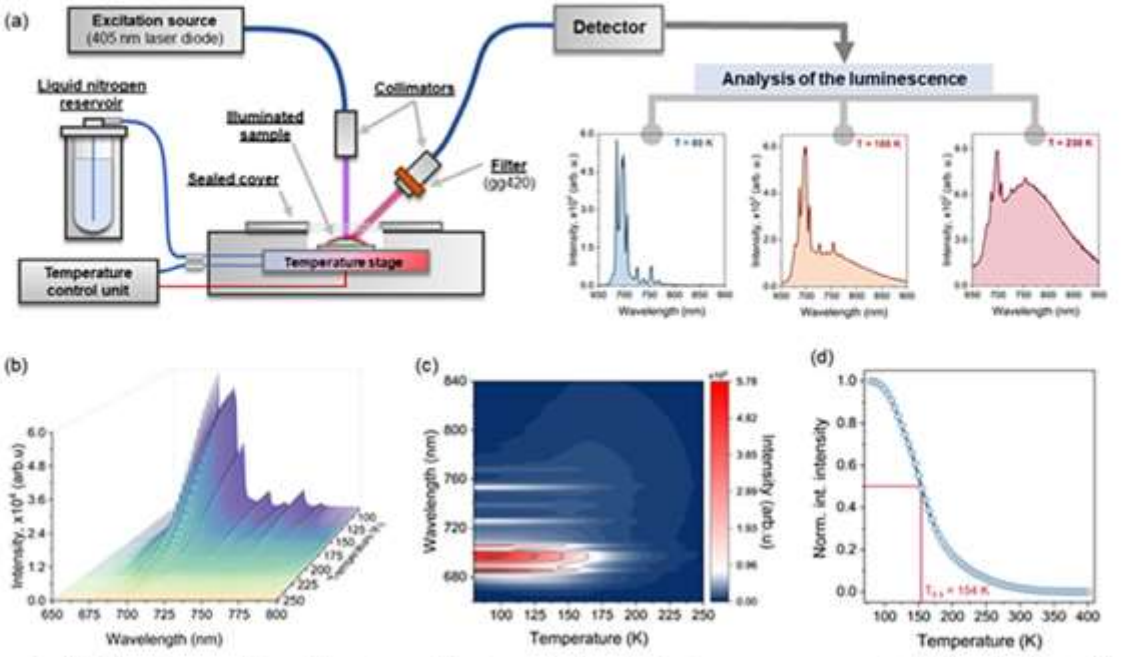

Figure 6. (a) Schematic representation of the setup used for temperature-dependent luminescence measurements; (b) thermal evolution of the exemplary compound $[DMA]Zn_{0.99}Cr_{0.01}(HCOO)_3$ with (c) heat map luminescence; (d) change of the normalized integrated intensity of the $[DMA]Zn_{0.99}Cr_{0.01}(HCOO)_3$ with $T_{0.5}$ marker.

characteristic of Cr^{3+} ions in double-perovskite hybrid materials has been reported previously.[1] By changing the composition of the host material and, consequently, crystal field strength, the change of emission type, range, and rate of thermal quenching of luminescence can be tuned.[21,33] In investigated materials, the narrow band observed at low temperatures is assigned to the $^2E_g \rightarrow {}^4A_{2g}$ spin forbidden transition. The excitation with 405 nm wavelength excites a higher $^4T_{2g}$ level, and due to the nonradiative energy transfer the population of ^2E_g level is increased. Temperature rise leads to the thermal population of the $^4T_{2g}$ level, which induces the occurrence of the broad spin allowed $^4T_{2g} \rightarrow {}^4A_{2g}$ transition. The influence of crystal field strength on the spectroscopic properties of investigated materials is particularly observable in Figure 5d.

The comparison of $[DMA]M^{II}_{0.97}Cr_{0.03}(HCOO)_3$ ($M^{II} = Zn^{2+}$, Mn^{2+}, and Mg^{2+}) shows that for the manganese-based sample (the lowest CF strength, according to M-O distance analysis) the $^4T_{2g} \rightarrow {}^4A_{2g}$ emission is significantly reduced and equated to $^2E_g \rightarrow {}^4A_{2g}$ peaks. On the other hand, for Zn- and Mg-based materials, exhibiting strong crystal fields with Dq/B parameters equal to 2.49 and 3.49, respectively, the broad spin allowed emissions are more intensive than narrow spin forbidden ones. Analogous results have been reported for $[EA]_2NaAl_{1-x}Cr_x(HCOO)_6$ double perovskites (EA = ethylammonium cation), where the change in crystal field strength induced different $^2E_g \rightarrow {}^4A_{2g}$ and $^4T_{2g} \rightarrow {}^4A_{2g}$ transition ratios.[1] The exemplary thermal evolution of the luminescence, including reciprocal emission intensities, in $[DMA]Zn_{0.99}Cr_{0.01}(HCOO)_3$ is better observed with a series of small temperature increments (5 degrees). For this purpose, the temperature-controlled stage has been used. A schematic representation of the measurement setup is presented in **Figure 6a**. The thermal evolution of the luminescence within the 80–250 K range is presented in Figure 6b. Due to the significantly higher intensity of the narrow $^2E_g \rightarrow {}^4A_{2g}$ emission, the temperature-induced creation of the broad $^4T_{2g} \rightarrow {}^4A_{2g}$ emission is unobservable. The heat map of the emission (Figure 6c), in turn, presents the formation of broad emission within the 110–175 K and its further extinction. The change of the normalized integrated intensity of the emission as a function of temperature is presented in Figure 6d.

Obtained results show the great influence of the temperature on the quenching of luminescence, especially within the 100–250 K range. The intensity of the emission was halved ($T_{0.5}$) when the system reached a temperature of around 154 K. Additionally, to provide more comprehensive spectroscopic data, the luminescence lifetime of representative materials was measured (λ_{em} = 686 nm). The comparison of the decay curves of samples containing 3 mol.% of Cr^{3+} ions is presented in Figure S8. Taking into consideration the coexistence of distinct Cr^{3+} sites (default and defected), a double exponential fitting was used to estimate the time decays τ_1 and τ_2, respectively. The following equation has been implemented:

$$I = I_0 + A_1 e^{-\left(\frac{t}{\tau_1}\right)} + A_2 e^{-\left(\frac{t}{\tau_2}\right)} \quad (2)$$

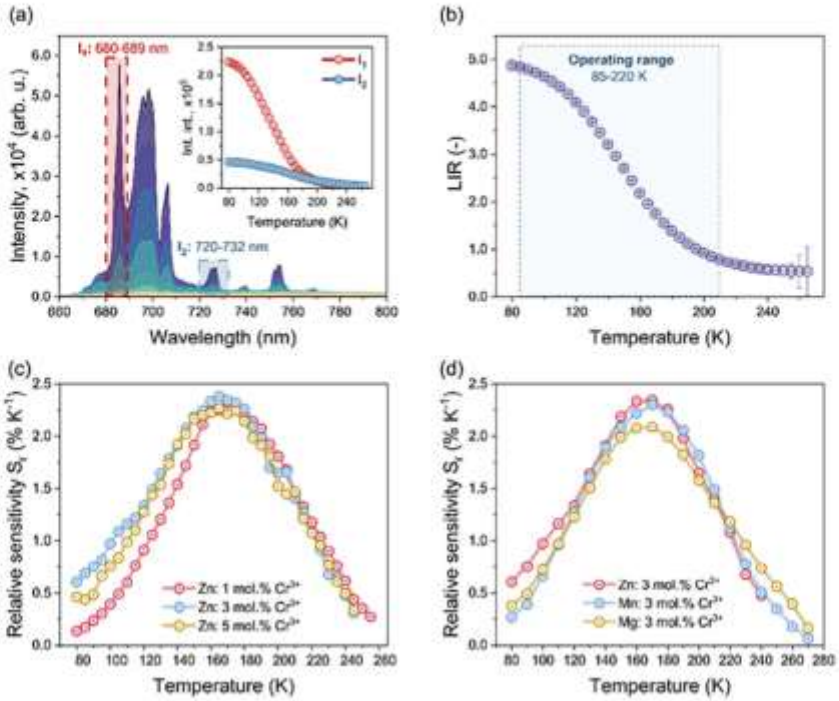

Figure 7. (a) Temperature-dependent emission spectra of $[DMA]M^{II}_{0.99}Cr_{0.01}(HCOO)_3$ with I_1 and I_2 markes; and changes in: (inside) I_1 and I_2 values; (b) luminescence intensity ratio (LIR) combined with LIR determination error bars and operating range of the thermometer; (c) relative sensitivity (S_r) of $[DMA]Zn_{1-x}Cr_x(HCOO)_3$ ($x = 0.01, 0.03, 0.05$) series; (d) comparison of S_r values for [DMA] $M^{II}_{0.97}Cr_{0.01}(HCOO)_3$ ($M^{II} = Zn^{2+}$, Mn^{2+}, and Mg^{2+}) series.

where I_0 stands for the initial luminescence intensity, A_1 and A_2 are pre-exponential coefficients, τ_1, and τ_2 are decay times and t is the time. The highest values of time components are observed for Zn-based materials (0.52 ms and 1.52 ms for τ_1, and τ_2, respectively), while the lowest values exhibit Mg-series (τ_1: 0.26 ms, and τ_2: 1.12 ms). Materials containing manganese(II) ions show τ_1, and τ_2 equal to 0.32 ms and 1.92 ms, respectively.

2.5. Luminescence Thermometry

The influence of the temperature on the intensity and character of the luminescence makes investigated hybrid materials interesting within the context of luminescent thermometry. Organic-inorganic materials with perovskite-type structures have been reported as promising solutions for high-sensitive temperature sensors.[1,20] Among various materials, hybrid perovskites containing Cr^{3+} ions exhibit particularly noteworthy optical and physicochemical properties. The comparison of two parts of the emission spectrum differing in temperature dependence is one of the most useful temperature estimation methods. Previous Authors' paper concerning spectroscopic and thermometric characteristics of double hybrid perovskite $[EA]_2NaAl_{1-x}Cr_x(HCOO)_6$ shows that temperature sensing based on comparison of the intensities of $^4T_{2g}\rightarrow{}^4A_{2g}$ and $^2E_g\rightarrow{}^4A_{2g}$ transitions is a promising approach and provides sufficient sensitivity.[1] The influence of the temperature on the luminescence intensity of the exemplary Zn-based material containing 1 mol.% of chromium ions is presented in **Figure 7a**.

Analogous results for all of the investigated materials are presented in Figures S9a–d, S10a–f, S11a–f (Supporting Information). Within the context of analyzed compounds, the intensity of the $^2E_g\rightarrow{}^4A_{2g}$ transition is notably greater than the $^4T_{2g}\rightarrow{}^4A_{2g}$ transition, thus, temperature estimation is based on the analysis of two parts of the spin-forbidden emission. To determine the sensing performance, the thermometric luminescence intensity ratio (LIR) was calculated. The LIR parameter is the ratio of thermometric bands:

$$LIR = \frac{I_1}{I_2} \tag{3}$$

where I_1 and I_2 stand for intensities of first- and second thermometric regions, respectively. For the calculation, two particular regions were chosen: I_1 (680–689 nm, R_1-line) and I_2 (720–732 nm). Both ranges are assigned to the $^2E_g\rightarrow{}^4A_{2g}$ transition. The following thermometric ranges were chosen to provide two temperature-dependent regions differing in the progressiveness of a thermal quenching. The I_1 range is assigned to the most intensive emission peak, which is a commonly reported approach. Investigated materials do not exhibit enough intensity of broadband $^4T_{2g}\rightarrow{}^4A_{2g}$ (compared to the emission from a ^2E_g level),

thus to provide sufficient signal-to-noise ratio the separate Stokes band (I_2) was chosen. The change of the I_1 and I_2 intensities as a function of the temperature of the system is presented in Figure 7a (inside). By combining intensities of both I_1 and I_2 intensities, it is possible to obtain a cumulative LIR parameter (Figure 7b). The analysis of the temperature operating range as well as temperature uncertainty determination was performed according to the procedure presented by Bednarkiewicz et al.[54] Analogous results for the Mn- and Mg-based series are presented in Figure S12a,b (Supporting Information). The increase in temperature causes the notable reduction of FIR parameters within the specific ranges: 80–265 K (Zn-compounds), 80–240 K (Mn-compounds), and 80–260 K (Mg-compounds). Within the context of luminescent thermometry, the mentioned ranges have been taken into consideration. Calculated values of LIR parameters constituted the basis for thermometric analysis.[25] To further demonstrate the thermometric characteristics, the relative thermal sensitivity S_r is calculated as:

$$S_r = \frac{1}{LIR} \cdot \left| \frac{dLIR}{dT} \right| \times 100\% \quad (4)$$

where $dLIR$ is the change of the thermometric parameter LIR at temperature change dT. The collation of relative sensitivity calculated for zinc materials is presented in Figure 7c. The corresponding results for magnesium materials are presented in Figure S12b–d (Supporting Information). For all of the investigated samples, a growth in temperature causes the initial increase of the S_r values, achieving the maximum values within the 150–180 K range, depending on the sample composition. Further growth in temperature induces a significant reduction of the relative sensitivity. The highest relative sensitivity (2.5%•K^{-1}) is observed for $[DMA]Mn_{0.95}Cr_{0.05}(HCOO)_3$. Among Zn- and Mg-based series, the highest S_r values are observed for the samples containing 3 mol.% (2.4%•K^{-1}) and 1 mol.% (2.2%•K^{-1}) of Cr^{3+} ions, respectively. The Mg-based materials exhibit the shift of maximal S_r values within the concentration series toward higher temperatures (Figure S12d, Supporting Information). Such a phenomenon is not observed for other materials. Also, less impact of the Cr^{3+} concentration on the maximum S_r compared to the Zn- and Mn-based compounds is observed. The influence of the chromium concentration on the useful sensing range (high S_r values) has been reported within the context of the hybrid perovskite $[EA]_2NaAl_{1-x}Cr_x(HCOO)_6$.[1] The tuning of the operating area, understood as the most accurate sensing range, significantly broadens the possibility of thermometric system optimization and adjusting to existing conditions. The studied materials show sufficient stability and repeatability within the cooling-heating intervals (Figure S13, Supporting Information). The stability of the material and the signal under varying temperature conditions is an important feature that significantly affects its usability. To provide a more comprehensive analysis of the thermometric potential of the investigated series of materials, the error of the temperature determination (δLIR) was taken into consideration according to Bednarkiewicz et al.[54] The comparisons of the error of LIR determination as a function of temperature are presented in Figure S14 (Supporting Information). The operating ranges are presented in Figures S15 and S17 (Supporting Information). To distinguish the operating range, the following conditions must be met:

Table 1. The collation of exemplary luminescence thermometers with relative sensitivity (S_r) at a given temperature (T) (H_3btb = 1,3,5-tris(4-carboxyphenyl)benzene; Btec = 1,2,4,5 Benzenetetracarboxylic acid).

Compound	S_r [%•K^{-1}]	T [K]	Refs.
$[DMA]Zn_{0.97}Cr_{0.03}(HCOO)_3$	2.4	165	This work
$[DMA]Mn_{0.95}Cr_{0.05}(HCOO)_3$	2.5	160	
$[DMA]Mg_{0.99}Cr_{0.01}(HCOO)_3$	2.2	150	
$[EA]_2NaAl_{0.79}Cr_{0.21}(HCOO)_6$	2.8	160	[1]
$Sr_2MgAl_{22}O_{36}$: Cr^{3+}	1.7	310	[34]
$ZnGa_2O_4$: Cr^{3+}	2.8	310	[35]
SrGdLiTeO$_6$: Mn^{4+}, Eu^{3+}	4.9	550	[55]
$Y_3Al_5O_{12}$: Ti^{4+}, Nd^{3+}	3.7	473	[56]
$Tb_{0.95}Eu_{0.05}$(btb)	2.8	14	[57]
Sr_2GeO_4: Pr^{3+}	9.0	22	[58]
$Y_2Al_2Ga_3O_{12}$: Nd^{3+}	0.45	100	[59]
$\{[Tb_{1.80}Eu_{0.20}(H_2Btec)(Btec)(H_2O)_2]\cdot 4H_2O\}_n$	16.1	11	[60]

$$\left(S_r(T) \geq S_{th}\right) * \left(dLIR(T) \geq \delta LIR(T)\right) \quad (5)$$

where S_{th} is the sensitivity threshold (depending on the specific application requirements), dLIR(T) is an increment in LIR value, and δLIR(T) is an error in the determination of LIR in given temperature T. Within the investigated series, the thermometric operating ranges reach temperature from 80 K up to 230 K. The presented thermometric analysis has been performed based on the investigation of two temperature-dependent ranges assigned to the spin-forbidden $^2E_g \rightarrow {}^4A_{2g}$ transition. The adopted paradigm of ratiometric thermometric analysis is based on the comparison of two independent temperature-sensitive transitions. Such an approach has been presented for $[EA]_2NaAl_{1-x}Cr_x(HCOO)_6$, where the calculation of the LIR parameters was based on the ratio of $^2E_g \rightarrow {}^4A_{2g}$ and $^4T_{2g} \rightarrow {}^4A_{2g}$ transitions. In this particular system, the intensity of the spin-allowed $^4T_{2g} \rightarrow {}^4A_{2g}$ transition was high enough to implement a two-band method. In this work, the thermometric analysis was performed based on a single-transition approach, which is not a commonly used technique. Obtained results, especially considering the relative sensitivity (up to 2.5%•K^{-1}) are comparable (**Table 1**) to conventional high-sensitive thermometric materials, mainly based on the lanthanide ions, and show the undeniable potential of the single-band approach.

To illustrate the potential and usefulness of the described optical thermometers, the experimental thermometric setup was prepared (**Figure 8a**). The copper pipe was partially placed in an insulated container made of extruded polystyrene foam filled with liquid nitrogen. The container was opened to allow liquid nitrogen to evaporate freely during the experiment. Several crystals of $[DMA]Mn_{0.95}Cr_{0.05}(HCOO)_3$ were placed on the surface of the pipe with a silver paste. The luminescence of the sample was constantly monitored. When the luminescence intensity achieved the highest value, which indicates the stabilization of the temperature gradient, the automated series of luminescence measurements was launched. From this point, a measurement

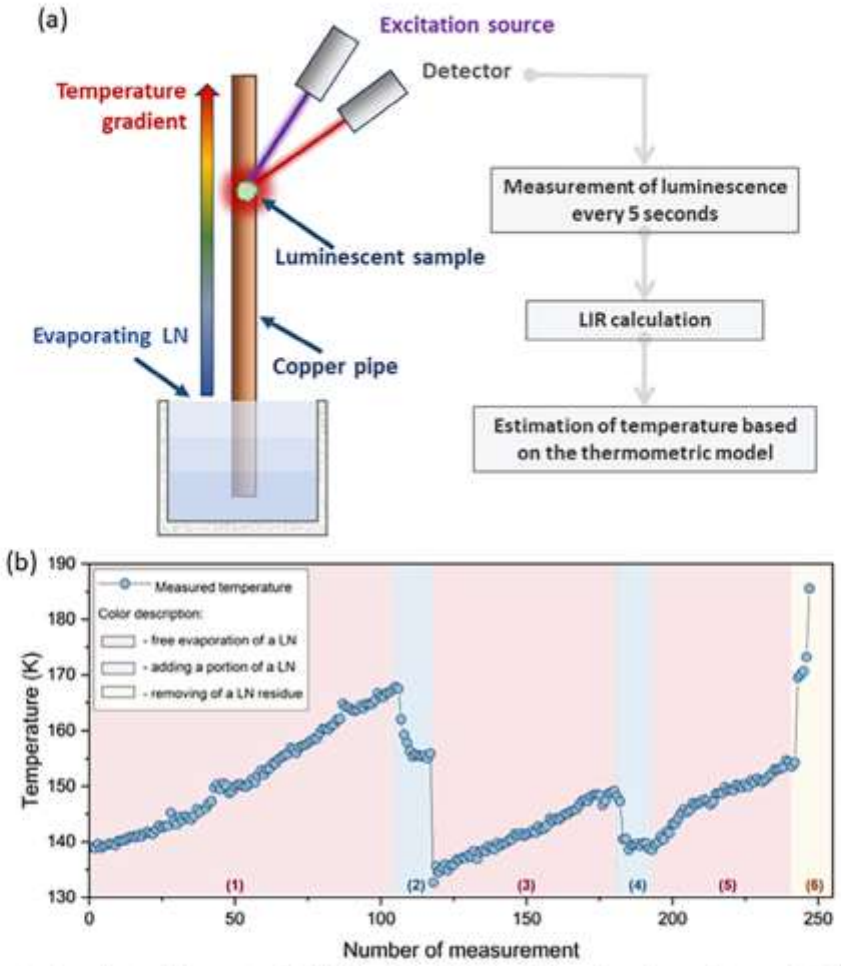

Figure 8. (a) Temperature-dependent emission spectra of $[DMA]M^{II}_{0.99}Cr_{0.01}(HCOO)_3$ with I_1 and I_2 markes; and changes in: (inside) I_1 and I_2 values; (b) luminescence intensity ratio (LIR) combined with LIR determination error bars and operating range of the thermometer; (c) relative sensitivity (S_r) of $[DMA]Zn_{1-x}Cr_x(HCOO)_3$ (x = 0.01, 0.03, 0.05) series; (d) comparison of S_r values for [DMA] $M^{II}_{0.97}Cr_{0.01}(HCOO)_3$ (M^{II} = Zn^{2+}, Mn^{2+}, and Mg^{2+}) series.

of the luminescent spectrum was performed every 5 s. During the experiment, the temperature of the sample fluctuated due to the evaporation of the liquid nitrogen (increase in temperature) as well as the refilling of the reservoir with a cooling medium (decrease in temperature). The obtained series of luminescent spectra was further processed following the methodology presented in this work. Calculated LIR values (based on I_1 and I_2 values) for every measurement were used to estimate temperature according to the thermometric model determined under control conditions. The graphical representation of the temperature estimated within the experiment is presented in Figure 8b. Within the initial part of the experiment (red range 1), the calculated temperature of the sample increased, which is caused by the reduction in the liquid nitrogen amount in the reservoir. When the container was refilled with the new portion of cooling medium the calculated temperature rapidly decreased (blue range 2). Within range 2, temporary stability in temperature was observed, however, shortly after temperature decreased rapidly. This phenomenon was caused by two-portion refilling. The temperature stabilization took place between two portions of liquid nitrogen. After the second portion, a linear increase in temperature was observed (range 3). When a certain amount of liquid nitrogen evaporated, the cooling medium reservoir was refilled again (range 4), which led to the rapid reduction in the material's temperature and further – temporary stabilization in temperature. Next, the system was left undisturbed and, due to the liquid nitrogen evaporation, an increase in temperature occurred (range 5). The terminal part of the experiment assumed the sudden removal of the whole cooling medium to induce a greater temperature increase. When all liquid nitrogen was removed from

the reservoir, the temperature significantly increased (range 6). The small fluctuations in temperature resulted from the unsteady state and air circulation in the setup environment.

The presented approach shows the potential of the luminescent temperature sensors for constant monitoring under non-ideal and unsteady conditions. As it is presented, it is possible to observe not only the small changes in temperature on the monitored material but also detect much greater temperature changes – within the context of the performed experiment, up to 35 K (within the 132–167 K range). What is more, results show a significant potential of the luminescent thermometry driven from its' remote and fast measurement, which allowed us to sufficiently visualize the moment of the LN refilling. The described results show that investigated formate-based organic-inorganic compounds with the general formula $[DMA]M^{II}_{1-x}Cr_x(HCOO)_3$ (M^{II} = Zn^{2+}, Mn^{2+}, and Mg^{2+}; x = 0.01, 0.03, 0.05) exhibit noteworthy optical properties, especially within the context of luminescence thermometry. The development of optical thermometers based solely on transition-metal luminescence is a promising direction toward non-lanthanide temperature sensor design, especially for low-temperature sensing solutions.

3. Conclusion

The slow-diffusion method was successfully used to obtain a series of metal-organic frameworks with the general formula $[DMA]M^{II}_{1-x}Cr_x(HCOO)_3$, where x = 0, 0.01, 0.03, and 0.05, while M = Zn^{2+}, Mn^{2+}, Mg^{2+}, Co^{2+}, and Ni^{2+}. Performed XRD measurements confirmed phase purity and the possibility of doping with Cr^{3+} ions. Due to the charge mismatch, occurring under an increase in Cr^{3+}/M^{2+}, it is possible to incorporate up to 5 mol.% of Cr^{3+}. The Raman and IR spectroscopy provided information about phonon properties and the influence of Cr^{3+} addition. The crystal field strength was estimated with DRS measurements or/and with M-O length analysis. The obtained results show the strong influence of the metal type and Cr^{3+} concentration on CF strength. A proposed approach using metal-ligand distances provides a particularly promising enrichment of the DRS-based results. Estimated CF strength corresponds to obtained temperature-dependent luminescence studies. Investigated materials exhibit the coexistence of temperature-sensitive bands, narrow spin-forbidden $^2E_g \rightarrow {}^4A_{2g}$ and broad spin-allowed $^4T_{2g} \rightarrow {}^4A_{2g}$. Observed luminescence can be used to develop a thermometric model according to the ratiometric approach. However, due to the small intensity of the spin-allowed transition, the luminescence intensity ratio of the new luminescent thermometers was based on two separate emission bands assigned to the $^2E_g \rightarrow {}^4A_{2g}$ transition. Obtained luminescent thermometers show high relative sensitivity up to 2.5%•K^{-1} for $[DMA]Mn_{0.95}Cr_{0.05}(HCOO)_3$ at 160 K. Comprehensive analysis of obtained thermometric results shows the crucial role of Cr^{3+} ions concentration and, simultaneously, metal type on obtained thermometric potential. The proposed thermometric system based on the series of temperature measurements confirms the extraordinary potential of Cr^{3+}-based hybrid materials. Performed time-resolved temperature analysis was successfully implemented for visualization of the temperature gradient within the 132–167 K range. Further development of thermosensitive compounds based on Cr^{3+} luminescence may result in the introduction of novel, lanthanide-free thermometric solutions.

4. Experimental Section

Synthesis: In this study, investigated materials were synthesized by using the low-diffusion method. To synthesize the crystals of $[DMA]M^{II}_{1-x}Cr_x(HCOO)_3$ (where M^{II} = Zn^{2+}, Mn^{2+}, Mg^{2+}, Co^{2+}, Ni^{2+}, and x = 0, 0.01, 0.03, 0.05), dimethylamine (DMA) solution (2M) in methanol (Sigma–Aldrich), formic acid (≥98%, POCH), anhydrous methanol (MeOH) (99.8%, Sigma–Aldrich), chromium(III) chloride hexahydrate(≥98%, Sigma–Aldrich), manganese chloride (≥99%, Sigma–Aldrich), magnesium chloride (≥98%, Sigma–Aldrich), zinc chloride (>99.999%, Sigma–Aldrich), were used as precursors without further purification.

At first, the stock solution of $CrCl_3$ (10^{-3} M) was dissolved in distilled water. After that, an aqueous solution A (heavy phase, the reaction to form dimethyl formate) and solution B (light phase, the source of metal ions) were prepared separately. To prepare solution A, DMA (8 mmol, 4 mL) was dissolved in 6 mL of MeOH, and then 2 mL of HCOOH was added. To prepare solution B, MCl_2 (2 mmol) was dissolved in 15 mL of MeOH. For doped samples, the proper volume of $CrCl_3$ was evaporated on a heater and then transferred to the B solution. Finally, solutions A and B were gently transferred to a test tube (1 cm diameter, 40 cm length) by using a syringe. After a few days, the cubic-shaped crystals started growing on the wall of the glass tube at the boundary between the two phases. After one week, it was collected and then washed several times with MeOH and left till dried in air. Instead of the crystals, white precipitation was obtained at the boundary between the two phases in the cases of Ni- and Co-based compounds. The solubility of the obtained compounds in methanol, ethanol, isopropanol, acetonitrile (AcCN), and N,N-dimethylformamide (DMF) was verified. For all solvents, the studied materials are insoluble (alcohols and AcCN) or partially soluble (DMF). The solubility test in water showed that they do not dissolve; however, a long exposure on the order of several months to moisture in the air causes partial decomposition of crystals on the surface. Therefore, crystals need to be protected for long-term storage.

Structural and Phonon Characteristics: The purity of the samples was examined by X-ray diffraction (XRD) technique in the range 2θ = 10–60° using X'PertPro system (PIXcel detector and Ni-filtered Cu$K\alpha$ radiation λ = 1.54056 Å). The Raman spectra were measured using a Bruker FT 110/S spectrometer operating at 1064 nm. The mid-IR ATR (attenuated total reflection) spectra were collected using a Nicolet iS50 infrared spectrometer equipped with the ATR module and diamond crystal.

Optical Spectroscopy: The diffuse reflection spectra were measured by using a Varian Cary 5E UV/VIS-NIR spectrophotometer (Varian Incorporation, Palo Alto, CA, USA). Emission spectra and temperature-dependent emission spectra of the samples were recorded using a Hamamatsu PMA-12 photonic multichannel analyzer equipped with a BT-CCD linear image sensor (Hamamatsu Photonics K.K, Shizuoka, Japan). The temperature was controlled by a Linkam THMS 600 Heating/Freezing Stage (The McCrone Group, Westmont, IL USA). To reduce the emission intensity-to-noise ratio, each emission spectrum at a given temperature was collected with an exposure time of 500 ms and 30 averages. The quantum efficiency (QE) of the selected sample was measured at 80 K under a 405 nm excitation line using the FLS 920 Fluorescence Quantum Yields Spectrometer with a standard measurement uncertainty of 10%.

Supporting Information

Supporting Information is available from the Wiley Online Library or from the author.

Acknowledgements

This research was supported by the National Science Centre (NCN) in Poland under project SONATA 16 no. 2020/39/D/ST5/01289 and partially developed under the project CICECO-Aveiro Institute of Materials UIDB/50011/2020, UIDP/50011/2020 & LA/P/0006/2020, financed by funds through the FCT/MEC (PID-DAC).

Conflict of Interest

The authors declare no conflict of interest.

Data Availability Statement

The data that support the findings of this study are openly available in Zenodo at https://doi.org/10.5281/zenodo.15129203, reference number 15129203.

Keywords

chromium(III) ions, hybrid perovskites, luminescence, thermometry

Received: April 3, 2025
Revised: June 24, 2025
Published online: July 16, 2025

[1] A. Kabański, M. Ptak, D. Stefańska, *ACS Appl. Mater. Interfaces* **2023**, *15*, 7074.
[2] J. Huang, Y. Yuan, Y. Shao, Y. Yan, *Nat. Rev. Mater.* **2017**, *2*, 17042.
[3] P. Peksa, J. Trzmiel, K. Fedoruk, A. Gagor, M. Šimėnas, A. Ciupa, S. Pawlus, J. Banys, M. Maczka, A. Sieradzki, *J. Phys. Chem. C* **2019**, *123*, 23594.
[4] R. Shang, G. C. Xu, Z. M. Wang, S. Gao, *Chem. - Eur. J.* **2014**, *20*, 1146.
[5] X. Y. Xu, B. Yan, *Dalton Trans.* **2016**, *45*, 7078.
[6] P. Jain, N. S. Dalal, B. H. Toby, H. W. Kroto, A. K. Cheetham, *J. Am. Chem. Soc.* **2008**, *130*, 10450.
[7] P. Jain, V. Ramachandran, R. J. Clark, D. Z. Hai, B. H. Toby, N. S. Dalal, H. W. Kroto, A. K. Cheetham, *J. Am. Chem. Soc.* **2009**, *131*, 13625.
[8] M. Šimenas, S. Balčiunas, M. Trzebiatowska, M. Ptak, M. Mączka, G. Völkel, A. Pöppl, J. Banys, *J. Mater. Chem. C* **2017**, *5*, 4526.
[9] M. Mączka, A. Pietraszko, L. Macalik, A. Sieradzki, J. Trzmiel, A. Pikul, *Dalton Trans.* **2014**, *43*, 17075.
[10] M. Ptak, A. Gągor, A. Sieradzki, B. Bondzior, P. Dereń, A. Ciupa, M. Trzebiatowska, M. Mączka, *Phys. Chem. Chem. Phys.* **2017**, *19*, 12156.
[11] M. Sánchez-Andújar, L. C. Gómez-Aguirre, B. Pato Doldán, S. Yáñez-Vilar, R. Artiaga, A. L. Llamas-Saiz, R. S. Manna, F. Schnelle, M. Lang, F. Ritter, A. A. Haghighirad, M. A. Senaris-Rodriguez, *CrystEngComm* **2014**, *16*, 3558.
[12] B. Pato-Doldán, M. Sánchez-Andújar, L. C. Gómez-Aguirre, S. Yáñez-Vilar, J. López-Beceiro, C. Gracia-Fernández, A. A. Haghighirad, F. Ritter, S. Castro-García, M. A. Senaris-Rodriguez, *Phys. Chem. Chem. Phys.* **2012**, *14*, 8498.
[13] M. Szafrański, W. J. Wei, Z. M. Wang, W. Li, A. Katrusiak, *APL Mater.* **2018**, *6*, 100701.
[14] T. Besara, P. Jain, N. S. Dalal, P. L. Kuhns, A. P. Reyes, H. W. Kroto, A. K. Cheetham, *Proc. Natl. Acad. Sci. U.S.A.* **2011**, *108*, 6828.
[15] H. D. Duncan, M. T. Dove, D. A. Keen, A. E. Phillips, *Dalton Trans.* **2016**, *45*, 4380.
[16] M. Mączka, A. Gągor, B. Macalik, A. Pikul, M. Ptak, J. Hanuza, *Inorg. Chem.* **2014**, *53*, 457.
[17] R. Yadav, D. Swain, H. L. Bhat, S. Elizabeth, *J. Appl. Phys.* **2016**, *119*, 064103.
[18] K. L. Svane, A. C. Forse, C. P. Grey, G. Kieslich, A. K. Cheetham, A. Walsh, K. T. Butler, *J. Phys. Chem. Lett.* **2017**, *8*, 6154.
[19] M. Mączka, B. Bondzior, P. Dereń, A. Sieradzki, J. Trzmiel, A. Pietraszko, J. Hanuza, *Dalton Trans.* **2015**, *44*, 6871.
[20] D. Stefańska, A. Kabański, T. H. Q. Vu, M. Adaszyński, M. Ptak, *Sensors* **2023**, *23*, 6259.
[21] L. Marciniak, K. Kniec, K. Elzbieciak-Piecka, K. Trejgis, J. Stefanska, M. Dramićanin, *Coord. Chem. Rev.* **2022**, *469*, 214671.
[22] M. Back, J. Ueda, M. G. Brik, S. Tanabe, *ACS Appl. Mater. Interfaces* **2020**, *12*, 38325.
[23] M. Back, J. Ueda, J. Xu, K. Asami, M. G. Brik, S. Tanabe, *Adv. Opt. Mater.* **2020**, *8*, 2000124.
[24] M. Back, J. Ueda, H. Nambu, M. Fujita, A. Yamamoto, H. Yoshida, H. Tanaka, M. G. Brik, S. Tanabe, *Adv. Opt. Mater.* **2021**, *9*, 2100033.
[25] C. D. S. Brites, P. P. Lima, N. J. O. Silva, A. Millán, V. S. Amaral, F. Palacio, L. D. Carlos, *Nanoscale* **2012**, *4*, 4799.
[26] M. D. Dramićanin, *J. Appl. Phys.* **2020**, *128*, 040902.
[27] W. Xu, J. Cui, F. Bai, L. Zheng, C. Hu, Z. Zhang, Z. Sun, Y. Zhang, *J. Mater. Chem. C* **2023**, *11*, 15233.
[28] T. V. Gavrilović, D. J. Jovanović, V. Lojpur, M. D. Dramićanin, *Sci. Rep.* **2014**, *4*, 4209.
[29] B. Zhang, X. Guo, Z. Zhang, Z. Fu, H. Zheng, *J. Lumin.* **2022**, *250*, 119110.
[30] J. Rocha, L. D. Carlos, F. A. A. Paz, D. Ananias, *Chem. Soc. Rev.* **2011**, *40*, 926.
[31] M. Zhang, M. Jia, T. Sheng, Z. Fu, *J. Lumin.* **2021**, *229*, 117653.
[32] K. Elzbieciak-Piecka, M. Suta, L. Marciniak, *Chem. Eng. J.* **2021**, *421*, 129757.
[33] A. L. Mullins, A. Ćirić, I. Zeković, J. A. G. Williams, M. D. Dramićanin, I. R. Evans, *J. Mater. Chem. C* **2022**, *10*, 10396.
[34] Q. Wang, Z. Liang, J. Luo, Y. Yang, Z. Mu, X. Zhang, H. Dong, F. Wu, *Ceram. Int.* **2020**, *46*, 5008.
[35] J. Ueda, M. Back, M. G. Brik, Y. Zhuang, M. Grinberg, S. Tanabe, *Opt. Mater. (Amst)* **2018**, *85*, 510.
[36] M. Back, E. Trave, J. Ueda, S. Tanabe, *Chem. Mater.* **2016**, *28*, 8347.
[37] M. Back, J. Ueda, M. G. Brik, T. Leśniewski, M. Grinberg, S. Tanabe, *ACS Appl. Mater. Interfaces* **2018**, *10*, 41512.
[38] X. Shan, M. Back, D. Chen, S. Miao, R. Shi, Y. Liang, *J Mater Chem C Mater* **2023**, *26*, 8952.
[39] R. Li, G. Wei, Z. Wang, Y. Wang, J. Li, S. He, L. Li, H. Suo, W. Ding, P. Li, *Laser Photon Rev* **2023**, *17*, 2200589.
[40] A. Ćirić, Z. Ristić, J. Periša, Ž. Antić, M. D. Dramićanin, *Ceram. Int.* **2021**, *47*, 27151.
[41] M. Maczka, T. Almeida da Silva, W. Paraguassu, K. Pereira da Silva, *Spectrochim. Acta A Mol. Biomol. Spectrosc.* **2016**, *156*, 112.
[42] J. C. Tan, P. Jain, A. K. Cheetham, *Dalton Trans.* **2012**, *41*, 3949.
[43] S. Marimuthu, S. Pandiaraj, M. Muthuramamoorthy, K. E. Alzahrani, A. N. Alodhayb, S. Pitchaimuthu, A. N. Grace, *Phys. Chem. Chem. Phys.* **2024**, *26*, 4262.
[44] A. Rossin, A. Ienco, F. Costantino, T. Montini, B. Di Credico, M. Caporali, L. Gonsalvi, P. Fornasiero, M. Peruzzini, *Cryst. Growth Des.* **2008**, *8*, 3302.
[45] M. Premila, A. Bharathi, R. Rajaraman, S. Hussain, P. D. Babu, C. S. Sundar, G. Amarendra, *J. Raman Spectrosc.* **2018**, *49*, 549.
[46] M. Mączka, M. Ptak, L. Macalik, *Vib. Spectrosc.* **2014**, *71*, 98.
[47] G. Kieslich, S. Sun, A. K. Cheetham, *Chem. Sci.* **2014**, *5*, 4712.
[48] G. Kieslich, S. Sun, A. K. Cheetham, *Chem. Sci.* **2015**, *6*, 3430.
[49] W. Stręk, P. Dereń, B. Jeżowska-Trzebiatowska, *Phys. B: Condens. Matter* **1988**, *152*, 379.
[50] M. G. Brik, A. A. Chaykin, *J. Lumin.* **2014**, *145*, 563.
[51] M. Ptak, M. Maczka, A. Gagor, A. Sieradzki, B. Bondzior, P. Dereń, S. Pawlus, *Phys. Chem. Chem. Phys.* **2016**, *18*, 29629.

[52] M. Ptak, D. Stefańska, A. Gagor, K. L. Svane, A. Walsh, W. Paraguassu, *Phys. Chem. Chem. Phys.* **2018**, *20*, 22284.
[53] L. Marciniak, M. Szalkowski, A. Bednarkiewicz, K. Elzbieciak-Piecka, *J. Mater. Chem. C* **2022**, *10*, 11040.
[54] A. Bednarkiewicz, L. Marciniak, L. D. Carlos, D. Jaque, *Nanoscale* **2020**, *12*, 14405.
[55] L. Li, G. Tian, Y. Deng, Y. Wang, Z. Cao, F. Ling, Y. Li, S. Jiang, G. Xiang, X. Zhou, *Opt. Express* **2020**, *28*, 33747.
[56] J. Drabik, B. Cichy, L. Marciniak, *J. Phys. Chem. C* **2018**, *122*, 14928.
[57] D. Ananias, C. D. S. Brites, L. D. Carlos, J. Rocha, *Eur. J. Inorg. Chem.* **2016**, *13*, 1967.
[58] C. D. S. Brites, K. Fiaczyk, J. F. C. B. Ramalho, M. Sójka, L. D. Carlos, E. Zych, *Adv. Opt. Mater.* **2018**, *6*, 1701318.
[59] M. Back, J. Xu, J. Ueda, S. Tanabe, *JCS-Japan* **2023**, *131*, 57.
[60] T. Arniaud, V. Jubera, H. Serier-Brault, *J Mater Chem C Mater* **2023**, *11*, 10951.

ADVANCED OPTICAL MATERIALS

Supporting Information

for *Adv. Optical Mater.*, DOI 10.1002/adom.202501057

Real-Time Temperature Monitoring with Cr^{3+}-Based Hybrid Formate Perovskites: Insights into the Relation Between Chemical Composition and Thermometric Performance

Adam Kabański, Maciej Ptak, Luís Dias Carlos and Dagmara Stefańska**

Real-time temperature monitoring with Cr^{3+}-based hybrid formate perovskites: insights into the relation between chemical composition and thermometric performance

Adam Kabański, Maciej Ptak, Luís Dias Carlos, Dagmara Stefańska**

A. Kabański, M. Ptak, D. Stefańska

Institute of Low Temperature and Structure Research, Polish Academy of Sciences, 50-422 Wroclaw, Poland

E-mail: a.kabanski@intibs.pl, d.stefanska@intibs.pl

L. D. Carlos

Phantom-g, CICECO – Aveiro Institute of Materials, Physics Department, University of Aveiro, 3810-193 Aveiro, Portugal

Table S1. Raman and IR wavenumbers together with assignment of observed bands

Raman (cm^{-1})	IR (cm^{-1})	Assignment
3116-3153	3110	νNH_2
3037-3059	3033-3063	$\nu_{as}CH_3$
2940-2979	2963-2972	ν_sCH_3
2884-2940	-	o + cb
2827-2870	2825-2885	νCH
2696-2800	-	o + cb
1610-1661	1627-1633	δNH_2
1556-1600	1559-1598	$\nu_{as}COO$
1442-1476	1457-1473	$\delta_{as}CH_3$
-	1390-1420	$\delta_sCH_3+\omega NH_2$
1364-1373	1356-1367	δCH_{ip}
1340-1356	1318-1350	ν_sCOO
-	1253-1257 + 1091-1105	ρCH_3
1059-1076	1069-1075	δCH_{op}
1026-1030	1024-1028	$\nu_{as}CNC$
893-899	888-899	ν_sCNC
790-804	807-831	δCOO
407-412	400-425	δCNC
308-325	-	τCH_3
57-257	-	lattice modes

key: δ, bending; ν, stretching; ρ, rocking; τ, twisting; ω, wagging; as, antisymmetric;
cb, combination band; ip, in-plane; o, overtone; op, out-of-plane; s, symmetric

Table S2. The collation of the band gap energies (E_g) and crystal field parameters of investigated materials

[DMA]$M_{1-x}Cr_x(HCOO)_3$		E_g	Dq (cm^{-1})	B (cm^{-1})	**Dq/B**	C (cm^{-1})	C/B
M	Cr^{3+} content						
Zn	0	5.72					
	0.01	5.71	1671	714	**2.34**	3103	4.35
	0.03	5.66	1693	680	**2.49**	3170	4.66
	0.05	5.62	1668	707	**2.36**	3117	4.41
Mg	0	6.15					
	0.01	6.11	1738	628	**2.77**	3289	5.24
	0.03	5.20	1718	638	**2.69**	3275	5.13
	0.05	5.49	1734	619	**2.80**	3308	5.34

Table S3. The collation of the relative (S_r) sensitivities

[DMA]$M_{1-x}Cr_x(HCOO)_3$		$S_{r,\,max}$ ($\%\cdot K^{-1}$)
M	x	
Zn	0.01	2.3 (170 K)
	0.03	**2.4 (165 K)**
	0.05	2.3 (165 K)
Mn	0.01	2.0 (170 K)
	0.03	**2.3 (170 K)**
	0.05	2.5 (160 K)
Mg	0.01	2.2 (150 K)
	0.03	**2.1 (170 K)**
	0.05	2.1 (180 K)

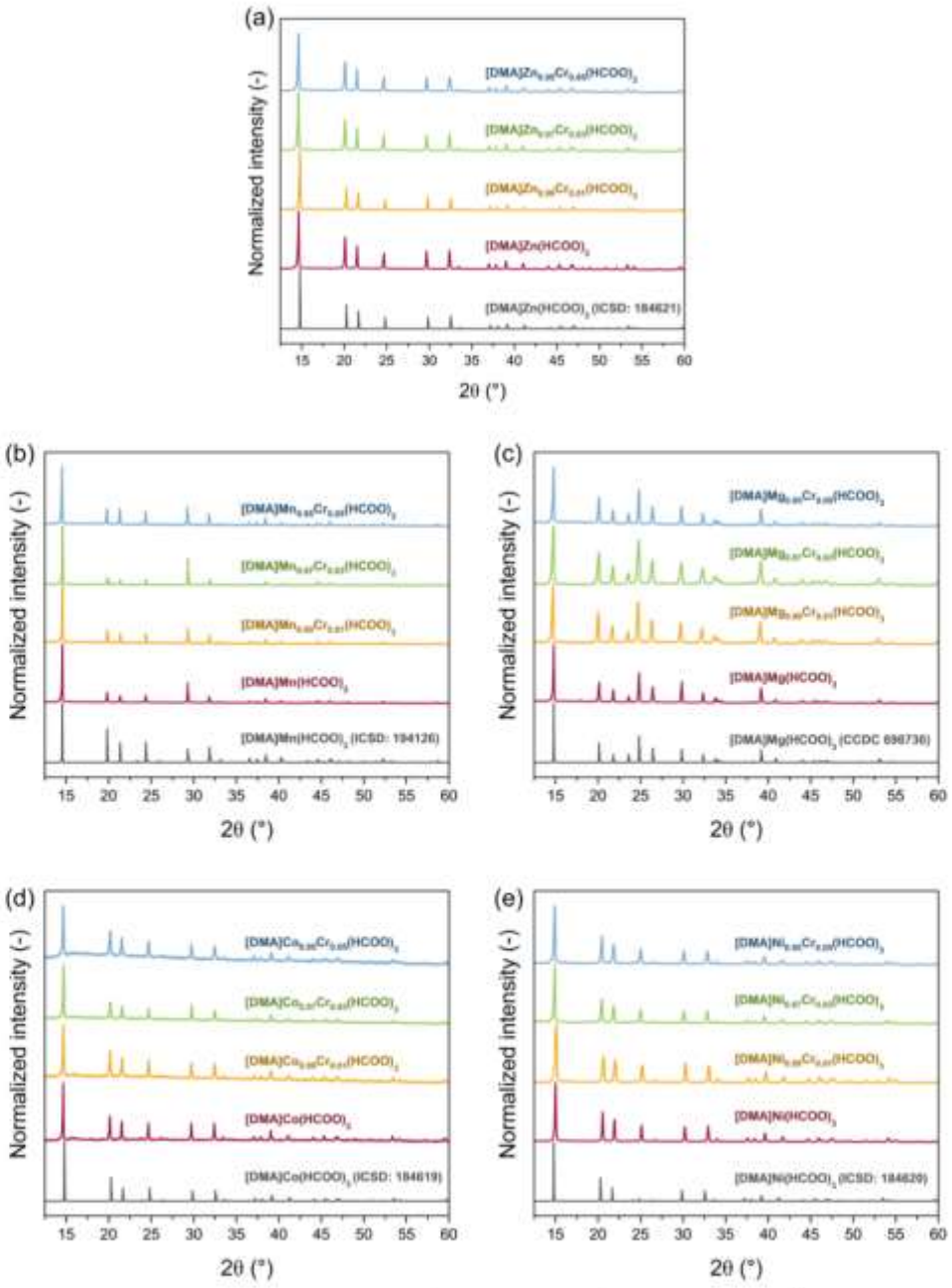

Figure S1. Experimental powder X-ray diffraction patterns for the $[DMA]M^{II}(HCOO)_3$, crystals with various concentration of Cr^{3+} ions, and where M^{II}= Zn^{2+} (a), Mn^{2+} (b), Mg^{2+} (c), Co^{2+} (d), and Ni^{2+} (e), compared to generated pattern based on the single-crystal data.

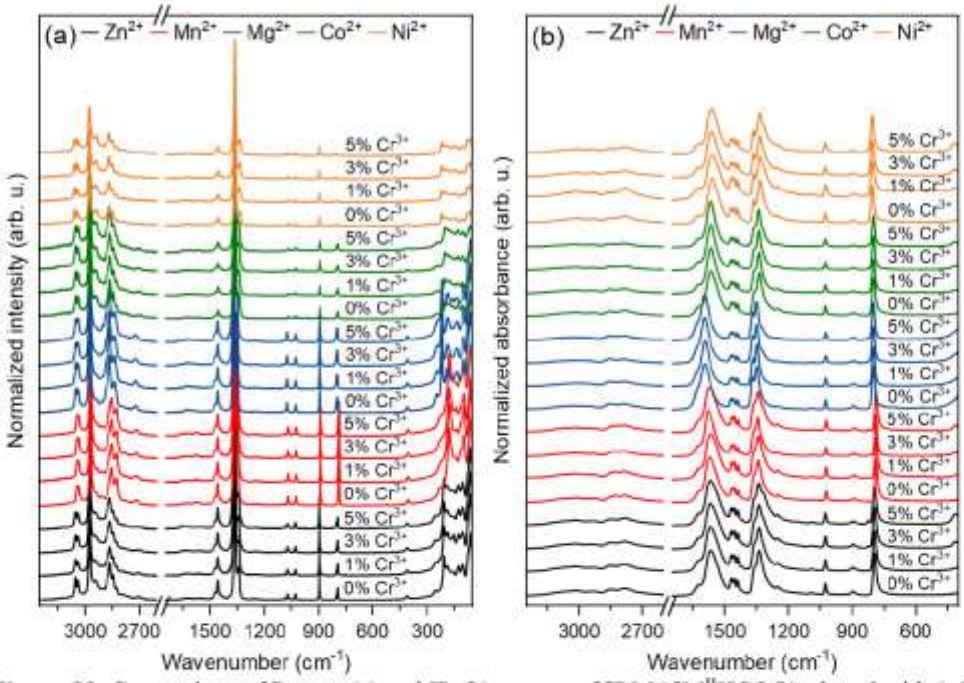

Figure S2. Comparison of Raman (a) and IR (b) spectra of $[DMA]M^{II}HCOO)_3$ doped with 1-5 mol% Cr^{3+} ions; $M^{II} = Ni^{2+}$, Co^{2+}, Mg^{2+}, Mn^{2+}, and Zn^{2+}.

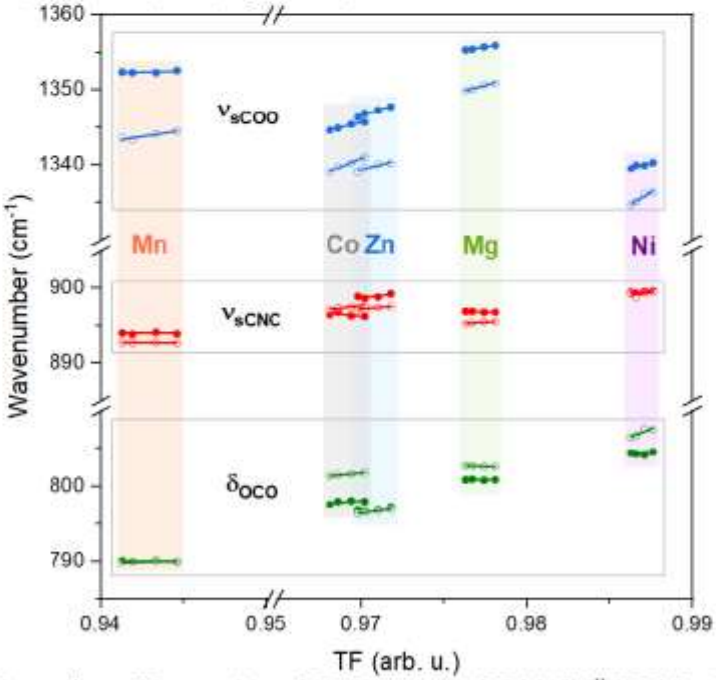

Figure S3. Comparison of Raman (a) and IR (b) spectra of $[DMA]M^{II}(HCOO)_3$ ($M^{II} = Mg^{2+}$, Mn^{2+}, and Zn^{2+}) doped with 3 mol% Cr^{3+} ions

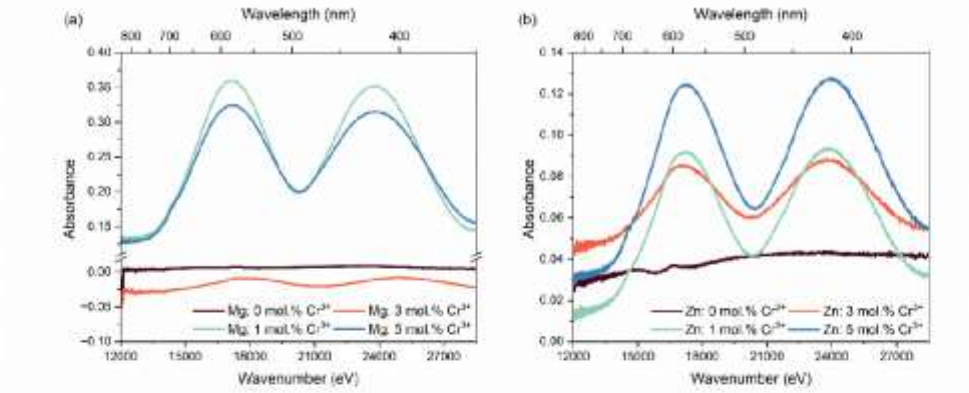

Figure S4. Diffuse reflectance spectra of (a) [DMA]$Mg_{1-x}Cr_x(HCOO)$ and (b) [DMA]$Zn_{1-x}Cr_x(HCOO)_3$, where x = (0, 0.01, 0.03, 0.05).

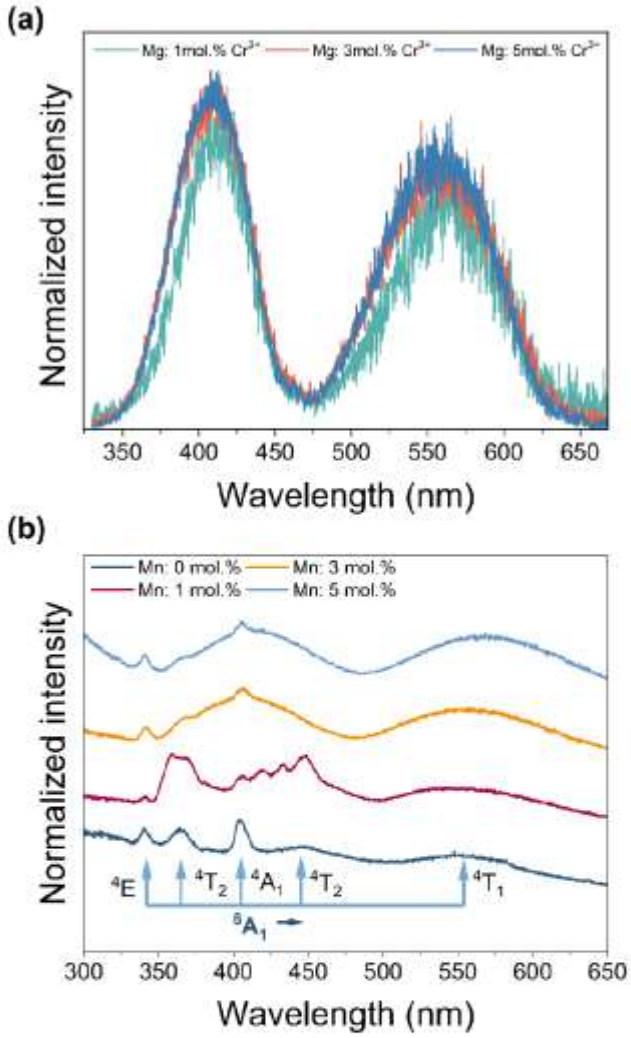

Figure S5. 80 K excitation spectra of $[DMA]Mg_{1-x}Cr_x(HCOO)$ monitored at 685 nm (a) and $[DMA]Mn_{1-x}Cr_x(HCOO)$ monitored at 699 nm. (b), where x = (0, 0.01, 0.03, 0.05).

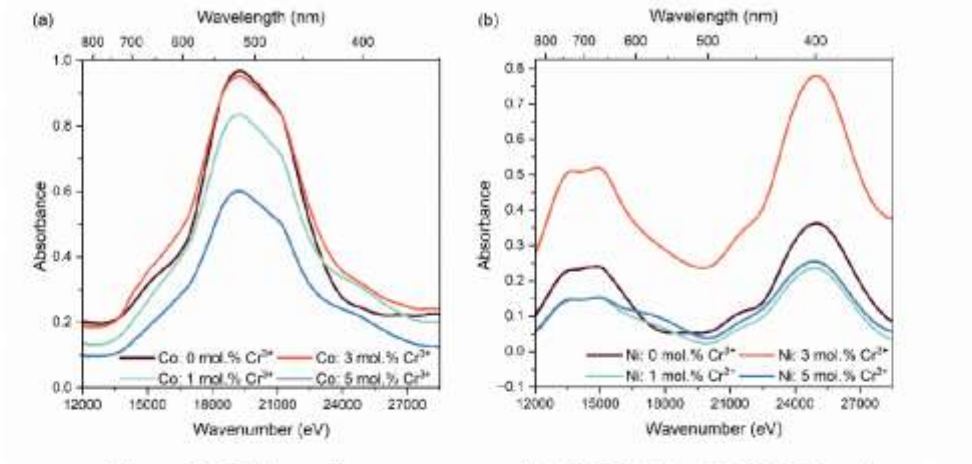

Figure S6. Diffuse reflectance spectra of (a) $[DMA]Co_{1-x}Cr_x(HCOO)$ and (b) $[DMA]Ni_{1-x}Cr_x(HCOO)_3$, where x = (0, 0.01, 0.03, 0.05).

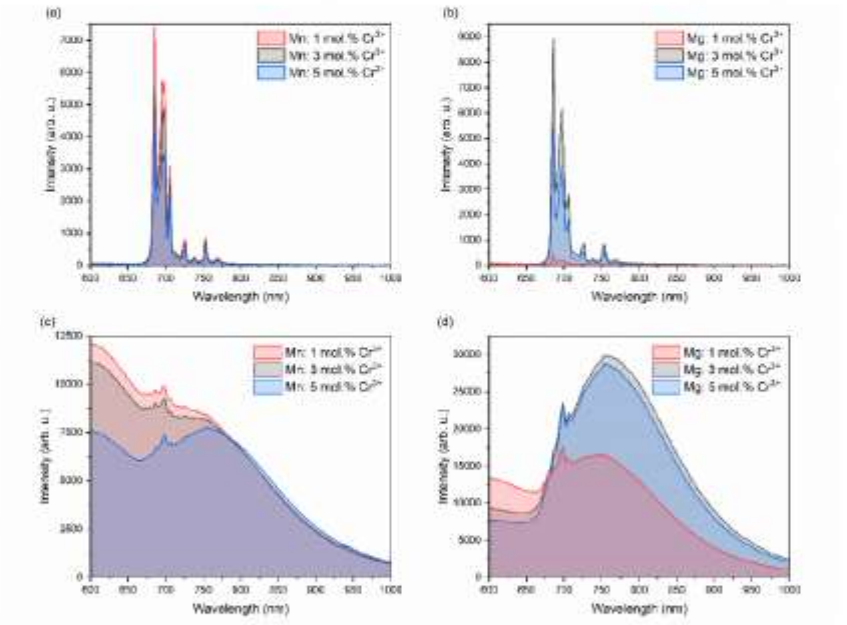

Figure S7. Comparison of emission intensity at 80 K: (a) $[DMA]Mn_{1-x}Cr_x(HCOO)_3$ and (b) $[DMA]Mg_{1-x}Cr_x(HCOO)_3$, where x = (0, 0.01, 0.03, 0.05); at 300 K: (c) $[DMA]Mn_{1-x}Cr_x(HCOO)_3$ and (d) $[DMA]Mg_{1-x}Cr_x(HCOO)_3$, where x = (0, 0.01, 0.03, 0.05)

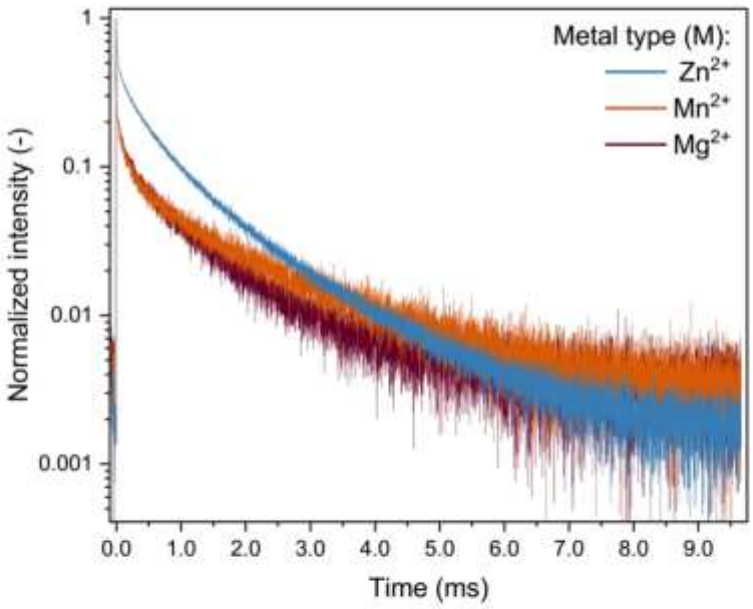

Figure S8. Decay profiles of $[DMA]M_{0.97}Cr_{0.03}(HCOO)_3$, where M = Zn^{2+}, Mn^{2+}, and Mg^{2+}

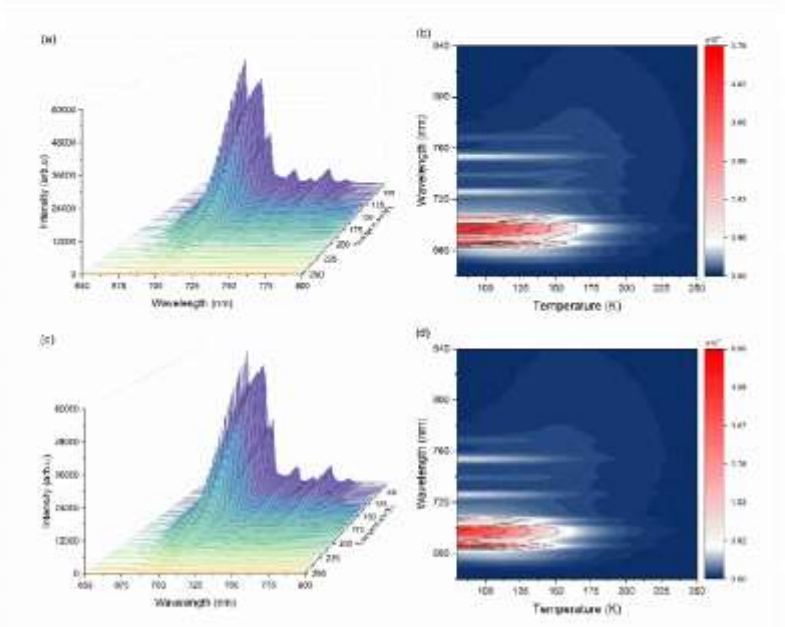

Figure S9. (a) Temperature-dependent luminescence and (b) emission map of $[DMA]Zn_{0.99}Cr_{0.01}(HCOO)_3$; (c) temperature-dependent luminescence and (d) emission map of $[DMA]Zn_{0.95}Cr_{0.05}(HCOO)_3$

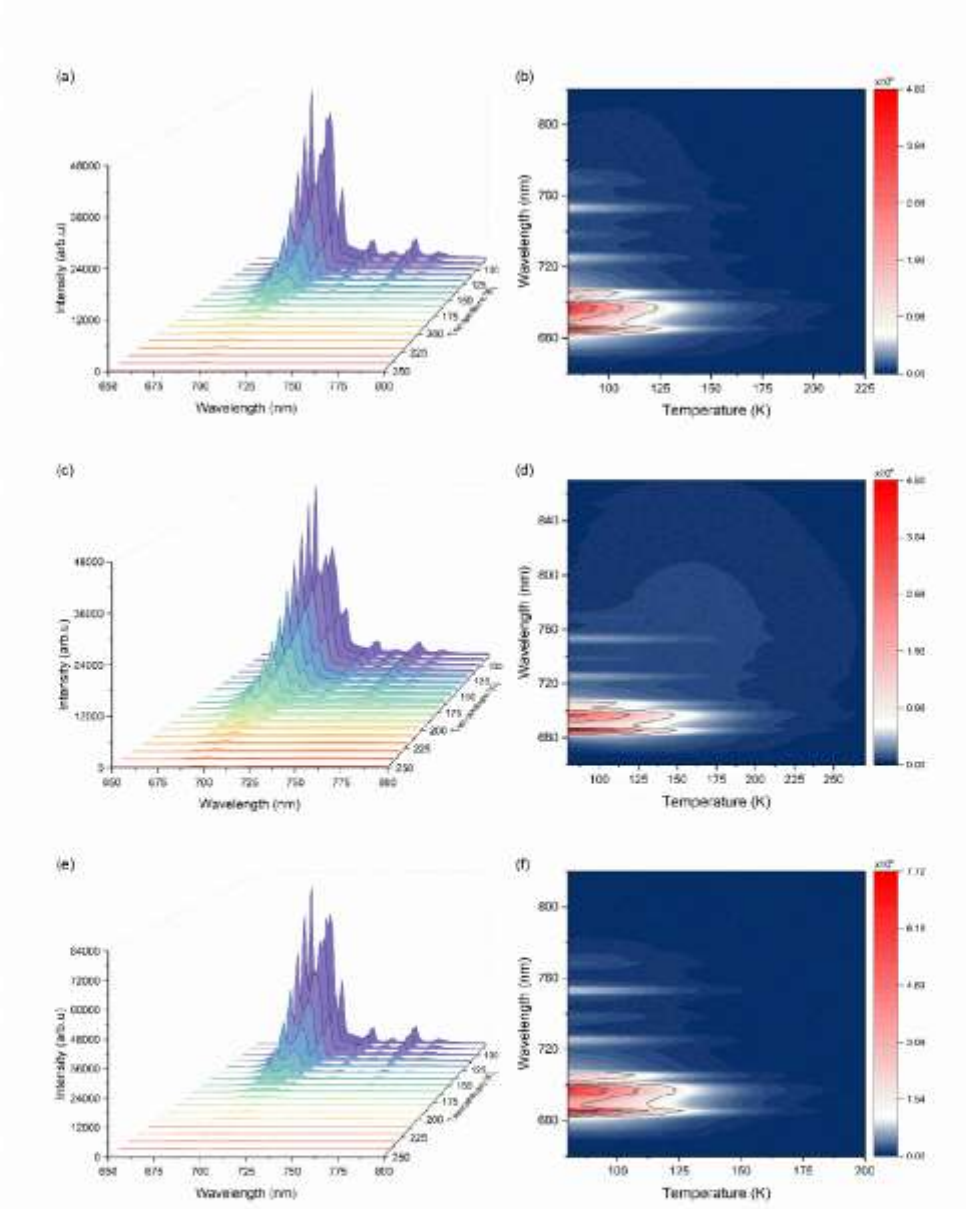

Figure S10. (a) Temperature-dependent luminescence and (b) emission map of $[DMA]Mn_{0.99}Cr_{0.01}(HCOO)_3$; (c) temperature-dependent luminescence and (d) emission map of $[DMA]Mn_{0.97}Cr_{0.03}(HCOO)_3$; (e) temperature-dependent luminescence and (f) emission map of $[DMA]Mn_{0.95}Cr_{0.05}(HCOO)_3$

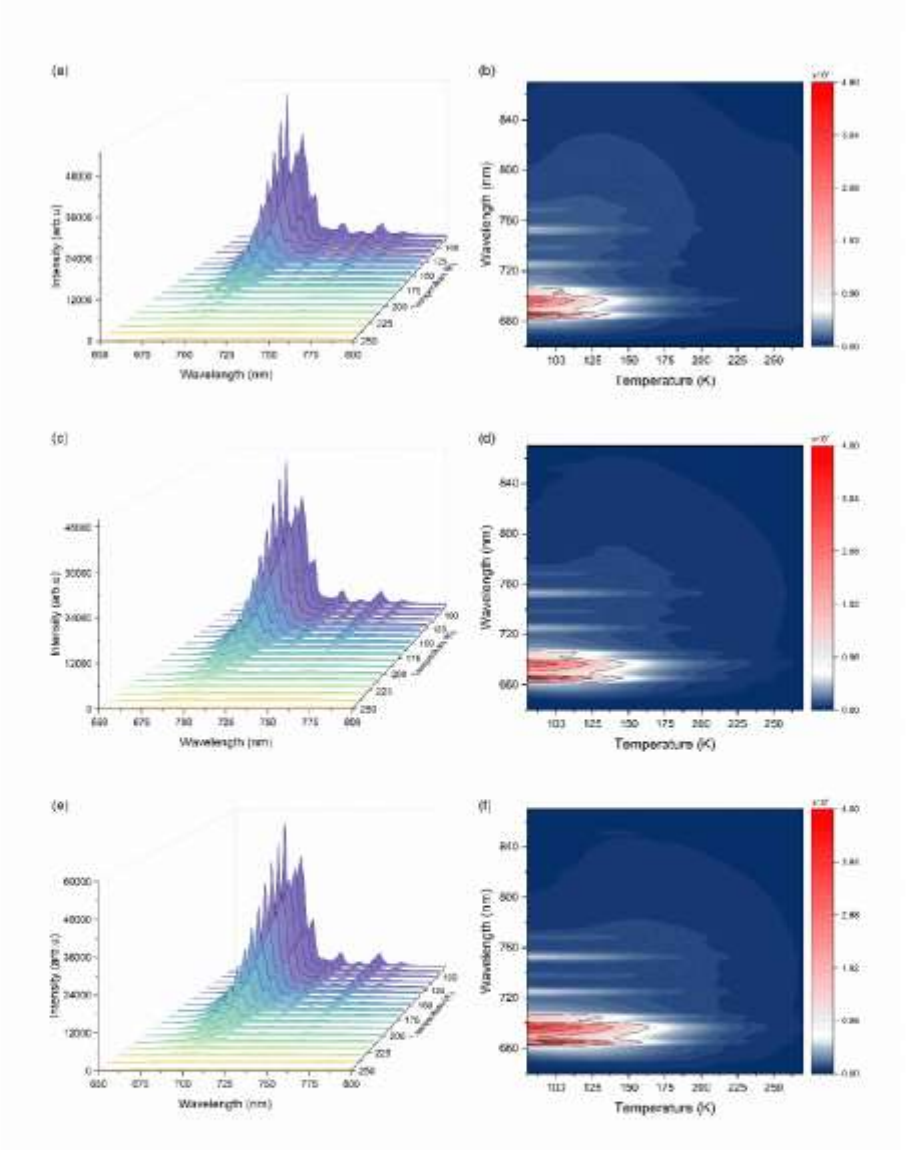

Figure S11. (a) Temperature-dependent luminescence and (b) emission map of $[DMA]Mg_{0.99}Cr_{0.01}(HCOO)_3$; (c) temperature-dependent luminescence and (d) emission map of $[DMA]Mg_{0.97}Cr_{0.03}(HCOO)_3$; (e) temperature-dependent luminescence and (f) emission map of $[DMA]Mg_{0.95}Cr_{0.05}(HCOO)_3$

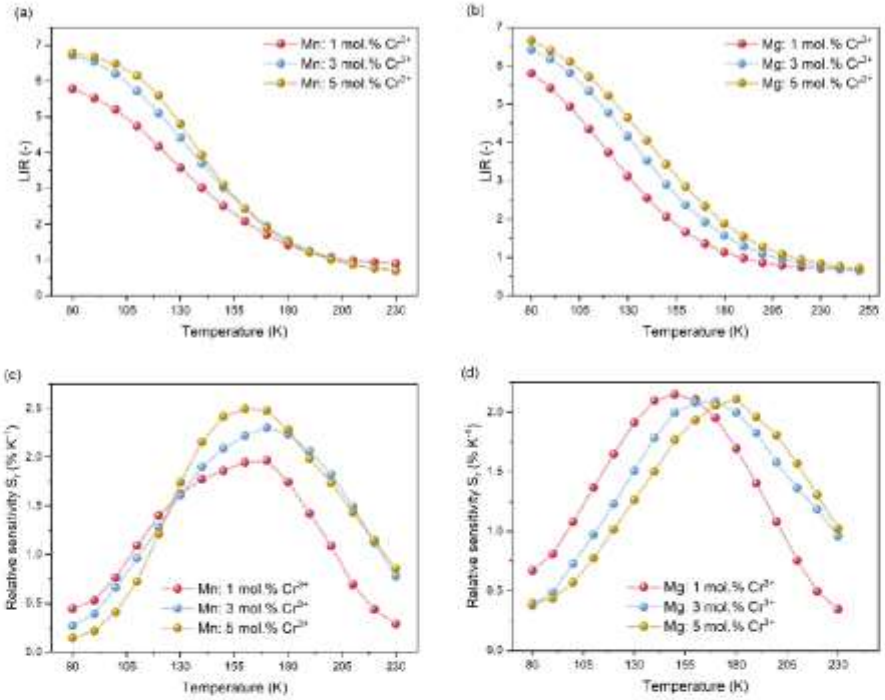

Figure S12. The change of the luminescence intensity ratio (LIR) in the function of temperature for: (a) $[DMA]Mn_{1-x}Cr_x(HCOO)_3$ and (b) $[DMA]Mn_{1-x}Cr_x(HCOO)_3$; the change of relative sensitivity (S_r) in the function of temperature: (c) $[DMA]Mn_{1-x}Cr_x(HCOO)_3$ and (d) $[DMA]Mg_{1-x}Cr_x(HCOO)_3$, where x = (0, 0.01, 0.03, 0.05)

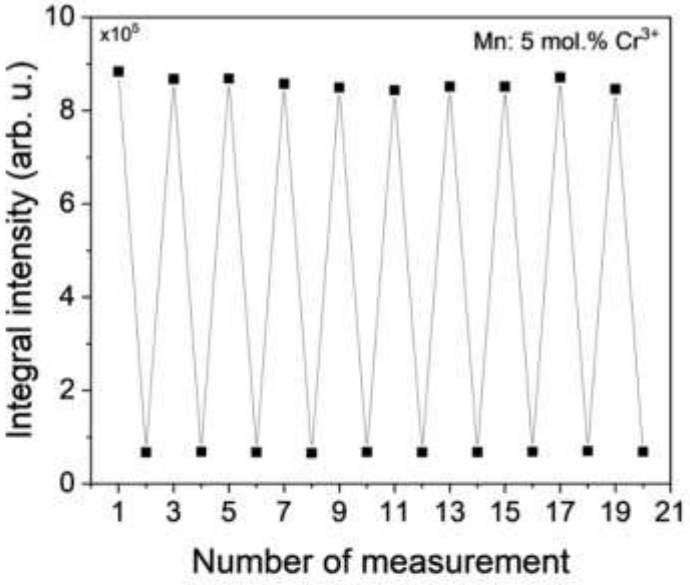

Figure S13. The thermal stability of the signal within the cooling-heating intervals (80-160 K)

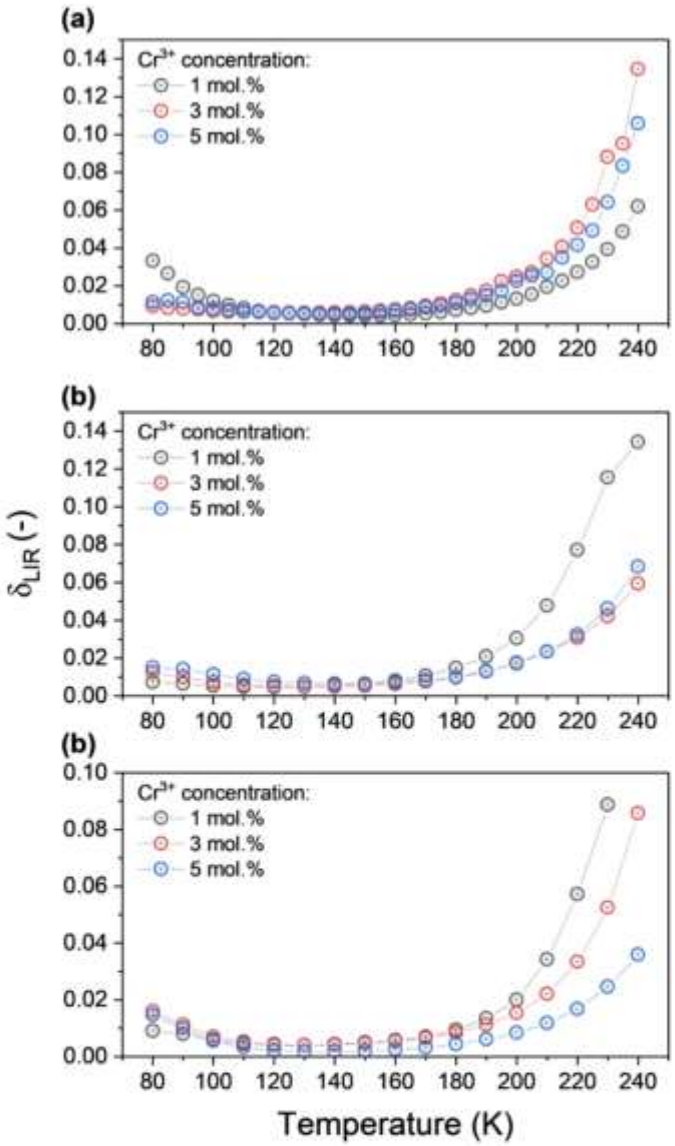

Figure S14. The comparison of the error of the LIR determination for: (a) $[DMA]Zn_{1-x}Cr_x(HCOO)_3$; (b) $[DMA]Mg_{1-x}Cr_x(HCOO)_3$; and (c) $[DMA]Mn_{1-x}Cr_x(HCOO)_3$, where x = (0, 0.01, 0.03, 0.05)

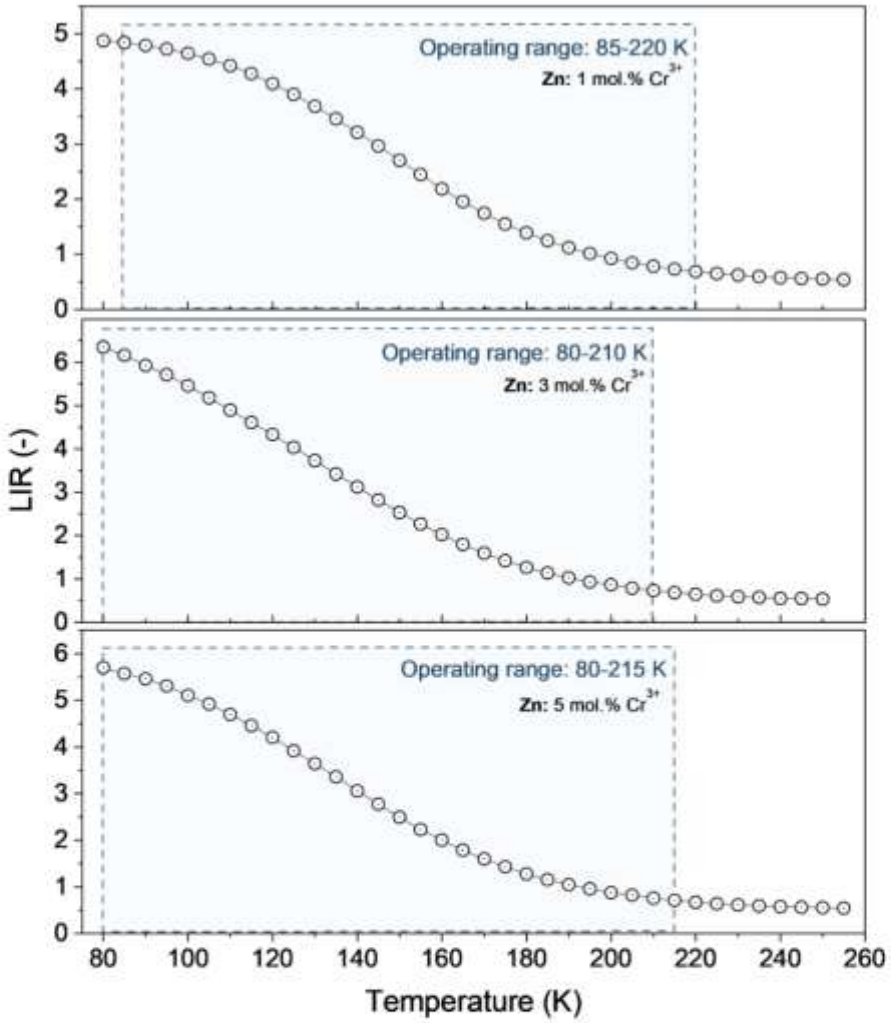

Figure S15. The comparison of the operating ranges for the $[DMA]Zn_{1-x}Cr_x(HCOO)_3$, where x = (0, 0.01, 0.03, 0.05)

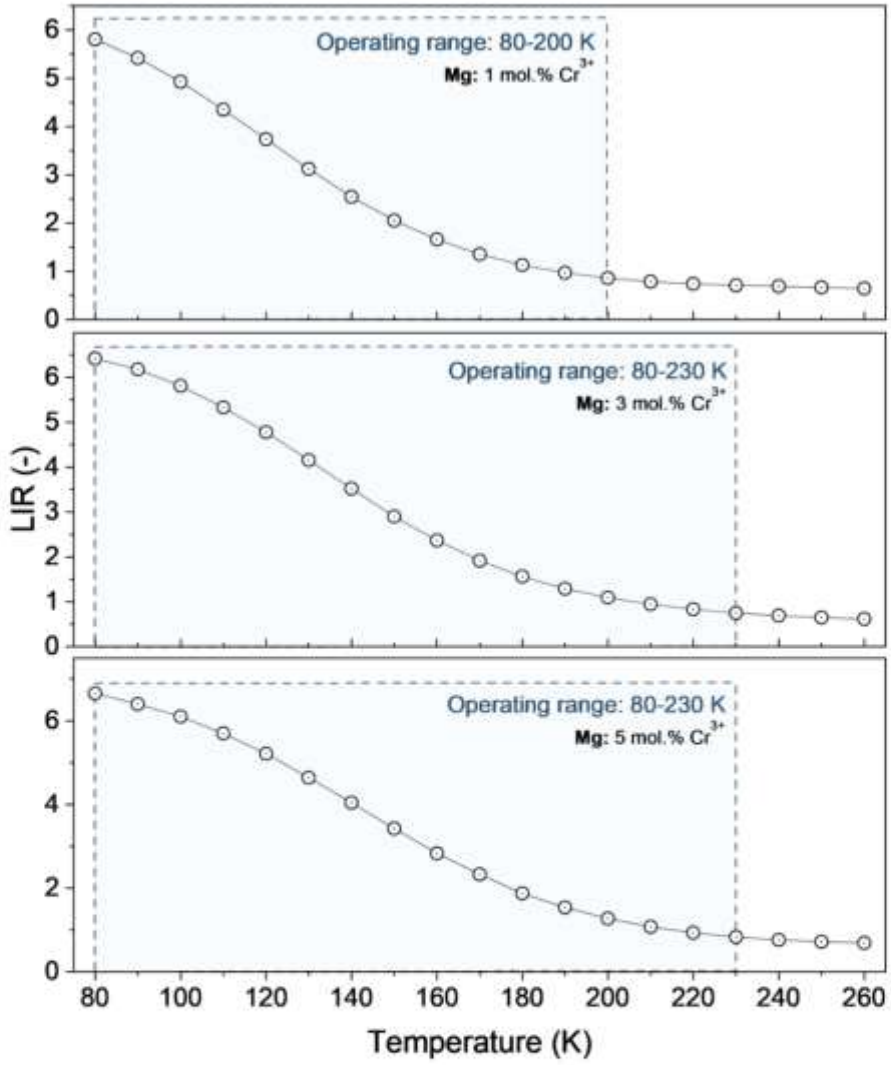

Figure S16. The comparison of operating ranges for the $[DMA]Mg_{1-x}Cr_x(HCOO)_3$, where x = (0, 0.01, 0.03, 0.05)

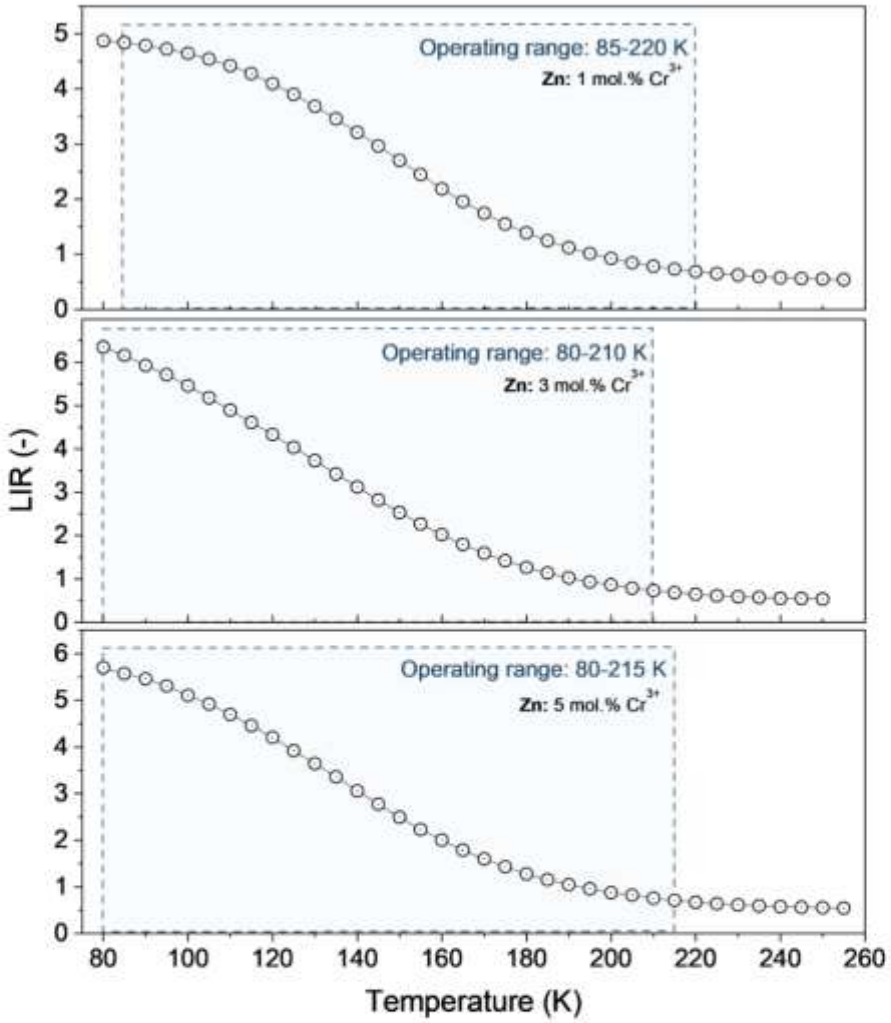

Figure S17. The comparison of the operating ranges for the $[DMA]Mn_{1-x}Cr_x(HCOO)_3$, where x = (0, 0.01, 0.03, 0.05)

10.4 Publication P4

Dalton Transactions

ROYAL SOCIETY OF CHEMISTRY

PAPER

View Article Online
View Journal | View Issue

Check for updates

Cite this: *Dalton Trans.*, 2025, **54**, 15899

High-sensitivity optical thermometry with Cr^{3+}-doped hybrid formate perovskites: comparative analysis of ratiometric and lifetime-based approaches

Adam Kabański, * Kacper Caputa and Dagmara Stefańska *

Optical thermometry, due to its properties such as rapid response, usability, high sensitivity, and remote measurements, is gaining increasing interest among researchers. Particularly promising materials for low-temperature thermometry applications are metal–organic frameworks (MOFs) containing chromium(III) ions. In this work, we present a method for optimising data for the development of a temperature sensor, with particular focus on the relative sensitivity parameter (S_r). As part of the optimisation process, we distinguish two approaches using different data analysis techniques and observe the impact of individual parameters on the temperature characteristics of the materials. Additionally, we present the structural and spectroscopic properties of a series of $[EA]Mg_xCr_{1-x}(HCOO)_3$, where EA = ethylammonium cation, and x = 0, 0.01, 0.03, and 0.05. These materials are characterised by a perovskite structure and exhibit a strong dependence of spectroscopic properties on the concentration of the dopant and temperature. The luminescence properties of chromium(III) ions change due to variations in the crystal field strength (Dq/B), which is measured using diffuse reflectance spectroscopy and photoluminescence techniques. The investigated materials exhibit particular temperature-dependent luminescence, which can be implemented as a basis for the thermometric model determination. Moreover, the influence of temperature on luminescence lifetime provides a secondary thermometric pathway, which has not been reported for hybrid formate perovskites before. The obtained optical ratiometric sensors are characterized by high relative sensitivity (up to 3.07% K^{-1} at 130 K) and a wide operating range (up to 80–170 K interval). The thermometric analysis of the lifetime-based model shows high relative sensitivity up to 2.97% K^{-1} (140 K). In this work, we investigated the influence of the chemical composition on the observed thermometric performance within a series of EA-based hybrid compounds and compared two thermometric approaches – ratiometric and lifetime-based. What is more, we provide a comprehensive comparison of the spectroscopic properties, especially concerning the thermometric potential, with those of other reported hybrid formates, differing in the type of organic cation. The presented results show a particular potential of hybrid formate perovskites doped with Cr^{3+} ions, especially within the context of highly sensitive luminescence thermometry.

Received 24th July 2025,
Accepted 27th September 2025

DOI: 10.1039/d5dt01748c

rsc.li/dalton

Introduction

Luminescence thermometry represents a novel and increasingly prominent approach to remote temperature monitoring, offering several advantages over conventional contact-based thermometric techniques.[1–3] Luminescent materials enable highly sensitive, rapid, and remote temperature measurements while reducing susceptibility to external disturbances such as strong electromagnetic fields.[4] The three most employed optical thermometric strategies include the analysis of emission lifetime variations, monitoring spectral shifts of specific bands, and the ratiometric method—based on comparing the emission intensities of two temperature-dependent spectral bands.[1,5,6] A wide range of luminescent materials with suitable spectroscopic characteristics are available for the development of thermometric models, with the majority based on inorganic host doping with rare-earth (RE) elements.[5,7,8] However, increasing attention has recently been directed towards compounds incorporating transition metal (TM) ions, owing to their thermometric performance, which is often comparable to those of RE-based systems.[6,9,10] The growing interest in luminescence thermometry is driving the search for new

Institute of Low Temperature and Structure Research, Polish Academy of Sciences, Wrocław, Poland. E-mail: a.kabanski@intibs.pl, d.stefanska@intibs.pl

materials and approaches that combine multimodal thermometric models, which may contribute to enhanced sensitivity and an extended operational range of such sensors.[11–14] In this context, hybrid organic–inorganic materials containing Cr^{3+} ions have emerged as particularly promising candidates for luminescence thermometry applications.[10,15]

The hybrid organic–inorganic compounds with perovskite-like structures are becoming more interesting due to a wide range of functional properties.[16–18] These materials, often forming metal–organic frameworks (MOFs), have attracted increasing attention because of remarkable magnetic, ferroelectric, multiferroic, and spectroscopic characteristics. Perovskite-like materials are defined with an ABX_3 structure, where A is an organic compound, B stands for divalent metal ions and X is an monovalent anion. Among them, the halide-based hybrid perovskites have been successfully implemented in photovoltaic applications.[19,20] The substitution of the A, B or X components can significantly change the properties of compounds.[21,22] Due to this, perovskite-like materials can be used far beyond this scope.

A particularly noteworthy subgroup comprises formate-based compounds ($X = HCOO^-$), which exhibit interesting features including ferroelectricity, multiferroicity, and both linear and nonlinear optical properties.[18,21,22] Within the context of luminescent materials, hybrid formates containing Cr^{3+} ions deserve special attention. Due to their chemical stability, strong luminescence, weak concentration quenching, and strong thermal quenching, these materials have been effectively applied as luminescent thermometers for remote temperature sensing.[10,15,23] The additive of Cr^{3+} ions results in a luminescent centre strongly sensitive to the local environment, described by the crystal-field (CF) strength. Chromium trivalent ions exhibit two main types of transitions observed in the luminescence spectrum: narrow spin-forbidden $^2E_g \rightarrow {}^4A_{2g}$ and broad spin-allowed $^4T_{2g} \rightarrow {}^4A_{2g}$. In a strong crystal field, only the narrow transition from ^2E_g is observed. However, in a weak crystal field, the broad emission from $^4T_{2g}$ becomes dominant.[24,25] Additionally, in the intermediate CF, there is a coexistence of these two types of transitions. At low temperatures the $^2E_g \rightarrow {}^4A_{2g}$ emission is dominant, while increasing the temperature induces the thermal population of $^4T_{2g}$, which leads to more intense occurrence of $^4T_{2g} \rightarrow {}^4A_{2g}$ emission. Increasing the temperature causes a change in the intensity of emission bands, like spin-allowed, spin-forbidden and Stokes lines, but the change does not progress equally. That is why the ratiometric method—based on comparing the emission intensities of two temperature-dependent spectral bands—can be performed. Also, the luminescence lifetime is another noteworthy approach applied to remote temperature sensing, due to its significant dependence on temperature.[26,27] This novel approach is not explored yet for hybrid perovskites containing Cr^{3+} ions. It is noteworthy that the implementation of the hybrid organic–inorganic compounds doped with Cr^{3+} ions provides the possibility of application of these compounds as highly sensitive luminescent thermometers for the cryogenic temperature range. The potential of luminescence thermometry in this temperature regime has been demonstrated for both inorganic and hybrid compounds containing lanthanide ions,[28,29] as well as for inorganic chromium-based materials.[30,31]

In this work, we report the synthesis and structural and spectroscopic properties of the series of $[EA]Mg_{1-x}Cr_x(HCOO)_3$, where $x = 0$, 0.01, 0.03, 0.05. The optical spectroscopic techniques, diffuse-reflectance spectroscopy, and luminescence lifetime measurements are applied to provide comprehensive results showing the relationship between structural and spectroscopic characteristics in hybrid materials containing Cr^{3+} ions. In particular, we examined the influence of chromium doping on changes in spectroscopic properties such as the temperature-dependent components of the emission spectra, the shape of the absorption spectra, and the luminescence lifetimes. The temperature-dependent character of the investigated parameters is used to determine the thermometric potential of the investigated compounds. For this purpose, two types of thermometric models, based on different approaches (ratiometric model and lifetime-based) are presented, including calculations of obtained sensitivities and sensing ranges. For the first time, the implementation of the lifetime-based approach in hybrid perovskites doped with Cr^{3+} is investigated.

At the same time, this represents the first attempt to compare thermometric properties based on the ratiometric method with those based on emission lifetimes in the context of hybrid formate perovskites. We believe that the optimization of the thermometric model is a critical step towards the development of more sensitive and accurate luminescent thermometric devices.

Experimental

Materials and instrumentation

The purity of the samples was examined using powder X-ray diffraction (PXRD) on an X'PertPro X-ray diffraction system (PIXcel detector and Soller slits for CuKα radiation, λ = 1.54056 Å). The diffuse reflection spectra (DRS) were obtained by using a Varian Cary 5E UV/VIS-NIR spectrophotometer (Varian Incorporation, Palo Alto, CA, USA). Emission spectra were measured with a Hamamatsu PMA-12 photonic multichannel analyser, equipped with a BT-CCD linear image sensor (Hamamatsu Photonics K.K, Shizuoka, Japan). The luminescence decay curves were recorded with a photoluminescence spectrophotometer FLS1000 (Edinburgh Instruments, Livingston, Scotland). The temperature-dependent measurements were conducted with a Linkam THMS 600 heating/freezing stage (The McCrone Group, Westmont, IL USA).

Synthesis

In the synthesis of $[EA]Mg_{1-x}Cr_x(HCOO)_3$ (where $x = 0$, 0.01, 0.03, 0.05) commercially available precursors (without further purification) such as ethylammonium hydrochloride (98%, Sigma-Aldrich), formic acid (≥98%, POCH), anhydrous methanol (MeOH) (99.8%, Sigma-Aldrich), chromium(III) chloride hexahydrate (≥98%, Sigma-Aldrich), magnesium chloride

(≥98%, Sigma-Aldrich), and triethylamine (≥98%, Sigma-Aldrich) were used. The compounds were synthesized using a low-diffusion technique. Initially, two solutions are prepared: solution A (heavy phase) and solution B (light phase). The preparation of solution A involved dissolving EA·HCl (8 mmol) in 7.5 ml of MeOH and then adding 1.5 ml of HCOOH and 0.7 ml of triethylamine. To obtain solution B, $MgCl_2$ (2 mmol) and a stoichiometric amount of $CrCl_3$ were dissolved in 5 ml of MeOH. The solutions were carefully layered in a glass test tube (1 cm in diameter and 18 cm in length) using a syringe. The formation of the materials takes place in the interface of two solutions. After one week, crystals were collected, thoroughly washed with ethanol, and air-dried. The phase purity of the synthesized samples was confirmed by powder X-ray diffraction (XRD), with the recorded patterns compared against simulated data derived from single-crystal structural parameters.

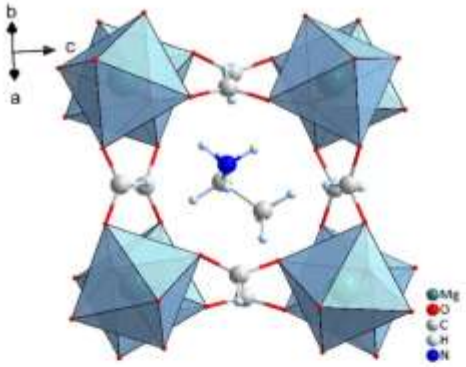

Fig. 1 The visualization of $[EA]Mg(HCOO)_3$ at room temperature (293 K), according to CCDC 901263.

Results

Structural and phonon characteristics

The structural and phonon properties of the investigated undoped material, $[EA]Mg(HCOO)_3$, have been studied in detail by Ciupa *et al.*[32] and Shang *et al.*[33] Therefore, in this work, we present a synthetic overview of its characteristics. At room temperature, the group of ethylammonium-based metal–organic frameworks containing formate linkers crystallizes in the non-centrosymmetric $Pna2_1$ space group (with ordered EA^+ cations). The observed phase transitions to the trigonal $R\bar{3}$ phase occur around 373 K (heating) and 316 K (cooling). The performed differential scanning calorimetry (DSC) and thermogravimetric analysis (TGA) measurements show an enthalpy change (ΔH) of 0.5 kJ mol^{-1}. The second phase transition, to the orthorhombic *Imma* phase, takes place around 426 K (heating) and 415 K (cooling). For this phase transition, the reported ΔH value is equal to 7.0 kJ mol^{-1}. The temperature of the decomposition is, in turn, equal to 470 K.[33] A visualization of the $[EA]Mg(HCOO)_3$ structure is shown in Fig. 1.

Reported Raman and IR studies provide comprehensive data on the phonon characteristics of $[EA]Mg(HCOO)_3$. The work of Ciupa *et al.*[34] confirms the presence of characteristic bands corresponding to internal vibrations of EA^+ and $HCOO^-$ ions, as well as modes related to the crystal lattice. The temperature-dependent study of $[EA]Mg(HCOO)_3$ shows that its IR and Raman spectra remain largely unchanged up to 370 K, but at 390 K, they undergo abrupt modifications, indicating a first-order phase transition. This transition is associated with a structural change to a trigonal phase and dynamic disorder of the EA^+ cations. It manifests as the disappearance, broadening, and merging of several vibrational bands, along with the appearance of new ones. These spectral changes confirm the structural distortion of the magnesium-formate framework above 374 K.[32]

To confirm the quality of the synthesized crystals and evaluate the structural impact of Cr^{3+} ion incorporation, powder X-ray diffraction (PXRD) analysis was performed. The diffraction patterns were compared with simulated patterns derived from single-crystal data sources (Fig. S1). The results confirmed sufficient purity of the materials. The incorporation of trivalent Cr^{3+} into the divalent Mg^{2+} sites results in the appearance of additional signals at approximately 18° and 34.5° in the sample containing 5 mol% of chromium(III) ions. These additional signals may be attributed to structural defects that destabilize the crystal lattice, thereby limiting the maximum achievable Cr^{3+} concentration. A similar limitation in dopant concentration has been reported for a series of DMA- and GUA-based hybrid formate perovskites doped with Cr^{3+} ions.[15]

Diffuse reflectance spectroscopy

Diffuse reflectance spectroscopy (DRS) was utilized to verify the incorporation of trivalent chromium ions (Cr^{3+}) within the hybrid organic–inorganic compounds. The collected DRS spectra for the studied samples are presented in Fig. 2. Materials doped with Cr^{3+} exhibit three distinct absorption features located near 14 536 cm^{-1} ($^4A_{2g} \rightarrow {}^2E_g$), 16 977 cm^{-1} ($^4A_{2g} \rightarrow {}^4T_{1g}$), and 23 257 cm^{-1} ($^4A_{2g} \rightarrow {}^4T_{2g}$), consistent with data reported for other Cr^{3+}-containing formate perovskites.[10,15,35]

The application of the described matrix lies in the absence of absorption bands in the 12 000–28 000 cm^{-1} range, which would otherwise overlap with the absorption of Cr^{3+} ions. The fact that no overlap of absorption bands is observed in the described compounds allows for the determination of Racah parameters and crystal field strength without interference from bands associated with other ions. The phenomenon of overlapping absorption bands has been reported, for instance, for compounds containing Mn^{2+}, Co^{2+}, and Ni^{2+} ions.[15,35]

The DRS results for Cr^{3+}-doped systems are commonly employed to extract crystal field and Racah parameters, which provide insights into the local environment of the optically active chromium(III) ions.[36,37] The Dq/B ratio, indicating the strength of the crystal field, is a key parameter used to describe the interaction between Cr^{3+} ions and their host lattice.[38–40] According to the Tanabe–Sugano diagram for the $3d^3$ electron

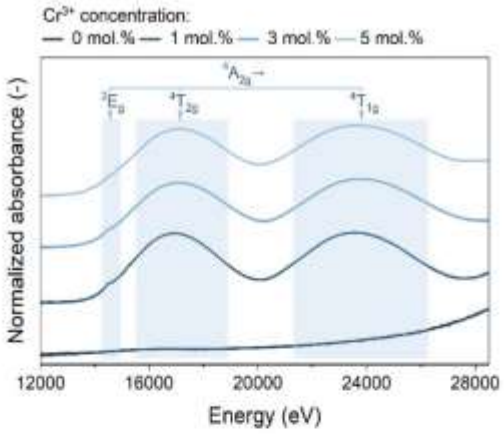

Fig. 2 The comparison of the DRS spectra for $[EA]Mg_{1-x}Cr_x(HCOO)_3$.

configuration characteristic of Cr^{3+}, the states ^2E_g and $^4T_{2g}$ overlap when the Dq/B value equals 2.3, defining the regime of intermediate crystal field strength. Values above and below this threshold correspond to strong and weak crystal fields, respectively. From the positions of the Cr^{3+} absorption bands, the parameters Dq, B, and C, and their ratio Dq/B were calculated and are presented in Table S1. The obtained Dq/B ratios for materials doped with 1 mol%, 3 mol%, and 5 mol% Cr^{3+} are 2.43, 2.45, and 2.61, respectively. The described materials exhibit medium/strong crystal fields, which facilitate the evaluation of their thermometric potential and the determination of the influence of this parameter on the resulting sensor sensitivities.

Optical properties

The investigated materials exhibit photoluminescence (PL) under excitation at a wavelength of 405 nm, which efficiently promotes the $^4A_{2g} \rightarrow {}^4T_{1g}$ transition of Cr^{3+} ions. At 80 K, the exemplary emission spectrum of the $[EA]Mg_{0.97}Cr_{0.03}(HCOO)_3$ sample shows several narrow bands, with the most intense peak observed at 686.5 nm, assigned to the R_1 line (Fig. 3a). This emission band is attributed to the spin-forbidden $^2E_g \rightarrow {}^4A_{2g}$ transition. Additional Stokes sidebands are located at 696.8 nm, 726.5 nm, and 754.5 nm. Moreover, a low-intensity broadband emission in the range of 720–1000 nm is observed, which is assigned to the spin-allowed $^4T_{2g} \rightarrow {}^4A_{2g}$ transition (see the inset of Fig. 3a and b). At the highest measured temperature (270 K), a very weak emission from the $^4T_{2g}$ level is still observable. However, it is approximately 5000 times weaker than the maximum emission intensity recorded for the R_1 line at 80 K. The intensity of this transition is significantly lower than that with an analogous process from the ^2E_g level.

The simultaneous presence of both Cr^{3+}-related emission bands, combined with a medium/strong crystal field, suggests a remarkably low energy of the thermal population of the $^4T_{2g}$ level. Such a phenomenon is reported for other hybrid perovskites doped with Cr^{3+} ions.[10,15,35] The excitation spectra of the representative sample are presented in Fig. S4.

The PL emission is strongly temperature-dependent, with notable changes in both the spectral shape and intensity. As the temperature increases, the overall luminescence intensity decreases due to thermal quenching. However, this process is not uniform across the entire spectrum. The R_1 line undergoes the most rapid quenching, whereas the relative contribution of the broadband emission increases with temperature. The comparison of the normalized PL spectra at the 80–200 K range is shown in Fig. 3c. The progress of the thermal quenching of a $^2E_g \rightarrow {}^4A_{2g}$ emission range (670–720 nm) is presented in Fig. 3d. The $T_{0.5}$ is equal to 108 K, which indicates a rapid thermal quenching. Complete quenching of luminescence occurs near 230 K. Temperature-dependent PL spectra for other materials are provided in Fig. S2a and b. A comparison of the normalized emission spectra at 80 K and 170 K for the concentration series is presented in Fig. S3a and S3b, respectively. The highest contribution of the broadband $^4T_{2g} \rightarrow {}^4A_{2g}$ is observed in the sample doped with 1 mol% of Cr^{3+} ions, which aligns with the DRS analysis result indicating the lowest CF strength. The lowest contribution of the broadband emission is observed for 3 mol% of Cr^{3+}. The differences in CR strength for closely doped materials are reported for other hybrid compounds containing Cr^{3+} ions. This might have resulted from differences in the distribution of energy levels of Cr^{3+} ions within the organic–inorganic structure. The investigated materials exhibit stability during heating–cooling cycles. The thermal stability of a representative material is presented in Fig. S5. The observed temperature-dependent emission behaviour, particularly the non-uniform quenching of spectral features, offers a promising foundation for the development of luminescence-based thermometric models.

Luminescence thermometry

Luminescence thermometry is gaining more interest because of the remote, rapid and high sensitivity sensing.[1,41,42] Currently, the most commonly described thermometric models are those based on the change in the intensity ratio between two emission bands (the ratiometric method) and those relying on changes in luminescence lifetime. The ratiometric method is widely applied in lanthanide compounds and thermometers based on the luminescence of Cr^{3+} ions. Nevertheless, the lifetime-based method shows considerable promise, particularly for materials prone to rapid thermal quenching of luminescence. Herein, we present a comparison of thermometric properties in sensors based on two types of thermometric models—a ratiometric model and a model based on luminescence lifetimes.

Ratiometric approach

Among different thermometric approaches, the ratiometric method is the most frequently reported method.[43–45] This strategy involves analysing the changes in the intensities of two emission bands with temperature. To evaluate the sensing capabilities of the studied materials, the luminescence inten-

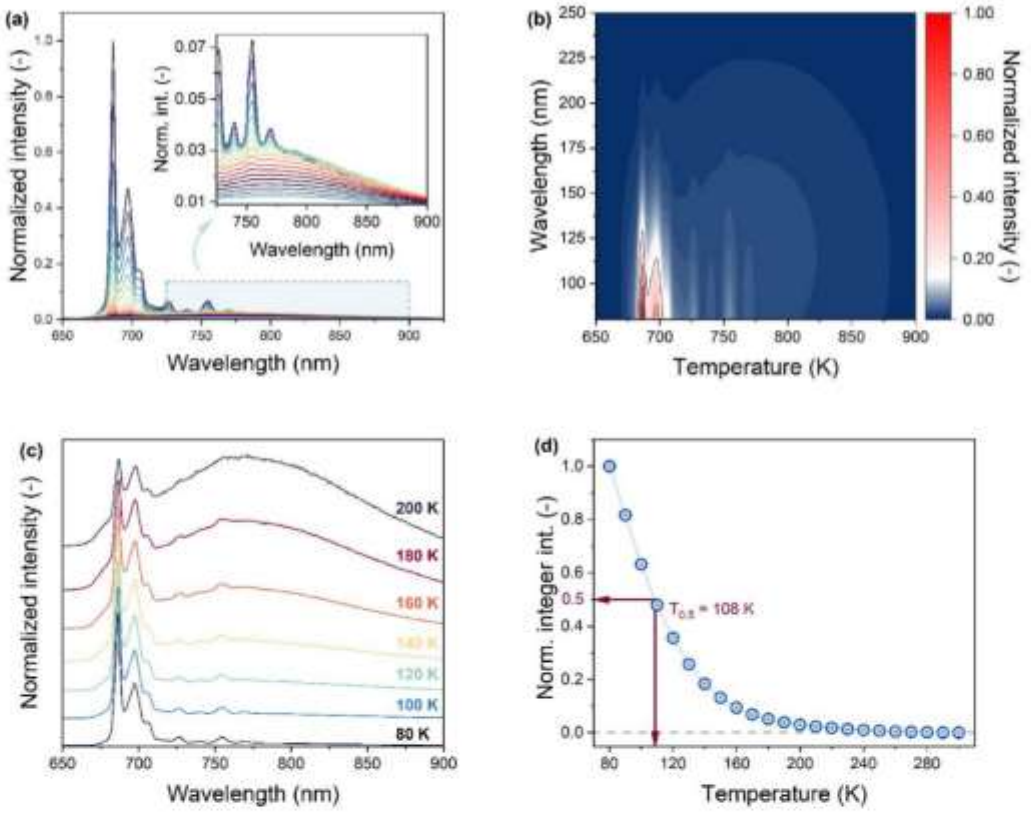

Fig. 3 (a) Temperature-dependent luminescence of $[EA]Mg_{0.97}Cr0.03(HCOO)_3$ with (inset graph) the area of the $^4T_{2g}$ emission; (b) emission map; (c) the comparison of the normalized emission spectra at various temperatures; and (d) thermal quenching of the $^2E_g \rightarrow {}^4A_{2g}$ luminescence with the $T_{0.5}$ marker.

sity ratio (LIR) is employed. This parameter represents the ratio between the intensities of selected thermally sensitive emission bands:

$$\mathrm{LIR} = \frac{I_1}{I_2} \tag{1}$$

where I_1 and I_2 stand for integral intensities of two thermometric regions. The selection of thermometric ranges I_1 and I_2 is presented in Fig. 4a. Within the investigated series, the implementation of ranges 675–692 nm (I_1) and 710–1000 nm (I_2) provides the optimal thermometric conditions. The chosen intervals show different quenching progressiveness, which is crucial from the thermometric point of view (Fig. 4b). The collation of the calculated LIR parameters for the series of $[EA]Mg_xCr_{1-x}(HCOO)_3$ (where x = 0, 0.01, 0.03, and 0.05) is presented in Fig. 4c.

The investigated materials exhibit different dependencies of the FIR parameter values on temperature. Materials containing 1 mol% and 5 mol% of chromium(III) show similar characteristics, whereas the material with 3 mol% of Cr^{3+} ions exhibits significantly higher LIR values. This results from a different shape of the luminescence spectra. For materials containing 1 mol% and 5 mol% chromium(III) ions, higher intensity of the broad $^4T_{2g} \rightarrow {}^4A_{2g}$ emission is observed. In the case of the material containing 3 mol% of chromium(III), the intensity of this transition is lower. This difference leads to substantially different LIR values. The suppression of the $^4T_{2g} \rightarrow {}^4A_{2g}$ emission causes the lower value of the I_2 parameter and, consequently, a higher LIR value. To provide a more comprehensive description of the usefulness of the obtained thermometers, the relative sensitivities (S_r) are calculated with the following equation:

$$S_r = \frac{1}{\mathrm{LIR}} \cdot \left|\frac{\mathrm{dLIR}}{\mathrm{d}T}\right| \tag{2}$$

where dLIR is the change of the LIR over the temperature change dT. The influence of temperature on the values of S_r is presented in Fig. 5a. The investigated materials are characterized by high relative sensitivity, which varies as a function of temperature. The maximum values of relative sensitivities are 2.69% K^{-1} (120 K), 3.07% K^{-1} (130 K), and 2.48% K^{-1} (120 K) for samples containing 1 mol%, 3 mol%, and 5 mol% of chromium(III) ions, respectively. The highest relative sensitivity was

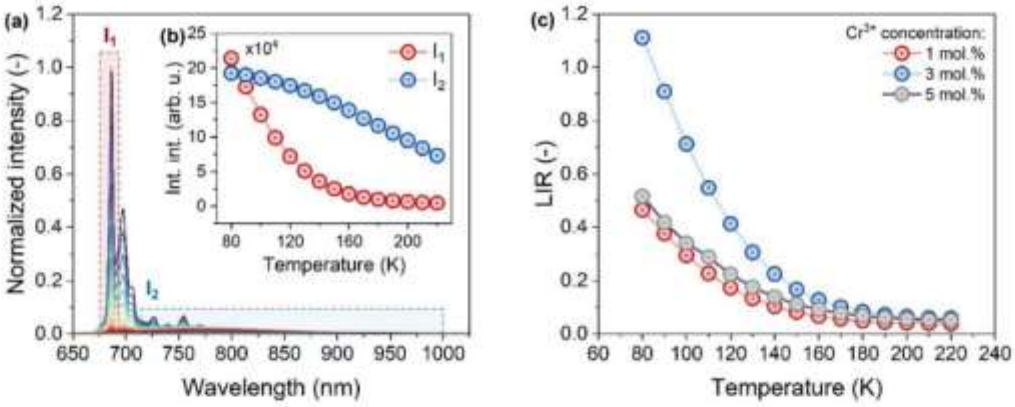

Fig. 4 (a) Temperature-dependent luminescence of $[EA]Mg_{0.97}Cr_{0.03}(HCOO)_3$; (b) thermal quenching of the I_1 and I_2 range with temperature; and (c) the temperature-driven reduction in the LIR parameter.

obtained for the sample containing 3 mol% of Cr^{3+} ions, which results from the most progressive reduction of the LIR parameter (Fig. 4c). The deviation from the observed trend at 100 K and 110 K is an instrumental anomaly resulting from a temporary instability of the apparatus.

The other materials, which exhibit similar LIR-temperature dependencies, also show analogous relationships between sensitivity and temperature.[10,15,35] The obtained results are a valuable addition to the current state of knowledge and highlight the particular potential of hybrid materials containing Cr^{3+} ions, where dLIR is the change of the LIR with the temperature change dT. The influence of temperature on the values of S_r is presented in Fig. 5a. The investigated materials are characterized by high relative sensitivity, which varies as a function of temperature. The maximum values of relative sensitivities are 2.69% K^{-1} (120 K), 3.07% K^{-1} (130 K), and 2.48% K^{-1} (120 K) for samples containing 1 mol%, 3 mol%, and 5 mol% of chromium(III) ions, respectively. The highest relative sensitivity was obtained for the sample containing 3 mol% of Cr^{3+} ions, which results from the most progressive reduction of the LIR parameter (Fig. 4c). The deviation from the observed trend at 100 K and 110 K is an instrumental anomaly resulting from a temporary instability of the apparatus.

The other materials, which exhibit similar LIR-temperature dependencies, also show analogous relationships between sensitivity and temperature.[10,15,35] The obtained results are a valuable addition to the current state of knowledge and highlight the particular potential of hybrid materials containing Cr^{3+} ions.

To further assess the thermometric efficiency, the operating range of the thermometer is determined following the methodology described by Bednarkiewicz *et al.*[46] The change in temperature detection uncertainty as a function of temperature is presented in Fig. 5b. Additionally, the operating ranges of each

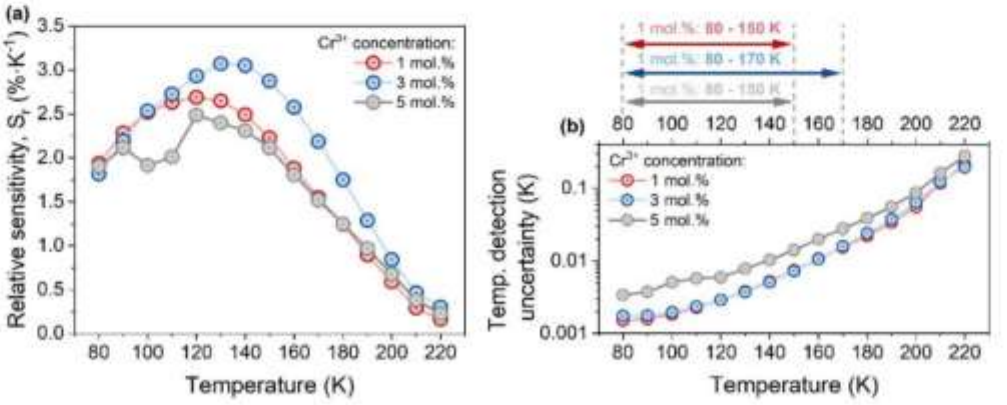

Fig. 5 (a) The comparison of the relative sensitivities of investigated thermometers and (b) temperature detection uncertainty with operating ranges.

thermometer are presented in the graph. The widest operating range is achieved for the sample containing 3 mol% of Cr^{3+} ions. The obtained results confirmed particular usefulness of optical sensors operating in strong crystal fields. Additionally, the thermal resolution of the readout is determined according to Brites *et al.*[5] The investigated materials show a sufficient thermal resolution within the operating ranges (Fig. S5). The thermal resolution less than 0.05 K within the operating range indicates the high practical potential of the presented approach for remote temperature sensing.

Lifetime-based method

The analysis of luminescence lifetimes represents an alternative approach, less commonly reported in the scientific literature, to thermometric model determination. Nevertheless, due to its potential for delivering reproducible signals and its applicability to materials exhibiting only a single emission band, the use of the lifetime-based method may significantly exceed the potential of optical thermometry.

The observed reduction in Cr^{3+} luminescence lifetime with increasing temperature is primarily attributed to the enhancement of non-radiative decay processes. In an octahedral crystal field environment, Cr^{3+} ions ($3d^3$ electron configuration) typically emit luminescence at low temperatures *via* spin-forbidden transitions from the $^2E_g \rightarrow {}^4A_{2g}$ level to the ground state. As the temperature rises, thermal activation facilitates a population of the higher-lying $^4T_{2g}$ state, leading to a redistribution of the spin-allowed and shorter-lived $^4T_{2g}$ emission. This results in a measurable decrease in the luminescence lifetime. Simultaneously, elevated temperatures increase the likelihood of non-radiative relaxation mechanisms, further contributing to the lifetime reduction. Regarding the influence of Cr^{3+} concentration, at low doping levels, Cr^{3+} ions remain well-isolated within the host lattice, minimizing concentration quenching. However, with increasing dopant concentration, the average distance between Cr^{3+} ions decreases, facilitating energy transfer between neighboring ions. This non-radiative migration can channel energy toward structural defects or impurity sites, where it is dissipated without photon emission, thereby shortening the observed lifetime. At even higher concentrations, Cr^{3+}–Cr^{3+} interactions may lead to the formation of ion pairs or clusters, introducing additional non-radiative pathways and significantly reducing both luminescence lifetime and intensity.

In lifetime-based thermometry, the luminescence intensity ratio (LIR) is replaced by the average luminescence lifetime (τ_{avg}) as a function of temperature. This parameter is defined by the following equation:

$$\tau_{avg} = \frac{I(t) \cdot t}{I(t)}$$

where $I(t)$ is the signal intensity at a given time t. The average luminescence lifetime is dependent on the chemical composition of the materials. The comparison of the τ_{avg} at 80 K is presented in Table 1. At 80 K, the reduction of the average luminescence lifetime takes place with an increase in Cr^{3+} ion concentration. Such a phenomenon is related to the concentration quenching and is reported for other series of hybrid perovskites containing Cr^{3+} ions.[10,15]

The investigated materials exhibit significant influence of temperature on luminescence decay (Fig. 6a). The resulting average decay times as a function of temperature are shown in Fig. 6b. A summary of the experimental conditions in decay curve determination is presented in Table S2. A decrease in the average luminescence lifetime is observed with increasing temperature, reflecting a quasi-Arrhenius-type behaviour. The applied method for determining the thermometric model involves first calculating the average luminescence lifetime as a function of temperature. Then, the dependence of τ_{avg} on T is fitted, which allows for obtaining a continuous variation of the τ parameter with temperature. To provide a continuous variation of the thermometric parameter, a nonlinear fitting procedure is applied using the following equation:

$$\tau_{fit}(T) = \frac{\tau_0}{1 + A \exp\left(-\frac{\Delta E}{kT}\right)}$$

where τ_0 is the average lifetime at the lowest investigated temperature, A is a preexponential parameter, k is the Boltzmann constant, and ΔE is thermal quenching energy. The detailed characteristics of the obtained fitting curves are summarized in Table S3.

The obtained fitting curves are further used to calculate relative sensitivity following the same principle as for the ratiometric approach:

$$S_r = \frac{1}{\tau_{fit}} \cdot \left|\frac{d\tau_{fit}}{dT}\right|$$

where $d\tau_{fit}$ is the change of the fitted thermometric parameter (τ_{fit}) over the temperature change dT. The influence of temperature on the calculated value of S_r is shown in Fig. 6c. The collation of the calculated values of τ_{avg} combined with fitting functions as well as relative sensitivities for other materials is presented in Fig. S7a–f.

Within the Mg-series, there is no visible correlation between the chemical composition of the thermometer and the obtained relative sensitivity. The highest relative sensitivity is observed for the material containing 1 mol% of Cr^{3+} ions (2.97% K^{-1}, 140 K). Other materials show significantly similar values equal to 2.90% K^{-1} (139 K) and 2.94% K^{-1} (138 K) for 3 mol% and 5 mol%, respectively. A summary of the maximal S_r values with the corresponding temperatures is presented in Table 1.

Table 1 A summary of the thermometric characteristics of the lifetime-based method

Cr^{3+} content	$\tau_{avg\ 80K}$	$S_{r,\ max}$	$T_{Sr,\ max}$
1 mol%	0.72 ms	2.97% K^{-1}	140 K
3 mol%	0.69 ms	2.90% K^{-1}	139 K
5 mol%	0.55 ms	2.94% K^{-1}	138 K

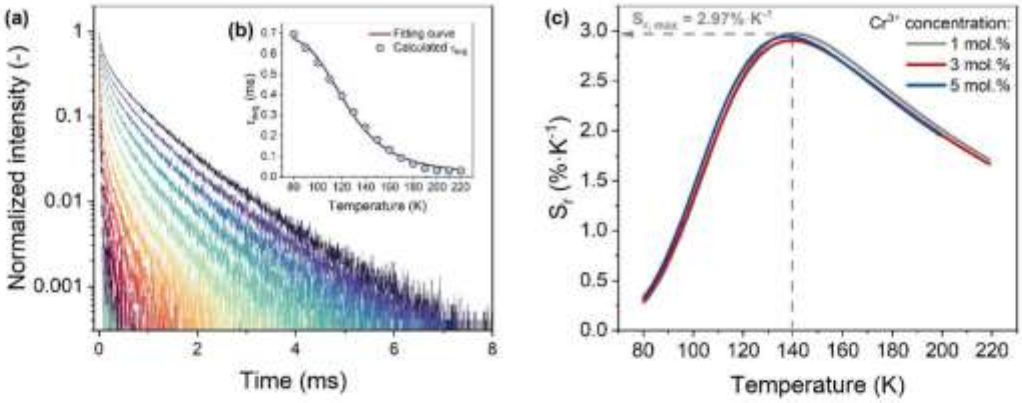

Fig. 6 (a) Temperature-dependent decay curves of an exemplary material containing 3 mol% of Cr^{3+}; (b) the change in the average luminescence lifetime as a function of temperature with fitting function; and (c) the change in relative sensitivity with temperature, where S_r, max denotes the highest value.

The obtained values of S_r are comparable to those with the ratiometric approach, which indicates the significant potential of the performed method in luminescence thermometry. The reduction of the temperature of the maximal S_r value ($T_{Sr,\ max}$) is correlated with increasing chromium(III) concentration. The change of the $T_{Sr,\ max}$ as a function of the chemical composition has been previously reported for a wide range of chromium concentrations (from 21 mol% to 100 mol%) in $[EA]_2NaAl_{1-x}Cr_x(HCOO)_6$. The obtained results of lifetime thermometry show a usefulness comparable to that of the ratiometric approach. The implementation of the double-mode luminescence thermometry may significantly extend the possibility of more accurate and precise temperature monitoring.

The thermometric properties of the investigated material can be contextualized by comparison with previously studied Cr^{3+}-doped hybrid formates. In the work by Kabański *et al.*, a series of $[DMA]M^{II}_{1-x}Cr_x(HCOO)_3$ (M^{II} = Zn^{2+}, Mn^{2+}, Mg^{2+}, Ni^{2+}, Co^{2+}; x = 0–0.05) crystallizing in the $R\bar{3}c$ phase was examined.[15] The investigated materials exhibit intermediate/strong crystal fields. The highest relative sensitivity of 2.5% K^{-1} (160 K) was reported for $[DMA]Mn_{0.95}Cr_{0.05}(HCOO)_3$. The Zn^{2+}- and Mg^{2+}-based derivatives showed maximal values of 2.4% K^{-1} (165 K) and 2.2% K^{-1} (150 K), respectively. In the Mg^{2+} series, a shift in the temperature with maximum sensitivity was observed with varying Cr^{3+} content—an effect not present in other single-perovskite systems.

Stefańska *et al.* investigated $[GA]M^{II}_{1-x}Cr_x(HCOO)_3$ (M^{II} = Zn^{2+}, Mn^{2+}, Mg^{2+}), crystallizing in the *Pnna* space group.[35] These materials exhibited no phase transitions and showed increasing crystal field strength (Dq/B = 2.29–2.43) with higher Cr^{3+} content. The spectroscopic properties suggest, in turn, lower crystal field strength compared to those of other reported series of hybrid materials. The highest S_r (2.08% K^{-1}, 90 K) was recorded for the Mg^{2+} sample doped with 1 mol% Cr^{3+}, while other compositions yielded about 1% K^{-1}.

Taking into account the size of the organic cations (DMA^+ < EA^+ < GUA^+),[39] it can be observed that an increase in amine size results in a decrease in the relative sensitivity of the thermometric materials. In the case of cations with comparable sizes, such as DMA^+ (272 pm) and EA^+ (274 pm), the linearity of the organic cation may become a significant parameter. The highest sensitivity among the investigated materials is observed for compounds containing the EA^+ cation, which features a more linear structure than DMA^+.

This may represent a significant milestone in the more conscious and efficient design of new thermometric materials.

Overall, Cr^{3+}-doped hybrid formates demonstrate significant potential for optical thermometry. Their tunable spectroscopic properties, driven by their chemical composition and structure, offer valuable adaptability for temperature sensing applications using both ratiometric and lifetime-based methods.

Conclusions

A series of materials with the general formula $[EA]Mg_{1-x}Cr_x(HCOO)_3$ (where x = 0, 0.01, 0.03, 0.05) was synthesized using a slow-diffusion method. Powder X-ray diffraction (pXRD) analysis confirmed the phase purity and structural stability of the materials across the investigated Cr^{3+} concentration range. Due to the charge mismatch between Cr^{3+} and Mg^{2+} ions, the maximum achievable doping level was limited to 5 mol%, consistent with findings for other reported hybrid compounds. Diffuse reflectance spectroscopy (DRS) analysis indicated a medium/strong crystal field, which was further supported by complementary spectroscopic measurements.

The synthesized materials exhibit pronounced luminescence upon 405 nm excitation. At 80 K, the emission from the ^2E level is significantly more intense than that from the $^4T_{2g}$ level. The emission intensity shows a strong dependence on

temperature, which enabled the development of a luminescence-based thermometric model relying on the intensity ratio of the two emission bands. The resulting emission-based thermometer demonstrated high relative sensitivity (up to 3.07% K^{-1}, 130 K).

Additionally, to further explore the thermometric potential, the temperature dependence of the luminescence lifetime was investigated for the first time in this class of hybrid compounds. The lifetime-based model exhibited relative sensitivity comparable to that of the ratiometric method (2.97% K^{-1}, 140 K). Moreover, comparative analysis with other hybrid compounds revealed a potential correlation between the cation size and expected relative sensitivity of the thermometric materials. An increase in amine size may lead to a decrease in sensitivity. Among similarly sized cations, the higher sensitivity observed for EA^+-based compounds may result from its more linear molecular structure compared to that of DMA^+.

This finding represents an important step toward the rational design of high-performance optical thermometers.

Author contributions

Conceptualization: D. S.; data curation: A. K. and K. C.; formal analysis: A. K., D. S. and K. C.; funding acquisition: D. S.; investigation: A. K. and K. C.; methodology: all authors; project administration: D. S.; supervision: D. S.; validation: D. S. and A. K.; writing – original draft: all authors; and writing – review and editing: all authors. All the authors have given their approval to the final version of the manuscript.

Conflicts of interest

There are no conflicts to declare.

Data availability

The data that support the findings of this study are openly available in Zenodo at: **https://doi.org/10.5281/zenodo.16408896**, reference number 16408896.

Supplementary information (SI) is available. See DOI: **https://doi.org/10.1039/d5dt01748c**.

Acknowledgements

This research was supported by the National Science Centre (NCN) in Poland under project SONATA 16 no. 2020/39/D/ST5/01289.

References

1 L. Đačanin Far and M. Dramićanin, *Nanomaterials*, 2023, **13**, 2904, DOI: **10.3390/nano13162904**.
2 C. D. S. Brites, P. P. Lima, N. J. O. Silva, A. Millán, V. S. Amaral, F. Palacio, *et al.*, *Nanoscale*, 2012, **4**, 4799, DOI: **10.1039/C2NR30764B**.
3 B. Harrington, Z. Ye, L. Signor and A. D. Pickel, *ACS Nanosci. Au*, 2024, **4**, 30–61, DOI: **10.1021/acsnanoscienceau.3c00074**.
4 M. Aragon-Alberti, M. Dyksik, C. D. S. Brites, J. Rouquette, P. Plochocka, L. D. Carlos, *et al.*, *J. Am. Chem. Soc.*, 2024, **146**, 33723–33731, DOI: **10.1021/jacs.4c04292**.
5 C. D. S. Brites, A. Millán and L. D. Carlos, Lanthanides in luminescent thermometry, in *Handbook on the Physics and Chemistry of Rare Earths*, ed. J. C. Bünzli and V. K. Pecharsky, Elsevier, Amsterdam, 2016, vol. 49, pp. 339–427. DOI: **10.1016/bs.hpcre.2016.03.005**.
6 L. Marciniak, K. Kniec, K. Elżbieciak-Piecka, K. Trejgis, J. Stefanska and M. Dramićanin, *Coord. Chem. Rev.*, 2022, **469**, 214671, DOI: **10.1016/j.ccr.2022.214671**.
7 C. D. S. Brites, S. Balabhadra and L. D. Carlos, *Adv. Opt. Mater.*, 2019, **7**, 1801239, DOI: **10.1002/adom.201801239**.
8 M. Back, J. Xu, J. Ueda and S. Tanabe, *J. Ceram. Soc. Jpn.*, 2023, **131**, 22167, DOI: **10.2109/jcersj2.22167**.
9 M. D. Dramićanin, *J. Appl. Phys.*, 2020, **128**, 153103, DOI: **10.1063/5.0014825**.
10 A. Kabański, M. Ptak and D. Stefańska, *ACS Appl. Mater. Interfaces*, 2023, **15**, 7074–7082, DOI: **10.1021/acsami.2c21994**.
11 I. Kachou, K. Saidi, Z. E. A. Aly Taleb, C. Hernández-Álvarez, M. Dammak and I. R. Martín, *Mater. Adv.*, 2025, **6**, 5546–5557, DOI: **10.1039/d5ma00489f**.
12 Y. Bahrouni, I. Kachou, K. Saidi, C. Hernández-Álvarez, M. Dammak and I. R. Martín, *J. Mater. Chem. C*, 2025, **13**, 13415–13425, DOI: **10.1039/D5TC01229E**.
13 K. Saidi, M. Yangui, C. Hernández-Álvarez, M. Dammak, I. R. Martín and M. Runowski, *ACS Appl. Mater. Interfaces*, 2024, **16**, 19137–19149, DOI: **10.1021/acsami.4c00313**.
14 C. Hernández-Álvarez, G. Brito-Santos, I. R. Martín, J. Sanchiz, K. Saidi, K. Soler-Carracedo, Ł. Marciniak and M. Runowski, *J. Mater. Chem. C*, 2023, **11**, 10221–10229, DOI: **10.1039/D3TC01712E**.
15 A. Kabański, M. Ptak, L. D. Carlos and D. Stefańska, *Adv. Opt. Mater.*, 2025, **13**, 2301057, DOI: **10.1002/adom.202501057**.
16 D. A. Egger, A. M. Rappe and L. Kronik, *Acc. Chem. Res.*, 2016, **49**, 573–581, DOI: **10.1021/acs.accounts.5b00540**.
17 Y. Liu, Y. Liu and Y. Guo, *Mater. Chem. Front.*, 2023, **7**, 5215–5246, DOI: **10.1039/D3QM00392F**.
18 M. Ptak, A. Sieradzki, M. Šimėnas and M. Maczka, *Coord. Chem. Rev.*, 2021, **448**, 214180, DOI: **10.1016/j.ccr.2021.214180**.
19 Z.-Q. Ma, Z. Yu, X. Zhu, P. Lin and L. Sun, *Energy Rep.*, 2022, **8**, 538–544, DOI: **10.1016/j.egyr.2021.12.087**.
20 P.-S. Shen, Y.-H. Chiang, M.-H. Li, T.-F. Guo and P. Chen, *APL Mater.*, 2016, **4**, 091502, DOI: **10.1063/1.4962142**.
21 J. Yao, Q. Pan, Z.-J. Feng, Y.-A. Xiong, T.-T. Sha, H.-R. Ji, *et al.*, *APL Mater.*, 2021, **9**, 011111, DOI: **10.1063/5.0039082**.

22 S. Chatterjee and A. J. Pal, *J. Mater. Chem. A*, 2018, **6**, 3793–3823, DOI: 10.1039/C7TA09829K.
23 M. Ptak, A. Kabański, B. Dziuk, S. Balciunas, G. Usevicius, J. K. Zaręba, *et al.*, *J. Mater. Chem. C*, 2024, **12**, 4663–4675, DOI: 10.1039/D3TC05078A.
24 M. Back, E. Trave, J. Ueda and S. Tanabe, *Chem. Mater.*, 2016, **28**, 8347–8356, DOI: 10.1021/acs.chemmater.6b03848.
25 A. Ćirić, Z. Ristić, J. Periša, Ž Antić and M. D. Dramićanin, *Ceram. Interfaces*, 2021, **47**, 27151–27156, DOI: 10.1016/j.ceramint.2021.06.094.
26 W. Liu, D. Zhao, R.-J. Zhang, Q.-X. Yao and S.-Y. Zhu, *Inorg. Chem.*, 2022, **61**, 16468–16476, DOI: 10.1021/acs.inorgchem.2c02514.
27 L. F. dos Santos, J. A. O. Galindo, K. O. Lima, A. R. Pessoa, A. M. Amaral, L. S. Menezes, *et al.*, *J. Lumin.*, 2023, **262**, 119946, DOI: 10.1016/j.jlumin.2023.119946.
28 M. Sójka, M. Runowski, T. Zheng, A. Shyichuk, D. Kulesza, E. Zych and S. Lis, *J. Mater. Chem. C*, 2022, **10**, 1220–1227, DOI: 10.1039/D1TC05022B.
29 T. Amiaud, V. Jubera and H. Serier-Brault, *J. Mater. Chem. C*, 2023, **11**, 10951–10956, DOI: 10.1039/D3TC02125D.
30 R. Li, G. Wei, Z. Wang, Y. Wang, J. Li, S. He, L. Li, H. Suo, W. Ding and P. Li, *Laser Photonics Rev.*, 2023, **17**, 2200589, DOI: 10.1002/lpor.202200589.
31 V. Mykhaylyk, Y. Zhydachevskyy, H. Krau, V. Stasiv, G. Leniec, V. Hreb, L. Vasylechko, V. Sydorchuk and A. Suchocki, *J. Mater. Chem. C*, 2023, **12**, 1341–1353, DOI: 10.1039/D3TC03913G.
32 A. Ciupa, M. Ptak, M. Mączka, J. G. da Silva Filho and P. T. C. Freire, *J. Raman Spectrosc.*, 2017, **48**, 972–982, DOI: 10.1002/jrs.5122.
33 R. Shang, G. Xu, Z. Wang and S. Gao, *Chem. Eur. J.*, 2014, **20**, 1146–1158, DOI: 10.1002/chem.201304111.
34 A. Ciupa, M. Ptak, M. Mączka, J. G. da Silva Filho and P. T. C. Freire, *J. Raman Spectrosc.*, 2017, **48**, 972–982, DOI: 10.1002/jrs.5122.
35 D. Stefańska, A. Kabański, T. H. Q. Vu, M. Adaszyński and M. Ptak, *Sensors*, 2023, **23**, 6259, DOI: 10.3390/s23126259.
36 P. Gluchowski and M. Chaika, *J. Phys. Chem. C*, 2024, **128**, 9641–9651, DOI: 10.1021/acs.jpcc.4c02250.
37 S. Adachi, *J. Lumin.*, 2021, **232**, 117844, DOI: 10.1016/j.jlumin.2020.117844.
38 C. Wang, A. Wadhwa, S. Cui, R. Ma, X. Qiao, X. Fan, *et al.*, *RSC Adv.*, 2017, **7**, 52435–52441, DOI: 10.1039/C7RA08679C.
39 S. Adachi, *ECS J. Solid State Sci. Technol.*, 2022, **11**, 106002, DOI: 10.1149/2162-8777/ac80e2.
40 X. Wang, Y. Zhao, M. Yin, T. Zhou and R.-J. Xie, *J. Phys. Chem. C*, 2023, **127**, 22799–22807, DOI: 10.1021/acs.jpcc.3c04557.
41 C. Li, L. Wang, D. Tu, X. Shang, M. Yang, J. Gong, *et al.*, *Light:Sci. Appl.*, 2025, **14**, 224, DOI: 10.1038/s41377-025-01301-1.
42 M. Runowski, S. Goderski, D. Przybylska, T. Grzyb, S. Lis and I. R. Martín, *ACS Appl. Nano Mater.*, 2020, **3**, 6406–6415, DOI: 10.1021/acsanm.0c01244.
43 Z. Wu, L. Li, X. Lv, H. Suo, C. Cai, P. Lv, *et al.*, *Chem. Eng. J.*, 2022, **438**, 135573, DOI: 10.1016/j.cej.2022.135573.
44 S. Liu, J. Ueda and S. Tanabe, *Appl. Phys. Lett.*, 2023, **123**, 071101, DOI: 10.1063/5.0168845.
45 M. Back, J. Ueda, J. Xu, D. Murata, M. G. Brik and S. Tanabe, *ACS Appl. Mater. Interfaces*, 2019, **11**, 38937–38945, DOI: 10.1021/acsami.9b13088.
46 A. Bednarkiewicz, L. Marciniak, L. D. Carlos and D. Jaque, *Nanoscale*, 2020, **12**, 14405–14421, DOI: 10.1039/D0NR03171A.

Supporting information

High-Sensitivity Optical Thermometry with Cr^{3+}-Doped Hybrid Formate Perovskites: Comparative Analysis of Ratiometric and Lifetime-Based Approaches

Adam Kabański, Kacper Caputa, Dagmara Stefańska**

Keywords: hybrid perovskite, luminescence, thermometry, chromium(III) ions, remote temperature sensing, optical thermometer

Table S1. The collation of the Racah parameters, Dq and Dq/B

Metal ion	Cr^{3+} content	Dq	B	C	Dq/B	C/B
Mg	1 mol.%	1671	687	3159	2.43	4.60
	3 mol.%	1685	688	3161	2.45	4.59
	5 mol.%	1679	642	3250	2.61	5.06

Table S2. The experimental conditions of the decay curves measurements

	Sample		
Parameter	1 mol.%	3 mol.%	5 mol.%
$\lambda_{exc.}$	405 nm		
$\lambda_{obs.}$	686.25 nm	686.5 nm	687.5 nm
Time gate	10 ms		
Step	2.5 µs		
Frequency	12.5 Hz		
Excitation bandwidth	3 nm		
Detection bandwidth	7 nm		
T_{min}	80 K		
T_{max}	270 K		

Table S3. The details of the fitting curves for lifetime-based thermometric models

Equation	$\tau_{fit}(T) = \frac{\tau_0}{1 + A exp\left(-\frac{\Delta E}{kT}\right)}$ k = 0.69503476		
	Sample		
	1 mol.%	3 mol.%	5 mol.%
τ_0	0.70832 ± 0.01491	0.68517 ± 0.01499	0.5423 ± 0.01218
A	992.51432 ± 300.64293	860.27072 ± 257.55884	865.08165 ± 271.08775
ΔE	600.59637 ± 30.13762	586.83573 ± 29.92761	579.99964 ± 30.86358
Reduced Chi-Sqr	2.68716E-4	2.58591E-4	1.53489E-4
R-Square (COD)	0.99619	0.996	0.99622
Adj. R-Square	0.99556	0.99534	0.99546

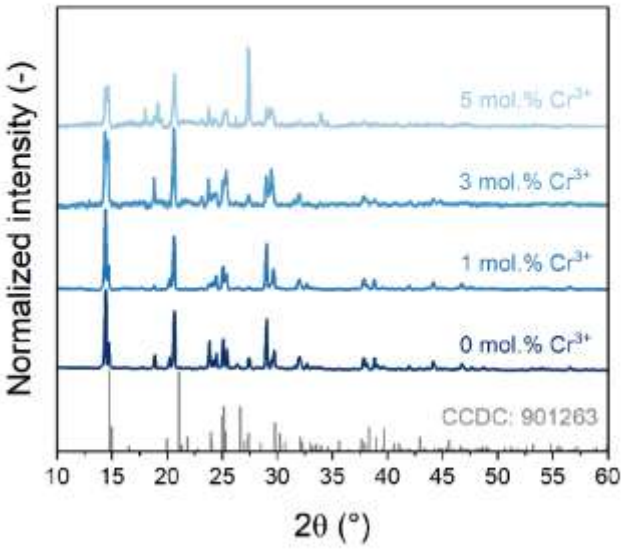

Figure S1. XRD pattern of the representative material with the comparison to the pattern calculated according to the CIF file

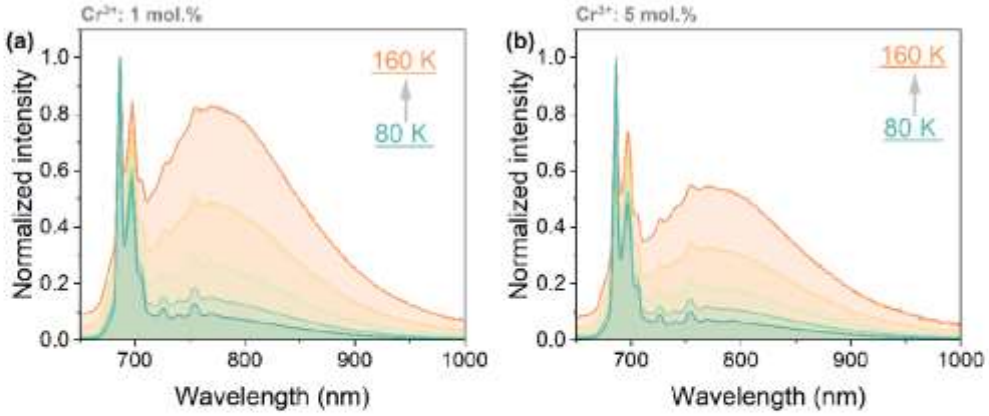

Figure S2. Temperature-dependent luminescence of: (a) $[EA]Mg_{0.99}Cr_{0.01}(HCOO)_3$; (b) $[EA]Mg_{0.95}Cr_{0.05}(HCOO)_3$

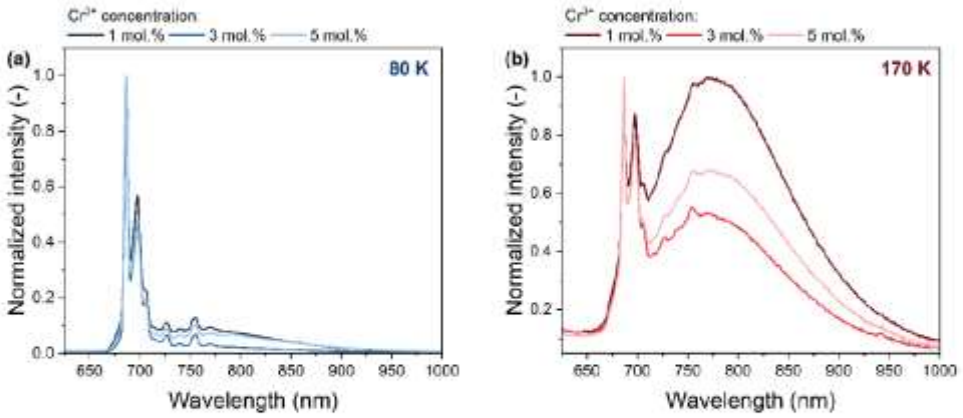

Figure S3. The comparison of the luminescent spectra for various concentrations of Cr^{3+} ions at (a) 80 K and (b) 170 K

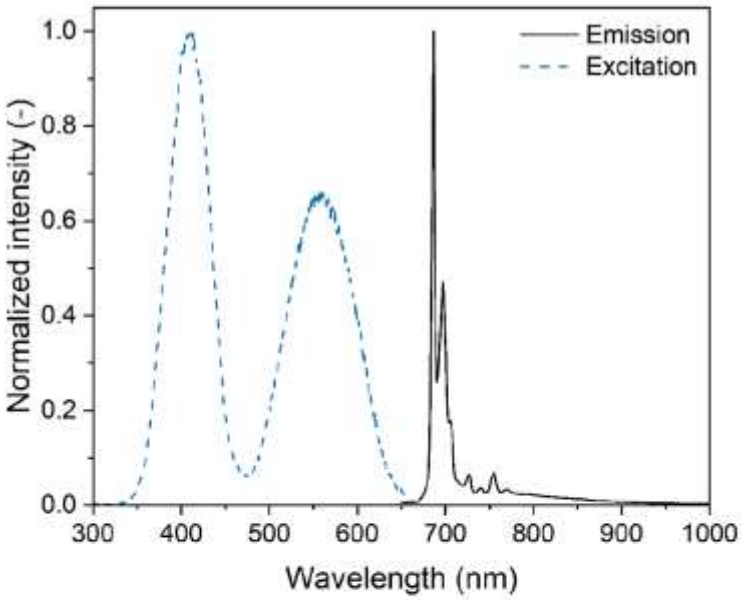

Figure S4. The excitation spectra of the $[EA]Mg_{0.97}Cr_{0.03}(HCOO)_3$ (dashed line) for the 686 nm combined with emission spectra under 405 nm excitation at 80 K

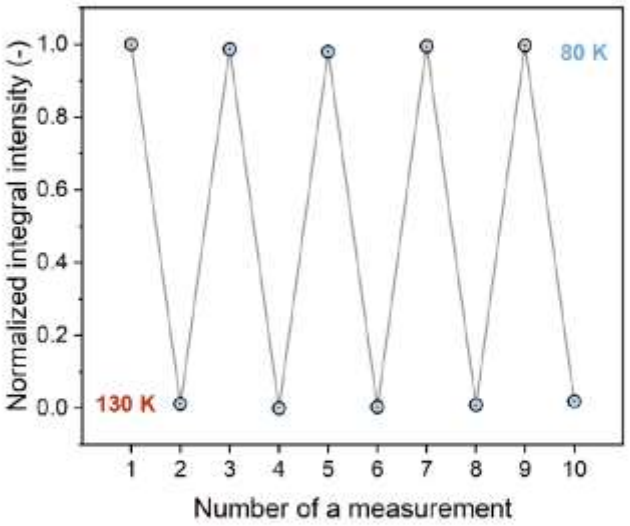

Figure S5. The comparison of the luminescent spectra for various concentrations of Cr^{3+} ions at (a) 80 K and (b) 170 K

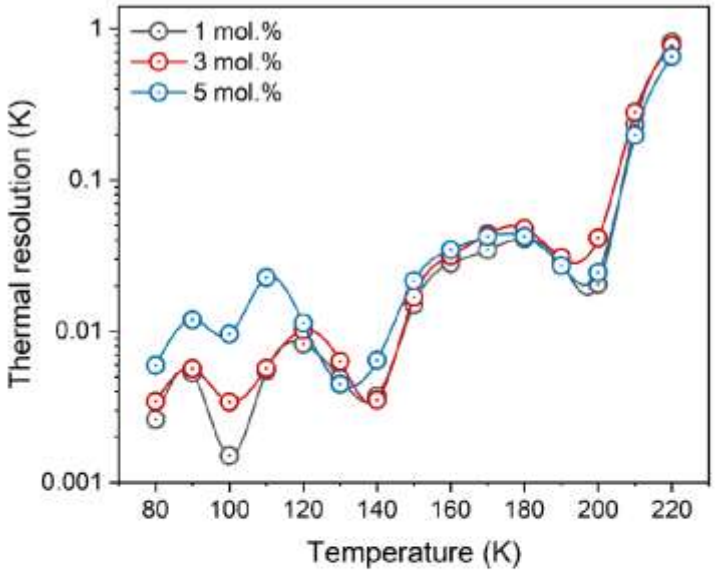

Figure S6. The thermal resolution of the redout

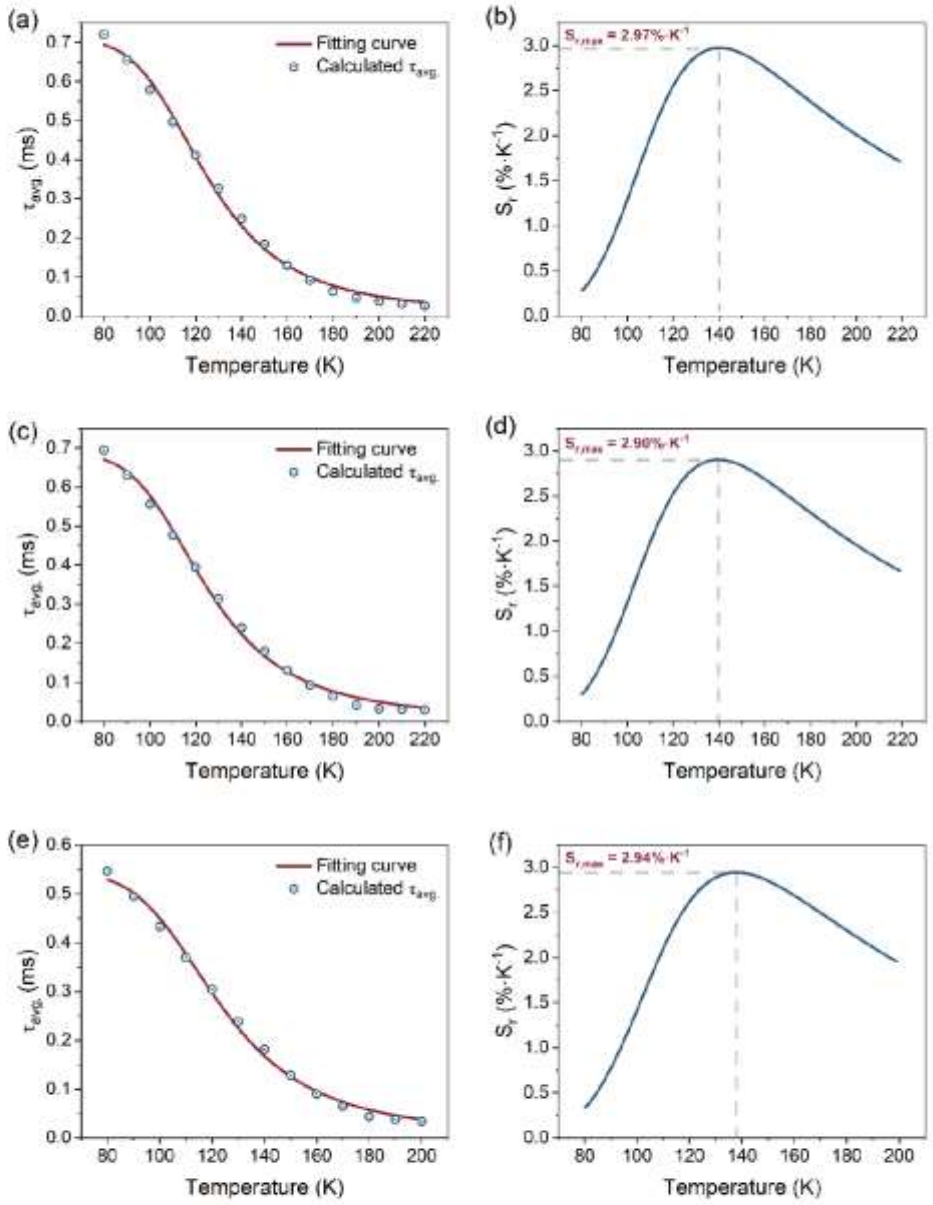

Figure S7. The change of the τ_{avg} and following S_r values for materials doped with 1 mol.% (graphs (a) and (b)), 1 mol.% (graphs (c) and (d)), 1 mol.% (graphs (e) and (f))

10.5 Publication P5

Journal of Materials Chemistry C

ROYAL SOCIETY OF CHEMISTRY

PAPER

View Article Online
View Journal | View Issue

Check for updates

Cite this: J. Mater. Chem. C, 2025, 13, 23935

Multimodal temperature sensing in hybrid perovskites doped with Cr^{3+}: a strategy for optimizing luminescent thermometers

Adam Kabański, * Kacper Caputa and Dagmara Stefańska *

Received 4th August 2025,
Accepted 17th October 2025

DOI: 10.1039/d5tc02943k

rsc.li/materials-c

Optical thermometry has gained significant attention due, in particular, to its usefulness, with high sensitivity, rapid response, and remote measurement capability. The group of metal–organic frameworks (MOFs) containing Cr^{3+} ions has become a promising material for developing a new branch of optical sensors for low-temperature solutions. Herein, we present possible ways to optimize thermometric properties, with particular emphasis on relative sensitivity (S_r). By comparing different methods of determining the thermometric model, it is possible to observe the impact of individual approaches on the obtained thermometric characteristics. What is more, we report structural and spectroscopic studies of a series of $[EA]Mn_{1-x}Cr_x(HCOO)_3$, where EA = ethylammonium cation, and x = 0, 0.01, 0.03, and 0.05. Described materials exhibit perovskite-like architectures and a strong dependence of spectroscopic properties on the composition of host materials, dopant concentration, and environmental temperature. XRD analysis provided information on the relationship between chemical composition and structural properties. Investigated samples exhibited spin-forbidden emission and a significantly red-shifted broad emission band. The particular usefulness of hybrid compounds containing Cr^{3+} for luminescence thermometry is confirmed with temperature-dependent (80–300 K) photoluminescence and lifetime measurements. The obtained results show the extraordinary potential of hybrid compounds for luminescence thermometry, depending on the chosen thermometric method (S_r up to 5.14% K^{-1} at 143 K). So far, this is the highest S_r value ever been reported for a luminescent thermometer based on hybrid organic–inorganic formate perovskite doped with Cr^{3+} ions. In this work, we demonstrate a comparison of different methods of thermometric model determination, based on the ratiometric approach and lifetime analysis. The presented results show the significant importance of thermometric model determination and optimization, which may not only increase the obtained sensitivity of the thermometer but also extend the operation range.

Introduction

Luminescence thermometry is a novel approach to remote temperature monitoring, and is gaining increasing attention due to its significant advantages over traditional contact thermometers.[1–4] Sensing solutions based on luminescent compounds provide high sensitivity, remote and fast measurements, and minimization of some effects of external factors, such as strong electromagnetic fields.[4–6] There are three most common approaches to optical temperature monitoring: analysis of a change in an emission lifetime; monitoring the spectral shift of a specific band; and the comparison of the emission intensity of two ranges differing in thermal quenching progressivity (a ratiometric method).[4,7,8] Nevertheless, other temperature-dependent spectroscopic properties – such as the full width at half maximum (FWHM) or polarization – can also serve as a basis for developing a thermometric model.[9–11]

There are many luminescent materials exhibiting sufficient spectroscopic properties to determine a thermometric model. The significant majority of such materials are based on inorganic host materials doped with rare-earth (RE) elements.[12–15] Nonetheless, compounds containing transition metal (TM) ions have attracted increasing attention due to their promising thermometric functionality, comparable to RE-based solutions.[4,7,16–18] Within the context of luminescence thermometry, the potential of transition metal ions is particularly evident in the group of hybrid organic–inorganic materials containing Cr^{3+} ions.[4,7,17,18]

Over the years, the group of hybrid organic–inorganic compounds with perovskite-like structures has attracted increasing

Institute of Low Temperature and Structure Research, Polish Academy of Sciences, Wrocław, Poland. E-mail: a.kabanski@intibs.pl, d.stefanska@intibs.pl

attention due to the exhibition of a wide variety of properties.[7,17–19] Such compounds, forming a metal–organic framework (MOF), are particularly known for their extraordinary magnetic, ferroelectric, multiferroic, and spectroscopic characteristics.[19,20] The general formula of perovskite-like materials can be distinguished as ABX_3, where A is an organic cation, B stands for divalent metal ions, and X is a monovalent anion. Nowadays, the subgroup of halide-based hybrid perovskites, such as $CH_3NH_3PbCl_3$, has been successfully implemented in photovoltaic systems.[21,22] However, the implementation potential of hybrid materials is significantly wider. By the replacement of A, B, and X linkers, a significant change in the ferroelectric, magnetic, optoelectronic, and luminescence properties can be observed. Among the various hybrid perovskites, the subgroup of formate-based compounds ($X = HCOO^-$) shows several interesting features, such as ferroelectricity and multiferroicity, as well as linear and nonlinear optical properties.[17,18,23] Considering luminescent materials, significant attention should be paid to hybrid formates containing Cr^{3+} ions. Due to their chemical stability, strong luminescence, weak concentration quenching, and strong thermal quenching, this group of hybrid compounds has been successfully applied as luminescent thermometers for remote temperature sensing.[7,17,18] The implementation of Cr^{3+} ions in a hybrid organic–inorganic structure provides a luminescence center that is strongly sensitive to the local environment, described by the crystal-field (CF) strength.[24,25] There are two main types of transitions observed in the luminescence spectrum of chromium trivalent ions: narrow spin-forbidden $^2E_g \rightarrow {}^4A_{2g}$ and broad spin-allowed $^4T_{2g} \rightarrow {}^4A_{2g}$. At low temperatures, only one type of emission is observed. The increase in temperature induces the thermal population of the higher energy level and, consequently, promotes the occurrence of both narrow $^2E_g \rightarrow {}^4A_{2g}$ and broad $^4T_{2g} \rightarrow {}^4A_{2g}$ emissions. However, in a strong crystal field, the emission from the ^2E_g level is the only one observed. In a weak CF, in turn, the narrow emission assigned to $^2E_g \rightarrow {}^4A_{2g}$ is fully suppressed, while broad emission from the $^4T_{2g}$ level becomes dominant. In the intermediate crystal field, the coexistence of these two types of emission may take place. What is more, in some Cr^{3+}-doped compounds, the creation of an additional emission band corresponding to the Cr^{3+}–Cr^{3+} pair luminescence may be observed.[26–29] Materials containing Cr^{3+} ions have found wide application in phosphors emitting in the visible and near-infrared regions.[30–32]

The increase in temperature causes the thermal quenching of luminescence. Nonetheless, the reduction in the intensity of spin-allowed and spin-forbidden emissions, as well as additional, longer-wavelength emission bands, does not progress equally. Thus, the determination of the thermometric model based on the intensity ratio between emission bands can be performed.[7,17] In the field of luminescence thermometry, both approaches, based on the analysis of different types of emission (from ^2E_g and $^4T_{2g}$ levels) as well as the intensity ratio between the R-lines, as in the case of ruby, can be encountered.[32–34]

The luminescence lifetime is also significantly dependent on the temperature. This particular change in spectroscopic properties is another noteworthy approach that may be applied to remote temperature sensing.[35,36] However, the luminescence thermometry based on the emission lifetime in hybrid perovskites doped with Cr^{3+} ions is an almost unexplored area.

Herein, we report the synthesis as well as structural and spectroscopic properties of the series of $[EA]Mn_{1-x}Cr_x(HCOO)_3$, where $x = 0, 0.01, 0.03, 0.05$. The structural characteristics of the obtained materials are investigated using various methods, such as PXRD. Optical spectroscopic techniques, including diffuse-reflectance spectroscopy and luminescence decay time measurements, are applied to provide comprehensive results showing the relation between structural and spectroscopic characteristics in hybrid materials containing Cr^{3+} ions. Particular attention is paid to the implementation of the investigated compounds as luminescent thermometers. We extend the conventional thermometric methods with an additional point of view by presenting a comparison of thermometric properties in systems operating independently in a ratiometric and lifetime-based manner. Such an approach may be a valuable way to increase the sensitivity and reduce the temperature detection uncertainty in hybrid perovskites containing Cr^{3+} ions. For this purpose, several types of thermometric models, based on different approaches (various ratiometric models and lifetime-based), are presented, including calculations of obtained sensitivities and sensing range. This work is an attempt to compare various thermometric approaches within the same material. We believe that optimization of the thermometric model is a required key step toward designing more sensitive and accurate luminescent thermometers.

Experimental

Synthesis

In the synthesis we used commercially available precursors (without further purification) such as ethylammonium hydrochloride (98%, Sigma-Aldrich), formic acid (≥98%, POCH), anhydrous methanol (MeOH) (99.8%, Sigma-Aldrich), chromium(III) chloride hexahydrate (≥98%, Sigma-Aldrich), manganese chloride (≥99%, Sigma-Aldrich) and triethylamine (≥98%, Sigma-Aldrich). To synthesize $[EA]Mn_{1-x}Cr_x(HCOO)_3$ (where $x = 0, 0.01, 0.03, 0.05$), the low-diffusion method was used. First, two solutions were prepared: A (heavy phase) and solution B (light phase). Preparing solution A involved dissolving EA (8 mmol, 0.6523 g) in 7.5 ml of MeOH, then adding 1.5 ml of HCOOH and 0.7 ml of triethylamine. Preparing solution B involved dissolving $MnCl_2$ (2 mmol, 0.2517 g, for the undoped sample) and a stoichiometric amount of $CrCl_3$ in 5 mL of MeOH. After that, a syringe was used to transfer the solutions to a test tube (1 cm diameter, 18 cm length). The crystals were collected after one week, washed several times with MeOH, and left to dry in air. The solubility of the obtained compounds was tested in methanol, ethanol, isopropanol, acetonitrile (AcCN), and *N*,*N*-dimethylformamide (DMF). The materials were found to be insoluble in the alcohols and AcCN, and only partially soluble in DMF. Solubility tests in water

revealed that the compounds did dissolve. Prolonged exposure to moisture in the air (over several months) led to partial surface decomposition of the crystals. However, photoluminescence studies showed no significant impact on the recorded emission spectra. Nevertheless, the crystals should be protected from moisture for long-term storage.

Materials and instrumentation

The purity of the samples was determined using powder X-ray diffraction (PXRD) on an X'PertPro X-ray diffraction system (PIXcel detector and Soller slits for CuKα Ni-filtered radiation, λ = 1.54056 Å, V = 40 kV, I = 30 mA). The diffuse reflection spectra were obtained by using a Varian Cary 5E UV/VIS-NIR spectrophotometer (Varian Incorporation, Palo Alto, CA, USA) with a 0.5 nm step. Emission and temperature-dependent emission spectra were registered using a Hamamatsu PMA-12 photonic multichannel analyzer equipped with a BT-CCD linear image sensor (Hamamatsu Photonics K.K, Shizuoka, Japan) under 100–200 ms exposure time (25-time-repetition). A long-pass GG550 filter was applied. Photoluminescence decay curves, including their temperature dependence, were obtained using an FLS1000 spectrofluorometer (Edinburgh Instruments, Livingston, UK) with a 10 ms gate and a 0.025 ms step. The sample temperature was controlled using a Linkam THMS600 heating/freezing stage (Linkam Scientific Instruments, Tadworth, UK).

Results

Structural properties

A series of materials were investigated with the general formula $[EA]Mn_{1-x}Cr_x(HCOO)_3$ belonging to a metal–organic framework (MOF) in which metal ions were connected by $HCOO^-$ linkers, forming a developed three-dimensional system. Organic cations were placed in the voids of the framework (Fig. 1). The structural properties of the undoped $[EA]Mg(HCOO)_3$ material have been reported recently.[17,18] At room temperature, $[EA]Mg(HCOO)_3$ crystallizes in the non-centrosymmetric $Pna2_1$ space group, without reported phase transitions.

To verify the quality of the obtained materials and assess the structural impact of Cr^{3+} ion incorporation, PXRD diffractograms were collected and compared with simulated patterns derived from single-crystal data. As shown in Fig. S1, all synthesized samples show sufficient quality and confirm the possibility of aliovalent doping with Cr^{3+} ions up to 5 mol%. Similar to related hybrid perovskite materials containing Mn^{2+} ions, it was possible to synthesize compounds with a maximum Cr^{3+} ion content of 5 mol%. This limitation arises from charge mismatch, which prevents the formation of a stable crystal structure at higher dopant concentrations. An increase in Cr^{3+} ion concentration leads to a widening of the peak separation near 14.8°, accompanied by a decrease in the separation of peaks around 20.5°. Additionally, diffraction lines near 19.5°, 21.6°, 26.8°, and 29.7° gradually disappear, while a new peak emerges around 25.8°. These changes in signal intensity and position are likely due to the formation of structural defects that destabilize the crystal lattice. Similar phenomena have been observed in other single-perovskite materials doped with Cr^{3+} ions, including those incorporating GA^+ and DMA^+ cations.[17,18] In the investigated single perovskite, Cr^{3+} ions replace Mn^{2+}, causing a valence mismatch. As a consequence, two optical Cr^{3+} sites can be expected to be regular and defective.

Diffuse reflectance spectroscopy

To indicate the presence of chromium trivalent ions in hybrid organic–inorganic materials, diffuse reflectance spectroscopy (DRS) is applied. For the investigated materials, the collation of DRS spectra is presented in Fig. 2. For the undoped sample, the presence of manganese(II) ions causes the creation of several low-intensity absorption bands assigned to the series of electronic transitions from the $^6A_{1g}$ energetical level. For the materials containing Cr^{3+} ions, three characteristic absorption bands of chromium(III) ions can be observed: ~14 500 cm^{-1} ($^4A_{2g} \rightarrow {}^2E_g$), ~1700 cm^{-1} ($^4A_{2g} \rightarrow {}^4T_{1g}$) and ~23 600 cm^{-1} ($^4A_{2g} \rightarrow {}^4T_{2g}$). Although most of the manganese(II) absorption bands are shadowed by absorption bands assigned to

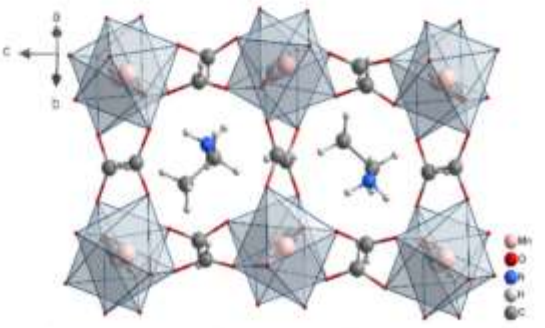

Fig. 1 The visualization of the $[EA]Mn_{1-x}Cr_x(HCOO)_3$.

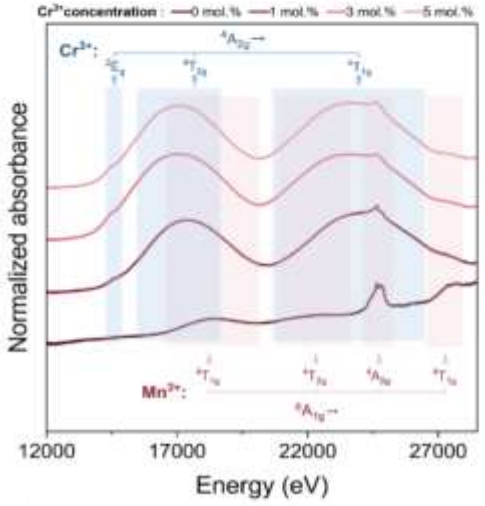

Fig. 2 The diffuse reflectance spectra of $[EA]Mn_{1-x}Cr_x(HCOO)_3$.

transitions in Cr^{3+} ions, the absorption band ~24 700 cm^{-1}, assigned to the $^6A_{1g} \rightarrow {}^4A_{2g}$ Mn^{2+} electronic transition, is still observable. Comparable results are reported for another Mn-based formate perovskite containing Cr^{3+} ions.[17]

Usually, the obtained results of diffuse-reflectance analysis for Cr^{3+}-based materials are used to determine the crystal field (CF) and Racah parameters. The Dq/B ratio describes the crystal field strength and is widely used to describe the interaction between host materials and Cr^{3+} ions.[7,17,18] However, due to the overlap of Cr^{3+}- and Mn^{2+}-related absorption bands, the calculated values are affected by considerable uncertainty.

Thus, the initial estimation of the crystal field strength should be performed according to the analysis of the metal–ligand distance, which was successfully implemented for other hybrid compounds doped with Cr^{3+} ions.[18] The analogous compound $[DMA]Mn(HCOO)_3$, where DMA^+ stands for dimethylammonium cation, shows a slightly higher value of distance-related crystal field parameter $1/R^5$ (0.0199) than the EA-based compound (0.0196). However, the obtained value is significantly lower than the CF strength for Zn^{2+} and Mg^{2+} – $[DMA]M(HCOO)_3$ derivatives, which are equal to 0.0236 and 0.0250, respectively. The collation of the octahedra parameters for the $[EA]Mn(HCOO)_3$ is presented in Table S1.

Optical properties

The undoped $[EA]Mn(HCOO)_3$ compound does not show the luminescence of the Mn^{2+} ions, which is caused by the significant concentration quenching. At 80 K, the emission spectra of $[EA]Mn_{0.97}Cr_{0.03}(HCOO)_3$ contain several narrow bands with the highest intensity observed for 685.4 nm (named R_1 line) as shown in Fig. 3a. This emission band is assigned to the $^2E_g \rightarrow {}^4A_{2g}$ spin-forbidden transition. The corresponding Stokes sidebands are localized at 697.1 nm, 725.4 nm, and 753.1 nm. An increase in concentration of the Cr^{3+} ions induces the formation of the broadband emission within the 720–950 nm range (Fig. 3b and Fig. S2). The materials exhibit temperature-dependent emission with the change of the shape and intensity of the emission spectra. An increase in temperature induces a reduction in luminescence intensity; however, the thermal quenching is not equally progressive within the monitored emission spectrum. The most rapid reduction in intensity is observed for the R_1 line. The contribution of the broadband emission, in turn, increases as the temperature rises. The comparison of the normalized PL spectra at 80 K and 160 K is presented in Fig. 3c and Fig. S3. The luminescence of all of the investigated materials is fully quenched at around 300 K.

Usually, Cr^{3+}-doped compounds may exhibit two types of emission – narrow spin-forbidden $^2E_g \rightarrow {}^4A_{2g}$ and broadband spin-allowed assigned to the $^4T_{2g} \rightarrow {}^4A_{2g}$ transition. However, the investigated materials exhibit a particular redshift of a broadband emission compared to other hybrid materials.[7,17,18] The highest contribution of the broadband emission is observed for the greatest concentration of the Cr^{3+} ions. The maximum of this particular band is around 815 nm. Typically, the broadband $^4T_{2g} \rightarrow {}^4A_{2g}$ emission is expected around 750–790 nm.[7,17,18] At first glance, it appears that the significant redshift of the broadband Cr^{3+}-based compounds may be attributed to the formation of the Cr^{3+}–Cr^{3+} pairs, which was presented for several inorganic materials doped with transition metal ions.[26–28,39] To verify the origin of the observed broadband emission, the excitation spectra at 80 K and 160 K have been measured (Fig. S4). There is a particular similarity between recorded excitation spectra of the R_1 line and broadband emission, however, the shift of the excitation band measured for the broadband emission is observed. Such a phenomenon was reported for a $LaMgGa_{10.3}Cr_{0.7}O_{19}$: between 890 nm and 1200 nm emission ranges.[29] However, the analysis of the luminescence decay curves for the two investigated emission bands provides additional information (Fig. 4 and Fig. S5). The comparisons of decay curves for the R_1 line measured at 80 K are presented in Fig. 4. Due to charge mismatch in the local environment of Cr^{3+} ions and possible local structural distortions, the observed luminescence decay kinetics exhibit a double exponential character. An increase in Cr^{3+} concentration leads to a reduction in average lifetime. Such a relation is reported for a series of hybrid perovskites containing Cr^{3+} ions.[7,17,18] An increase in temperature induces a reduction in the luminescence lifetime. A more

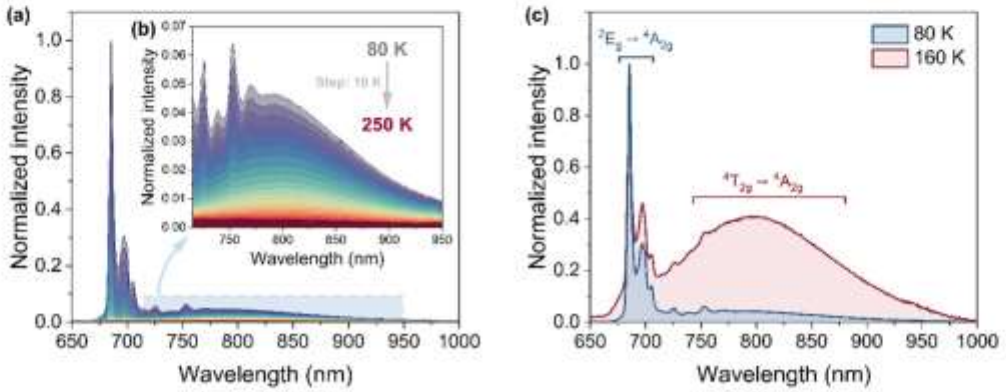

Fig. 3 (a) The temperature-dependent luminescence of $[EA]Mn_{0.97}Cr_{0.03}(HCOO)_3$; (b) the focus on broadband emission range; (c) the comparison of normalized luminescence spectra of Mn-based compound doped with 3 mol% of Cr^{3+} ions at 80 K and 160 K.

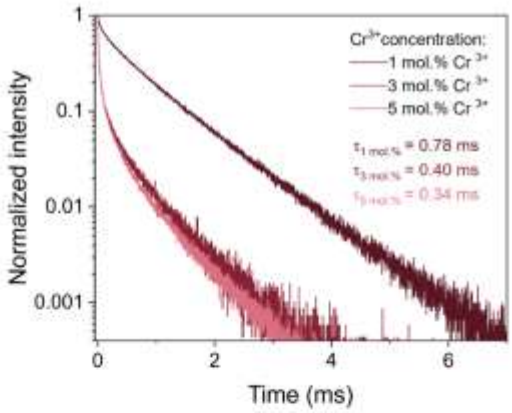

Fig. 4 The comparison of the decay curves of $[EA]Mn_{1-x}Cr_x(HCOO)_3$, x = (0.01, 0.03, 0.05) at 80 K under 405 nm excitation, with calculated values of average luminescence lifetimes.

comprehensive analysis of the temperature-dependent luminescence lifetimes is presented in a further part of the work (see section Luminescence thermometry). The luminescence lifetime for the broadband emission monitored at 815 nm is also double exponential with very short decay time 16 μs (τ_1) and 47 μs (τ_2) at 80 K and 0.8 μs (τ_1) and 6.7 μs (τ_2) at 160 K (Fig. S5). The determined LT values are characteristic of the $^4T_{2g} \rightarrow {}^4A_{2g}$ electronic transition, typically, the LT of the emission band associated with Cr^{3+}–Cr^{3+} pairs should be much longer, around ms.[26–28,39] It should be noticed that a red shift of the $^4T_{2g} \rightarrow {}^4A_{2g}$ transition may also occur and be related to the reduction of the crystal field interacting with Cr^{3+} ions and increasing the average Cr^{3+}–O^{2-} distance. To compare, the average Cr^{3+}–O^{2-} distance in the investigated Mn analog is significantly longer (2.1949 Å) than that for the Mg-based ethylammonium formates (2.1025 Å).[37,38] Moreover, the registered PL is attributed to Cr^{3+} located in two distinct Cr^{3+} sites (regular and distorted). An analogous situation has been reported recently for other single perovskite materials doped with Cr^{3+} ions, containing GA^+ and DMA^+ cations.[17,18] The broadband emission is actually a superposition of two emission bands associated with depopulation of the $^4T_{2g}$ level by these two Cr^{3+} ions. If the amount of distorted Cr^{3+} position is significant in relation to Cr^{3+} in the regular environment, it is visible on the emission spectrum as a redshift of the band's center of gravity.

Luminescence thermometry

In this work, we focus on the comparison and analysis of the performance of two main thermometric approaches (Fig. 5): ratiometric and lifetime-based. The ratiometric method is further divided into three groups to construct the differing thermometric parameters, LIR (luminescence intensity ratio). Analysis of the influence of different thermometric ranges may show the most suitable combination of investigated bands for luminescence thermometry. The lifetime-based approach is based on the analysis of the average luminescence lifetime observed for the R_1 line.

Ratiometric approach

One of the most common approaches is the comparison of intensities of two emission bands as a function of temperature, which is the so-called ratiometric approach.

To determine the sensing performance of the investigated materials, the luminescence intensity ratio (LIR) is calculated. This parameter is defined as the ratio of intensities of specific thermometric ranges:

$$\mathrm{LIR} = \frac{I_A}{I_B} \quad (1)$$

where I_A and I_B stand for integral intensities of thermometric regions A and B, respectively. The thermometric range is understood as the portion of the emission spectrum that is used to calculate the integral intensity, which is later applied to determine the LIR. To optimize the thermometric method, four integration regions are selected (Fig. 5). Next, three luminescence intensity ratios are determined as a ratio between the I_1 range and: I_2 (LIR_{12}); I_3 (LIR_{13}); I_4 (LIR_{14}), and their impact on the sensitivity is compared. The collation of the range used for the analysis is presented in Table 1. The comparison of the temperature dependence on the normalized integral intensities of thermometric regions I_1–I_4 for an exemplary compound of the material doped with 3 mol% of Cr^{3+} ions is presented in Fig. 6a. The significant similarities of values calculated for I_1 and I_2 indicate that both thermometric ranges can be assigned to the same $^2E_g \rightarrow {}^4A_{2g}$ transition. The different progressivity of the thermal quenching of luminescence is observed for the I_3 and I_4 ranges. Differences in the progress of thermal quenching in specific thermometric areas lead to changes in the shape of the obtained dependencies between the LIR parameter and temperature (Fig. 6b). The most rapid decrease in the LIR value is observed for the LIR_{14} parameter. This change is related to the differences between the progressivity of thermal quenching of consistent thermometric ranges (I_1 and I_4). A less progressive decrease is observed for LIR_{12} and LIR_{13} parameters. Due to the significantly similar shape of the temperature dependencies of the I_1 and I_2 ranges, the observed change in LIR_{12} is extended. To determine the usefulness of thermometers, the relative sensitivity (S_r) is calculated using the following equation:

$$S_r = \frac{1}{\mathrm{LIR}} \cdot \left|\frac{\mathrm{dLIR}}{\mathrm{d}T}\right| \quad (2)$$

where dLIR is the change of the thermometric parameter LIR at temperature change dT. The influence of the temperature on the calculated value of S_r for an exemplary sample of $[EA]Mn_{0.97}Cr_{0.03}(HCOO)_3$ is presented in Fig. 6c. The highest relative sensitivity (3.91% K^{-1}) is observed for the thermometric model based on the LIR_{14} parameter. The lowest, in turn, is calculated for the LIR_{12} system (0.47% K^{-1}). The observed significant difference is related to the less dynamic reduction of the LIR_{12} parameter. From the thermometric point of view, the implementation of two ranges differing in temperature

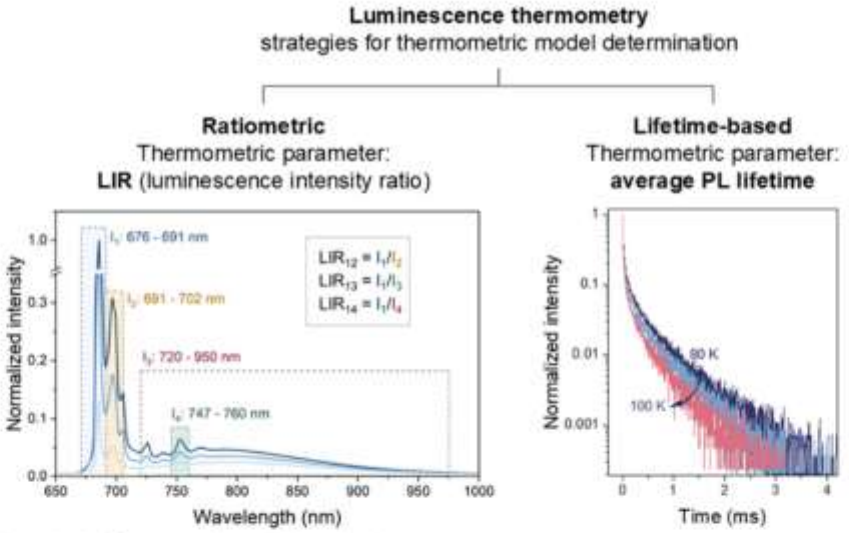

Fig. 5 The investigated methods of thermometric model determination.

Table 1 The summary of the thermometric characteristics for the ratiometric method

Cr^{3+} content	Thermometric ranges		$S_{r,max}$	$T_{S_{r,max}}$	Operating range
1 mol%	LIR:	I_1 (676–691 nm) I_4 (720–950 nm)	3.34% K^{-1}	120 K	80–160 K
3 mol%	LIR_{12}:	I_1 (676–691 nm) I_2 (691–702 nm)	0.47% K^{-1}	150 K	100–180 K
	LIR_{13}:	I_1 (676–691 nm) I_3 (747–760 nm)	3.44% K^{-1}	140 K	80–180 K
	LIR_{14}:	I_1 (676–691 nm) I_4 (720–950 nm)	3.91% K^{-1}	140 K	80–160 K
5 mol%	LIR:	I_1 (676–691 nm) I_4 (691–950 nm)	2.78% K^{-1}	120 K	80–140 K

response is necessary to provide high sensitivity. Thus, the general prediction concerning relative sensitivity can be performed only *via* a comparison of the progressivity of thermal quenching of the thermometric ranges.

To further determine the thermometric performance, the operating range of the thermometer is evaluated according to the procedure presented by Bednarkiewicz *et al.*[40] To distinguish the operating range, the following conditions must be fulfilled:

$$(S_r(T) \geq S_{th}) \wedge (dLIR(T) \geq \delta LIR(T)) \quad (3)$$

where S_{th} is the sensitivity threshold, $dLIR(T)$ is an increment in LIR value, and $\delta LIR(T)$ is an error in the determination of LIR in a given temperature T. Sensitivity threshold depends on the specific application requirements and is determined arbitrarily. The widest range of operation range (80–180 K) is calculated for the LIR_{13} model. However, other thermometric models exhibit sufficient operating ranges equal to 100–180 K and 80–160 K for LIR_{12} and LIR_{14}, respectively. The application of specific ranges has a crucial role in the optimization of thermometric performance in Cr^{3+}-based hybrid compounds. Considering the operational range of 80–180 K and the maximum relative

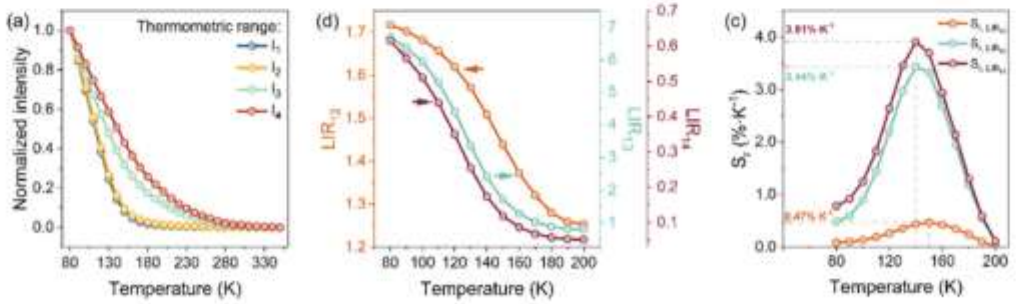

Fig. 6 The thermometric analysis of the exemplary compound of $[EA]Mn_{0.97}Cr_{0.03}(HCOO)_3$: (a) the comparison of the thermal quenching of thermometric areas; (b) the change in thermometric parameters LIR as a function of temperature; (c) relative sensitivities for various thermometric models.

sensitivity achieved within 120–150 K – depending on the material and the method used – the described compounds show potential for application in temperature monitoring systems for cryogenic devices. Luminescence thermometry based on hybrid compounds containing Cr^{3+} ions overcomes the limitations of other thermometric techniques, such as thermal imaging.[7,18] The usefulness of such compounds has also been confirmed in the context of time-resolved thermometry, demonstrating the feasibility of developing systems for remote, real-time temperature monitoring under cryogenic conditions. The presented results show the particular usefulness of the ratiometric approach based on the LIR_{14} parameter.

Thus, considering the overall clarity of the work, further comparison of the investigated series of hybrid compounds will be limited to this particular method. The LIR and S_r values for other investigated compounds are presented in Fig. S6. The comparison of the uncertainty of the LIR determination is shown in Fig. S7. The collation of the thermometric ranges, maximal relative sensitivities, as well as operating ranges is presented in Table 1.

Among the investigated materials, the highest relative sensitivity is observed for the material doped with 3 mol% of Cr^{3+} (3.91% K^{-1}). However, all of the tested materials exhibit higher sensitivity compared to other hybrid perovskites containing chromium trivalent ions[4,7,17,18] (Table 2). It may be attributed to the higher contribution of the broadband emission resulting from a higher concentration of Cr^{3+} ions. If the investigated thermometric range overlaps the emission from the $^4T_{2g}$ level, its intensification improves the thermometric performance. However, the obtained results for the combination of I_1 and I_3 ranges (LIR_{13}) show an undoubted potential of the approach based on additional phonon bands. This particular approach may be significantly useful within the context of materials exhibiting a strong crystal field. In this case, the creation of wide $^4T_{2g} \rightarrow {}^4A_{2g}$ emission is, in principle, not observed. Thus, the construction of the thermometric model based on other temperature-sensitive bands may provide sufficient conditions for highly sensitive temperature sensing.

Lifetime-based method

Optical thermometry based on luminescence decay time is another valuable approach. Although this approach is not as commonly reported as a ratiometric method, it has some noteworthy advantages, such as higher stability of the signal (immunity to excitation intensity variations and phosphor concentration) as well as the possibility of its implementation for phosphors exhibiting a single emission band.[42,43] Moreover, due to the significantly lower sensitivity of the lifetime-based thermometric model to photon-environment interactions compared to the ratiometric approach, this method may be particularly useful in systems where the luminescence of the surrounding medium may affect the observed emission spectrum of the luminescent probe. It may also be successfully implemented in materials showing one particularly intense emission band, such as the R_1 line in chromium(III)-based materials.[26,44,45] The particular usefulness of the LT-based approach has been presented for a series of $[EA]Mg(HCOO)_3$ hybrid perovskites doped with Cr^{3+} ions.[33] Within the context of investigated materials, for the exemplary compound $[EA]Mn_{0.99}Cr_{0.01}(HCOO)_3$, the increase in temperature leads to the reduction of the lifetime of the R_1 line of Cr^{3+} luminescence (Fig. 7a). To determine the thermometric model, the average luminescence decay times ($\tau_{avg.}$) are calculated with the following formula:

$$\tau_{avg} = \frac{\int I(t)t\mathrm{d}t}{I(t)\mathrm{d}t} \quad (4)$$

where $I(t)$ is the signal intensity at a given time t. The applied calculation method provides a comparable lifetime form for hybrid Cr^{3+}-based materials, in which the decay curve may exhibit single- and double-exponential decay form, depending on the presence of more than one (*e.g.*, nominal and defected) chromium(III) site.[18] The obtained values of average decay times as a function of temperature are presented in Fig. 7b. The average lifetime of luminescence significantly decreases with increasing temperature, exhibiting characteristics of quasi-Arrhenius decay. To provide a continuous change of the thermometric parameter, understood as an average decay time for the given temperature, the nonlinear fitting is performed with the following formula:

$$\tau_{fit}(T) = \frac{\tau_0}{1 + A\exp\left(-\frac{\Delta E}{kT}\right)} \quad (5)$$

where τ_0 is the average lifetime at the lowest investigated temperature, A is a preexponential parameter, k is the Boltzmann constant, and ΔE is equal to the energy of the thermal quenching. The ΔE values were 928 cm^{-1}, 666 cm^{-1}, and 638 cm^{-1} for the sample containing 1 mol%, 3 mol%, and 5 mol% of Cr^{3+} ions, respectively. This low activation energy confirms that the energy separation between the ^2E_g and $^4T_{2g}$ levels remains small. Very rapid luminescence quenching is observed even at relatively low temperatures, whereas the high temperature sensitivity is found to be beneficial for the development of luminescent thermometers operating at low temperatures. The obtained fitting curves are further used to

Table 2 Comparison of the highest relative sensitivity (S_r) with the following temperature (T) of selected hybrid luminescent thermometers containing Cr^{3+} ions operating in a ratiometric regime

Material	$S_{r,max}$ (% K^{-1})	$T_{S_{r,max}}$ (K)	Source
$[EA]Mn_{0.99}Cr_{0.01}(HCOO)_3$	3.34	120	This work
$[EA]Mn_{0.97}Cr_{0.03}(HCOO)_3$	3.91	140	
$[EA]Mn_{0.95}Cr_{0.05}(HCOO)_3$	2.78	120	
$[GA]Zn_{0.99}Cr_{0.01}(HCOO)_3$	1.08	90	17
$[GA]Mn_{0.97}Cr_{0.03}(HCOO)_3$	1.20	100	
$[GA]Mg_{0.99}Cr_{0.01}(HCOO)_3$	2.08	90	
$[DMA]Zn_{0.97}Cr_{0.03}(HCOO)_3$	2.4	165	18
$[DMA]Mn_{0.95}Cr_{0.05}(HCOO)_3$	2.5	160	
$[DMA]Mg_{0.99}Cr_{0.01}(HCOO)_3$	2.2	150	
$[EA]_2NaAl_{0.71}Cr_{0.21}(HCOO)_6$	2.84	160	7
$[EA]_2NaCr_{0.931}Ga_{0.069}(HCOO)_6$	2.114	150	41

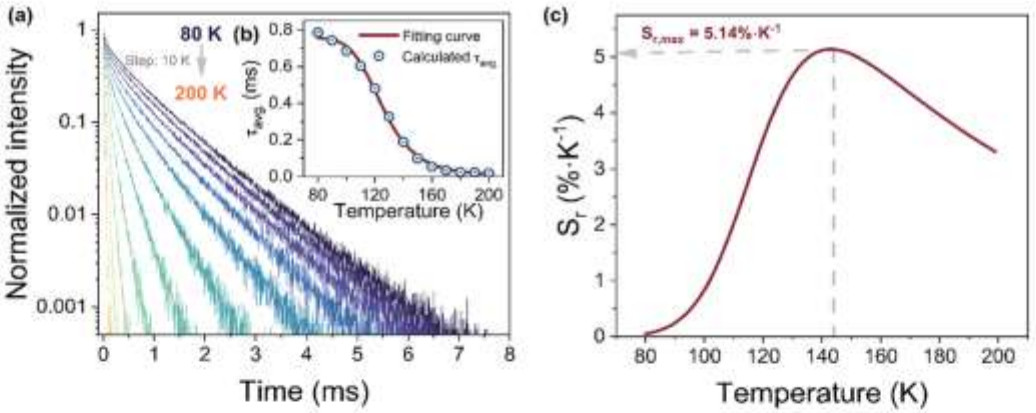

Fig. 7 (a) Temperature-dependent decay curves measured for [EA]$Mn_{0.99}Cr_{0.01}(HCOO)_3$; (b) the change in the average luminescence lifetime in a function of temperature with fitting function; (c) the change in relative sensitivity with temperature.

determine the relative sensitivity of the optical thermometer according to the formula

$$S_r = \frac{1}{\tau_{fit}} \cdot \left| \frac{d\tau_{fit}}{dT} \right| \quad (6)$$

where $d\tau_{fit}$ is the change of the fitted thermometric parameter τ_{fit} at temperature change dT. The influence of the temperature on the calculated value of S_r for an exemplary sample of [EA]$Mn_{0.99}Cr_{0.01}(HCOO)_3$ is presented in Fig. 7c.

The analogous thermometric analysis including the average lifetime combined with a fitting function as well as relative sensitivity determination, is presented in Fig. S8. The collation of the average decay time at 80 K ($\tau_{avg,\ 80K}$) and maximal relative sensitivities is presented in Table 3.

The obtained results confirm the high applicability of the approach based on luminescence lifetime analysis. The achieved relative sensitivity of the thermometers (up to 5.14% K^{-1}) surpasses the values obtained using the ratiometric method. The reduction of the average luminescence lifetime takes place with an increase in Cr^{3+} ion concentration. Such a phenomenon is reported for another series of hybrid perovskites containing Cr^{3+} ions.[33,46] Moreover, the reduction of the temperature of the maximal S_r value ($T_{S_{r,max}}$) is correlated with increasing chromium(III) concentration. An increase in Cr^{3+} ion concentration enhances emission from the $^4T_{2g}$ level, thermally coupled with the ^2E_g level, leading to faster thermal quenching of ^2E_g emission (the base of the thermometric model) and a shift of the relative sensitivity maximum toward lower temperatures. The change of the $T_{S_{r,max}}$ as a function of the chemical composition is reported for a wide range of chromium concentration (from 21 mol% to 100 mol%) in $[EA]_2NaAl_{1-x}Cr_x(HCOO)_6$.[7] This may indicate the high applicability of Cr^{3+}-based luminescent thermometers operating in a strong crystal field. There is no clear correlation between the increase in Cr^{3+} concentration and the calculated values of relative sensitivities obtained with the ratiometric method. Within in context of a lifetime-based approach, in turn, the enhancement of the emission attributed to $^4T_{2g} \rightarrow {}^4A_{2g}$ transition leads to a decrease in relative sensitivity. Therefore, special attention should be paid to materials with low doping concentrations and exhibiting a strong crystal field. The obtained results of lifetime thermometry show an extraordinarily high potential of this particular approach for highly sensitive luminescent thermometry. The change of the default thermometric model may significantly improve the relative sensitivity by 1.80% K^{-1}, as it is shown for Mn-based compound doped with 1 mol% of Cr^{3+}. The reproducibility of the thermal sensing behavior was further assessed through successive heating and cooling cycles (Fig. S9). The results show minimal deviation from the initial values, indicating that the behavior of the investigated materials reliably reverses and repeats over multiple thermal cycles.

Table 3 The summary of the thermometric characteristics of the lifetime-based method

Cr^{3+} content	$\tau_{avg,\ 80K}$ (ms)	$S_{r,max}$ (% K^{-1})	$T_{S_{r,max}}$ (K)
1 mol%	0.78	5.14	143
3 mol%	0.40	4.32	128
5 mol%	0.34	4.23	126

Conclusions

The presented results show the significant potential of hybrid organic–inorganic perovskites doped with Cr^{3+} ions for luminescence thermometry. The implemented slow-diffusion method enables the synthesis of chemically stable hybrid compounds differing in Cr^{3+} concentration. Investigated materials exhibit remarkable spectroscopic characteristics, especially temperature-dependent luminescence and emission lifetime. Observed temperature-dependent spectroscopic features are successfully implemented for thermometric model determination. In this work, we present a comparison of different thermometric approaches and the resulting variety of relative sensitivities and operating ranges. The investigated

materials show a presence of several emission ranges, differing in thermal quenching progressivity. Such a phenomenon is fundamental for ratiometric model determination based on various thermometric ranges. We demonstrate the importance of consciously selecting the operating range of luminescent thermometers. The highest relative sensitivities can be achieved for ranges exhibiting possibly the greatest difference in the progressivity of thermal quenching. The presented results show high relative sensitivity of investigated materials up to 3.91% K^{-1}. It was also observed that there were small changes in the calculated utility range, which confirms the possibility of optimizing the constructed thermometric models. Moreover, the analysis of the potential of the luminescence lifetime-based approach is presented. Due to the presence of the significant thermal-quenching of luminescence lifetime, the determination of the thermometric model can be performed. The obtained results confirm the great potential of the investigated material. The spectacular relative sensitivities (up to 5.14% K^{-1}) show a possibility of the construction of a dual-parametrical thermometric system. Further development of luminescent thermometers based on both ratiometric and lifetime-based approaches may result in more sensitive and accurate sensing solutions. Undoubtedly, the presented series of $[EA]Mn_{1-x}Cr_x(HCOO)_3$, where x = 0, 0.01, 0.03, and 0.05, exhibits significant potential within the context of luminescence thermometry.

Author contributions

Conceptualization: D. S. data curation: A. K., and K. C. formal analysis: A. K., D. S., and K. C. funding acquisition: D. S. investigation: A. K., and K. C. methodology: all authors. Project administration: D. S. supervision: D. S. validation: D. S. and A. K. writing – original draft: all authors. Writing – review and editing: all authors. All the authors have given their approval to the final version of the manuscript.

Conflicts of interest

There are no conflicts to declare.

Data availability

Supplementary information (SI) is available. See DOI: https://doi.org/10.1039/d5tc02943k.

The data that support the findings of this study are openly available in Zenodo at: https://doi.org/10.5281/zenodo.16573642, reference number 16573642.

Acknowledgements

This research was supported by the National Science Center (NCN) in Poland under project SONATA 16 no. 2020/39/D/ST5/01289.

Notes and references

1 B. Harrington, Z. Ye, L. Signor and A. D. Pickel, *ACS Nanosci. Au*, 2024, **4**, 30–61, DOI: 10.1021/acsnanoscienceau.3c00051.
2 C. D. S. Brites, P. P. Lima, N. J. O. Silva, A. Millán, V. S. Amaral, F. Palacio and L. D. Carlos, *Nanoscale*, 2012, **4**, 4799, DOI: 10.1039/C2NR30663H.
3 M. D. Dramićanin, *J. Appl. Phys.*, 2020, **128**, 040902-1–040902-18, DOI: 10.1063/5.0014825.
4 L. Marciniak, K. Kniec, K. Elżbieciak-Piecka, K. Trejgis, J. Stefanska and M. D. Dramićanin, *Coord. Chem. Rev.*, 2022, **469**, 214671, DOI: 10.1016/j.ccr.2022.214671.
5 W. Piotrowski, K. Kniec and L. Marciniak, *J. Alloys Compd.*, 2021, 159386, DOI: 10.1016/j.jallcom.2021.159386.
6 B. del Rosal, E. Ximendes, U. Rocha and D. Jaque, *Adv. Opt. Mater.*, 2017, **5**, 1600508, DOI: 10.1002/adom.201600508.
7 A. Kabański, M. Ptak and D. Stefańska, *ACS Appl. Mater. Interfaces*, 2023, **15**, 7074–7082, DOI: 10.1021/acsami.2c19957.
8 M. T. Abbas, N. Z. Khan, J. Mao, L. Qiu, X. Wei, Y. Chen and S. A. Khan, *Mater. Today Chem.*, 2022, 100903, DOI: 10.1016/j.mtchem.2022.100903.
9 T. Zheng, L. Luo, P. Du, S. Lis, U. R. Rodríguez-Mendoza, V. Lavín and M. Runowski, *Chem. Eng. J.*, 2022, **446**, 136839, DOI: 10.1016/j.cej.2022.136839.
10 X. Tang, Y. Yue, X. Chen and X. Wang, *Opt. Express*, 2012, **20**, 14152, DOI: 10.1364/OE.20.014152.
11 E. Gao, R. Wei, D. Zhang, Z. Zhu, Q. Gao and B. Li, *J. Anal. At. Spectrom.*, 2023, **38**, 1116–1124, DOI: 10.1039/D3JA00044C.
12 B. Zhang, X. Guo, Z. Zhang, Z. Fu and H. Zheng, *J. Lumin.*, 2022, **250**, 119110, DOI: 10.1016/j.jlumin.2022.119110.
13 X. Lai, X. Ge, J. Li, J. Zhu and P. Du, *J. Lumin.*, 2024, **275**, 120815, DOI: 10.1016/j.jlumin.2024.120815.
14 T. V. Gavrilović, D. J. Jovanović, V. Lojpur and M. D. Dramićanin, *Sci. Rep.*, 2014, **4**, 4209, DOI: 10.1038/srep04209.
15 T. H. Q. Vu, B. Bondzior, D. Stefańska and P. J. Dereń, *J. Lumin.*, 2023, **257**, 119750, DOI: 10.1016/j.jlumin.2023.119750.
16 M. N. Bessadok, D. Ananias, A. Bouri, C. Bouzidi, C. Barthou and L. El Mir, *J. Lumin.*, 2024, **269**, 120480, DOI: 10.1016/j.jlumin.2024.120480.
17 D. Stefańska, A. Kabański, T. H. Q. Vu, M. Adaszyński and M. Ptak, *Sensors*, 2023, **23**, 6259, DOI: 10.3390/s23146259.
18 A. Kabański, M. Ptak, L. D. Carlos and D. Stefańska, *Adv. Opt. Mater.*, 2025, **13**, e01057, DOI: 10.1002/adom.202501057.
19 M. Ptak, A. Sieradzki, M. Šimėnas and M. Maczka, *Coord. Chem. Rev.*, 2021, **427**, 214180, DOI: 10.1016/j.ccr.2021.214180.
20 F. Z. Zeggai, Z. Ait-Touchente, K. Bachari and A. Elaissari, *Chem. Phys. Impact*, 2025, **10**, 100864, DOI: 10.1016/j.impact.2025.100864.
21 H. P. Hsu, L. C. Li, M. Shellaiah and K. W. Sun, *Sci. Rep.*, 2019, **9**, 13086, DOI: 10.1038/s41598-019-49926-z.
22 Z. Fan, K. Sun and J. Wang, *J. Mater. Chem. A*, 2015, **3**, 18809–18828, DOI: 10.1039/C5TA04235F.
23 K. Yananose, E. R. Clark, P. J. Saines, P. Barone, A. Stroppa and J. Yu, *Inorg. Chem.*, 2023, **62**, 17299–17309, DOI: 10.1021/acs.inorgchem.3c02557.

24 P. J. Dereń, A. Watras, A. Gągor and R. Pażik, *Cryst. Growth Des.*, 2012, **12**, 4752–4757, DOI: 10.1021/cg300435t.
25 K. Elżbieciak-Piecka, J. Drabik, D. Jaque and L. Marciniak, *Phys. Chem. Chem. Phys.*, 2020, **22**, 25949–25962, DOI: 10.1039/D0CP03453C.
26 M. Szymczak, A. Antuzevics, P. Rodionovs, M. Runowski, U. R. Rodríguez-Mendoza, D. Szymański, V. Kinzhybalo and L. Marciniak, *ACS Appl. Mater. Interfaces*, 2024, **16**, 64976–64987, DOI: 10.1021/acsami.4c11806.
27 G. Chen, Y. Jin, L. Yuan, B. Wang, J. Huo, H. Suo, H. Wu, Y. Hu and F. Wang, *ACS Appl. Mater. Interfaces*, 2024, **16**, 30185–30195, DOI: 10.1021/acsami.4c03419.
28 A. P. Vink, M. A. de Bruin, S. Roke, P. S. Peijzel and A. Meijerink, *J. Electrochem. Soc.*, 2001, **148**, E313, DOI: 10.1149/1.1375169.
29 S. Liu, J. Du, Z. Song, C. Ma and Q. Liu, *Light:Sci. Appl.*, 2023, **12**, 181, DOI: 10.1038/s41377-023-01275-y.
30 W. Liu, L. Yuan, H. Wu, H. Dong and Y. Jin, *Mater. Horiz.*, 2024, **11**, 6399–6407, DOI: 10.1039/D4MH01157K.
31 J. Yang and Y. Jin, *Opt. Lett.*, 2025, **50**, 5185, DOI: 10.1364/OL.569903.
32 Z. Li, H. Wu and Y. Jin, *Ceram. Int.*, 2025, **51**, 28319–28326, DOI: 10.1016/j.ceramint.2025.04.044.
33 A. Kabański, K. Caputa and D. Stefańska, *Dalton Trans.*, 2025, **54**, 15899–15908, DOI: 10.1039/D5DT01748C.
34 B. Zhu, N. Li, S. Ren, Y. Liu, D. Zhang, Q. Wang, Q. Shi, Q. Wang, S. Li, B. Zhang, W. Wang and C. Liu, *Spectrochim. Acta, Part A*, 2022, **264**, 120321, DOI: 10.1016/j.saa.2021.120321.
35 L. F. dos Santos, J. A. O. Galindo, K. O. Lima, A. R. Pessoa, A. M. Amaral, L. S. Menezes and R. R. Gonçalves, *J. Lumin.*, 2023, **262**, 119946, DOI: 10.1016/j.jlumin.2023.119946.
36 Y. Hua, J. S. Yu and L. Li, *Ceram. Int.*, 2024, **50**, 41228–41236, DOI: 10.1016/j.ceramint.2024.07.434.
37 Z. Wang, B. Zhang, T. Otsuka, K. Inoue, H. Kobayashi and M. Kurmoo, *Dalton Trans.*, 2004, 2209–2216, DOI: 10.1039/B404466E.
38 I. E. Collings, J. A. Hill, A. B. Cairns, R. I. Cooper, A. L. Thompson, J. E. Parker, C. C. Tang and A. L. Goodwin, *Dalton Trans.*, 2016, **45**, 4169–4178, DOI: 10.1039/C5DT03263F.
39 R. H. P. Awater and P. Dorenbos, *J. Lumin.*, 2017, **188**, 487–489, DOI: 10.1016/j.jlumin.2017.05.011.
40 A. Bednarkiewicz, L. Marciniak, L. D. Carlos and D. Jaque, *Nanoscale*, 2020, **12**, 14405–14421, DOI: 10.1039/D0NR03568H.
41 M. Ptak, A. Kabański, B. Dziuk, S. Balciunas, G. Usevicius, J. K. Zaręba, J. Banys, M. Šimėnas, A. Sieradzki and D. Stefańska, *J. Mater. Chem. C*, 2024, **12**, 4663–4675, DOI: 10.1039/D3TC04529C.
42 G. Li, G. Li, Q. Mao, L. Pei, H. Yu, M. Liu, L. Chu and J. Zhong, *Chem. Eng. J.*, 2022, **430**, 132923, DOI: 10.1016/j.cej.2022.132923.
43 W. Liu, D. Zhao, R. J. Zhang, Q. X. Yao and S. Y. Zhu, *Inorg. Chem.*, 2022, **61**, 16468–16476, DOI: 10.1021/acs.inorgchem.2c02707.
44 S. Ren, Y. Wu, Q. Wang, B. Yang, Q. Shi, S. Li and D. Zhang, *J. Lumin.*, 2022, **251**, 119264, DOI: 10.1016/j.jlumin.2022.119264.
45 V. B. Mykhaylyk, H. Kraus, L. I. Bulyk, I. Lutsyuk, V. Hreb, L. Vasylechko, Y. Zhydachevskyy, A. Wagner and A. Suchocki, *Dalton Trans.*, 2021, **50**, 14820–14831, DOI: 10.1039/D1DT02836G.
46 H. Gao, B. Devakumar and X. Huang, *Ceram. Int.*, 2025, **51**, 8321–8328, DOI: 10.1016/j.ceramint.2024.12.261.

Supplementary Information (SI) for Journal of Materials Chemistry C.

Supporting information

Multimodal temperature sensing in hybrid perovskites doped with Cr^{3+}: strategy for optimizing luminescence thermometers

Adam Kabański, Kacper Caputa, Dagmara Stefańska**

Keywords: *hybrid perovskite, luminescence, thermometry, chromium(III) ions, remote temperature sensing, optical thermometer, time-resolved thermometry*

Table S1. Octahedra parameters and predicted crystal field strength for undoped materials

Compound	Octahedra parameters	
	Lengths	**Details**
[EA]Mn(HCOO)$_3$ ICSD 110521 T = 290 K	l(Mn1-O4) = 2.2042(15) Å l(Mn1-O5) = 2.2043(18) Å l(Mn1-O2) = 2.1801(17) Å l(Mn1-O3) = 2.1867(17) Å l(Mn1-O6) = 2.1765(19) Å l(Mn1-O1) = 2.2175(15) Å	Average bond length = **2.1949 Å** Polyhedral volume = 14.0692 Å^3 Distortion index (bond length) = 0.00628 Quadratic elongation = 1.0014 Bond angle variance = 4.8427 deg.^2 Effective coordination number = 5.9905 **Crystal field = 0.0196**

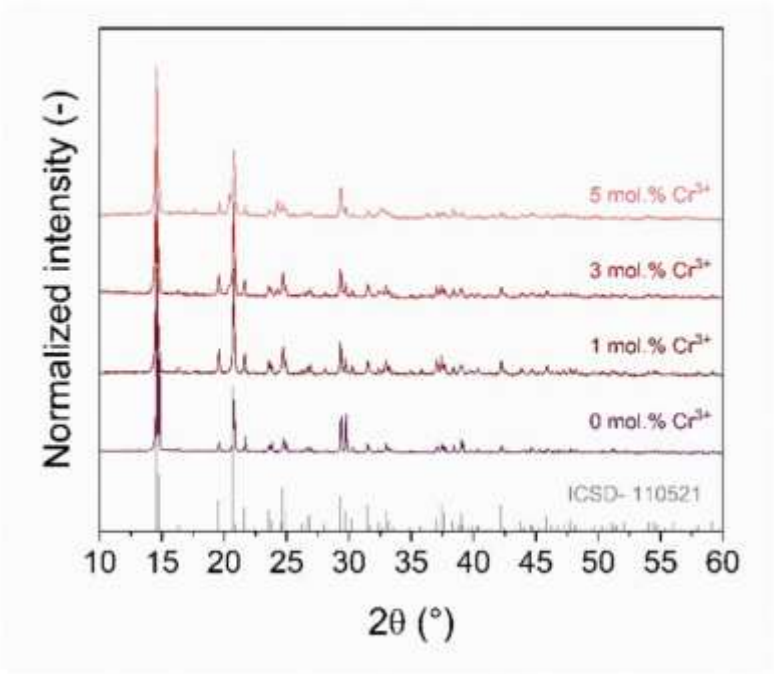

Figure S1. PXRD diffractograms of investigated samples combined with the generated pattern according to CIF file

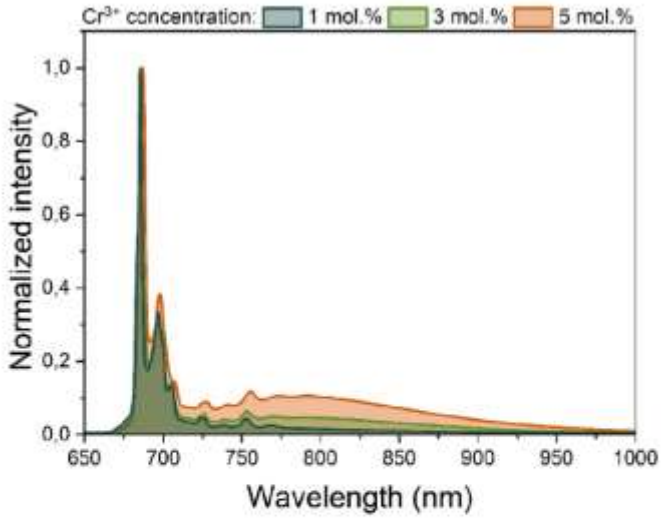

Figure S2. Normalized emission intensity at 80 K of $[EA]Mn_{1-x}Cr_x(HCOO)_3$, where x=0.01, 0.03, 0.05.

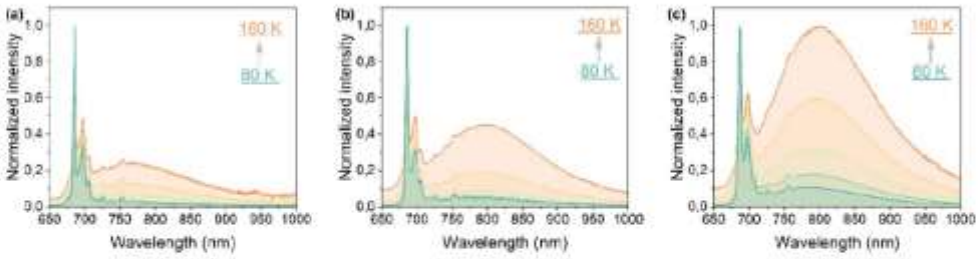

Figure S3. Comparison of emission intensity with the increase of the temperature for: (a) $[EA]Mn_{0.99}Cr_{0.01}(HCOO)_3$ (b) $[EA]Mn_{0.97}Cr_{0.03}(HCOO)_3$ (c) $[EA]Mn_{0.95}Cr_{0.05}(HCOO)_3$.

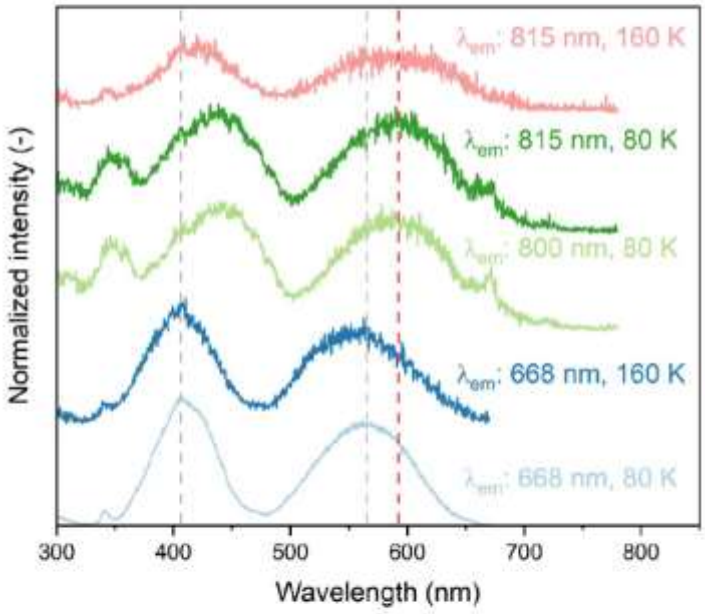

Figure S4. Comparison of excitation spectra measured for $[EA]Mn_{0.95}Cr_{0.05}(HCOO)_3$ sample

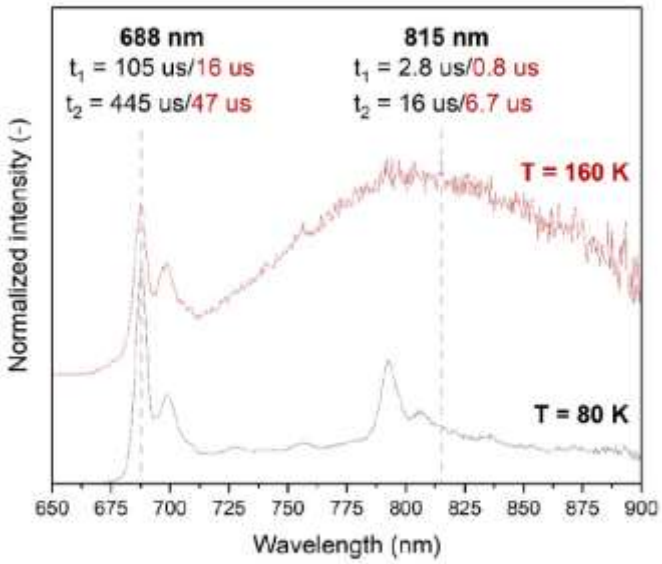

Figure S5. 80 K and 160 K PL spectra for the representative sample [EA]$Mn_{0.97}Cr_{0.03}(HCOO)_3$ registered under 405 nm excitation with luminescence lifetimes monitored at 688 nm and 815 nm

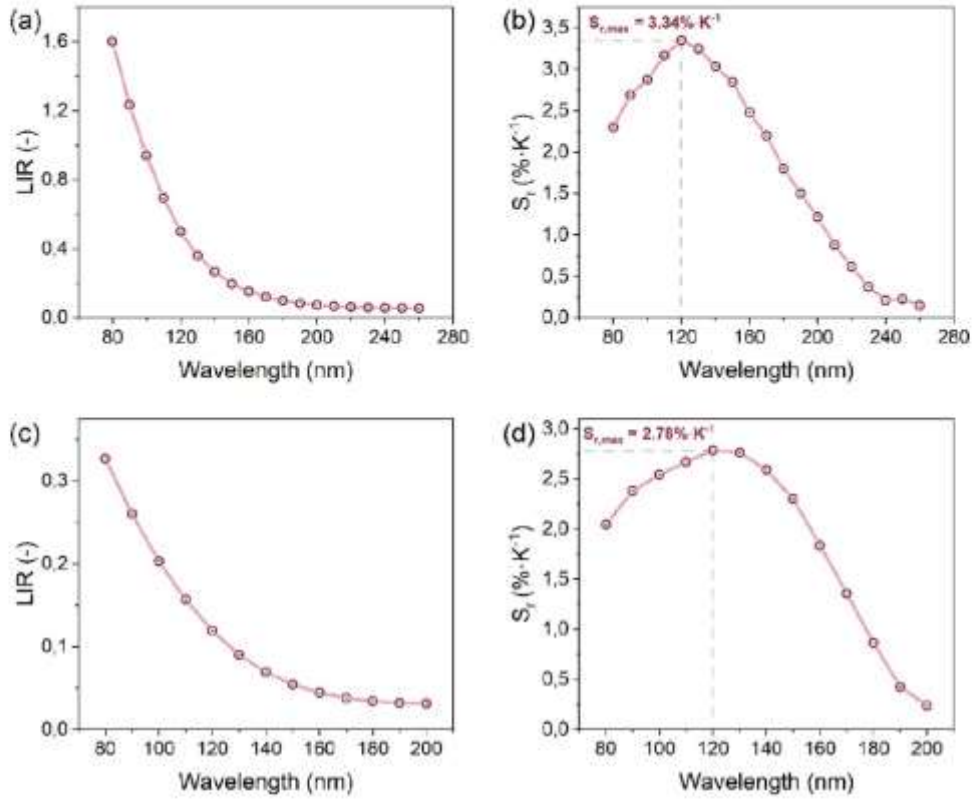

Figure S6. Comparison of the thermometric performance: (a) LIR and (b) S_r values for $[EA]Mn_{0.99}Cr_{0.01}(HCOO)_3$; (c) LIR and (d) S_r values for $[EA]Mn_{0.97}Cr_{0.03}(HCOO)_3$

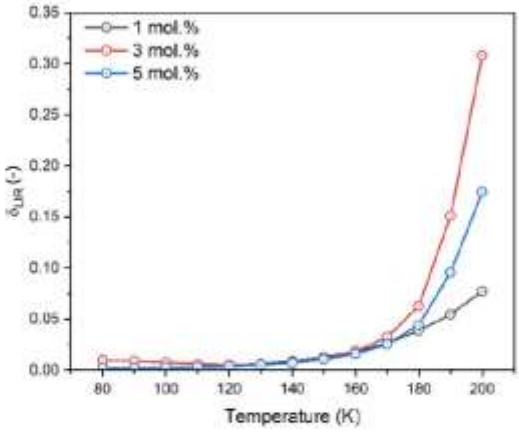

Figure S7. The comparison of the uncertainty of the LIR determination

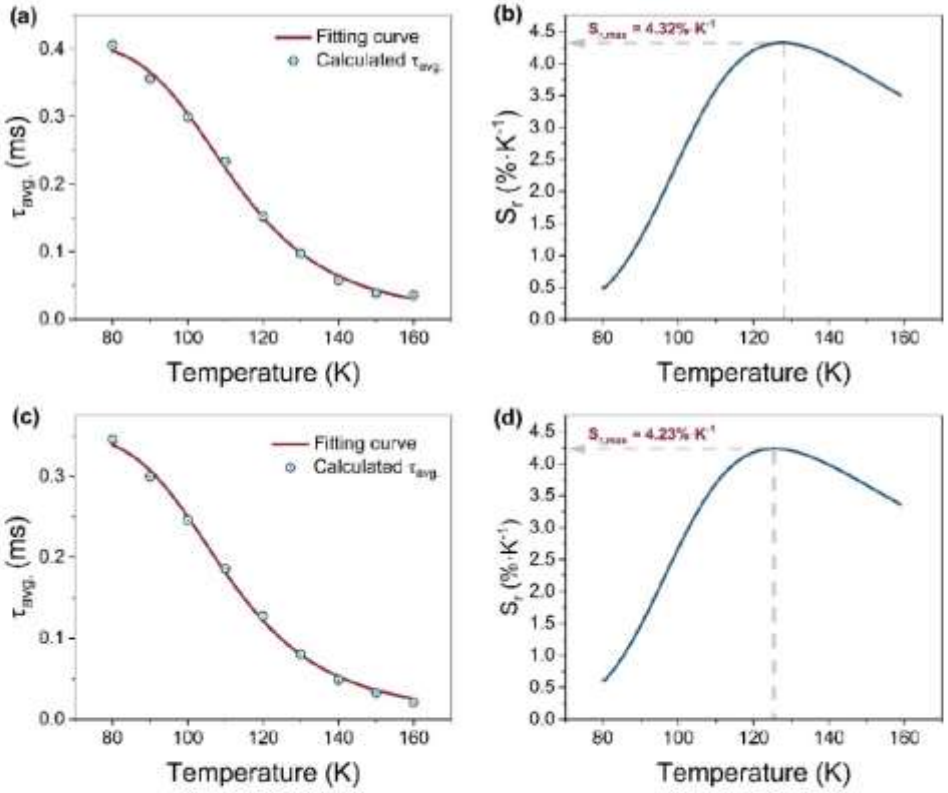

Figure S8. Comparison of the thermometric performance: (a) τ_{avg}, and (b) S_r values for $[EA]Mn_{0.97}Cr_{0.03}(HCOO)_3$; (c) LIR and (d) S_r values for $[EA]Mn_{0.95}Cr_{0.05}(HCOO)_3$;

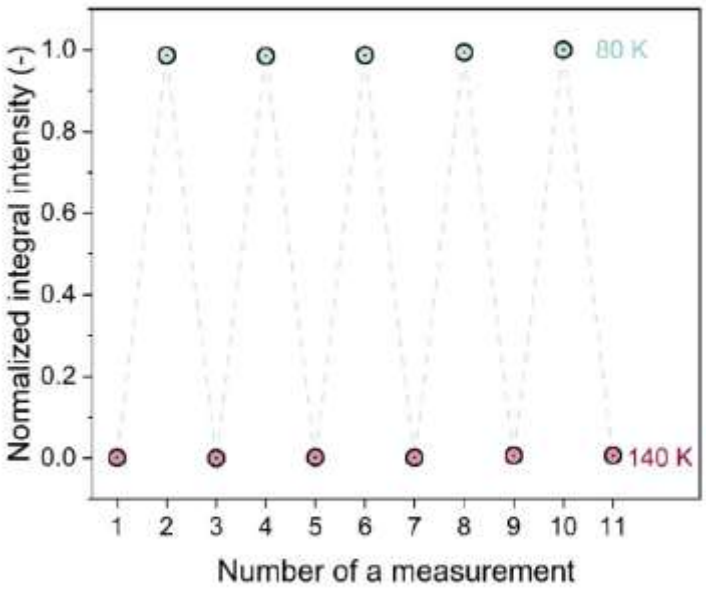

Figure S9. The thermal stability of the signal within the cooling-heating intervals (80-140 K) for the $[EA]Mn_{0.97}Cr_{0.03}(HCOO)_3$

11. Copies of co-authors' statements

dam Kabański

stitute of Low Temperature and Structure Research,
)lish Academy of Sciences
kólna 2, 50-422 Wrocław, Poland

Declaration of the co-authorship of the publications

:onfirm my participation in the following publications:

(P1) **Kabański A*,** Ptak M., and Stefańska D.* **(2023)**. *Metal–Organic Framewor ıermometer Based on Cr^{3+} Ion Luminescence*, ACS Applied Materials & Interfac)74-7082 DOI: 10.1021/acsami.2c19957

(P2) Ptak M.*, **Kabański A.**, Dziuk B., Balciunas S., Usevicius G., Zeręba J., menas M.*, Sieradzki A., Stefańska D. **(2024)** *Mechanism of isosymmetric pola sorder phase transition in pyroelectric $[CH_3CH_2NH_3]_2NaGa(HCOO)_6$ double p* urnal of Materials Chemistry C 12(13), 4663-4675 DOI: 10.1039/D3TC04529C

(P3) **Kabański A.*,** Ptak M, Carlos L.D., Stefańska D.* **(2025)**. *Real-Time Ten onitoring with Cr^{3+}-Based Hybrid Formate Perovskites: Insights into the Relation hemical Composition and Thermometric Performance*, Advanced Optical Mate)1057 DOI:10.1002/adom.202501057

(P4) **Kabański A.*,** Caputa K., Stefańska D.* **(2025)** *High-sensitivity optical ther th Cr^{3+}-doped hybrid formate perovskites: comparative analysis of ratiometric and sed approaches*, Dalton Transactions 54, 15899–15908 DOI: 10.1039/D5DT01748

(P5) **Kabański A.*,** Caputa K., Stefańska D.* **(2025)** *Multimodal temperature s brid perovskites doped with Cr^{3+}: strategy for optimizing luminescence therm* urnal of Materials Chemistry C 2025 DOI: 10.1039/D5TC02943K

the above-mentioned works, my contribution consisted of:

l: conceptualization; planning and conducting syntheses; planning and pe ectroscopic measurements and thermometric analyses; preparation of materials f easurements; analysis of spectroscopic and structural measurement results; prepa

P2: co-participation in the synthesis of the investigated compounds; planning and performing spectroscopic measurements and thermometric analyses; preparation of compounds for pXRD measurements; analysis of measurement results; preparation of figures; participation in the preparation of the initial and final versions of the manuscript.

P3: conceptualization; planning the structure of the manuscript; spectroscopic and structural measurements; thermometric analysis; preparation of compounds for pXRD measurements; analysis of spectroscopic and structural measurement results; preparation of figures; description of the results; preparation of the initial and final versions of the manuscript; development of the concept and preparation of a setup for time-dependent thermometric measurements; preparation of responses to reviewers; data archiving after preparation of the final manuscript.

P4: conceptualization; planning the structure of the manuscript; spectroscopic and structural measurements as well as thermometric analysis; preparation of compounds for pXRD measurements; processing and interpretation of spectroscopic and structural measurement results; preparation of figures and description of the results; preparation of the initial and final versions of the manuscript; development of a concept for optimization of thermometric properties; preparation of responses to reviewers; data archiving after preparation of the final manuscript.

P5: conceptualization; planning the structure of the manuscript; spectroscopic and structural measurements; thermometric analysis; preparation of compounds for pXRD measurements; analysis of spectroscopic and structural measurement results; preparation of figures; description of the results; preparation of the initial and final versions of the manuscript; development of the concept and performance of multimodal thermometric analysis; preparation of responses to reviewers; data archiving after preparation of the final manuscript.

Adam Kabański

Prof. Mantas Simenas

Vilnius University
Institute of Applied Electrodynamics and Telecommunications (IAET)
3 Universiteto St., LT-01513 Vilnius, Lithuania

Declaration of the co-authorship of the publication

I confirm my participation in the following publication:

- (P2) Ptak M.*, Kabański A., Dziuk B., Balciunas S., Usevicius G., Zeręba J., Banys **Simenas M.*,** Sieradzki A., Stefańska D. (**2024**) *Mechanism of isosymmetric polar orde disorder phase transition in pyroelectric $[CH_3CH_2NH_3]_2NaGa(HCOO)_6$ double perovski* Journal of Materials Chemistry C 12(13), 4663-4675 DOI: 10.1039/D3TC04529C

Wrocław, 25.11.2025

dr hab. Maciej Ptak, prof. INTiBS PAN

Institute of Low Temperature and Structure Research
Polish Academy of Sciences
Okólna 2, 50-422 Wrocław, Poland

Declaration of the co-authorship of the publications

I confirm my participation in the following publications:

- **(P1)** Kabański A*, **Ptak M**., and Stefańska D.* **(2023)**. *Metal–Organic Framework Optical Thermometer Based on Cr^{3+} Ion Luminescence*, ACS Applied Materials & Interfaces 15(5), 7074-7082 DOI: 10.1021/acsami.2c19957

- **(P2) Ptak M.***, Kabański A., Dziuk B., Balciunas S., Usevicius G., Zeręba J., Banys J., Simenas M.*, Sieradzki A., Stefańska D. **(2024)** *Mechanism of isosymmetric polar order–disorder phase transition in pyroelectric $[CH_3CH_2NH_3]_2NaGa(HCOO)_6$ double perovskite*, Journal of Materials Chemistry C 12(13), 4663-4675 DOI: 10.1039/D3TC04529C

- **(P3)** Kabański A.*, **Ptak M**, Carlos L.D., Stefańska D.* **(2025)**. *Real-Time Temperature Monitoring with Cr^{3+}-Based Hybrid Formate Perovskites: Insights into the Relation Between Chemical Composition and Thermometric Performance*, Advanced Optical Materials 13, e01057 DOI:10.1002/adom.202501057

included supervising IR and Raman measurements, assisting in analyzing results, preparing figures, participating in discussion and interpretation of results, editing, and reviewing manuscripts. I also declare that my contribution and that of A. Kabański to the publication (P2) were equal.

Maciej Wojciech Ptak

Elektronicznie podpisany przez Maciej Wojciech Ptak
Data: 2025.11.25 14:05:59 +01'00'

[Aveiro, November 26 2025]

prof. Luis Dias Carlos

Phantom-g, CICECO – Aveiro Institute of Materials,
Physics Department, University of Aveiro,
Aveiro, 3810-193 Portugal

Declaration of the co-authorship of the publication

I confirm my participation in the following publications:

- **(P3)** Kabański A.*, Ptak M, **Carlos L.D.,** Stefańska D.* (**2025**). *Real-Time Temperature Monitoring with Cr^{3+}-Based Hybrid Formate Perovskites: Insights into the Relation Between Chemical Composition and Thermometric Performance*, Advanced Optical Materials 13, e01057 DOI:10.1002/adom.202501057

Reading and comment of the initial draft of the manuscript and its final version and validation of the thermometric analysis.

Wrocław, 25.11.2025

inż. Kacper Caputa

Institute of Low Temperature and Structure Research,
Polish Academy of Sciences
Okólna 2, 50-422 Wrocław, Poland

Declaration of the co-authorship of the publications

I confirm my participation in the following publications:

- (**P4**) Kabański A.*, **Caputa K.**, Stefańska D.* (**2025**) *High-sensitivity optical thermometry with Cr^{3+}-doped hybrid formate perovskites: comparative analysis of ratiometric and lifetime-based approaches*, Dalton Transactions 54, 15899–15908 DOI: 10.1039/D5DT01748C

- (**P5**) Kabański A.*, **Caputa K.**, Stefańska D.* (**2025**) *Multimodal temperature sensing in hybrid perovskites doped with Cr^{3+}: strategy for optimizing luminescence thermometers*, Journal of Materials Chemistry C 2025 DOI: 10.1039/D5TC02943K

I performed luminescent measurements, analyzed collected data, prepared drawings, participated in writing, developed methodology, and prepared the final versions of original drafts.

Kacper Caputa

inż. Kacper Caputa

Wrocław, 19.12.2025

dr inż. Jan K. Zaręba

Wrocław University of Science and Technology
Institute of Advanced Materials
Wybrzeże Wyspiańskiego 27, 50-370 Wrocław

Declaration of the co-authorship of the publication

I confirm my participation in the following publication:

- (P2) Ptak M.*, Kabański A., Dziuk B., Balciunas S., Usevicius G., **Zaręba J.K.**, Banys J., Simenas M.*, Sieradzki A., Stefańska D. (**2024**) *Mechanism of isosymmetric polar order–disorder phase transition in pyroelectric $[CH_3CH_2NH_3]_2NaGa(HCOO)_6$ double perovskite*, Journal of Materials Chemistry C 12(13), 4663-4675 DOI: 10.1039/D3TC04529C

I conducted temperature-resolved second-harmonic generation measurements, drafted the corresponding section of the manuscript, and reviewed and edited the text prior to publication.

Jan K. Zaręba

Gediminas Usevicius

Vilnius University
Institute of Applied Electrodynamics and Telecommunications (IAET)
3 Universiteto St., LT-01513 Vilnius, Lithuania

Declaration of the co-authorship of the publication

I confirm my participation in the following publication:

- (P2) Ptak M.*, Kabański A., Dziuk B., Balciunas S., **Usevicius G.**, Zeręba J., Banys J., Simenas M.*, Sieradzki A., Stefańska D. (**2024**) *Mechanism of isosymmetric polar order–disorder phase transition in pyroelectric $[CH_3CH_2NH_3]_2NaGa(HCOO)_6$ double perovskite*, Journal of Materials Chemistry C 12(13), 4663-4675 DOI: 10.1039/D3TC04529C

I contributed to the work by conducting continuous-wave and pulsed electron paramagnetic resonance (EPR) spectroscopy experiments described under "EPR" subsection of "Results and discussion", analyzed the EPR data and I was responsible for preparing EPR related figures (Fig. 6, 7). In addition, I helped with the initial draft of "EPR" subsection and proof reading of the publication.

Wrocław, 16.01.2026

dr hab. Dagmara Stefańska, prof. INTiBS PAN

Institute of Low Temperature and Structure Research,
Polish Academy of Sciences
Okólna 2, 50-422 Wrocław, Poland

Declaration of the co-authorship of the publications

I confirm my participation in the following publications:

- **(P1)** Kabański A*, Ptak M., and **Stefańska D.* (2023)**. *Metal–Organic Framework Optical Thermometer Based on Cr^{3+} Ion Luminescence*, ACS Applied Materials & Interfaces 15(5), 7074-7082 DOI: 10.1021/acsami.2c19957

- **(P2)** Ptak M.*, Kabański A., Dziuk B., Balciunas S., Usevicius G., Zeręba J., Banys J., Simenas M.*, Sieradzki A., **Stefańska D. (2024)** *Mechanism of isosymmetric polar order–disorder phase transition in pyroelectric $[CH_3CH_2NH_3]_2NaGa(HCOO)_6$ double perovskite*, Journal of Materials Chemistry C 12(13), 4663-4675 DOI: 10.1039/D3TC04529C

- **(P3)** Kabański A.*, Ptak M, Carlos L.D., **Stefańska D.* (2025)**. *Real-Time Temperature Monitoring with Cr^{3+}-Based Hybrid Formate Perovskites: Insights into the Relation Between Chemical Composition and Thermometric Performance*, Advanced Optical Materials 13, e01057 DOI:10.1002/adom.202501057

- **(P4)** Kabański A.*, Caputa K., **Stefańska D.* (2025)** *High-sensitivity optical thermometry with Cr^{3+}-doped hybrid formate perovskites: comparative analysis of ratiometric and lifetime-based approaches*, Dalton Transactions 54, 15899–15908 DOI: 10.1039/D5DT01748C

- **(P5)** Kabański A.*, Caputa K., **Stefańska D.* (2025)** *Multimodal temperature sensing in hybrid perovskites doped with Cr^{3+}: strategy for optimizing luminescence thermometers*, Journal of Materials Chemistry C 2025 DOI: 10.1039/D5TC02943K

As the Supervisor of M.Sc. Adam Kbański, I was responsible for the conceptualization of the research and I also contributed to the review, editing, and preparation of the final versions of the manuscripts. I confirm that M.Sc. Adam Kbański acted as the main co-author and made a significant contribution to the above-mentioned publications.

Dagmara Stefańska

Instytut Niskich Temperatur i Badań Strukturalnych im. Włodzimierza Trzebiatowskiego Polskiej Akademii Nauk
Institute of Low Temperature and Structure Research Polish Academy of Sciences

• ul. Okólna 2, 50-422 Wrocław | Poland • tel. +48 71 343 5021 • intibs@intibs.pl • www.intibs.pl

Wrocław, 22.12.2025

Błażej Dziuk

cław University of Science and Technology
tute of Advanced Materials
rzeże Wyspiańskiego 27, 50-370 Wrocław

Declaration of the co-authorship of the publication

ıfirm my participation in the following publication:

2) Ptak M.*, Kabański A., **Dziuk B.**, Balciunas S., Usevicius G., Zeręba J., Banys J.,

Wrocław, 19.12.2025

dr hab. inż. Adam Sieradzki, prof. PWr

Wrocław University of Science and Technology
Faculty of Fundamental Problems of Technology
Department of Experimental Physics
Wybrzeże Wyspiańskiego 27, 50-370 Wrocław

Declaration of the co-authorship of the publication

I confirm my participation in the following publication:

- **(P2) Ptak M.*,** Kabański A., Dziuk B., Balciunas S., Usevicius G., Zeręba J., Banys J., Simenas M.*, Sieradzki A., Stefańska D. (**2024**) *Mechanism of isosymmetric polar order–disorder phase transition in pyroelectric $[CH_3CH_2NH_3]_2NaGa(HCOO)_6$ double perovskite*, Journal of Materials Chemistry C 12(13), 4663-4675 DOI: 10.1039/D3TC04529C

My contribution included performing the calorimetric measurements (DSC), analyzing the data, and writing the section describing these results.

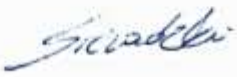

Wilnus, 13.01.2026

Prof. Juras Banys

Vilnius University
Institute of Applied Electrodynamics and Telecommunications (IAET)
3 Universiteto St., LT-01513 Vilnius, Lithuania

Declaration of the co-authorship of the publication

I confirm my participation in the following publication:

- (P2) Ptak M.*, Kabański A., Dziuk B., Balciunas S., Usevicius G., Zeręba J., **Banys J.**, Simenas M.*, Sieradzki A., Stefańska D. **(2024)** *Mechanism of isosymmetric polar order–disorder phase transition in pyroelectric $[CH_3CH_2NH_3]_2NaGa(HCOO)_6$ double perovskite*, Journal of Materials Chemistry C 12(13), 4663-4675 DOI: 10.1039/D3TC04529C,

including methodological supervision of the preparation of the initial draft and final version of the manuscript.

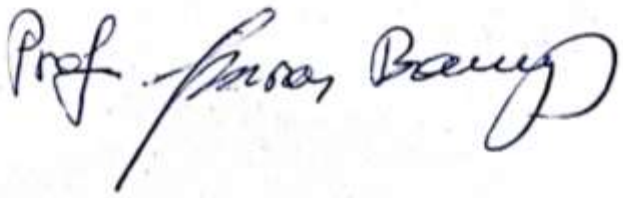

Dr Sergejus Balciunas

Vilnius University
Institute of Applied Electrodynamics and Telecommunications (IAET)
3 Universiteto St., LT-01513 Vilnius, Lithuania

Declaration of the co-authorship of the publication

I confirm my participation in the following publication:

- (P2) Ptak M.*, Kabański A., Dziuk B., **Balciunas S.,** Usevicius G., Zeręba J., Banys J., Simenas M.*, Sieradzki A., Stefańska D. (**2024**) *Mechanism of isosymmetric polar order–disorder phase transition in pyroelectric $[CH_3CH_2NH_3]_2NaGa(HCOO)_6$ double perovskite*, Journal of Materials Chemistry C 12(13), 4663-4675 DOI: 10.1039/D3TC04529C

12. *Curriculum vitae* and scientific achievements

Adam Kabański, MSc Eng.

ORCID: 0000-0003-3348-1261

Scopus ID: 57356202600

Educational background

2021/10 - 2025/01	**PhD studies** *Institute of Low Temperature and Structure Research of Polish Academy of Sciences*
2020/03 - 2021/09	**Master studies** *Wroclaw University of Science And Technology/Institute of Low Temperature and Structure Research of Polish Academy of Sciences* Division of Optical Spectroscopy Field of study: Advanced Nano- and Biomaterials (MONABIPHOT)
2016/10 – 2020/02	**Bachelor Studies** *Wroclaw University of Science And Technology* Field of study: Chemical and Process Engineering

Scientific and professional experience

2025/10 - Present	**Chemical Technician** *Institute of Low Temperature and Structure Research of Polish Academy of Sciences*
2020/03 - Present	**Investigator** **NCN Preludium 22 (2023/49/N/ST5/00521)** *Institute of Low Temperature and Structure Research of Polish Academy of Sciences* Title: Layered hybrid perovskites with broadband luminescence and tunable optoelectronic properties Principal Investigator (PI): dr inż. Dawid Drozdowski
2016/10 – 2020/02	**Investigator (scholarship)** **NCN Sheng 2 (2021/40/Q/ST5/00220)** *Institute of Low Temperature and Structure Research of Polish Academy of Sciences* Title: Tunable wavelength emission source excited by CW laser diode: phenomenon, mechanism, control and applications Principal Investigator (PI): prof. dr hab. Wiesław Stręk

2022/10 – 2025/03 **Volunteer**
NCBiR LIDER XII (19/0103/L-12/20/NCBR/2021)
Institute of Low Temperature and Structure Research of Polish Academy of Sciences
Title: Opracowanie technologii wytwarzania kompozytów emitujących światło białe o wysokim współczynniku CRI dedykowanych do oświetlenia LED
Principal Investigator (PI): dr hab. Dagmara Stefańska, prof. INTiBS

2021/10 – 2025/06 **Investigator (PhD candidate)**
NCN Sonata 16 (2020/39/D/ST5/01289)
Institute of Low Temperature and Structure Research of Polish Academy of Sciences
Title: Hybrid organic-inorganic perovskites as high-sensitive luminescent thermometers
Principal Investigator (PI): dr hab. Dagmara Stefańska, prof. INTiBS

2020/09 – 2021/09 **Volunteer (Master thesis)**
Department of Biomedical Physicochemistry
Institute of Low Temperature and Structure Research of Polish Academy of Sciences
Title: Investigating the effect of matrix composition on the spectroscopic properties of Bi^{3+} and Eu^{3+} ions in the $YV_xP_{1-x}O_4$ system
Supervisor: dr inż. Adam Watras

2019/08 – 2019/09 **Intern at Department of Technology**
Volkswagen Poznań (Antoninek)
Topic: Industry wastewater treatment and microbial fuel cells technology

2019/07 – 2019/08 **Intern at Mechanochemical Synthesis Group**
Center of Advanced Technologies
Adam Mickiewicz University
Topic: MIDA-boronates – mechanochemical and wet organic synthesis; organoboron chemistry

2019/07 – 2019/08 **Intern at Mechanochemical Synthesis Group**
Center of Advanced Technologies
Adam Mickiewicz University
Topic: Synthesis and functionalization of silsesquioxanes, mechanochemical synthesis, organic synthesis

2019/06 – 2021/03 **Project coordinator**
Faculty of Chemistry Scientific Students Association *Allin*
Wroclaw University of Science and Technology
Topic: Triboluminescence phenomenon based on the metal complexes

Associations and Organizations

2022/04 – present	**Member of Scientific Section, Academic Radio LUZ** *Wroclaw University of Science and Technology*
2016/10 – present	**Member (Honorary) of Faculty of Chemistry Scientific Students Association *Allin*** *Wroclaw University of Science and Technology*

Courses and Certificates

2020/12	**Reaxys & Reaxys Medicinal Chemistry training** *Elsevier* *Student's Section of the Polish Chemical Society*
2018/03	**ChemCAD Suite** *Nor-Pas As*
2018/03	**Infrared Spectroscopy in Routine Laboratory Tests** *Perkin Elmer Inc.*

Scientific publications

Included to the Dissertation

P1 **Kabański A***, Ptak M., and Stefańska D.* (**2023**). *Metal–Organic Framework Optical Thermometer Based on Cr^{3+} Ion Luminescence*, ACS Applied Materials & Interfaces 15(5), 7074-7082 DOI: 10.1021/acsami.2c19957
https://pubs.acs.org/doi/full/10.1021/acsami.2c19957

P2 Ptak M.*, **Kabański A.**, Dziuk B., Balciunas S., Usevicius G., Zeręba J., Banys J., Simenas M.*, Sieradzki A., Stefańska D. (**2024**) *Mechanism of isosymmetric polar order–disorder phase transition in pyroelectric $[CH_3CH_2NH_3]_2NaGa(HCOO)_6$ double perovskite*, Journal of Materials Chemistry C 12(13), 4663-4675 DOI: 10.1039/D3TC04529C
https://pubs.rsc.org/en/content/articlelanding/2024/tc/d3tc04529c

P3 **Kabański A.***, Ptak M, Carlos L.D., Stefańska D.* (**2025**). *Real-Time Temperature Monitoring with Cr^{3+}-Based Hybrid Formate Perovskites: Insights into the Relation Between Chemical Composition and Thermometric Performance*, Advanced Optical Materials 13, e01057 DOI:10.1002/adom.202501057 https://advanced.onlinelibrary.wiley.com/doi/10.1002/adom.202501057

P4 **Kabański A.***, Caputa K., Stefańska D.* (**2025**) *High-sensitivity optical thermometry with Cr^{3+}-doped hybrid formate perovskites: comparative analysis of ratiometric and lifetime-based approaches*, Dalton Transactions 54, 15899–15908 DOI: 10.1039/D5DT01748C https://pubs.rsc.org/en/content/articlelanding/2025/dt/d5dt01748c

P5 **Kabański A.***, Caputa K., Stefańska D.* (**2025**) *Multimodal temperature sensing in hybrid perovskites doped with Cr^{3+}: strategy for optimizing luminescence thermometers*, Journal of Materials Chemistry C 13, 23935-23944 DOI: 10.1039/D5TC02943K https://pubs.rsc.org/en/content/articlelanding/2025/tc/d5tc02943k

---

Other publications

P6 S. Targońska, Charczuk N., **Kabański, A.**, Marcinkowska K., Sulecka-Zadka J., Szymanowska D., Śmieszek A., Wiglusz R., *Bridging the Effects of Noncontact Temperature Sensing and Cellular Biofunctionality in Nanosized Dysprosium(III)-Doped Fluorapatite* (**2025**) Small, e07537, DOI: 10.1002/smll.202507537

P7 Rowińska M., Korolevych O., **Kabański A**., Stefańska D., Bednarchuk T., Piecha-Bisiorek A., Gągor A.* *Hybrid Bismuth(III)-Halide Double Perovskite-Derived Ferroelastic $(Pip)_2[KBiBr_6]$ with Excitonic and Bi(III) Luminescence due to Electronic Confinement along Inorganic Pillars* **(2025)** Chemistry of Materials, 37, 18, 7125-7135 DOI: 10.1021/acs.chemmater.5c01183

P8 Adaszyński M, Adamczak K., **Kabański A**., Jerzykiewicz M., Stefańska D., *Blue-to-NIR energy transfer for bifunctional application in indoor agriculture and high-temperature luminescent thermometry* (**2025**) Journal of Alloys and Compounds, 1039, 183250 DOI: 10.1016/j.jallcom.2025.183250

P9 Drozdowski D., **Kabański A**., Stefańska D., Ptak M., Mączka M., Gągor A. *Layered methylhydrazinium lead halide perovskites: new crystal polymorphs with a tailored band gap and photoluminescence colour via halide substitution* (**2024**) Journal of Materials Chemistry C, 12, 6653-6662 DOI: 10.1039/D4TC00865K

P10 Stefańska D., **Kabański A**., Vu T.H.Q., Adaszyński M., Ptak M. *Structure, Luminescence and Temperature Detection Capability of $[C(NH_2)_3]M(HCOO)_3$ ($M = Mg^{2+}, Mn^{2+}, Zn^{2+}$) Hybrid Organic–Inorganic Formate Perovskites Containing Cr^{3+} Ions* (**2023**) Sensors, 23, 14, 6259 DOI: 10.3390/s23146259

P11 Goszyk J., Adaszyński M., **Kabański A**., Ptak M., Stefański M., Pikul A., Sahraoui B., Kuśmierz M., Myśliwiec J., Szukalski A., *Synthesis route and structural, magnetic,*

optical, and non-linear optical properties of triboluminescent [Cu(NCS)(py)$_2$(PPh$_3$)] complex (**2023**) Polyhedron, 243, 116545 DOI: 10.1016/j.poly.2023.116545

P12 Stefańska D., **Kabański A**., Adaszyński M., Ptak M., Lisiecki R., Starościk N., Hanuza J. *Broadband near-infrared luminescence properties of Sc$_2$(MoO$_4$)$_3$: Cr^{3+} molybdates* (**2023**) Spectrochimica Acta Part A: Molecular and Biomolecular Spectroscopy, 296, 122699 DOI: 10.1016/j.saa.2023.122699

P13 Pelczarska A.J, Stefańska D., **Kabański A**., Ptak M., Lisiecki R., Szczygieł I., Hanuza J. *Structural and optical properties of a new structural modification of Na$_{3+3x}$Yb$_{2-x}$(PO$_4$)$_3$:1% Eu phosphate, where x = 0,1-0,5 and prospective thermometric applications of the compound* (**2023**) Journal of Alloys and Compounds, 944, 169228 DOI: 10.1016/j.jallcom.2023.169228

P14 Drozdowski D., Fedoruk K., **Kabański A**., Mączka M., Sieradzki A., Gągor A. *Broadband yellow and white emission from large octahedral tilting in (110)-oriented layered perovskites: imidazolium-methylhydrazinium lead halides* (**2023**) Journal of Materials Chemistry C, 11, 4907-4915 DOI: 10.1039/D3TC00401E

P15 Szukalski A., **Kabański A**., Goszyk J., Adaszyński M., Kaczmarska M., Gaida R., Wyskiel M., Myśliwiec J. *Triboluminescence Phenomenon Based on the Metal Complex Compounds - A Short Review* (**2021**) Materials, 14, 23, 7142 DOI: 10.3390/ma14237142

P16 **Kabański A**. *Synteza, właściwości oraz implementacja kompleksowych związków tryboluminescencyjnych* (**2021**) Monografia „Kwadrans dla Chemii", Sekcja Studencka PTChem, Oficyna Edukacyjna Krzysztof Pazdro, 59, ISBN: 978-83-7594-208-8

Conferences

2025/08/24-29 **The International Conference on Excited States of Transition Elements (ESTE 2025)**
Oral presentation
Sosnówka, Jelenia Góra, Poland
Title: *Multimodal temperature sensing in hybrid perovskites doped with Cr^{3+} ions*
Authors: A. Kabański, K. Caputa, D. Stefańska

2025/06/27-07/01 **XLV Max Morn Symposium: 13th International Symposium "Optics&Its applications"**
Oral presentation
Wrocław, Poland
Title: *Real-time luminescent thermometry of hybrid perovskites containing Cr^{3+} ion*
Authors: A. Kabański, M. Ptak, L.D. Carlos, D. Stefańska

2025/04/26-30 **Spring Meeting of the Youth Section of the Polish Chemical Society (SMPTChem)**
Oral presentation
Bąkowo, Poland
Title: *Time-resolved luminescent thermometry of hybrid perovskites containing Cr^{3+} ions*
Authors: A. Kabański, M. Ptak, L.D. Carlos, D. Stefańska

2024/10/11-13 **Conference of Doctoral Students of PAS (KonDokPan 2024)**
Oral presentation
Warsaw, Poland
Title: *Luminescent thermometry: novel approach to remote temperature sensing*
Authors: A. Kabański, M. Ptak, D. Stefańska

2024/09/22-25 **XVII International Conference on Molecular Spectroscopy**
Poster presentation
Wojanów, Poland
Title: *Temperature-dependent structural and spectroscopic properties of Cr^{3+}-doped $[EA]_2NaGa(HCOO)_6$ double perovskite*
Authors: A. Kabański, M. Ptak, D. Stefańska

2024/09/26-30 **The 7th International Conference on the Physics of Optical Materials & The 4th International Conference on Phosphor Thermometry**
Oral presentation
Becic, Montenegro
Title: *Imidazolium-based double perovskites containing Cr^{3+} ions for highly sensitive luminescent thermometry*
Authors: A. Kabański, M. Ptak, D. Stefańska

2024/08/07-12 **The 8th International Workshop on Advanced Spectroscopy and Optical Materials**
Oral presentation
Gdańsk, Poland
Title: *Imidazolium-based double perovskites containing Cr^{3+} ions for highly sensitive luminescent thermometry*
Authors: A. Kabański, M. Ptak, D. Stefańska

2024/06/06-07 **XVII Copernican Seminar of Doctoral Students**
Oral presentation, The best presentation award
Toruń, Poland
Title: *Luminescent thermometry of hybrid perovskites containing Cr^{3+} ions*
Authors: A. Kabański, M. Ptak, D. Stefańska

2024/05/16-17 **PhoBiA Annual Nanophotonics International Conference 2024 (PANIC2024),**
Poster presentation
Wrocław, Poland
Title: *Single- and double hybrid perovskites containing Cr^{3+} for highly sensitive luminescent thermometry*
Authors: A. Kabański, M. Ptak, D. Stefańska

2023/09/12 **Winter Meeting of the Youth Section of the Polish Chemical Society (SMPTChem)**
Poster presentation
Toruń, Poland
Title: *Hybrid organic-inorganic perovskites containing Cr^{3+} ions as highly sensitive luminescent thermometers*
Authors: A. Kabański, M. Ptak, D. Stefańska

2023/10/11-13 **Conference of Doctoral Students of the PAS (KonDokPAN 2023)**
Oral presentation
Toruń, Poland
Title: *Luminescence thermometry based on hybrid organic-inorganic perovskites containing Cr^{3+} ions*
Authors: A. Kabański, M. Ptak, D. Stefańska

2023/09/03-08 **International Conference on Excited States of Transition Elements (ESTE 2023)**
Oral presentation
Świeradów-Zdrój, Poland
Title: *The effects of the metal substitution on thermometric properties of $[EA]M_{1-x}Cr_x(HCOO)_3$ (M = Mn, Mg); $x \in (0, 0.01, 0.03, 0.05)$ hybrid perovskites*
Authors: A. Kabański, T.H.Q. Vu, M. Ptak, D. Stefańska

2023/08/27-09/01 **20th International Conference On Luminescence**
Oral presentation
Paris, France
Title: *Influence of the metal type on spectroscopic properties of organic-inorganic optical thermometer* $[DMA]M_{1-x}Cr_x(HCOO)_3$ *(M = Zn, Mn, Mg);* $x \in (0, 0.01, 0.03, 0.05)$
Authors: A. Kabański, T.H.Q. Vu, M. Ptak, D. Stefańska

2023/05/18-19 **10th Doctoral Symposium on Chemistry**
Oral presentation, honorable mention
Łódź, Poland
Title: *Hybrydowe materiały o strukturze perowskitu zawierające jony* Cr^{3+} *jako wysokoczułe termometry luminescencyjne*
Authors: A. Kabański, M. Ptak, D. Stefańska

2023/05/15-19 **PhoBiA Annual Nanophotonics International Conference 2024 (PANIC2023)**
Oral presentation
Wrocław, Poland
Title: *Highly sensitive luminescent thermometers based on hybrid formate perovskites contaning dimethylammonium cation*
Authors: A. Kabański, M. Ptak, D. Stefańska

2022/09/11-14 **International Conference on Molecular Spectroscopy (ICMS)**
Oral presentation, best presentation award
Szczawnica, Poland
Title: *Organic-inorganic optical thermometer based on* Cr^{3+} *luminescence*
Authors: A. Kabański, M. Ptak, D. Stefańska

2022/09/04-09 **21st International Conference on Dynamical Processes in Excited States of Solids**
Poster presentation, best poster award
Wrocław, Poland
Title: T*he influence of the* Cr^{3+} *ions concentration on temperature-depending luminescence of* $[DMA]Zn_{1-x}Cr_x(HCOO)_3$
Authors: A. Kabański, T.H.Q. Vu, M. Ptak, D. Stefańska

2022/05/30-07/03 **PhoBiA Annual Nanophotonics International Conference 2022 (PANIC 2022),**
Oral presentation
Wrocław, Poland
Title: *The influence of temperature and* Cr^{3+} *ions concentration on spectroscopic properties of* $[EA]_2NaCr_xAl_{1-x}(HCOO)_6$
Authors: A. Kabański, M. Ptak, D. Stefańska

Organized and participated events

2025/09/16-18	**Preparation of the scientific lecture during Lower Silesian Science Festival (DFN 2025)** *Institute of Low Temperature and Structure Research of Polish Academy of Sciences*
2025/07/02-08	**Conduction of the scientific workshop "Niskie Łąki 2025"** *Institute of Low Temperature and Structure Research of Polish Academy of Sciences*
2024/10/22-25	**Member of the organizing committee** of the XVII International Conference on Molecular Spectroscopy
2024/09/03	**Conduction of the scientific lecture during Lower Silesian Science Festival (DFN 2024)** *Institute of Low Temperature and Structure Research of Polish Academy of Sciences*
2024/07/03-09	**Conduction of the scientific workshop "Niskie Łąki 2024"** *Institute of Low Temperature and Structure Research of Polish Academy of Sciences*
2023/10/13-15	**Member of the organizing committee** of the 7th Conference of Doctoral Students of the PAS (KonDokPAN 2023) *Institute of Low Temperature and Structure Research of Polish Academy of Sciences*
2023/07/28-08/04	**Conduction of the scientific workshop "Niskie Łąki 2023"** *Institute of Low Temperature and Structure Research of Polish Academy of Sciences*
2023/09/16-22	**Conduction of the scientific lecture during Lower Silesian Science Festival (DFN 2023)** *Institute of Low Temperature and Structure Research of Polish Academy of Sciences*
2022/09/4-9	**Member of the organizing committee** of the 21st International Conference on Dynamical Processes in Excited States of Solids *Institute of Low Temperature and Structure Research of Polish Academy of Sciences*
2022/06/29-07/05	**Conduction of the scientific workshop "Niskie Łąki 2022"** *Institute of Low Temperature and Structure Research of Polish Academy of Sciences*

2022/09/16-21	**Conduction of the scientific lecture during Lower Silesian Science Festival (DFN 2022)** *Institute of Low Temperature and Structure Research of Polish Academy of Sciences*

Scholarships and awards

2026/01/14	**Scholarship** from the **Mieczysław Bekker Programme** (National Agence for Academic Exchange) for **the post-doc fellowship** in the Chongqing University of Posts and Telecommunications, Chongqing, China
2025/11/04	**Honorable mention** in the Max Born Scholarship competition in the field of physical and chemical sciences, Wrocław Academic Centre
2024/09/22-25	**Brukker Award** (for **the best poster**) during XVII International Conference on Molecular Spectroscopy, Wojanów, Poland **Financial support for participation in a subsequent conference**
2023/12/08	Participartion in Scentific Section (Academic Radio LUZ), the **finalist of the "Popularyzator Nauki" award** in the "Media" category (organizer: Polish Press Agency), Warsaw, Poland
2023/10/11-13	**Honorable mention** during the Conference of Doctoral Students of the PAS (KonDokPAN2023), Wroclaw, Poland
2023/05/18-19	**Honorable mention** during 10th Doctoral Symposium on Chemistry, Łódź, Poland
2022/10/07	**Award** of the Director of the ILTSR for **the Best PhD Student** of the academic year 2021/2022, Wrocław, Poland
2022/09/11-14	**The best presentation award** during the International Conference on Molecular Spectroscopy, Szczawnica, Poland
2022/09/4-9	**The best poster award** during the 21st International Conference on Dynamical Processes in Excited States of Solids, Wrocław, Poland

Other significant achievements

2025/10	**The implementation of the 3D printing techniques for the design and fabrication of spectroscopic equipment** *I significantly expanded the capabilities of the existing measurement setup by designing and fabricating, using 3D printing, an attachment that enables the integration of a temperature-controlled stage (Linkam THMS600) with an optical microscope coupled to a Photoluminescence Spectrometer FLS 1000 (by Edinburgh Instruments). Further, I subsequently developed a modular system for measuring samples placed in various holders, as well as prepared adapters allowing the use of the optical filters available in the laboratory.*
2021/10-2025/12	**Supervising 10 interns and thesis-students** As part of my scientific activities, I was actively involved in working with interns and thesis students. I introduced them to laboratory practices in both chemical and spectroscopic laboratories, as well as to the methodology of conducting measurements and the subsequent data processing.